Photonic Properties of Organic Micro-Resonators and Ferroelectric Polar Crystal: Two-Photon Luminescence, Second Harmonic Generation, and Terahertz Wave Production

Thesis Submitted for the Degree of

DOCTOR OF PHILOSOPHY

BY

UPPARI VENKATARAMUDU

Reg. No: 12CHPH17

School of Chemistry

University of Hyderabad

Hyderabad-500046, India

Septmeber-2018

CERTIFICATE

This is to certify that the thesis entitled **"*Photonic Properties of Organic Micro-Resonators and -Ferroelectric Polar Crystal: Two-Photon Luminescence, Second Harmonic Generation, and Terahertz Wave Production*"** submitted by **Uppari Venkataramudu** bearing registration number **12CHPH17** in partial fulfillment of the requirements for award of Doctor of Philosophy in the School of Chemistry is a bonafide work carried out by him under my supervision and guidance. This thesis is free from plagiarism as certified by the I.G.M library. This thesis work has not been submitted previously in part or in full to this or any other University or Institution for the award of any degree or diploma. Further, the student has 3 publications before submission of the thesis for adjudication and has produced evidence for the same in the form of reprints.

Parts of this thesis have been published in the following four publications:

1. U. Venkataramudu et al. *Phys. Chem. Chem. Phys.,* **2016**, *18*, 15528. (Chapter-2)
2. U. Venkataramudu et al. *J. Mater. Chem. C,* **2017**, *5*, 7262. (Chapter-3)
3. U. Venkataramudu et al. *Manuscript submitted* (Chapter-4)
4. U. Venkataramudu et al. *J. Mater. Chem. C,* **2018**, DOI: 10.1039/C8TC02638F (Chapter-5)

He has also presented oral/poster presentations in the following conferences:

1. **Invited oral presentation** in EAS-8-2017, CSIR-NIIST, Thiruvananthapuram, Kerala, India.
2. **Oral presentation** in CHEMFEST-2017, SoC, UoH, Hyderabad, India.
3. **Oral presentation** in ICPPC-, Mahatma Gandhi University, Kerala, India.
4. **Best poster prize** in RSC India Road Show, University of Hyderabad, India.

Further, the student has passed the following courses towards fulfillment of the coursework requirement for Ph. D. degree:

	Course	Title	Credits	Pass/Fail
1.	CY-801	Research Proposal	3	Pass
2.	CY-805	Instrumental Methods B	3	Pass
3.	CY-454	Chemical and Statistical Thermodynamics	3	Pass
4.	CY-850	Chemistry of Materials	4	Pass

Prof. Rajadurai Chandrasekar
(Thesis Supervisor)

Prof. T.P. Radhakrishanan
Dean
School of Chemistry

DECLARATION

I hereby declare that the matter embodied in this thesis is the result of investigations carried out by me in the School of Chemistry, University of Hyderabad, Hyderabad, India under the supervision of Prof. Rajadurai Chandrasekar.

In keeping with the general practice of reporting scientific observations, due acknowledgments have been made wherever the work described is based on the findings of other investigators. Any omission or error that might have crept in is regretted.

Uppari Venkataramudu

Dedicated to my beloved parents & my brother

CONTENTS

Acknowledgements

Though only my name appears on the cover page of this thesis, many people are the reason for its production. Foremost, my sincere gratitude to my supervisor, Prof. R. Chandrasekar, for his constant guidance, cooperation, and encouragement. His optimistic approach towards science was admirable and inspiring. I consider my association with him as a cherishable memory in my life.

I would like to thank the present and former Deans, School of Chemistry, for their constant inspiration and for allowing me to avail the facilities at the school. I am extremely thankful to Prof. T. P. Radhakrishnan and Prof. Anunay Samanta, who allowed me to listen to their lectures on Materials Chemistry, Classical and Statistical Thermodynamics courses. I am very much grateful to Prof. Samar Kumar Das, Prof. Kumaraswamy and Prof. D. B. Ramachary for their constant support throughout my research career.

I would like to thank all the non-teaching staff of the School of Chemistry for their cooperation on various occasions, especially, I thank Mr. Bhaskar (LCMS operator), Mr. Satyanarayana (NMR technician), Parveige (HRMS madam), Mr. Durgaprasad Anna (FESEM, TEM operator), Mr. Sunil (FESEM operator), and Mr. Subramanyam (PXRD).

I am extremely thankful for fruitful collaborations with Prof. Surajit Dhara, Prof. S. Srinath, Asst. Prof. Sriram Gopal (School of Physics, University of Hyderabad), and Prof. Anil Kumar Choudhary (ACRHEM) for their instrumental support during my research work. I would also sincerely thank Dr. Ahamad Mohiddon for his most valuable and timely assistance during optical waveguiding measurements on SNOM instrument (CFN, UoH) is impressive. I sincerely acknowledge Mr. C. Sahoo for NLO studies and measurements, Mr. D. Ganesh for THz measurements, Ms. S. Leelasree for electrical measurements, and Dr. Rasana for liquid crystals studies.

I extend my sincere thanks to all my teachers starting from my school to the university for their impressive teaching and education throughout my academics, especially Prof. C. Venkata Rao who taught me moral values and importance of education in society, Mr. Ranganath sir who inspired me with his behavior and character towards human values as well as education. I

would like to acknowledge few of my teachers like Prof. Srinivasulu, Mr. Venugopal Rao, Mr. Venkateswra Reddy, Mrs. Narendra, and Mr. Madanna.

It is a great joy to thank my lab mates, Dr. N. Chandrasekar, Dr. Supratim Basak, Dr. Pramithi, Dr. Ajay, Dr. Narayana, Dr. Annadhasan and Dr. Krrishna, Radhika, Anjana, Ravi, Jyothi, Vinay, Vinod for their help, pleasant company and cooperation during my Ph.D. tenure. From the bottom of my heart, I thank my seniors Dr. N. Chandrasekar Dr. Supratim Basak, Dr. Pramiti Hui, Dr. Ajay and Dr. Narayna for their outstanding support, discussions. I wish to thank my junior Mr. Ravi, Ms. Jyothi, and Mr. Vinay for their help when I was in need.

I would also like to express my sincere thanks to all my beloved seniors in the school of chemistry with whom I have wonderful memories on this campus.

I am really fortunate for my close association with some of my friends in HCU which include Dr. Sudheer, Dr. Kesav, Dr. Sudhakar anna, Satyanarayana (Badam), Suresh, Dr. Ramu anna (ILS), Ramakrishna, Sunny, Naveen (mama), Dr. Sreenu, Mohan, Billa, Konda Reddy, Dr. Kouishk (for discussions on organic synthesis), Dr.Navendu (for lot of scientific discussions), Sudipta, Ranjani, Srujana, Lasya, Divya, Dr. Chandu anna, Dr. Hari anna, Dr. Guptha anna, Praveen, Sankar, Rangu Prasad, Anand, and so many others.

It's my pleasure to acknowledge my lovable friends from my hometown Venkatesh, Ravi, Raju, Uday, Vijay, Hemalatha, Rupa and some other. It is indeed my great pleasure to thank my B.Sc. Classmates, M. D. Rafi, A. Rajasekhar, Ramesh, Sidu, Ashok. I especially thank my M.Sc. Classmates Sekhar, Laxman, Gangu Naidu, Upendra, Jagadheesh (Bava), Kiran, Puspa lingam, Ramakrishna(Raki baba), Mahesh, Dr. Balaji, Giri, Sreenu, Puspha latha, Sudha rani, Deepthi for memorable moments which I have shared with them.

Finally, I am greatly indebted from the bottom of my heart to my parents Sri. Sreeramulu garu & Smt. Mangamma garu, without their sacrifice and mental support I would not have reached up to this stage. The way I grew up, the values I imbibed, the education I received and the person I am now is all because of them. I am grateful for my caring and loving brother Ugandhar who has always been an ardent listener, strong supporter and constant encouragement during the last period of my Ph.D. life which is never forgettable. My sister, Ramadevi, always showered unconditional love and support on me. I remember, she gave her pocket money to pay my school admission fee and this I can never repay back.

LIST OF ACRONYMS

μ	dipole moment
μm	micrometer
μ_r	relative permeability
^1H	proton
a_0	Bohr radius
a_{ex}	exciton Bohr radius
AFM	atomic force microscope
c	concentration
c	speed of the light in vacuum
$\chi^{(1)}$	linear electric susceptibility
$\chi^{(2)}$	second order nonlinear susceptibility
$\chi^{(3)}$	third order nonlinear susceptibility
CB	conduction band
CCDC	Cambridge crystallographic data center
cm	centimeter
CT	charge transfer
CVD	chemical vapor deposition
CW	continuous wave
D	electric displacement field
D	diameter of a micro-sphere
ε	materials permittivity
E_B	exciton-binding energy
E_{at}	atomic field strength
E	electric field

EDXS	energy dispersive X-ray spectroscopy
EM	electro magnetic
ε_o	free space permittivity
EP	exciton polariton
ε_r	relative permittivity
FDTD	finite-difference time-domain
FESEM	field emission scanning electron microscopy
FLIM	fluorescence life time imaging microscopy
F-P	Fabry-Pèrot
FSR	free spectral range
FWHM	full width at half maximum
GM	Göppert-Mayer
HOMO	highest occupied molecular orbital
Hz	Hertz
IR	infrared
I	Intensity of incident light
k(ω)	wave vector
L	cavity length
l_c	coherence length
LPEF	long pass edge filter
LSP	localized surface plasmon
LUMO	lowest unoccupied molecular orbital
m*	effective mass
MHz	megahertz
mp	melting point
mW	milli Watt
n	refractive index

n_2	nonlinear refractive index
n_{eff}	effective refractive index
NIR	near infrared
*n*J	nano Joule
NLO	non-linear optics
nm	nanometer
NMR	nuclear magnetic resonance
ns	nano second
OPA	one photon absorption
P(t)	induced polarization
PDT	photo dynamic therapy
PL	photoluminescence
PM	Phase matching
Q-Factor	quality factor
RPM	rotation per minute
RT	room temperature
SAED	selected area electron diffraction
SHG	second harmonic generation
SNOM	scanning near filed optical microscopy
T	temperature
t	time
TCSPC	time-correlated single photon counting
TE	transverse electric
TEM	transmission electron microscope
TIR	total internal reflection
TM	transverse magnetic
TPA	two photon absorption

TPL	two photon luminescence
τ_P	photon life-time
THz	Terahertz
UV	ultra violet
VB	valance band
Vis	visible
WGM	whispering gallery mode
z_0	Rayleigh range
α_o	linear absorption coefficient
β	first hyperpolarizability
α	linear polarizability
γ	second hyperpolarizability
$\grave{\sigma}_2$	Two photon absorption cross-section
Δ	heat
δ	NMR chemical shift in ppm
Δλ	line width of peak at full width at half maximum
Θ	analyzer angle
θ	polar angle
λ_{max}	wavelength maximum or absorption maximum
μJ	micro joules
π-π	pi-pi
τ	FL life-time
ω	angular frequency

1

Introduction

1.1. Nano/Micro-Photonics – an Introduction:

The concept of nano-science has evolved from the visionary lecture delivered by *Richard Feynman*, at *California Institute of Technology* entitled *"**there is plenty of room at the bottom**"*.[1,2] After the invention of advanced microscopy techniques, the principle of nano-science and technology[3] has been applied to various fields of research such as Chemistry, Physics, Mathematics, Biology, Medicine, Engineering, etc. As a result of this interdisciplinary approach, many technological breakthroughs and innovations have been achieved in various disciplines, particularly in the area of nano-photonics by combining chemistry and physics.[4-8]

Research in the area of nano-photonics provides an alternative opening to overcome the restrictions in electronic and opto-electronic devices.[9-11] The key technologies in nano-photonics are based on the development of optical methods and the creation of low-cost novel materials suitable for the production of high performance miniaturized photonic devices. For decades, chemists and materials scientists have been playing an important role in the synthesis of molecular materials and their miniaturization into micro- or nano-structures suitable for photonic devices.[12-16] From the perspective of chemical composition, nano-photonic materials can be categorized into inorganic and organic materials. The former materials have been most extensively examined from the beginning of the upsurge of nano-science and the latter materials are not well explored so far though it is superior to inorganics. To understand the advantage of organic nano-photonic structures over inorganic structures, it is important to look into the physics of these materials during the light-matter interaction. For example, in semiconductors, the most interesting forms of light-matter interaction is the formation of exciton-polaritons (EP).[17-20] By the absorption of light from the irradiation source, the electron in the ground state of semiconducting materials will go to the excited state leaving a hole, thereby forming an electron-hole pair, called an exciton. In the confined system, exciton and photon combine to produce a quasi-particle called EP. This exciton can either recombine into a photon (radiative recombination) or thermally dissipate (non-radiative).

An important difference between inorganic and organic semiconductor materials is their exciton binding energies (E_B). The stability of EPs can be expressed by using the E_B, the E_B is associated with Bohr radius[£] [21] (a_o) by

$$E_B = \frac{q^2}{2\varepsilon_r a_o} \qquad \cdots\cdots\cdots\rightarrow 1.1$$

Where q is the electron charge and ε_r is the relative permittivity or dielectric constant.[#] The dielectric constant is related to materials permittivity (ε) and free space permittivity (ε_0) by the relation $\varepsilon_r = {}^{\varepsilon}/_{\varepsilon_0}$. The ε_r is a dimensionless number, is generally a complex-valued and it is not a constant but a function of frequency, $\varepsilon_r(\omega)$.

Another important difference between organic and inorganic semiconductor is their ε_r values, which is in the range of 3 and 6-12, respectively. The band structure of inorganic semiconductor consists of discrete bands with filled valance bands and the empty conduction band.[22-25] The band structure of organic semiconductors is composed of orbitals by the highly occupied molecular orbital (HOMO) and lowest unoccupied molecular orbital (LUMO) represent the energy gap (Figure 1.1).

The Wannier-Mott excitons are the lowest-lying electronic excitations in inorganic semiconductors.[26] In Wannier-Mott excitons, the separation of electron-hole is an order of magnitude greater than lattice dimensions. This is due to the large ε_r values and consequence reduction of the Coulomb interaction between the electrons and holes (decrease of E_B). Wannier-Mott excitons dissociate at room temperature (RT), because of their lower binding energy (E_B ~ 10-20 meV) in comparison to RT thermal energy (k_BT = 25.6 meV, where is k_B Boltzmann's constant).

[£]The Bohr radius, which is conventionally defined as the radius of the maximum probability for finding the ground state electron in the hydrogen atom is defined as $a_0 = \frac{h^2}{4\pi^2 me^2}$ = 0.529 Å, 0.053 nm, 53 pm. Here a_0 is Bohr radius, h is plank constant, m stands for mass of electron and e corresponds to electron charge.

[#]Generally the value of $n = \sqrt{\varepsilon_r}\mu_r$, where μ_r is the relative permeability. For a non-magnetic material, μ_r ~ 1. Therefore $n = \sqrt{\varepsilon_r}$. Since ε_r is the complex function with the real and imaginary parts, $\varepsilon_r = \varepsilon'_r + i\varepsilon''_r$ and so the value of n also a complex function, $\varepsilon_r = n^2 = (n' + in'')^2$.

ε_r is related to the refractive index (n) and electric susceptibility (χ) of the material by the following relation; $n = \sqrt{\varepsilon_r} = \sqrt{1+\chi}$

The Frenkel type excitons are characteristic excitons in organic semiconductors (charge-transfer character).[28] The Frenkel excitons are stable at RT because of their strong binding energy (E_B, 0.1 – 10 eV) facilitated by the location the electron and hole in the range of Bohr radius (small a_0). The E_B of organics is higher than inorganic

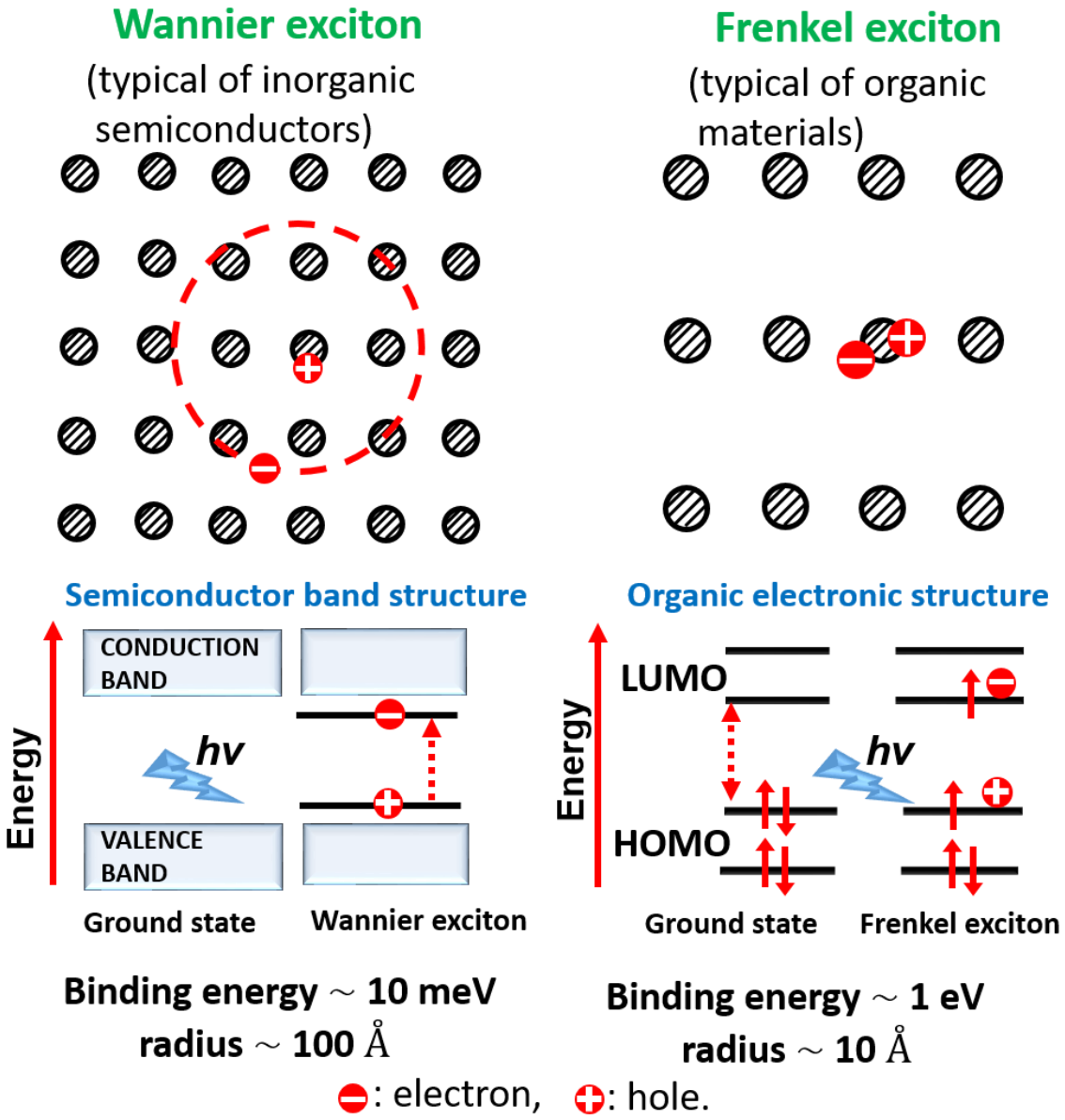

Figure 1.1: Types of excitons propagation in inorganic and organic semiconducting molecules and their corresponding band structure diagram, respectively.[27]

semiconductors. In charge transfer excitons, the carriers are typically located on nearest or next-nearest neighbour molecules. This remarkable excited-state (exciton) features

make organics essentially dissimilar from their inorganic systems, which after forming EPs provide excellent photonic properties down to micro-scale such as subwavelength waveguides, high-quality resonators, and RT lasers.[29]

The organic nano-structures materials exhibit relatively high optical loss compared with inorganic materials it is because of the low n (low ε_r) of former and, they still attract the attention of materials chemists and physicists because of their diverse structural shapes and opto-electronic properties. The optical and opto-electronic properties of organic solid state materials are dependent exclusively on their weak intermolecular interactions[30] because organic nanostructures are shaped through interactions such as hydrogen bonding[31], π–π stacking[32], van der Waals forces[33] and charge transfer interactions.[34-36] These weak intermolecular interactions allow fabrication of more simplistic superior organic nano-structures under mild conditions compared to their inorganic counterparts. Further, it is established that well-ordered organic molecules in the solid state show diverse energy/electron transfer processes and have excessive charge-carrier mobility,[37,38] thus allowing intense luminescence, effective photon confinement, stronger EP coupling, etc. Organic materials also show tunable optical properties based on molecular design (conjugation, symmetry, polarizability, refractive index), size and shape-dependent light confinement, flexibility, optical (linear and nonlinear), opto-electrical, and opto-mechanical properties.[39-42]

The above attributes offer organic nano-materials better optoelectronic and photonic performances such as optical waveguiding, emission at diverse wavelengths, low-threshold nano-lasers, light-emitting devices, photon-detecting devices, etc.

1.2. Fabrication Methods for Photonic Structures:

Fabrication methods are classified into Top-down and Bottom-up approaches based on the way of the assembly of atoms or molecules within in the system.[43-45] Using the above techniques organic molecules can be easily processed into nano-/micro-structures of various shapes via solution and sublimation based technologies.

1.2.1. Top-Down Approach:

Breaking down a large piece of a macro-scopic material down to nano-scopic level in an orderly fashion is known as a top-down approach. Renowned techniques, such as photolithography and electron beam lithography,[46] anodization, ion- and plasma-

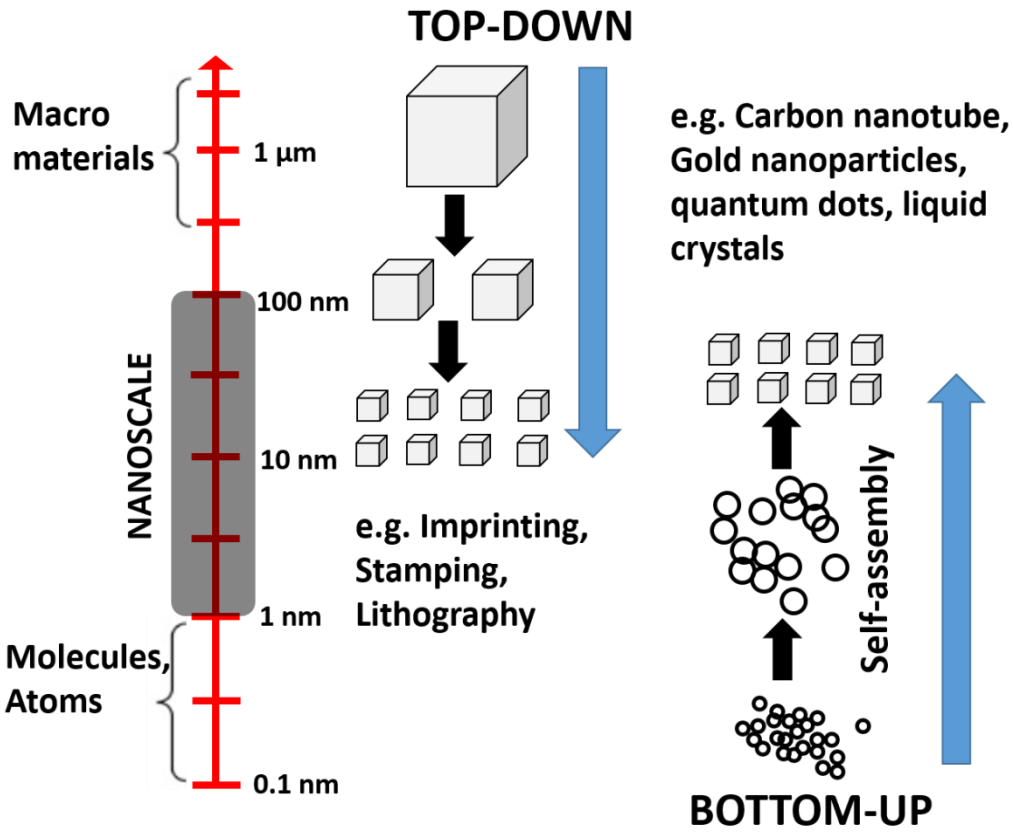

Figure 1.2: Approaches toward nano-/micro-structure production.

etching, and micro-contact printing all belongs to this type of approach. Here the former technique can be used to achieve feature less than 100 nm. Nano-imprint lithography can be used to achieve sizes down to 10 nm, and further improvement of this technique is still in the research stage (Figure 1.2). [47-49]

1.2.2. Bottom-Up Approach:

In the bottom-up approach "smaller atomic and molecular components are arranged into larger nano-/micro-scopic assemblies. This type of assembly is driven by intermolecular interactions viz. hydrogen bonds (~5–30 kJ/mol), π–π interaction

(~8–12 kJ/mol), and van der Waals forces (~2–4 kJ/mol), which are weaker than the chemical bonds between atoms (~150–1000 kJ/mol).[50-52] The examples of bottom-up methods are, self-assembly of nanoparticles or polymers, [53] small organic molecules, [54] chemical or electrochemical reactions for precipitation of nanostructures, sol-gel processing, laser pyrolysis, and chemical vapor deposition (CVD). Although the use of the bottom-up self-assembly principle for miniaturization is cost-effective, the potential of self-assembly is not in small size but in a complex organization and collective action.[55,56]

1.3. Organic Photonic Solids:

1.3.1. Organic Optical Waveguides:

An optical waveguide is a physical micro-and nano-structure is one of the essential tools of miniaturized nano-photonic devices. These structures are used for guiding the electromagnetic waves into the desired path from one point to other along a

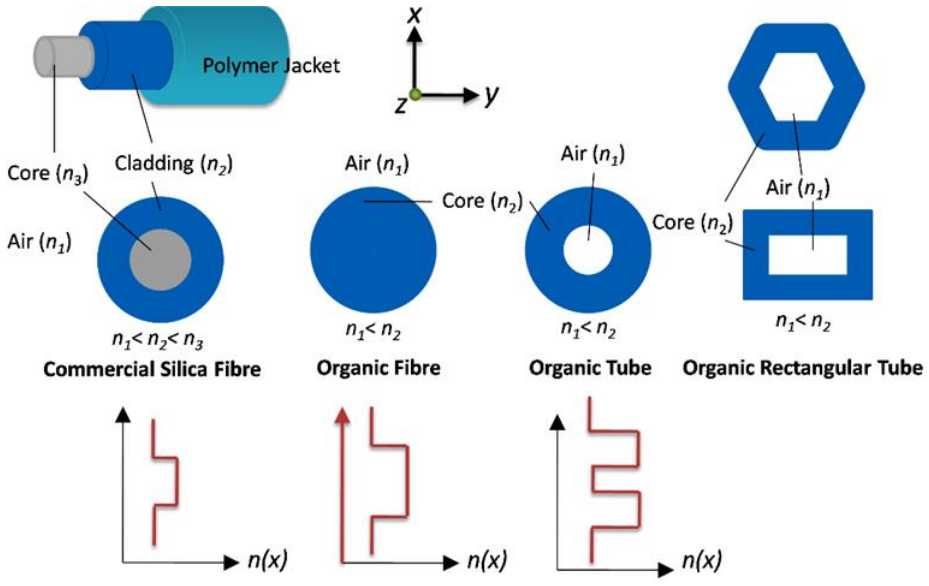

Figure 1.3: Cartoon representation of the cross-sections of various organic optical waveguides in comparison with a commercial silica fiber. *n* = refractive index. Reproduced from ref. 62 with permission from The Royal Society of Chemistry.

particular direction.[57,58] In 2009, Prof. K. Kao has received the Noble Prize in Physics for his breakthrough experiment on the light transmission in silica fibers for optical communication.[59] Commercial optical fibers are much thicker than the human hair (10

– 100 μm) composed of either transparent polymers or silica (Figure 1.3). These fibers consist of core and cladding, where refractive index (*n*) of the core is higher than that of the cladding. Consequently, the light is transmitted inside the core because of total internal reflection (TIR). Due to the high refractive index ($n \sim 1.56$-1.6), organic one dimensional (1D) structures such as fibers, tubes, and rods, can also confine photons and propagate them along their long axis. One of the exciting properties of organic optical waveguides is their micro-size, high-flexibility, which are important to alter the target of the guided source light down to micro-domain. Organic optical waveguides are categorized into two types such as *active waveguides*[60,61] and *passive waveguides* [62-65] based on the type of light-organic matter interaction within the structures (Figure 1.3).

1.3.2 Active Organic Optical Waveguides:

In an organic *active optical waveguide*, the building block molecules absorb the input laser radiation and propagate the spontaneously emitted fluorescence (FL) towards the output end of the elongated structure via EP type propagation mechanism.[66-69] One of the main criteria to excite an active optical waveguide is that the wavelength of the interacting light should be within the solid-state absorbance range of the molecular matter. Nano-/micro-organic optical waveguides fabricated from small organic building blocks possess 1D structure for example nano-wires, nano-fibers, nano-ribbons, nano-rods, and nano-tubes, etc. Besides, 1D-waveguides, 2D structures such as sheets, and tiles have drawn much more attention due to their directional 2D light propagation (1D optical confinement). Recently, multidimensional shape-shifting organic waveguides are also of interest since these shapes can be exploited in directional waveguiding and also in light harvesting applications.

For example, Zhao et al prepared tubular 1D micro-rods and micro-tubes from 9,10-bis(phenylethynyl)anthracene (BPEA) molecule via self-assembly technique on a quartz substrate. BPEA is a light-emitting dye with very high luminescence efficiency.[70] The FL microscopy image of the BPEA tubes displayed a typical green to yellow emission. Further, a very bright luminescence spot which appeared at both tips of each tube and relatively weaker emission from the tube bodies confirmed their optical waveguiding

characteristics (Figure 1.4a). Further BPEA tubes let the locally excited FL propagate along the long axis of the elongated structures and out-couple at the tube tips (Figure 1.4b). The refractive index of the BPEA is ~1.65, and that of the quartz substrates is ~1.5 at the measured wavelength. The small difference in the refractive indices results in a substantial optical energy leakage from the micro-rods. However, in tubular structures, propagation of light at the boundary of BPEA and the air inside the tube, eliminating the optical loss considerably.

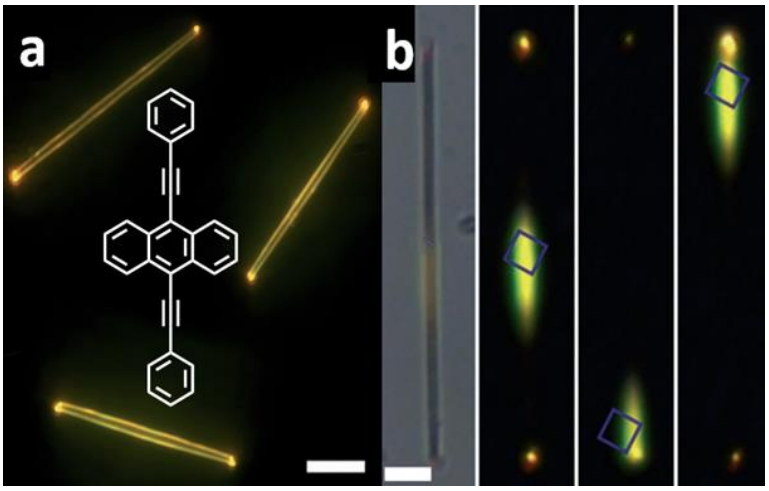

Figure 1.4: a) FL microscopy image of some isolated BPEA tubes excited with blue light (460–490 nm). Scale bar is 20 µm. b) Bright-field image and micro area FL images obtained by exciting the identical tube at three different positions. Scale bar is 10 µm. The squares indicate the excited positions. Reprinted with permission from ref. 70. Copyright 2013 Wiley-VCH Verlag GmbH & Co. KGaA, Weinheim.

1.3.3 Passive Organic Optical Waveguides:

Passive optical waveguides,[63,64] on the other hand do not absorb (*elastic light-matter interaction*) the input light source, except some weak scattering interactions (Raman scattering, etc.,), consequently they guide the source laser light along the waveguide. The function of passive organic waveguides is quite similar to commercial optical fibers. Passive organic waveguides can be activated by exciting them with a light source of a wavelength away from the molecular absorbance window of the material. Thereby electronic excitation and PL can be avoided and the input light can be guided to the output end of the waveguide. In 2013, for the first time, Chandrasekar et al. at the University of Hyderabad have demonstrated, the

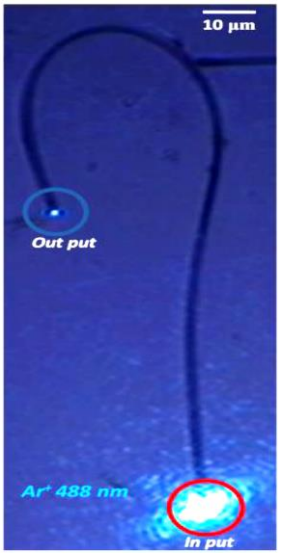

Figure 1.5: Passive optical waveguiding behavior of an organic bent tube. Reproduced from ref. 62 with permission from The Royal Society of Chemistry.

passive waveguiding nature of self-assembled organic submicro-structures (Figure 1.5).[65,66]

1.4. Optical Micro-Cavities:

Optical cavities or resonators play an essential role in laser devices, optical filtering, nonlinear optics (NLO) and so on.[71-76] Photons are trapped in all dimensions depending upon the geometry of the optical cavities, subsequent producing optical resonance within a small volume of materials. This optical confinement enhances light-matter interactions within or surface of the cavity (dye material, single molecule, single virus, etc.) and thus improving the intensity of the resultant optical signal compared with that in free space.[77-81]

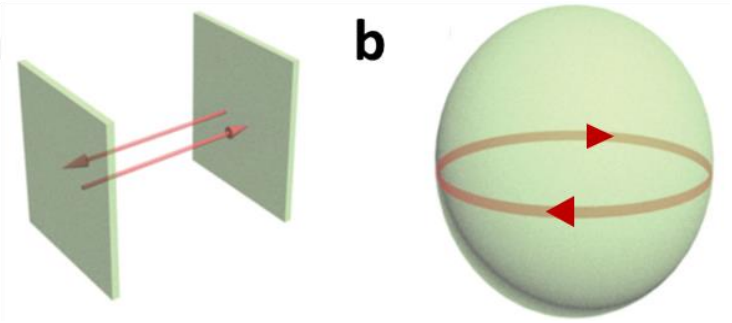

Figure 1.6: Micro-cavity configurations according to different confinement methods. a) Fabry–Perot micro-cavity. b) Whispering gallery mode micro-cavity.

In a conventional optical cavity, trapped light reflects several times between the mirrors and subsequently, only a certain number of frequencies of light will be sustained by the constructive interference, while the remaining will be suppressed by destructive interference. [82-85]

Generally speaking, the configuration of micro-cavities can be classified based on light confinement geometries as (Figure 1.6);[86-90]

- Fabry–Perot (F-P) micro-cavity
- Whispering-gallery-mode (WGM) micro-cavity

In this thesis F-P and WGM resonators are presented, hence their basics will be discussed briefly in the following sections.

1.4.1. F-P Micro-Cavities:

In F-P resonators extremely reflecting mirrors are employed and numerous reflecting light beams superimpose to produce interference patterns, producing clearer optical fringes. For this purpose, a combination of mirrors which are mounted parallel to

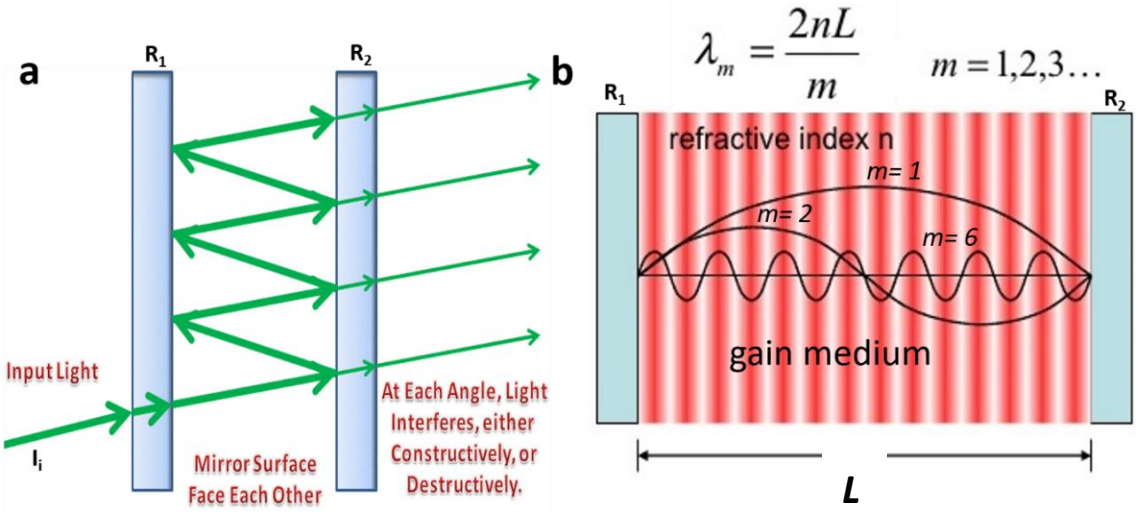

Figure 1.7: a) F-P micro-cavity with two mirrors (R_1 and R_2). Here R_1 is fully reflective and R_2 is partial reflective mirrors. b) F-P resonator representing with standing waves.

each other is used.[91] Amongst organic micro-structures mainly, nano-wires, micro-rods, micro-sheets and micro-tapes act as F-P resonators (Figure1.8).[92- 94]

To understand the function of F-P resonators, at the start, let us consider a beam of unicolor light of wavelength λ, and intensity I_i is incident on the flat parallel mirror

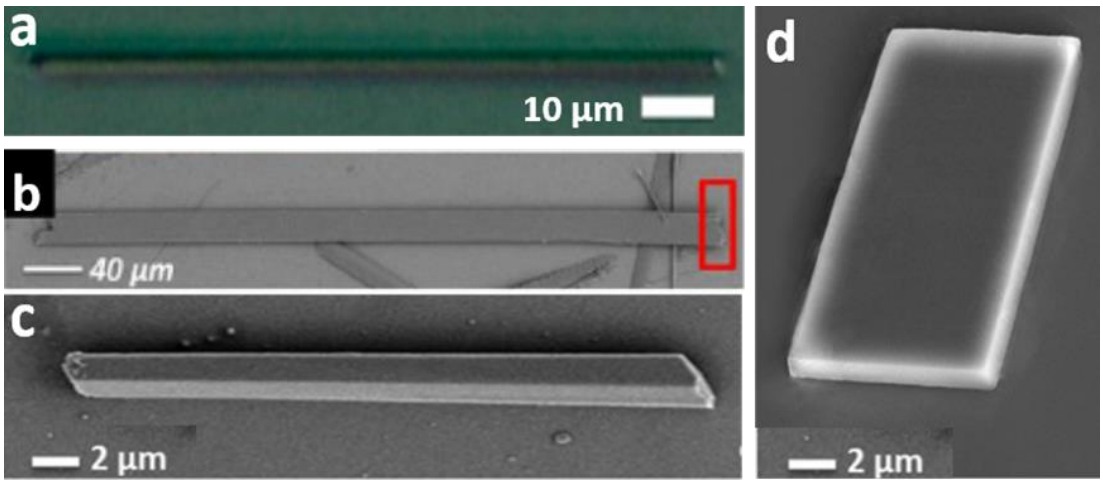

Figure 1.8: The different geometries of organic F-P resonators. The geometries a, b, c and d are nanowire, nano-/micro-tapes or ribbons, micro-rod, and micro-sheet, respectively.

separated by some distance (also known as cavity length L) to a second mirror and is reflected several times back and forth by the reflecting surface of the mirrors. At resonant condition, that is, when the round-trip path length of light is equal to an integer number of the light λ, constructive optical interference takes place inside the cavity. [94] This is mathematically expressed as,

$$n.L = m.\frac{\lambda}{2} \qquad \cdots\cdots\cdots\rightarrow 1.2$$

where n, and L are the phase refractive index of crystal and round-trip distance, respectively, and m (an integer) is the order of mode. If the above condition is not fulfilled, due to destructive interference, the light is almost completely suppressed.

For 1D organic structures such as micro-wires, micro-rods, nano-/micro-tapes, and 2D structures like micro-sheets, and micro-tiles the expected resonator type is F-P (Figure 1.8). For example, Zhao et al reported F-P type micro-wire (MW) cavities composed of 2-(2'-hydroxyphenyl)benzothiazole (HBT) molecules, (Figure 1.9a), which were self-assembled via a liquid-phase method.[95] The FL microscopy image of the HBT micro-wire, shown in Figure 1.9b presents an intense green FL. The scanning electron

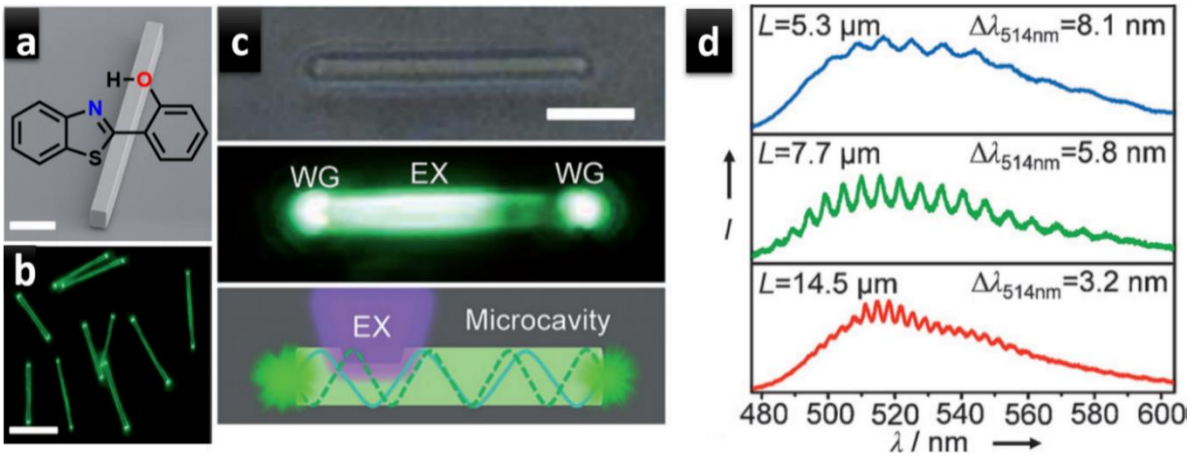

Figure 1.9: a) SEM image of a HBT micro-wire with square cross-section and smooth face. Scale bar: 2 μm, chemical structure of HBT. b) FL image of some discrete HBT wires excited with the UV band (330-380 nm) of a mercury lamp. Scale bar: 10 μm. c) Bright-field (top) and FL (middle) images of a single HBT wire (L=14.5 μm) excited with a pulsed laser (355 nm). EX: excited spot; WG: waveguided spot. Scale bar: 5 μm. Bottom: depiction of a nanowire waveguide, with cleaved ends defining a F-P cavity. d) Modulated FL spectra collected at the guided tips of three HBT nanowires with different lengths. Reprinted with permission from ref. 95. Copyright 2013 Wiley-VCH Verlag GmbH & Co. KGaA, Weinheim.

microscopy (SEM) image showed a distinct wire-like morphology with smooth surfaces of HBT micro-wire (Figure 1.9a). When a single HBT micro-wire was excited locally with a focused femto-second pulse laser beam (355 nm, 150 fs), a guided propagating green light from excitation point to the tip ends was observed (Figure 1.9c). This revealed that the photons can be efficiently confined and guided along the wire axis, and outcoupled selectivity from the tips. The HBT micro-wire can be treated as F-P cavity, with two flat end facets serving as mirrors for the reflection action to occur. This leads to a discrete set of resonant modes in the FL spectra (Figure 1.9d). To investigate the micro-cavity effects, FL spectra were collected from the end tips of HBT micro-wire of different lengths (L = 5.3, 7.7, 14.5 μm). As shown in Figure 1.9d, with an increase of cavity length the modulated FL spectra presented an increasing number of modes. This is because the mode spacing (Δλ) or free spectral range (FSR) is inversely related to nano-wire length (L) as per the equation

$$FSR\ (or)\ \triangle\lambda = \lambda^2/2Ln_g \qquad \cdots\cdots\cdots\rightarrow 1.3$$

where n_g is the group refractive index as a function of wavelength. The linear relationship between $\lambda^2/2Ln_g$ and the length of the nanowires indicates that the FL modulation is resulted from the axial F-P-type cavity resonance. [Discussed in detail section 1.4.4]

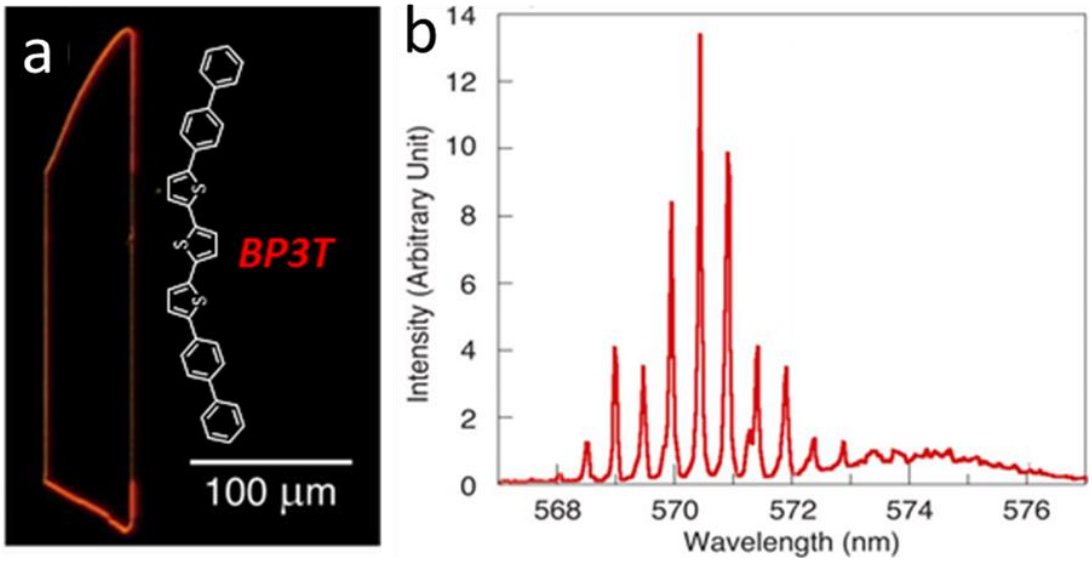

Figure 1.10: a) The FL image of a BP3T crystal under ultraviolet light and BP3T chemical structure. b) Spectrum of the BP3T crystal due to the natural F-P resonance of parallel crystal edges. Reprinted with permission from ref.96. Copyright 2013 Springer Nature.

Similarly, Bisri et al reported a single-crystal F-P micro-crystal cavity composed of 5,5''-di([1,1'-biphenyl]-4-yl)-2,2':5',2''-terthiophene (BP3T) molecules, self-assembly via a liquid-phase method.[96] Figure 1.10a presents the FL microscopy image of the BP3T single crystal with sharp and parallel crystal edges showing a strong orange FL from its edges. The high-resolution FL spectrum of BP3T crystal clearly depicts sharp modes due to F-P resonance (Figure 1.10b).

1. 4. 2. Optical WGM Micro-Cavities:

The term whispering-gallery-waves (acoustic waves) was first coined by Lord Rayleigh in to describe the sound amplification phenomenon of the gallery located under the dome of St. Paul's Cathedral in London.[97,98] Later, Raman and Sutherland visited the

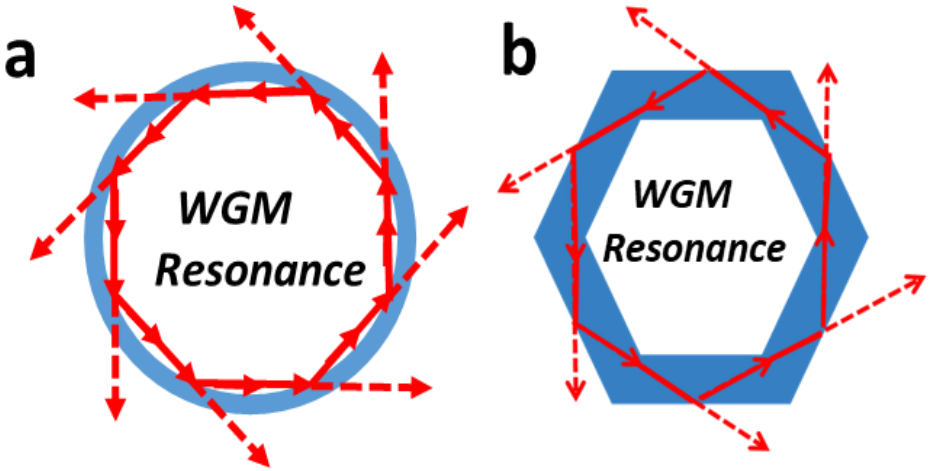

Figure 1.11: a, b) Schematic of light confinement inside a spherical and hexagonal WGM micro-cavities by total internal reflection.

same cathedral and conducted a series of experiments to improve the observation made by Lord Rayleigh.[99] This effect can also be observed in light waves trapped within micro-sized circular or spherical or hexagonal structures producing WGMs or resonances in the FL spectrum. These modes correspond to the frequency of the waves circling around the cavity. In a 2D WGM micro-cavity, light is confined as a result of numerous TIR which occurs at the interface of the cavity surface and air (Figure 1.11). Further, the strong optical confinement is due to the large refractive index contrast between the resonator material and its surrounding.[100,101]

Suppose if the circular cavity is optically lossless then self-interference between waves occurs after the light traveling one round, light waves which satisfy the following fundamental resonance condition can be self-reinforced while others are blocked.

$$m\lambda = 2\pi n_{eff} R \qquad \cdots\cdots\cdots\rightarrow 1.4$$

n_{eff} is the effective refractive index of the resonant mode, R is the resonator radius, λ is the light wavelength in vacuum, and m is an integer giving the number of wavelengths in a round trip of the resonator (mode number).

WGM resonators (WGMRs) can sustain transverse electric (TE) and transverse magnetic (TM) modes[¢].[102,103] The following equations are needed to comprehend the polarized resonant wavelengths inside the cavity.[104]

$$\lambda_{TE} \approx \frac{2\pi R n_1}{m+1.856m^{\frac{1}{3}}+\left(\frac{1}{2}-\frac{n_1}{\sqrt{n_1^2-1}}\right)} \qquad \cdots\cdots\cdots\rightarrow 1.5$$

$$\lambda_{TM} \approx \frac{2\pi R n_1}{m+1.856m^{\frac{1}{3}}+\left(\frac{1}{2}-\frac{1}{n_1\sqrt{n_1^2-1}}\right)} \qquad \cdots\cdots\cdots\rightarrow 1.6$$

Equations 1.5 and 1.6 are the expression for the TE and TM resonant modes in a WGM micro-cavity surrounded by air. The prerequisite for a WGM micro-cavity is $n_1 > 1$ so that light can be confined via total internal reflection. Thus, $\frac{n_1}{\sqrt{n_1^2-1}}$ is larger than $\frac{1}{n_1\sqrt{n_1^2-1}}$ and TE modes resonate at longer wavelengths than TM modes for the same mode number m.

Importantly, circular resonant cavities provide much higher quality (Q) factors compared to WGM cavities. The optical resonant modes which are formed in cavities is dependent on the geometric properties, such as size, shape, and composition of the supporting structure. Till now, various structures are reported for sustaining optical

[¢] In the TE mode, the electric field is transverse to the direction of propagation while the magnetic field is normal to the direction of propagation. In the TM mode, the magnetic field is transverse to the direction of propagation while the electric field is normal to the direction of propagation.

WGMs. These WGMRs are fabricated by using both organic and inorganic molecules. Here, organic WGM resonators are highly advantageous in providing different resonator geometries such as micro-spheres, micro-rings, micro-disks, micro-tubes, micro-capillaries, micro-bubbles, and micro-hemispheres (Figure 1.12) which are tested in various applications.[106–111]

WGMRs provide high *Q*-factor, low mode volume, and a large optical storage density.[112] These are important parameters, which can define and characterize WGMRs, some of them are discussed below.

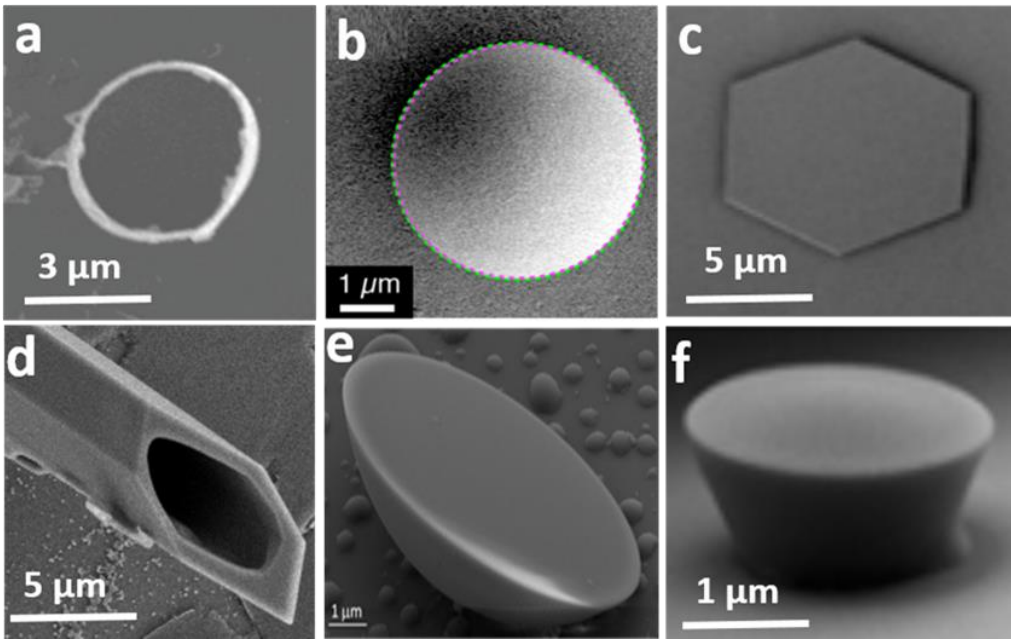

Figure 1.12. Geometries of organic WGMRs: a) micro-ring, b) micro-sphere, c) micro-sheet, d) micro-tube, e) micro-hemisphere and f) micro-frustum.

1.4.3. Q-Factor:

In order to measure the light trapping efficiency of a micro-cavity, *Q*-factor is used. It is defined as the ratio of the optical energy stored in the cavity to the energy dissipated per cycle. It can be estimated from an intense optical mode of the resonance spectrum according to the following equation.

$$Q = \frac{\lambda}{\Delta\lambda} = \frac{\text{Stored Optical energy}}{\text{Optical Power loss}} \qquad \cdots\cdots\cdots\rightarrow 1.7$$

where λ is the resonance wavelength of the peak, and $\Delta\lambda$ is the line width (FWHM) of the resonant mode. Consequently, Q-factor can be simply calculated from the transmission or PL spectrum of the resonant mode. The Q-factor[112-115] is also affected by various optical losses which occur in a resonator. The total optical losses of a resonator coupled to a waveguide consist of material absorption loss (Q_{mat}), scattering loss (Q_{ss}), radiation loss (Q_{rad}), and external coupling loss (Q_{ex}). Totally all these loss mechanisms are known as the intrinsic loss of the resonator. The global Q-factor is estimated by the individual loss terms according to where Q_{mat} is associated with light absorption of the material constituting the resonator, Q_{ss} signifies scattering loss due to surface in homogeneities and contaminants, Q_{rad} is connected to the radiation loss, i.e., leakage of light through the curvature surface, and Q_{ex} relates to the loss induced by the waveguide coupling or light coupling.[113-115]

$$\frac{1}{Q} = \frac{1}{Q_{mat}} + \frac{1}{Q_{ss}} + \frac{1}{Q_{rad}} + \frac{1}{Q_{ex}} \qquad \cdots\cdots\cdots\rightarrow 1.8$$

Scattering loss can be decreased by reducing the resonator surface roughness or removing impurities attached to the resonator surface by improving the fabrication process. Radiation loss directly depends on the size of the resonator and can be reduced by increasing the size to a certain extent. When the resonator size is larger than a certain value, light bending radiation loss becomes insignificant compared to other loss mechanisms.

High-Q micro-cavities are extremely important for the realization of low-threshold lasers. Regrettably, organic F-P type micro-wire cavities usually show very small Q-factors (from hundreds to thousands) because of their low end/lateral-facet reflectivity. This is because of the undesired out-coupling of photons from such F-P-type cavities.[116] In comparison, organic micro-rings or micro-disks can support WGM resonances, where the FL photons can be firmly confined by TIR at the cavity periphery, possibly contributing to a very high Q-resonances. The Q-factor is directly related to photon

lifetime (τ_P) of a resonator, τ_P is the time necessary for the optical energy in the resonator cavity to decay to 1/e of its original value.[116]

1.4.4. Free Spectral Range:

The free spectral range (FSR) is used to describe the size-effect of an optical resonator on the number of modes. FSR value characterizes the spacing (in optical frequency or wavelength) between two successive optical modes belong to the same family.[117] FSR gives a quantitative measure of the length or diameter of the cavity (see equations 1.3).

The FSR or Δλ can be calculated from the distance between two adjacent angular mode numbers m and $m-1$. In a WGM micro-cavity, we have the following equation for the fundamental modes (radial mode number r = 1):

$$2n_{eff}\pi R = m\lambda_m = (m-1)\lambda_{m-1} = (m-1)(\lambda_m + \Delta\lambda) \qquad \cdots\cdots\cdots\rightarrow 1.9$$

where n_{eff} is the effective index or n_g group refractive index, in case of pulse laser excitation. R is the radius of the WGM micro-cavity, $m\lambda_m$ and $(m-1)\lambda_{m-1}$ are wavelengths of two successive modes. The FSR is related to R by the following equation.

$$\text{FSR} = \Delta\lambda = \frac{\lambda^2}{2n_g\pi R} \qquad \cdots\cdots\cdots\rightarrow 1.10$$

In correspondence with the refractive index, n_g of a material can be defined as the ratio of the vacuum velocity of light to the group velocity in the medium.

1.5. Polar Molecular Crystals:

In a polar crystal, there is a direction which is not transformed in the opposite direction by any symmetry operation of the crystal class; that direction is named as the *polar axis* of the crystal. The unit cells of polar crystals possess a nonzero dipole moment due to non-centrosymmetric nature.[118] Hence these crystals are NLO active and further, it is exploited for various advanced technological applications, such as pyroelectricity, piezoelectricity, ferroelectricity, second harmonic generation (SHG), terahertz (THz) production, and electro-optic effect.[118-120]

In centrosymmetric crystals, the center of symmetry transforms each direction in the opposite one thereby making them non-polar. Interestingly, only 10, out of the 21 crystal classes are polar. Structural point of view, ferroelectric polar crystalline materials are generally classified as inorganic, organic-inorganic, supramolecular and single-component-organics.[121-126] Amongst the later type of crystals, molecules owning high molecular hyperpolarizability (β) add together due to near parallel order of the molecular dipoles thus increase the macroscopic second-order nonlinear susceptibility ($\chi^{(2)}$). The dipole-dipole intermolecular forces play a significant role in crystals of dipolar organic molecules. Further, organic polar crystals are decisive for their optical transparency, stability, light-weight, lower-cost, solution processability, and environmentally friendly nature.[127]

A recent example of a polar organic crystal which is grown from 2-[3-(4-hydroxystyryl)-5,5-dimethylcyclohex-2-enylidene]malononitrile (OH1) molecule shown in Figure 1.13a.[128] The molecule OH1 is nearly planar with the exception of the $C(CH_3)_2$

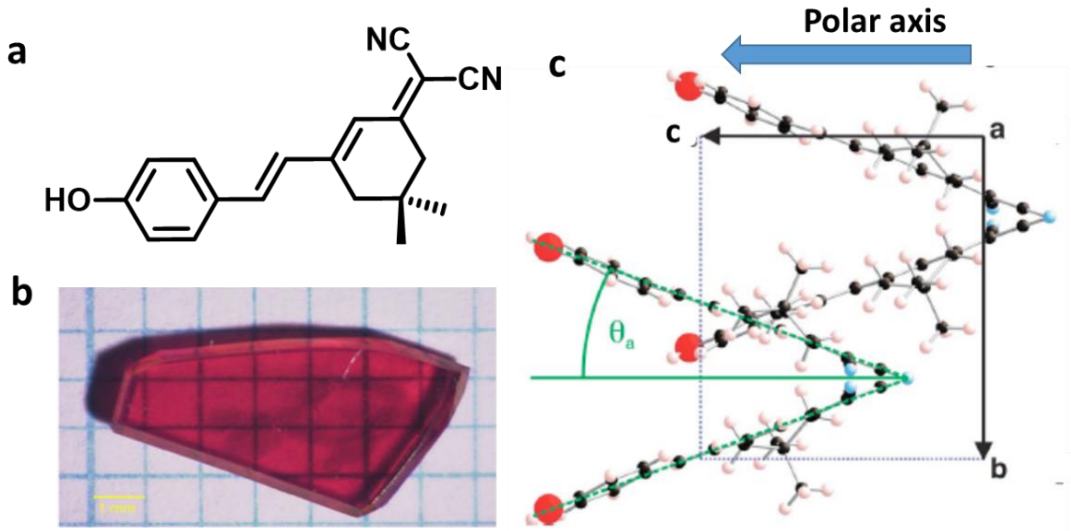

Figure 1.13: a) Chemical formula of the molecule OH1. b) photograph of OH1 c) View of the unit cell of OH1 projected along the *a* axis. The charge transfer axes of the molecules form an angle θ_a= ±20.2° with the crystallographic *c* axis in this plane. Reprinted with permission from ref.128. Copyright 2013 Wiley-VCH Verlag GmbH & Co. KGaA, Weinheim.

group. It crystallizes in the orthorhombic space group $Pna2_1$ (point group mm_2) with four molecules within the unit cell. The main direction of the first hyperpolarizability β of the molecules (charge transfer axis) forms an angle of θ= ±28° with the polar *c* axis. The

molecular arrangement in the *bc* plane of the unit cell is presented in Figure 1. 13(c). The angle between the polar axis and the projection of the molecular main axis β onto the *bc* plane is θ_a = ±20.2°. The dielectric axes also coincide with the crystallographic axes because of the orthorhombic symmetry of the crystal.

1.6. Ferroelectricity:

Polar crystalline materials act as ferroelectrics via electric switching of their inherent electric polarization.[129-135] After the discovery of Rochelle salt, a double salt of tartaric acid, $[KNaC_4H_4O_6]\cdot 4H_2O$ with the ferroelectric transition temperature (T_c) of 296 K, the pursuit for room temperature ferroelectric materials is an ever-continuing one.[136] Especially, ferroelectric random access memory and ferroelectric field-effect transistors are contemporary goals for practical applications.[137]

In a ferroelectric material, the individual dipole moments add up producing a net permanent dipole moment or macroscopic polarization (P). Therefore P cannot be generated in a structure which has a center of symmetry, because any dipole moment produced in one direction would be forced by symmetry to be zero. Consequently, non-centrosymmetric materials exhibit ferroelectrics property.

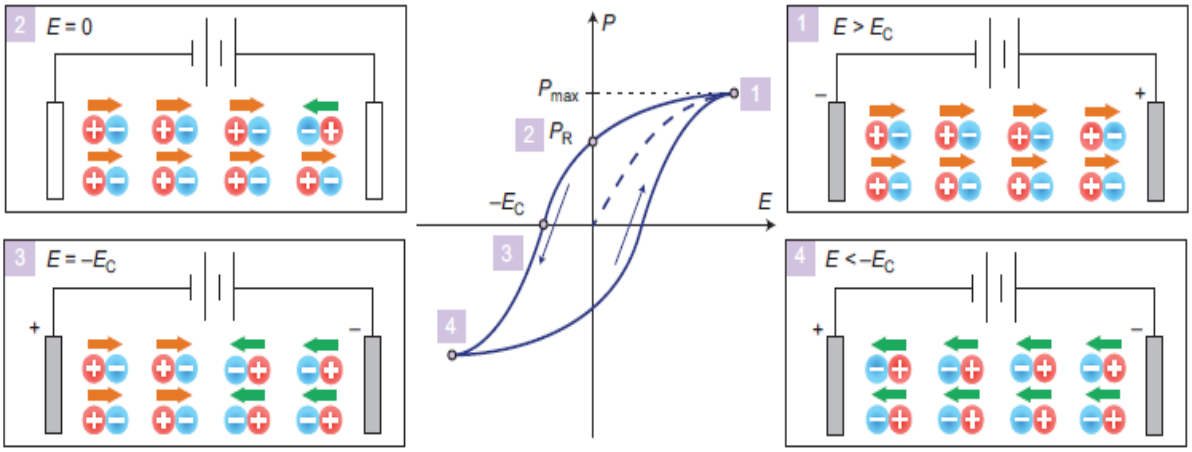

Figure 1.14: The hysteresis loop of electric field (E) against polarization (P) is one type of evidences for ferroelectricity. This electronic behaviour occurs because of the lattice distortion that rearranges the orientation of dipoles within a material in the presence of an electric field. The polarization value in the absence of an electric field is known as the remnant polarization (P_r) and the electric field needed to reverse the polarization is called the coercive field (E_C). Reprinted with permission from ref.138. Copyright 2013 Springer Nature.

In ferroelectric materials, the critical electric field necessary for reversing the polarization is known as a coercive field (E_c) (Figure 1.14). The electric displacement (D) as a function of field strength (E) accordingly draws a hysteretic curve (D–E loop) between opposite polarities, and this electric bistability can be used for non-volatile memory elements. When the applied electric field returns to zero, a remnant polarization P_r remains which is either positive or negative depending on the history of the applied field. The field at which the polarization switches sign is called the coercive field E_c. To enable low voltage switching, E_c must be small or the ferroelectric needs to be thin.

Ferroelectric materials differ from dielectrics by their behavior in response to an electric field. A dielectric is an electrically insulating material which becomes polarized in an electric field. Its behavior is described by the electric displacement field D, which is defined as:

$$D = \varepsilon_0 E + P \qquad \cdots\cdots\cdots\rightarrow 1.11$$

with ε_0 the permittivity of free space, E the electric field and P the polarization density. Both D and P have charge per unit area (C/m^2) as dimensions. Most dielectrics are adequately termed as linear, homogeneous, isotropic and instantaneously responsive to the electric field. In such a case, the polarization P *or* P_{lin} is proportional to the applied field E. Hence, a measurement of D versus E forms a straight line through the origin:

$$P_{lin} = \varepsilon_0 \chi E \qquad \cdots\cdots\cdots\rightarrow 1.12$$

$$D = \varepsilon_0(1 + \chi)E = \varepsilon_0 \varepsilon_r E \qquad \cdots\cdots\cdots\rightarrow 1.13$$

where, P_{lin} is the linear polarization, χ the electric susceptibility, and ε_r the relative permittivity or dielectric constants, which are dependent on the nature of dielectric material.

The hysteresis loop of the electric field (E) against polarization (P) is one type of evidence for ferroelectricity (Figure 1.14). For a true ferroelectric material, the remnant polarization is persistently reversible by an electric field. These bistable states are thermodynamically stable due to cooperative interactions which favour a parallel alignment of electric dipoles. The appearance of these dipoles depends on the type of ferroelectric material those are (i) displasive type and (ii) order-disorder type (Figure

1.15).[139-141] The first type is triggered by the relative displacement of ions, which generates spontaneous polarization, an example is as $PbTiO_3$. This type of ferroelectricity involves some structural instability that produces spontaneous lattice deformations into a polar state. This state can happen only when an electrostatic attractive force is originally in a subtle balance with the rival short-ranged repulsion force between the ions. The second type is the *order-disorder* ferroelectric which is composed of polar ions

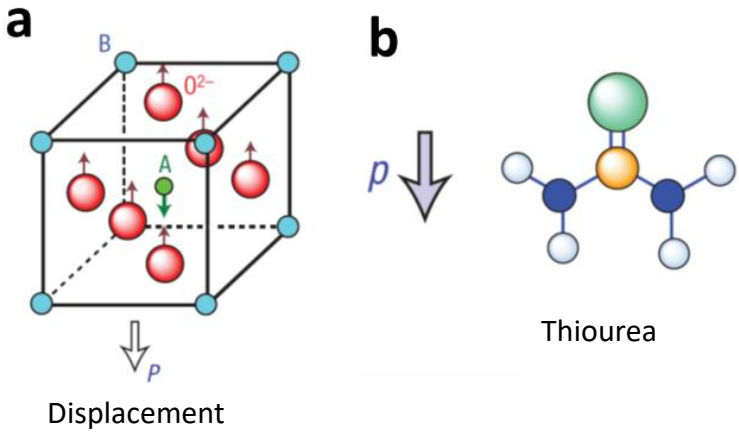

Figure 1.15: Representation of ferroelectric materials and the origin of their dipole moment *p* or polarization *P* (open arrows). a) Typical examples of displasive type ferroelectric inorganic materials. b) Conventional organic ferroelectric substances. Reprinted with permission from ref.142. Copyright 2013 Springer Nature.

or molecules with a permanent dipole. In the paraelectric phase, these permanent dipoles are randomly oriented which results in a zero net dipole. In the ferroelectric phase, the permanent dipoles are aligned in such way that a net macroscopic dipole arises. An example is the organic compounds like thiourea, OH1, 2,2,6,6,-tetramethyl-1-piperidinyloxy (TEMPO) free radical and copolymers of vinylidenefluoride and trifluoroethylene.[142,143]

In ferroelectric materials, the Curie temperature (T_c) defined the paraelectric to a ferroelectric phase transition. In addition to usual ferroelectricity, upon femtosecond optical pumping polar organic crystals might display technologically useful second-order nonlinear optical (NLO) effects such as (i) second harmonic generation (SHG)[144,145] under proper phase-matching conditions, wherein two low energy photons (ω) are destroyed in non-centrosymmetric materials to create one photon of twice the energy (2ω) and (ii) terahertz (THz) generation[146] via optical rectification of femtosecond laser

pulses. SHG is useful in ultra-fast all-optical processing, electro-optical modulation, and frequency conversion, sensors, and memory device applications[147-150] and THz is essentially useful to investigate phase transitions, ferroic order excitations, magnetization dynamics, ferroelectric excitations, superconductive properties, and linear and nonlinear phonon excitations.[151-154]

1.7. Nonlinear Optical Properties:

In NLO materials, the response of an optical material is no longer proportionate to the amplitudes of applied electric and magnetic fields.[155-160] NLO phenomena are only observable during the interaction of highly intense light such as a pulse laser with NLO material. Here the laser light is sufficiently intense to modify the optical properties of matter (for example an electronic intensity of 5×10^{11} V/m binds the electron in a hydrogen atom) and hence produce detectable NLO effects. The NLO response of atoms

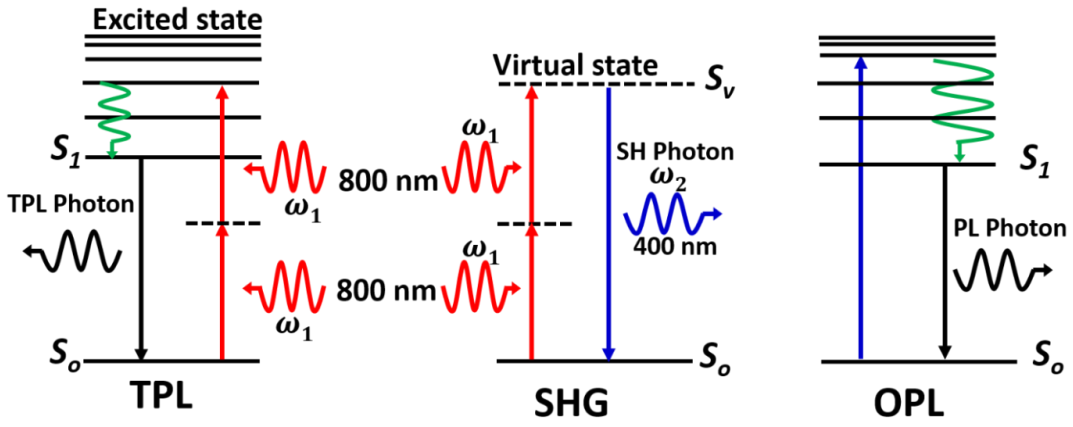

Figure 1.16: Graphical representation of TPL, SHG, and OPL processes. Here S_0 is ground state, S_1 is first excited state, and S_v corresponds to virtual state.

arises due to an anharmonized distortion of the electron clouds of an atom induced by the incident intense light energy. The electric field, *E* causes a separation of charge in the direction collinear to it due to the displacement of the positively charged nucleus in the *E*-direction and the negatively charged electron cloud in the opposite direction. The response of an optical material is articulated in terms of the induced macroscopic polarization.[161-165]

In NLO materials the polarization (P) depends upon the strength of the input electric field (E).[166-169] The interaction time between the electrical oscillations and the bound electrons in the atoms is extremely short, producing an instantaneous response of the medium. To describe more precisely the concept of an optical nonlinearity, let us consider how the dipole moment per unit volume or time-dependent polarization $P(t)$ depends on the strength $E(t)$ of an applied field.

In linear optical materials, the induced polarization is proportional to the amplitude of the applied electric field:

$$P(t) = \varepsilon_0 \chi E(t) \qquad \cdots\cdots\cdots\rightarrow 1.14$$

In NLO materials, the relation between P and E is no longer linear. The microscopic polarization P_{micro} induced in an atom or a molecule by an external optical field E can be written as Equation 1.15, where the vector quantities P_{micro} and E are related by the tensor quantities α, β and γ, which are often denoted to as the linear polarizability, first hyperpolarizability, and second hyperpolarizability, respectively.

$$P_{micro}(t) = \alpha E(t) + \beta E^2(t) + \gamma E^3(t) + \cdots \qquad \cdots\cdots\cdots\rightarrow 1.15$$

Similarly, the simplest form of macroscopic polarization P_{macro} induced in a medium by optical fields can be represented by a power series in the optical fields as given in Equation 1.16,[170] where E is the total optical field, the $\chi^{(n)}$ is the nth-order dipole susceptibility.

$$P_{macro}(t) = \varepsilon_0[\chi^{(1)}E(t) + \chi^{(2)}E^2(t) + \chi^{(3)}E^3(t)] + \cdots \qquad \cdots\cdots\cdots\rightarrow 1.16$$

$$P_{macro}(t) = P^{(1)}(t) + P^{(2)}(t) + P^{(3)}(t) + \cdots \qquad \cdots\cdots\cdots\rightarrow 1.17$$

Where $\chi^{(2)}$and $\chi^{(3)}$are known as the second- and third-order NLO susceptibilities, respectively. Typical values can range from 1 to 100 pm/V for $\chi^{(2)}$and from 10^{-24} to 10^{-19} m^2/ V^2 for $\chi^{(3)}$.

The ratio of successive terms in the polarization P can be described approximately by Equation 1.18, where E_{at} is atomic field strength at a distance equal to the Bohr radius a_o of the proton. So, $E_{at} = {}^{e}/_{4\pi\varepsilon_o a_o^2} = 5.15\times10^9$ V/ cm. This corresponds to laser power 7×10^{16} W/ cm^2, while irreversible NLO effects appear generally with laser powers less than 10^{11} W/ cm^2.

$$\left|P^{(n+1)}/_{P^{(n)}}\right| \sim \left|E/_{E_{at}}\right| \qquad \cdots\cdots\cdots\rightarrow 1.18$$

$\chi^{(1)}$ is of the order of unity for condensed matter, $\chi^{(2)} = \chi^{(1)}/(E_a)^2 = {}^{1}/_{E_a} \cong 1.94 \times 10^{-12}$ m/V and $\chi^{(3)} = \chi^{(1)}/(E_a)^2 \cong 3.78 \times 10^{-24}$ m^2/V^2.

1.7.1. Second-Order NLO Interactions:

The important outcomes of the second-order NLO effects are (i) SHG) and (ii) THz production. In the former case, two low energy photons (ω) are destroyed in non-centrosymmetric materials to create one photon of twice the energy (2ω), whereas in the latter case, and THz pulses are generated via optical rectification (OR) of the fundamental femtosecond laser pulses. The second-order term of the nonlinear polarization is given in eq. 1.19,

$$P^{(2)}(t) = \varepsilon_0 \chi^{(2)} E(t)^2 \qquad \cdots\cdots\cdots\rightarrow 1.19$$

As pointed out earlier, second-order NLO interactions can arise only in non-centrosymmetric crystals, that is, in crystals that do not exhibit inversion symmetry $\big(P(-E)\big) = -P(E)$ which leads to the cancellation of induced polarization.

The principal prerequisite for a material to produce a second-order NLO response is noncentrosymmetry of the structure along the direction of the electric field. Consider a material with inversion center such that it is symmetric in all directions. If the electric field with time-dependent magnitude

$$E(t) = E_\omega \cos \omega t \qquad \cdots\cdots\cdots\rightarrow 1.20$$

is incident upon such a medium, the magnitude of the subsequent second-order polarization filed is written as

$$P_2(t) = \varepsilon_0 \chi^{(2)} \mathrm{E}^2(t)$$

Due to the inversion symmetry, the following relation must exist:

$$-P_2(t) = \varepsilon_0 \chi^{(2)}[-\mathrm{E}^2(t)] \quad \cdots\cdots\cdots\rightarrow 1.21$$

$$-P_2(t) = \varepsilon_0 \chi^{(2)}\mathrm{E}^2(t) \quad \cdots\cdots\cdots\rightarrow 1.22$$

Equations 1.21 and 1.22 can both be true only if the polarization field is zero, representing $\chi^{(2)}$= 0 for centrosymmetric media. Further, this can be exemplified by bearing in mind that the induced dipole moment of a second-order NLO molecule in a sinusoidal electric field polarization in the plane of the page, both linear media and centrosymmetric nonlinear media yield a polarization field that includes only odd harmonics.

In a second-order NLO process, the resultant nonlinear polarization created in a NLO medium can be written as

$$P^{(2)}(t) = \frac{1}{2}\varepsilon_0 \chi^{(2)} E_0^2 + \frac{1}{2}\varepsilon_0 \chi^{(2)} E_0^2 \cos 2\omega t \quad \cdots\cdots\cdots\rightarrow 1.23$$

Equation 1.23 shows that $P^{(2)}(t)$ consists of two terms, the first term is a non-frequency contribution known as OR and second term contributes to generation of 2ω (SHG).

OR, which is the generation of a steady polarization or low-frequency polarization in certain nonlinear crystals by the action of an intense femtosecond pulse optical field, was first observed in crystals of KH_2PO_4 (KDP) upon transmission of ruby-laser radiation. As per the linear electro-optic effect, the polarization of a crystal is changed by the application of an electric field. On the other hand in case of OR process, the reverse happens; a change in the polarization of an NLO material generates a direct current (DC). One of the important outcomes of OR process from the NLO material is a generation of radiation in the order of THz in the range of 0.1 THz and 20 THz. OH1 crystal as discussed earlier in section 1.5 is well-known for the generation of THz waves.[171-173]

1.7.2. THz Radiation Generation:

The THz frequency gap is positioned between high-frequency electronics (microwaves) and long-wavelength photonics (Far IR).[174-178] THz generation via OR process is currently the driving force for developing and optimizing advanced NLO

materials. For this, the crystal should be transparent in the THz region and must possess a high electro-optic coefficient. Many dielectric crystals like ZnTe, GaP and organic crystals such as DAST, and OH1 are known for THz generation via OR process (Figure 1.17). The organic materials show higher THz wave generation efficiency than inorganic materials, due to the low dispersion of the dielectric constant (refractive index).

OR is a second-order mixing process in which an envelope of a femtosecond pulse interacting in NLO crystal produces a time-varying low-frequency polarization in the THz

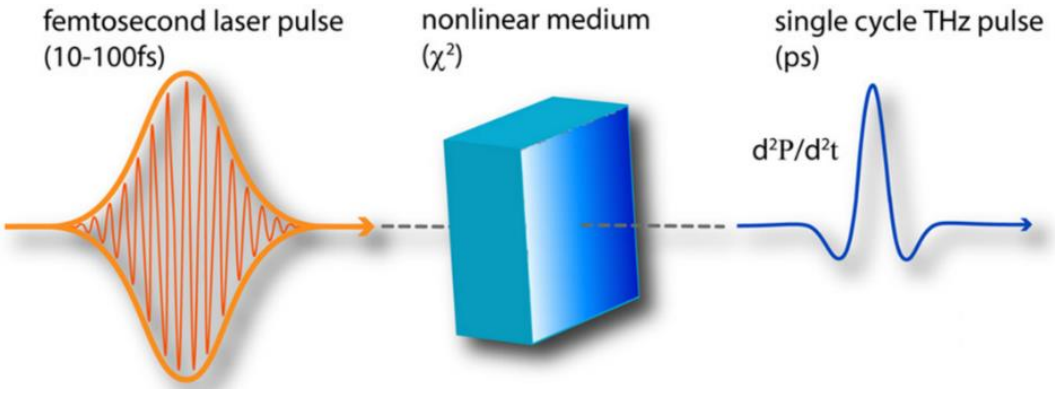

Figure 1.17: THz generation through optical rectification in a nonlinear medium (taken from internet source).

region. For efficient conversion, the optical group velocity (v_g) of the generating pulse should match with generated THz phase velocity which is given in equation 1.24.

$$E_{THz}(t,\omega) \propto \frac{\partial^2 P(t,\omega)}{\partial t^2} \propto \omega_x I(\omega_x) \qquad \cdots\cdots\cdots\rightarrow 1.24$$

Fundamentally, the produced THz wave is proportional to second order derivative of second order polarization (from equation 1.24) and the second order polarization is proportional to the intensity of the femtosecond pulse. Basically, THz is second order derivate of optical pulse envelope (Figure 1.17).

The THz radiation range is dependent upon the duration of the pulse. The shorter the pulse, the broader the possible THz frequency range will be. For instance, a femtosecond laser pulse with a pulse length of 20 fs can generate a broadband THz pulse in a NLO crystal extending up to about 20 THz. The main requirement for OR is again good phase matching between the pump optical wave and the generated THz wave, often referred to

as velocity matching, because the generated THz wave should travel at a speed close to the pump optical pulse in the crystal.

1.7.3. Phase Matching Condition:

The efficiency of the NLO frequency conversion will be maximum only when the second harmonic (SH) waves generated by different atoms interfere constructively or, at best, do not cancel each other (Figure1.18a). For an efficient production of SHG and THz, the condition, $k_2 = 2k_1$ is to be satisfied, where $k_1$and k_2 are wave vectors. This requires same *phase velocity* of both SH and fundamental beam and can be written more generally for 2D space as

$$k_2 = 2k_1;\ \Delta k = 0 \qquad \cdots\cdots\cdots\rightarrow 1.25$$

The above relation is known as *perfect phase matching condition*,[179-182] were Δk is phase mismatch factor. The phase matching condition needs conservation of linear momentum to endure a mutual interaction over extended regions of space between the fundamental and the generated harmonic field.

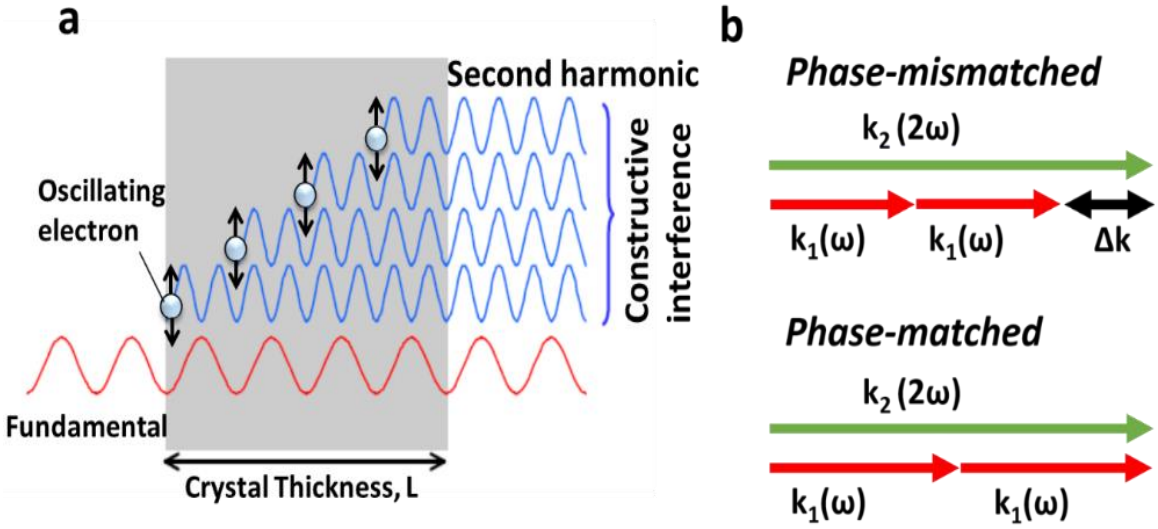

Figure 1.18: a) Second harmonic generation is phase-matched when both the fundamental and the SH waves travel with the same velocity. b) Vectorial representation of phase-mismatched and phase-matched conditions.

That is, for efficient SHG and THz generation, the *n* of the material should be the same at frequencies ω and 2ω. Nevertheless, most optical materials demonstrate dispersion of refractive index, wherein the normal dispersion region, the refractive index

increases with increasing frequency of light, thus usually, $n_{2\omega} > n_{\omega}$. Hence, mostly the above condition in Eq. 1.26 is not met, and therefore generally the phase mismatch factor is non-zero $\Delta k \neq 0$. Here, the coherence length l_c relates to the distance over which the SHG intensity drops to zero after propagating in the material.

$$l_c = \frac{2\pi}{\Delta k} = \frac{2\pi}{k_{2\omega} - 2k_{\omega}} = \frac{\lambda_{\omega}}{2(n_{2\omega} - n_w)} \qquad \cdots\cdots\cdots\rightarrow 1.26$$

λ_{ω} is the wavelength of the fundamental beam. The l_c indicates the maximum (homogeneous) crystal or medium length that is use full in producing the SH power.

1.7.4. Two-Photon Absorption and Emission:

The theory for two-photon excitation was first proposed by Maria Göppert-Mayer,[183] which was later experimentally substantiated by Kaiser and Garret.[184] In two-photon absorption (TPA), the molecule interacts with two photons of light simultaneously in its ground state and gets excited whereas, in one photon absorption (OPA) the electron gets promoted to its excited state from its ground state by absorbing one photon. In TPA, the virtual or intermediate transition state is of importance for understanding and describing the total event. TPA is of a great interest in numerous applications[185,186] including microscopy, optical power limiting, 3-D fluorescence imaging, photodynamic therapy, non-invasive bioimaging, localized release of bio-active species, up-converted lasing, micro-fabrication and three-dimensional data storage.

In two-photon excitation process a fluorophore or chromophore simultaneously absorb two photons and gets electronically excited as shown Figure 1.16. In contrary, the normal OPA process typically requires high energy photons in the ultraviolet or blue/green spectral range. Nevertheless, the same excitation process can be generated in two-photon active materials by the simultaneous absorption of two less energetic photons (in the infrared spectral range) under suitably intense laser illumination.

Distinctive from OPA, TPA is governed by different selection rules, [187-190] in highly symmetric molecular systems an entirely different set of electronically excited states can be accessed and probed. An elegant description of selection rules for TPA can be found in ref. [185]. In particular, a TPA transition is allowed only between two states

possessing same parity. In molecules with an inversion center, allowed two-photon transitions are from a gerade (g) state to another g state or from an underage (u) to another u state, but not between g and u states, whereas in one photon transition opposite parity (from g to u, or vice versa) is allowed. Consequently, in centrosymmetric molecules, if the transition from the ground state to any given excited state is one-photon allowed then TPA is not allowed and vice versa. For molecules without center of inversion, certain transitions can be both one-photon and two-photon allowed.[191] The observation of these one-photon forbidden transitions provides invaluable molecular information complementary to the one-photon spectrum. The theoretical basis for TPA is as follows:

According to the basic theory of TPA, the weakening of a light beam passing through an optical medium of thickness z can be written as:

$$\frac{dI(Z)}{dz} = -\alpha I(z) - \beta I^2(z) - \gamma I^3(z) \qquad \cdots\cdots\cdots\rightarrow 1.27$$

Here I is the intensity of the incident light beam propagating along the z -axis and α, β, and γ, are one-, two-, and three- *photon absorption coefficients* of the transmitting medium.

The nonlinear refraction (n_2) can be related to the real part of $\chi^{(3)}$ and written as

$$n_2 = \frac{3}{4\varepsilon_0 n_0(\omega)^2 c} Re\left[\chi^{(3)}\right] \qquad \cdots\cdots\cdots\rightarrow 1.28$$

Where ε_0 is the free-space permittivity, $n_0(\omega)$ is the linear refractive index at frequency (ω), and c is the speed of light in vacuum.[190] The unit of n_2 is m^2/W. This quantity expresses itself as a change in the refraction of a material that is dependent on input intensity:

$$n = n_0 + n_2 I \qquad \cdots\cdots\cdots\rightarrow 1.29$$

The change in refractive index induces a phase change in the incident optical field and this phase change is intensity-dependent:

$$\Delta\phi = \frac{2\pi}{\lambda_o} n_2 IL \qquad \cdots\cdots\cdots\rightarrow 1.30$$

Where L is the length of the nonlinear material and λ_o is the wavelength of the optical field. This intensity-dependent phase change can affect the field propagation in space by speeding up or retarding the phase front and causing certain propagation effect such as self-focusing and self-defocusing.

The magnitude of TPA can be characterized as a TPA coefficient (β) or TPA cross section (σ). Just like the nonlinear refractive index, the TPA coefficient is a macroscopic quantity and can be related to the imaginary part of $\chi^{(3)}$ and is written as

$$\beta = \frac{3\omega}{2\varepsilon_0 n_0(\omega)^2 c^2} Im\left[\chi^{(3)}\right] \qquad \cdots\cdots\cdots\rightarrow 1.31$$

Where the units of β is in m/W; moreover, β can also be written as a term in the overall absorption coefficient (α),

$$\alpha = \alpha_0 + \beta I \qquad \cdots\cdots\cdots\rightarrow 1.32$$

Where α_0 is the linear absorption coefficient.

Normally, it is assumed that the incident light has a uniform transverse intensity distribution and the initial intensity is not dependent on time. The intensity attenuation via TPA can be described as a function of propagation distance in the z-direction i.e. TPA appears when there is no linear absorption (α_0 = 0),

$$\frac{dI(z)}{dz} = -\beta I^2(z) \qquad \cdots\cdots\cdots\rightarrow 1.33$$

The effect of $\beta(\lambda)$ induce an intensity- dependent attenuation of the amplitude of the incident optical field as it propagates through a TPA medium.

$\beta(\lambda)$ is a macroscopic parameter which depends also on the concentration of the TPA molecules, therefore,

$$\beta(\lambda) = \grave{\sigma}_2(\lambda) N_0 = \grave{\sigma}_2(\lambda) N_A d_0 \times 10^{-3} \quad \text{[in units of cm/ GW]} \qquad \cdots\cdots\cdots\rightarrow 1.34$$

Where, $\sigma`_2(\lambda)$ is the molecular TPA cross-section, in units of cm^4/ GW that illustrates average TPA per molecule, N_0 is the molecular density in units of $1/cm^3$, N_A is Avogadro's

number, and d_0 is the molar concentration of the absorbing molecules in units of M. Similar expression for TPA cross section is

$$\sigma_2(\lambda) = \sigma`_2(\lambda).h\nu \text{ [in cm}^4\text{/(photon/s) or cm}^4\text{ s units]} \quad \cdots\cdots\cdots\rightarrow 1.35$$

Here 1GM = 10^{-50} cm^4 s.

The magnitude and phase of $\chi^{(3)}$ are associated to its real and imaginary components (determined by the Z-scan technique) as follows: $|\chi^{(3)}| = \sqrt{[Re(\chi^{(3)})^2 + Im(\chi^{(3)})^2]}$ and $\phi = arctan[Im(\chi^3)/\, Re(\chi^3)]$. This can be equivalently expressed as (where ϕ is argument of $\chi^{(3)}$)

$$Re(\chi^{(3)}) = |\chi^{(3)}| \bullet cos\,\phi, Im(\chi^{(3)}) = |\chi^{(3)}| \bullet sin\,\phi \quad \cdots\cdots\cdots\rightarrow 1.36$$

Re($\chi^{(3)}$) is associated with nonlinear refraction while the $Im(\chi^3)$ is related with nonlinear absorption.[184]

7.1.5. NLO Materials:

Swift progressions in the field of photonics have increased the demand for new NLO materials. NLO materials possess applications in various fields, such as optical data storage, telecommunications, and optical information processing. These materials nonlinear response is determined by the nature of the electronic environment of the medium, its symmetry and the nature of the nonlinear interaction. These applications and properties have attracted many chemists to perform the chemical synthesis, and physicists to target and characterize their functional properties. These materials can be organic, inorganic, semiconductors and polymers.[186]

Inorganic materials can be covalent or ionic, which are commercially available and are used as modulators, optical switches, electro-optic devices, frequency doubler or parametric oscillators. Examples of inorganic materials are lithium niobate ($LiNbO_3$), potassium dihydrogen phosphate (KDP), and BariumBoronoxide (BBO). Semiconductor materials like gallium arsenide or Cadmium selenide (these being used as quantum dots) are also used extending Indium antimonide (InSb) has one of the largest known $\chi^{(2)}$ value.

$LiNbO_3$ is the most widely investigated material for electro-optic device applications KDP is used in high-powered near-IR lasers because it produces phase-matched SHG.[189]

Organic materials are chemically bonded molecular units interacting through weak van der Waals interactions. They are emergence as an alternative to inorganic materials because of their specific advantages such as fast response time, cost-effective, intrinsic tailor ability and versatility from the chemical synthesis.[184-187] Aromatic organic dye compounds and compounds with extensive π-electron delocalization can act as nonlinear materials. These molecules can be easily dispersed in solutions and crystallized into molecular solids. Basically organic NLO single crystals require molecules with electron donating and accepting groups connected by a conjugated linker. There is a tradeoff between the nonlinearity and the wavelength range of optical transparency. Longer π-conjugated units normally give a larger hyperpolarizability β but also lower the energy of the first allowed optical transition. The hyperpolarizabilities are strongly dependent on the length L of the molecular system.[184]

$$\alpha \propto L^3$$

$$\beta \propto L^3 \qquad \cdots\cdots\cdots\rightarrow 1.37$$

In addition to longer conjugated π system, the use of suitable functionality at the end of the π-system can augment the required asymmetric electronic distribution in either the ground state or the excited state configuration or both. These functional groups can be electron donating (D) or accepting (A) nature connected to the elongated π-systems. Mostly, D groups possess *p* character (sp^3) bonding and often have accessible electron pairs on a *p*-orbital, and the A groups are categorized by more *s*-character (sp^2 or *sp*) bonding. Representative D groups are $-O^-$, $-NMe_2$, $-NH_2$, $-OCH_3$ and $-CH_3$, and typical acceptors are $-CN$, $-CF_3$, $-CHO$, $-COCH_3$, $-NO_2$ and $-N_2^+$.

The second generation NLO materials are made from organic compounds and polymers. Among these, the most central feature of these organic compounds is their high nonlinear optical coefficients. It can be several orders of magnitude higher than those of the best inorganic compounds. Though difficult, a virtuous molecular design may lead to NLO material possessing both high nonlinearity and a wide transparency range, which is imperative for practical applications using non-resonant NLO interactions.[189]

Organic NLO materials may be used in a crystalline form, such as N-(4-nitrophenyl)-(L)-prolinol (NPP) and 4-*N*,*N*-dimethylamino-4′-*N*′-methyl-stilbazolium tosylate (DAST). Exciting NLO molecules include compounds having benzobisthiazole, benzobisoxazole and benzobisimidazole units, substituted benzenes, and conjugated molecules and polar aromatic compounds.[187,190,191] Dye molecules such as thiacyanine (TC), 4-Dicyanomethylene-2-methyl-6-p-dimethylaminostyryl-4H-pyran (DCM), tartraphenine (yellow dye), porphyrin, and photochromic molecules have been used individually or in combination with optically transparent polymers such as polystyrene, polydimethyl siloxane (PDMS), polymethylmethacrylate (PMMA) to fabricate micro-photonic devices for instance optical waveguides, modulators, optical-filters, mach-zehnder circuits, resonators, and lasers. In this context, our group, for the first time, has exploited NLO organic dye molecules to fabricate ultrathin organic surfaces covered with WGM micro-resonators to achieve high SHG output.[278] Particularly, organic NLO materials with room temperature ferroelectricity is of great interest. Recently, several approaches have been followed on a trial-and-error basis to understand and achieve high THz conversion power with broad bandwidth in pure organic crystalline materials (such as OH1, DAST, NPP, graphene[279]) using OR process. One of the current challenges in organic materials is discovering novel ferroelectrics with NLO characteristics for electro-optical applications.

The main work of thesis entitled "*Photonic Properties of Organic Micro-Resonators and Ferroelectric Polar Crystal: Two-Photon Luminescence, Second Harmonic Generation, and Terahertz Wave Production*" is given in four chapters (2-5). The motivation of this thesis work is discussed in the introduction part of each chapter.

2

Single-Particle to Single-Particle Transformation of an Active Type Organic Micro-Tubular Homo-Structure Resonator into a Passive Type Hetero-Structure Resonator

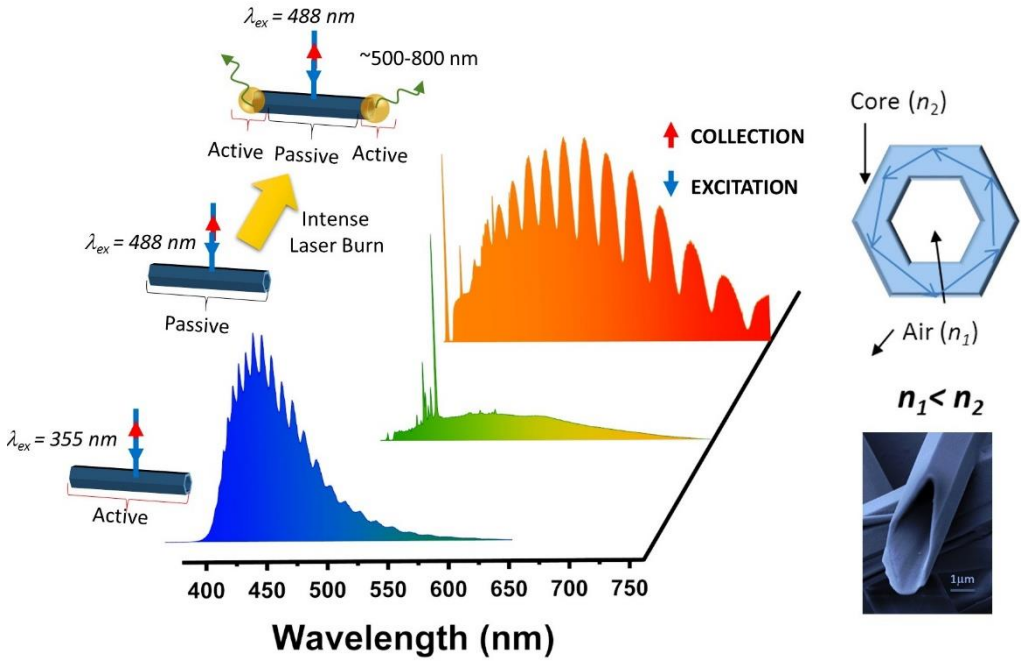

*This chapter is adapted from:

U. Venkataramudu, D. V. krishnarao, N. Chandrasekhar, M. A. Mohiddon, and R. Chandrasekar
Phys. Chem. Chem. Phys. **2016**, *18*, 15528.

2.1. Abstract:

*Organic micro-tubes with hexagonal cross-section are self-assembled from back-to-back coupled 2,6-bis(pyrazolyl pyridine) connected to 1,4-positions of biphenyl (**M-1**) molecules. These micro-tubes upon electronic excitation with a UV laser display an active type polarized WGM resonance in the visible part of the electromagnetic spectrum (400-600 nm). Due to photonic cavity effect, these tubes show FL signal intensity five times greater than the corresponding powder state. Further, the same tubes which are passive to a visible laser, produce yellow-orange emitting carbonaceous lumps when burnt with an intense laser beam (488 nm Ar^+ laser; 42 mW) forming a chemically binary heterogeneous micro-structure. This binary hetero-structure upon excitation with a visible laser at the passive tubular part showed emission in the Vis-near infrared range (500-800 nm) with WGMs thus producing a passive/active type hetero-structure photonic resonator.*

2.2. Introduction:

WGM emission has been exhibited by organic micro-resonators of different shapes viz. rings, spheres, hemispheres, and fibers, but one of the missing geometry

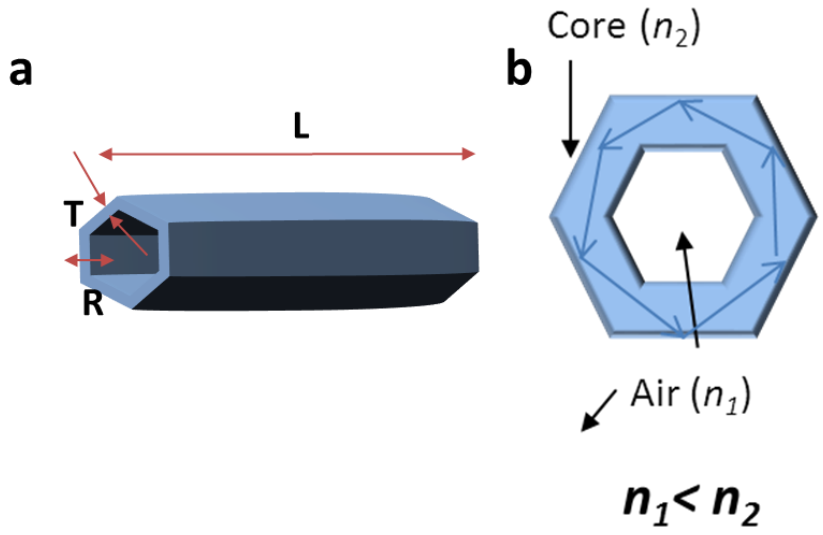

Scheme 1: a) The cartoon represents the length (L), radius (R), and thickness (T) of a self-assembled hexagonal submicro-tube. *n* stands for the refractive index. b) The cartoon of submicro-tube with hexagonal cross-sections, represents light confinement within hexagonal wall of submicro-tube.

is tubular shape.[101,206-208,192-203] Tubular ring resonators have advantages over the other resonators as the air medium within a hollow area and around the tube provides a tight confinement of the trapped light (Scheme 1). Due to the WGM resonance, the micro-resonator enhances the normal FL intensity by many folds.[202,204] In this context, the tubular resonators with a hexagonal cross-section are interesting and recently ZnO hexagonal tubes showed wall thickness (T) dependent mode patterns.[205]

So far almost all the reported resonators are active type in nature i.e., the electronic excitation of a molecular building block followed by trapping the FL light within the micro-resonator. A passive type resonator can be realized in a photonic hetero-structure waveguide when it is comprised of chemically distinctive active and passive type segments (two-in-one). For example, a visible light active structure,

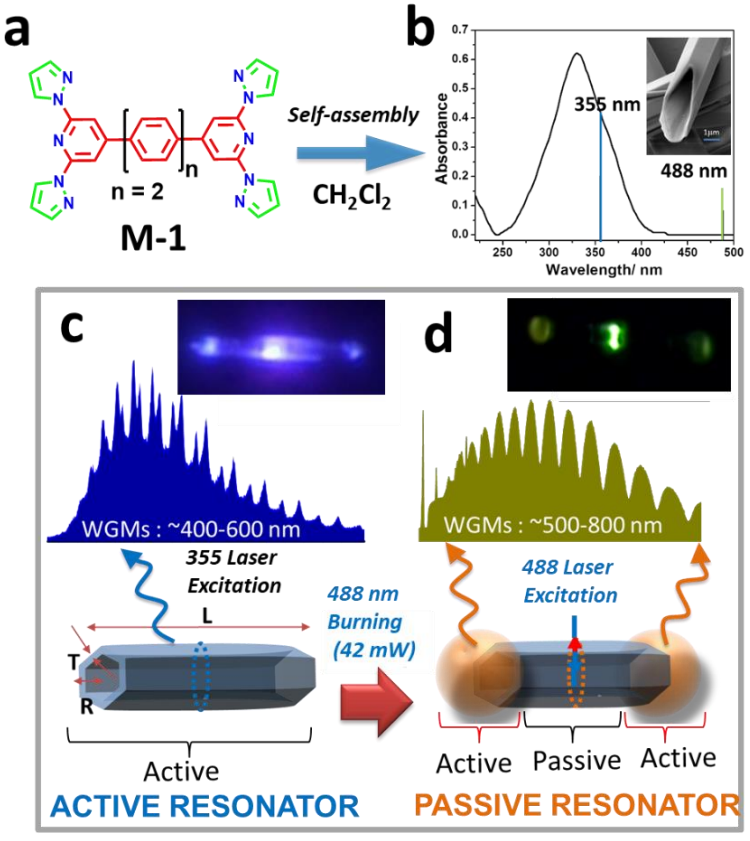

Figure 1: a) Self-assembly of molecule **M-1** into hexagonal micro-tubes.[208] b) Solid state absorbance of **M-1**. The inset shows the FESEM image of a micro-tube. c) FL image and spectrum of an active type submicro-tubular resonator excited with a 355 nm UV laser. The cartoon represents the length (L), radius (R), and thickness (T) of a submicro-tube. d) FL image and spectrum of a tip burnt tube (hetero-structure) acting as a passive resonator under visible laser excitation. The bottom cartoon represents the passive type photonic hetero-structure resonator.

locally created in a visible light passive waveguide, might act as a passive type resonator if the excitation and detection are performed in the passive part of the waveguide. To our knowledge, there is no report verified this concept due to difficulties in creating two-in-one hetero-structures displaying excitation wavelength and position dependent emissions. There are reports, which demonstrated both the active and passive type wave guiding tendency of a single epitaxially grown binary hetero-structure[212] and a self-assembled single homo-structure.[213]

Recently, for the first time, Chandrasekar et al. demonstrated the passive type wave guiding tendency of organic hexagonal submicro-tubes down to the single particle level.[62,70,207,210] These submicro-tubes were fabricated via solvent-assisted self-assembly of a back-to-back coupled 2,6-bis(pyrazolyl pyridine) (BPP) (acceptors) units connected to 1,4-position of biphenyl (donor) (Figure 1a), **M-1**.[208] These tubes acted as passive waveguides upon excitation with visible lasers, since the laser energy is outside the molecular absorption window (Figure 1b).[69] we have also evidently observed that at high visible (488 nm) laser power these waveguides burn and subsequently form highly luminous lumps. Hence these submicro-tubes were taken as test candidates for creating hetero-structure waveguides cum resonators (Figure 1d).

This chapter presents (i) self-assembly of active type WGM submicro-tubular resonators from **M-1** by bottom-up self-assembly technique (Figure 1c). (ii) Single-particle to single-particle *in situ* transformation of an active type submicro-tubular resonator into a passive type hetero-structure resonator using a high power 488 nm laser (Figure 1c, d), (iii) detailed investigation of the hetero-structure resonator using various microscopy techniques (Figure 1d), (iv) comparative performance analysis of these active and passive type single-particle resonators using single-particle micro-FL and polarization-resolved spectroscopy studies, and v) the NLO properties such as TPA and TPL of **M-1** in thin film and self-assembled submicro-tubes.

2.3. Results and Discussion:

2.3.1 Synthesis of M-1:

The molecule **M-1** was synthesised as per the reported procedure.[208]

2.3.2 Single Crystal Molecular Structure of M-1:

Molecules of **M-1** upon slow solvent evaporation in a mixture of MeOH and DCM (2:3) readily formed colourless needle-shaped single crystals. Single crystal X-ray analysis of the formed crystals revealed the trigonal *R-3* space group (Figure 2, Appendix B). In the solid state, the torsion angle (Φ) of the two BPP units and the 4,4'-

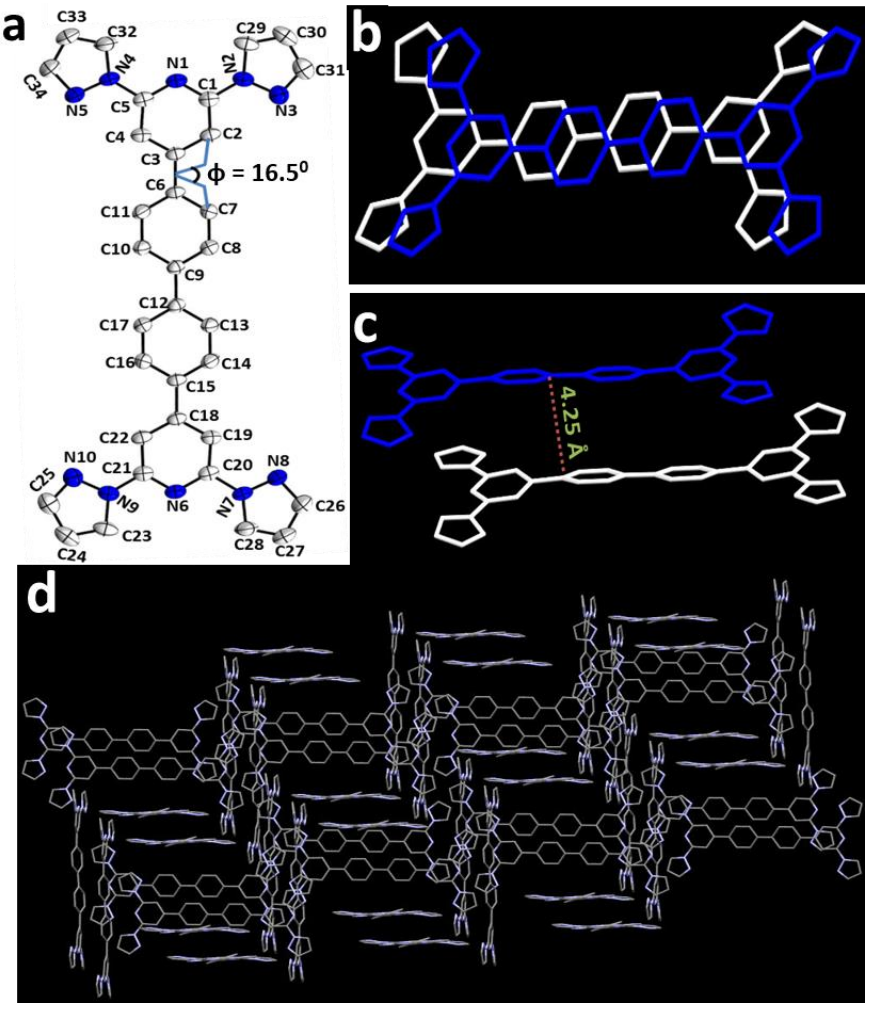

Figure 2: a) Single crystal X-ray structure of **M-1** with atomic labels. b) Top-view and side-view of π-π stacked dimer of **M-1**. c) The solid state molecular packing of **M-1** along the crystallographic *b*-axis.

biphenyl ring bridge is about 16.5° (Figure 2a). The presence of pyrazole ring nitrogens in **M-1** played a pivotal role in the supramolecular ordering and self–assembly through intermolecular hydrogen bonding interactions. The two pyrazolyl rings in BPP core adopted a transoid conformation around the C–N single bonds due to the repulsive interaction of the lone pairs of the ring nitrogen atoms (N1, N3, and N5) and C–H•••N hydrogen bonding interactions. Each unit cell comprises eleven

molecules of **M-1**. The distance between two adjacent layers of molecules is ~4.25 Å which is away from a typical π···π interaction distance. The other bonding type weak intermolecular interactions between the molecules of **M-1** drive their self-assembly into submicro-tube with hexagonal cross-sections. The molecular packing view of **M-1** along the crystallographic *b*-axis displayed a layer type arrangement of molecules (Figure 2c).

2.3.3. Fabrication of Submicro-Tubes from Molecule M-1:

The submicro-tubes were fabricated as per our reported procedure.[208] Briefly, in a clean test tube 0.2 mg of compound **M-1** was dissolved in 1 mL of DCM (c ~ 0.35 × 10^{-3} M) and 2-3 drops of the clear solution was slowly evaporated on a clean

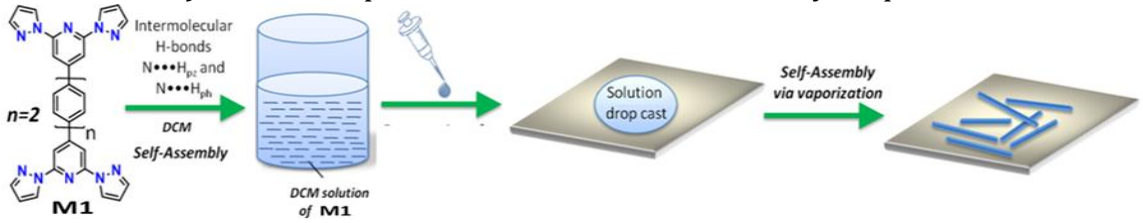

Figure 3: Schematic representation of a solvent-mediated self-assembly of **M-1** into micro-tubes

glass substrate at RT to get nearly micro-tubes (Figure 3). These micro-tubes were studies by FESEM, TEM, AFM and single-particle micro-FL spectroscopy studies.

2.3.4. Single-Particle Photonic Studies:

In the solid-state, molecule **M-1** showed absorption maximum (λ_{max}) at 330 nm with its absorption tail extending up to ~ 410 nm (Figure 1b). Electronic excitation within the molecular absorption range displayed a blue FL spectrum with a peak maximum at 451 nm. Excitation beyond the absorption range (with visible lasers) produced characteristic Raman signals corresponding to **M-1** vibrational modes. For single-particle micro-FL spectroscopy studies (reflection mode) the tubes (n~1.6) were self-assembled on a clean glass substrate (Figure 4a). UV laser excitation (355 nm) of one of the tips of a tube showed the active type optical wave guiding tendency along the tube axis (Figure 4a, b, see the red circle). The micro-FL spectrum collected from the irradiation area showed a spectrum with a broad feature with an intensity maximum centered around 440 nm (Figure 4g). Interestingly, laser irradiation away

from the tube ends showed a high-intensity spectrum with a periodic modulation of the FL intensity indicating the resonator behavior of the tube (Figure 4c–g). A maximum FL intensity was detected for the localized optical excitation performed at the middle part of the tube (Figure 4e and g). It is expected that the observed FL

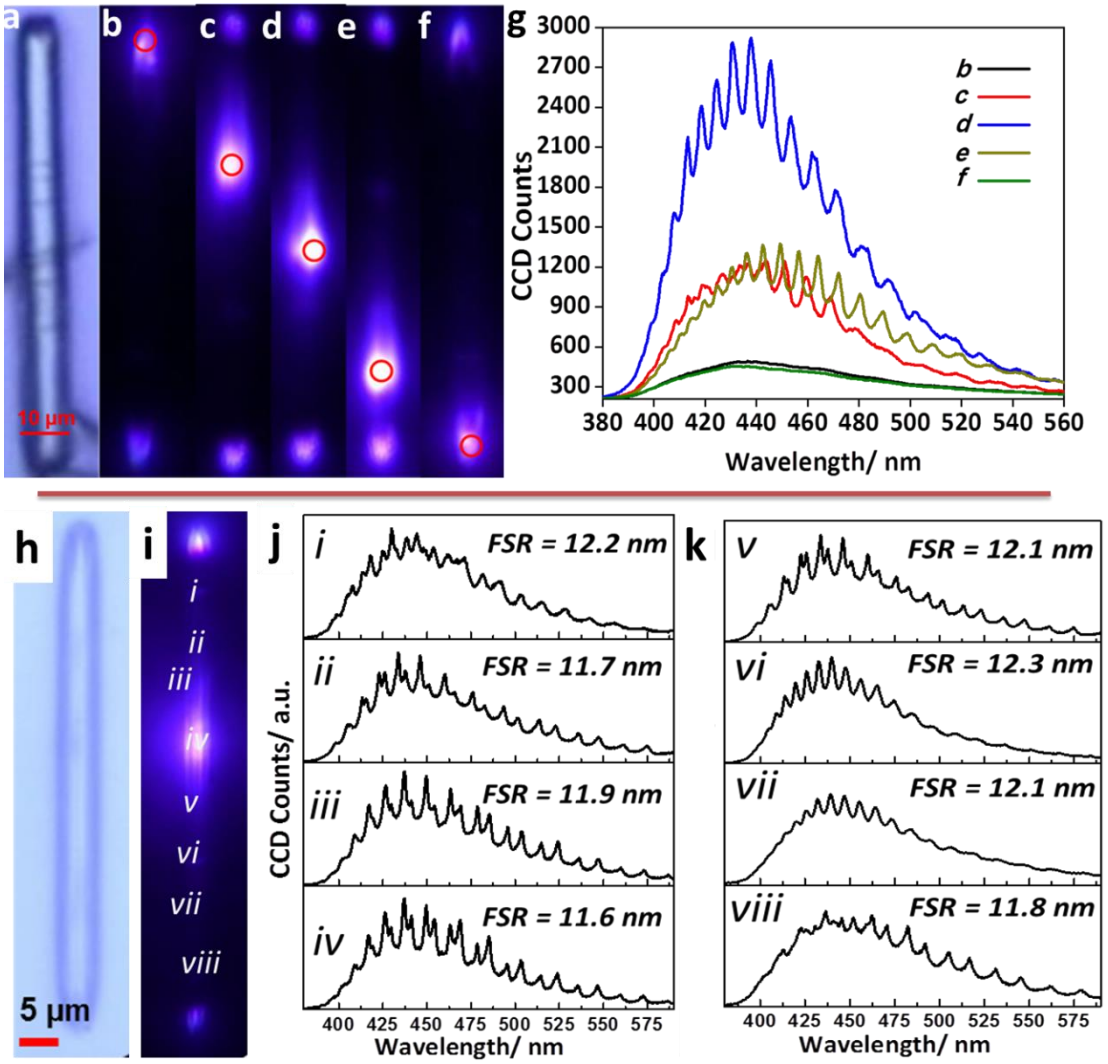

Figure 4: a) Optical micrograph of a submicro-tube. b-f) FL images of a waveguiding submicro-tube selectively excited at five different positions. The red circles show the laser excitation and spectral collection points. g) The corresponding FL spectra with WGM resonance. h) Bright field image of a tube. i) FL image of a tube with labels. j,k) The corresponding FL spectra displaying position sensitive TM/TE modes.

intensity modulation is due to the repeated TIR of the trapped FL light inside the hexagonal tube walls, thereby creating WGM resonance (Scheme1). Further compared to the powder state, the photonic micro-tubes showed five times enhancement in the FL signal intensity due to the optical cavity effect (Figure 4).

The FSR values of different tubes are intricate by two parameters. For example, in tubular resonators, apart from diameter (D), according to a plane wave model,[209] the wall thickness T and R should satisfy the relationship $T \geq \sqrt{3}R/8$, so that TIR (at the interface of the tube wall and air) and optical interference can occur to produce WGMs. Although the dimension D is feasible to estimate, the measurement of T is not possible for any tubular structure with a confocal optical set-up. Furthermore, several micro-FL spectroscopy measurements performed along the tube axis showed only a slight variation of the FSR values (~11.6 – ~12.2 nm) for the same wavelength modes

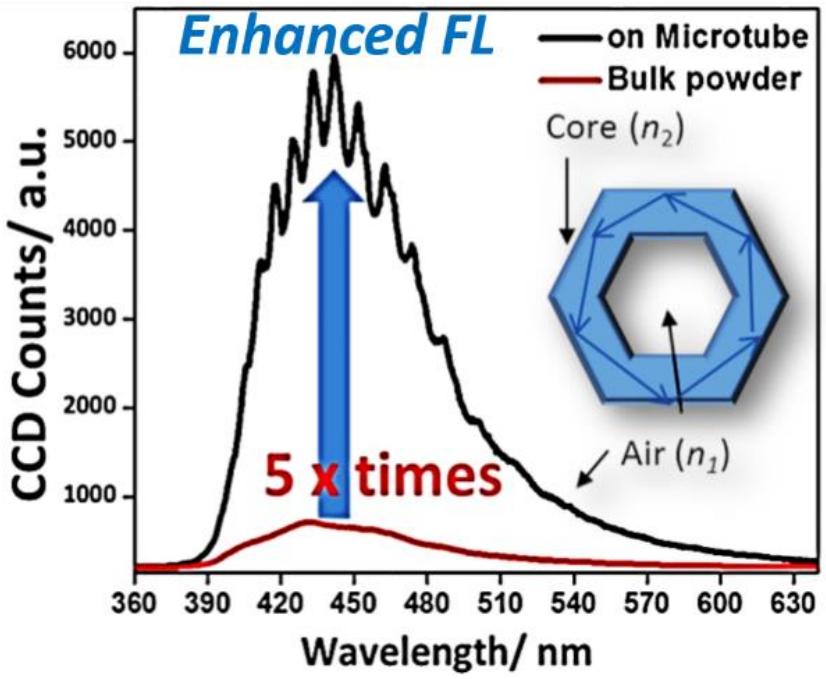

Figure 5: Comparative WGM peak intensity from micro-tube and spontaneous solid-state emission from the thin film.

(Figure 4 h-k). The variation of the FSR values can be attributed to the small disparity between the tube D and T values. Interestingly the observed FL spectra consisted of pairs of several sharp lines. The observations of these split peaks are very much sensitive to the measurement positions. Generally, these polarized pairs of peaks correspond to TE and TM modes indicating the orientation of the electric and magnetic fields, which appear due to the collapse of TE/TM degeneracy (see section 1.4.2 for more details).

One of the important findings of this single-particle experiment is that the recorded out-coupled emission intensity from the micro-tube is several orders of magnitude higher than the corresponding homogeneous thin film (Figure 4). This

emission enhancement is because of tight confinement of photons within the mirror-like reflecting hexagonal optical cavity structure. Further, compared to the powder state, the photonic micro-tubes showed five times enhancement in the FL signal intensity due to the optical cavity effect (Figure 5).

2.3.5. Polarization-Resolved Experiments:

A close look at the peaks observed in the FL spectra showed the presence of TE and TM modes (Figure 4 and 6) which is characteristics of a WGM cavity. To

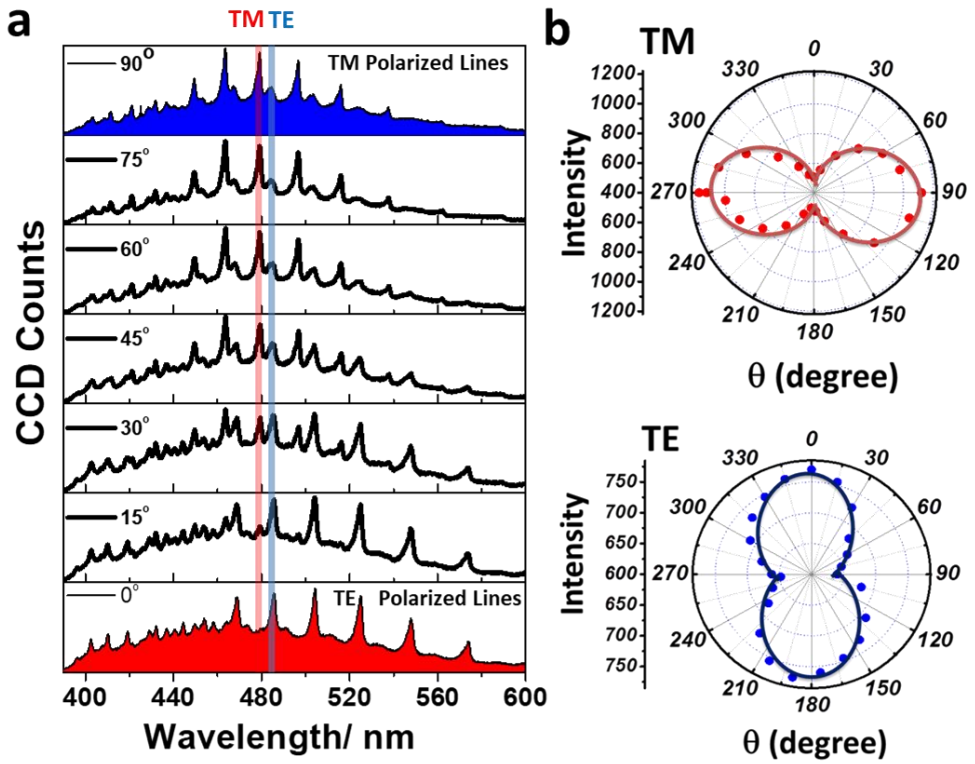

Figure 6: a) Polarization-resolved active type single-particle FL spectra of a tube supporting WGM resonance (λ_{ex} = 355 nm). b) The polar plots of the emission intensity observed for TM (red line) and TE (blue line) polarized modes.

investigate the type of polarization of the pairs of multiple sharp lines observed in the WGM spectrum, polarization-resolved single-particle microscopy studies were performed (Figure 6a). Generally, for the same angular mode number (*m*), the TM modes resonate at shorter wavelengths than TE modes.[204] The intensity of these pairs of peaks (TM/TE) is sensitive to the polarizer angle (θ). For instance, the intensities of ~480 nm (TM) and ~485 nm (TE) modes are very much responsive to the θ values. At a polarizer angle of 90°, the spectrum mostly consisted of strong TM polarized WGM resonance modes. At 30°, equal intensities of TE and TM modes were

recorded. Interestingly at 0°, the spectrum displayed a clear TE polarized WGMs (Figure 6). In agreement with the experiment the TM/TE polar plots showed vertically and horizontally oriented lobes (Figure 6b). This result indicated that these tubular micro-resonators can be employed to generate polarized micro-lasers.

Further, in tubular resonators, the *Q*-factor gives an estimation of light trapping efficiency and also an important quantity for lasing applications. The *Q*-factor of the tubes as a function of D exhibited an increasing trend beyond D~3.5 μm, reaching a maximum value of 280 for TM modes (Figure 7). The lower magnitude and the slight

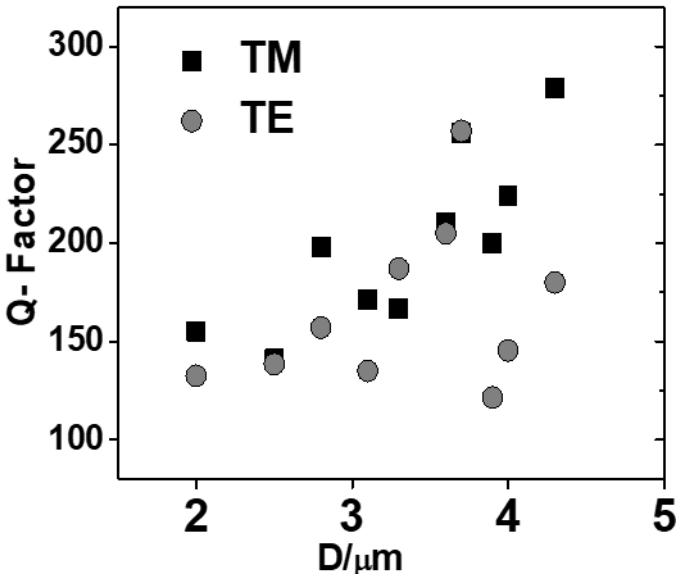

Figure 7: A plot of *Q* versus D for the TM and TE modes.

variation of the *Q*-values for D values ~ 2.0–3.5 μm are probably due to various loss factors such as radiation (curvature) loss due to smaller D, scattering loss due to surface inhomogeneity and leakage of the light to the surrounding at the air–organic/ glass–organic interfaces as an evanescent field. The evanescent field occurs via the Goos-Hänchen shift during each TIR along the circular tube wall. During each TIR, due to the above shift, light leaks into the low dielectric medium (n_1) as evanescent waves. The property of the evanescent wave is very much dependent upon wall thickness (T) in tubular geometries. The *Q*-factor specifies light confinement and the evanescent wave indicates light loss (low *Q*). Additionally, for each mode, the TM-polarized peak showed higher *Q*-values than the TE-polarized peak as a result of larger light loss (in comparison to TM modes) during each reflection of the TM-polarized wave along the circular path.[211]

2.3.6. Effect of the Substrate:

To investigate the influence of a substrate on the resonator characteristics of submicro-tubes, nano-manipulation was performed using a confocal microscope equipped with an atomic force microscope (AFM).[204] One of the selected tubes was picked up by an AFM cantilever by placing some force on the tube and the cantilever carrying the tube was titled and subjected to single-particle photonic studies (Figure

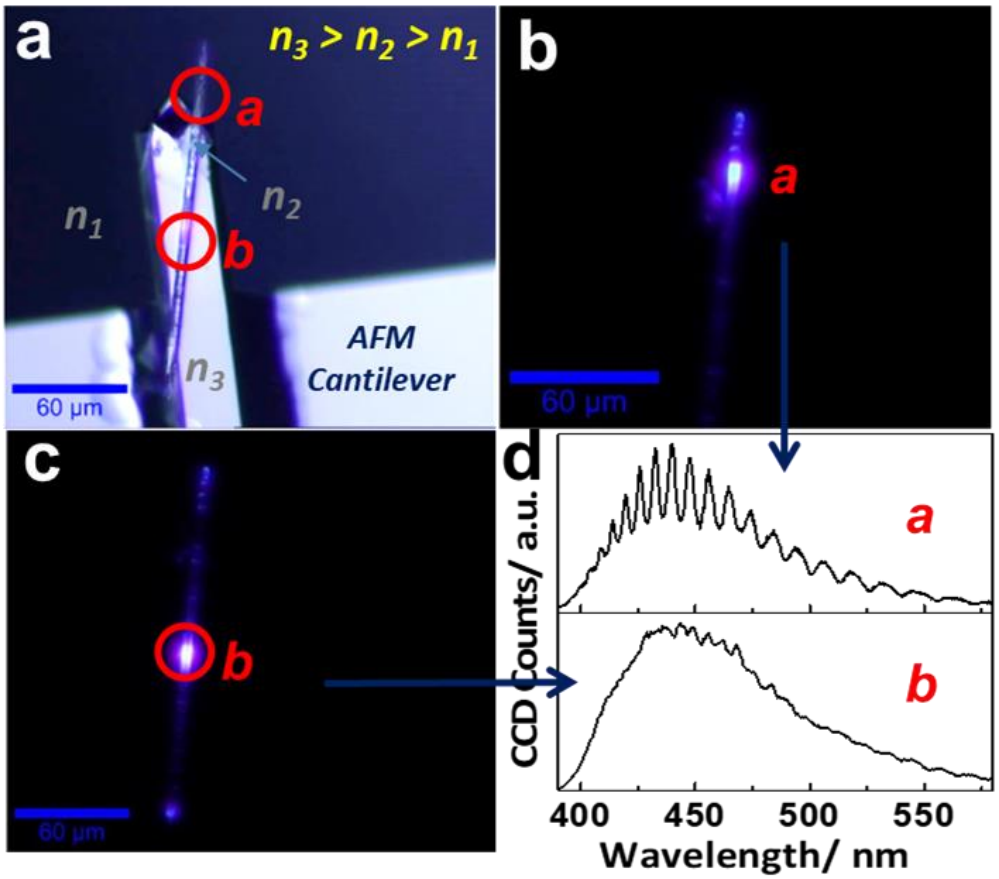

Figure 8: a) An AFM cantilever carrying a tube. b) FL image displaying laser excitation of tube area (position *a*), which is not in contact with AFM cantilever. c) FL image exhibiting excitation of tube area (position *b*) which is in contact with the cantilever. d) The corresponding spectra recorded at positions *a* and *b*.

8a). Upon local excitation (355 nm) of a tube area, which is not in contact with any substrate, a clear, highly-resolved WGM resonance peak (Figure 8b, see label a) was observed, whereas the tube area which is in contact with the AFM cantilever (n = 2.01) showed the poorly-resolved spectrum due to the seepage of light to the high refractive index medium (Figure 8c, see label b). Further, this experiment also confirmed the origin of WGMs from the submicro-tubes.

2.3.7. Fabrication of hetero-structure resonator:

Interestingly, when a single submicro-tube attached to AFM cantilever (Figure. 9a) was point focused with a 488 nm Ar^+ laser beam (power = 42 mW), the tip of the tube started burning[210] in a few seconds with a bright yellow-orange radiance forming a black color lump (Figure 9b, c) at the tube ends. Continued burning

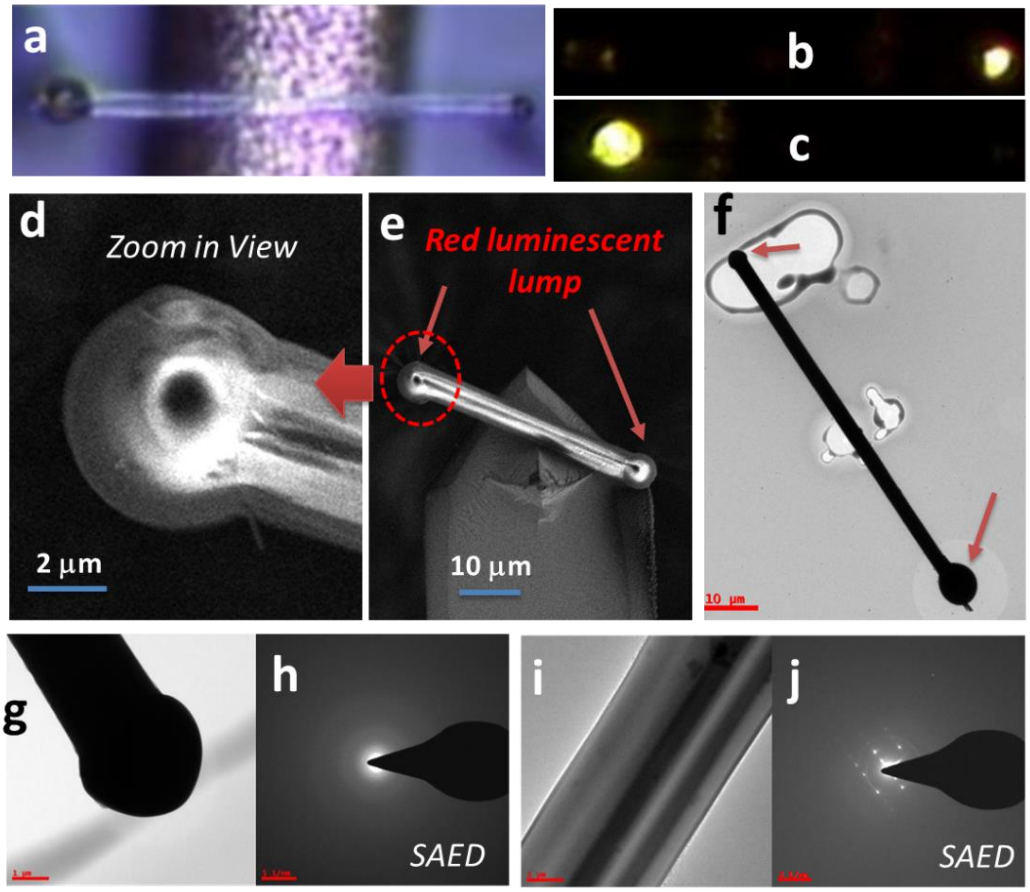

Figure 9: a) Bright-field confocal micrograph of a single tube with carbonaceous lumps at both ends. b and c) FL images of the same tube captured during tip burning. d, e) FESEM images of the tube with spherical lumps. f, g) TEM image of the tube with lumps on its both ends. h) Selected area electron micrograph collected from the lump shown in g. j) Selected area electron micrograph collected from the tube body shown in j.

decreased the tube length by converting the organic matter into a dark carbonaceous mass (Figure 10) thereby creating a hetero-structure. FESEM studies of the same hetero-structure (attached to a cantilever) revealed the formation of a nearly spherical lump with a smooth surface morphology shaped by the surface tension effect (Figure 8d and e). Furthermore, energy dispersive X-ray analysis (EDAX) of the

lump exhibited the presence of C and N elements. The AFM cantilever carrying a hetero-structure was carefully transferred into a carbon coated TEM grid for further investigation (Figure 9f). The TEM micrograph exhibited a dark contrast without any notable distinction between the tube and the lump, but selected area electron diffraction (SAED) analysis of the tube and the lump demonstrated their single

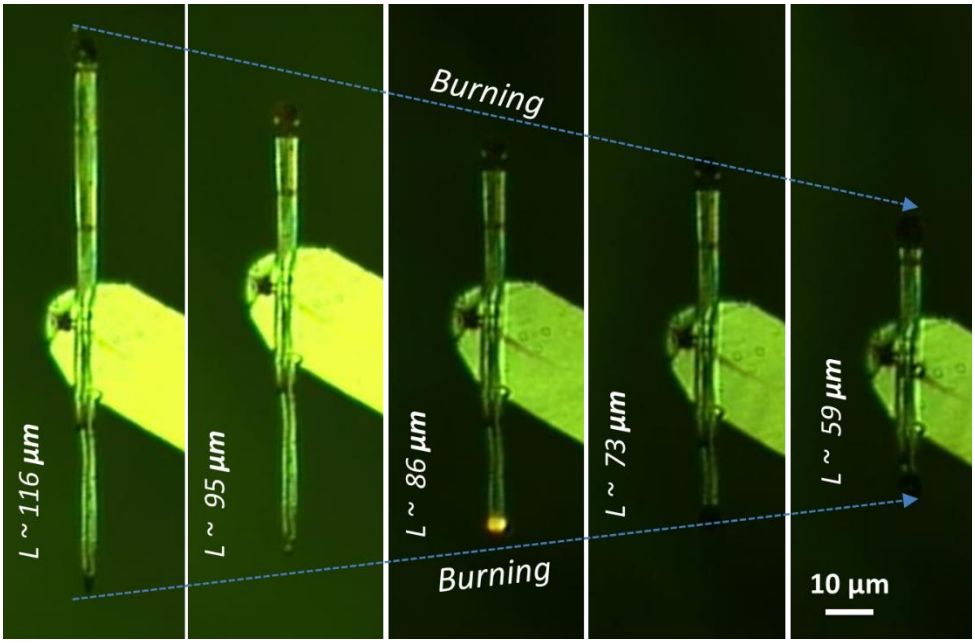

Figure 10: Controlling the length of the tube by laser burning.

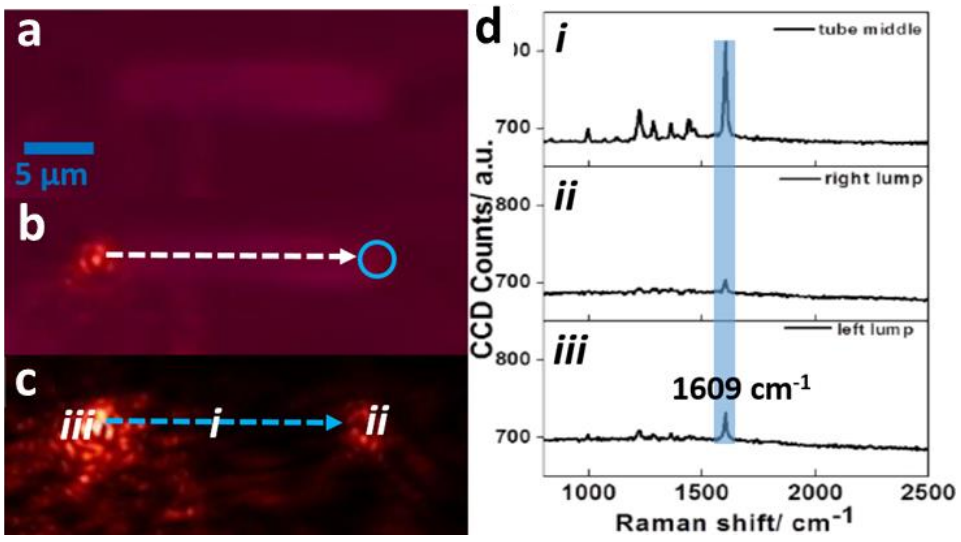

Figure 11: a) Bright-field optical micrograph of a tube with lumps. b, c) Bright-field and FL image of a optical tube with lumps showing a passive wave guiding nature by 633 nm laser excitation. d) A selected area Raman spectra of a tube with lumps collected at different positions.

crystalline (with diffraction spots) and amorphous natures, respectively (Figure 9h and j). Single-particle micro-Raman spectroscopy studies (633 nm: He–Ne) of a hetero-structure exhibited a strong Raman signal from the tubular area, whereas the lumps showed a signal at 1609 cm^{-1} (without any PL) corresponding to the sp^2 carbon (C=C) indicating a possible conversion of the building block molecules **M-1** into other low band-gap organic solid matter (Figure11). It can be also noted that the weak Raman signals correspond to **M-1** observed in the spectrum probably occurred due to excitation of tubular part. The chemical composition of the visible light absorbing and yellow-orange emitting lump is not clear yet. Nevertheless, the final hetero-structure consisted of both active and passive type binary constituents which are chemically and electronically different.

2.3.8. Passive Type Hetero-Structure Tubular Resonator:

The homo-structure submicro-tubes, when excited with a 488 nm laser displayed a Raman spectrum, which corresponds to molecule **M-1** (Figure 12b). However, during selective excitation (488 nm laser) and collection at the carbonaceous lump (active part) of the chemically binary hetero-structure (Figure 12a) showed a broad Vis-NIR emission (500–750 nm) with a weak signature of WGMs (Figure 12c and e). Conversely when the excitation (488 laser) and collection were performed at the tubular part of the hetero-structure a notable yellow-orange FL spectrum (500–750 nm) together with Raman signals (sharp: C=C; 1609 cm^{-1}) was observed due to the contributions from both tube (Raman) and lumps (FL) (Figure 12d). Remarkably, the broad Vis-NIR spectrum is also comprised of strong WGM resonance peaks with a very high FSR value. This observation demonstrates the occurrence of the passive type WGM resonance in the passive tubular part attached to FL lumps. The mechanism of the formation of the passive type WGM resonance within the hetero-structure is as follows: upon CW excitation with a 488 laser, the waveguiding tube passively propagates the 488 nm radiation towards carbonaceous lumps. This 488 nm light was absorbed by the carbonaceous matter subsequently releasing a broad 500–750 nm range emission (act as a FL source). Apart from

scattering loss, some part of this emission passively propagates into the hexagonal tubular structure via TIR and generates WGM resonance.

The FWHM of each peak was rather broad reducing the *Q*-value. This is possibly due to light loss into the high *n* cantilever and reduced FL life-times which broaden the resonance modes, resulting in low-quality factors. An illustration defining the transformation of an active type single-particle resonator into a passive type single-particle hetero-structure resonator is given in Figure 13. Besides, a similar

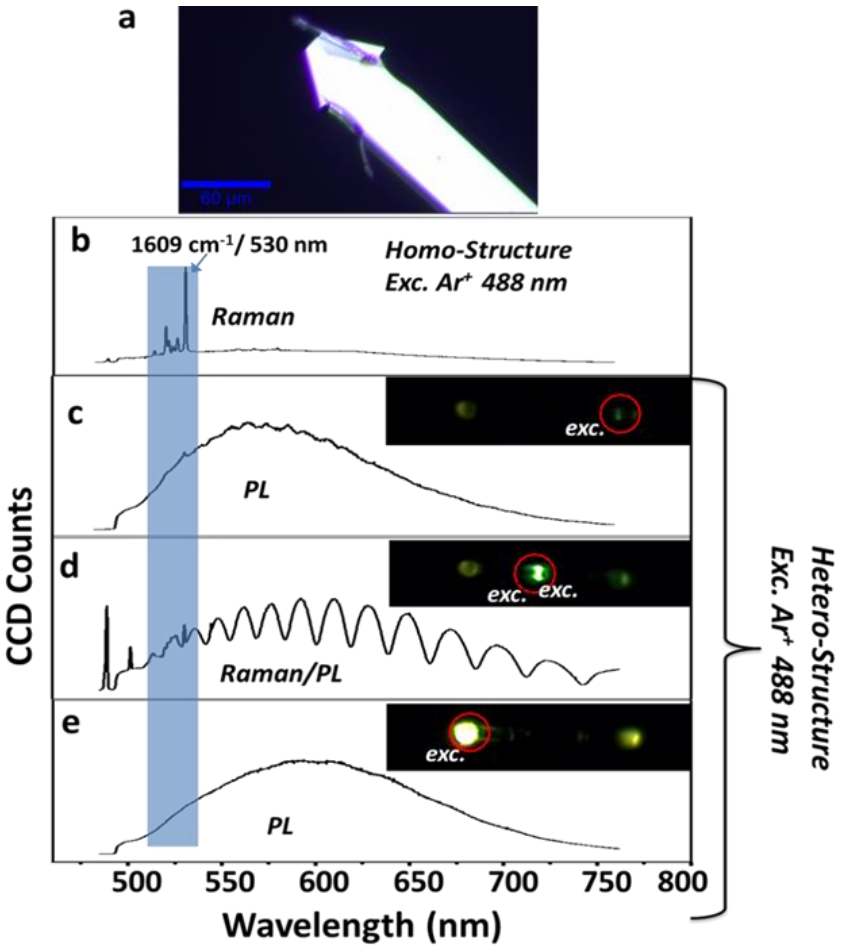

Figure 12: a) An AFM cantilever carrying a hetero-structure tube. b) Single-particle micro-Raman spectrum of a homo-structure tube. c-e) Selected area single-particle micro-Raman/FL spectra of a hetero-structure excited (488 nm) at the right lump, three different areas of the tube, and left lump, respectively. The red circles show the excitation/collection spot. The insets show the corresponding FL images.

hetero-structure resonator created on a glass surface demonstrated WGM resonance in the Vis-NIR spectrum (500–750 nm) with TE/TM modes and slightly improved *Q*-values (~200).

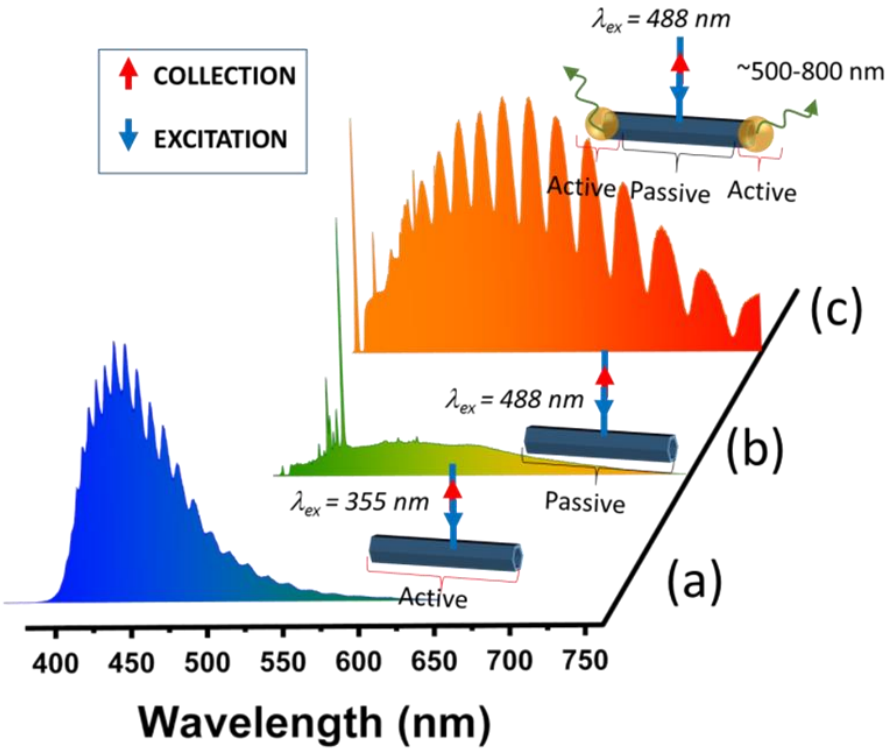

Figure 13: a) Single particle micro-FL spectrum of a tube supporting WGMs. b) Single-particle micro-Raman spectrum of a tube which is passive to 488 nm light. c) Single particle micro-FL/Raman spectra of a burnt tube.

2.3.9. NLO Spectroscopy Studies:

To study the NLO properties of molecule **M-1** in the solid state, a thin film of the sample was excited with a Ti: Sapphire 800 nm femto second pulse laser, with pulse width 100 fs, and a repetition rate 1 kHz. The two-photon excited fluorescence (TPL) signal was detected by a charged coupled device (CCD). The experiment was performed by keeping the sample at focal volume having a spot size of 101.8 µm and exposed by linearly polarized light with different input powers. The intensity at the focus was increased from 0.5 mW to 5.0 mW by adjusting the wave plate and the corresponding TPL spectra are shown in Figure 14a. Compared to one photon luminance (OPL) the TPL of molecule **M-1** in the thin film showed 65 nm red-shifted band with a maximum intensity at ~440 nm, indicating their different excited-state emission processes (Figure 14a red line). A plot of TPL band intensity with the square of pump power of **M-1** showed a slope of 1.9 (Figure 14b) within the experimental accuracy. This result revealed that the second-order origin of the TPL signal. Similar experiements on a group of submicro-tubes exhibited a greenish-blue emission and

the obtained a broad TPL spectrum showed a maximum at 450 nm, which is akin to TPL of **M-1** in the crystalline state (Figure 14a blue line).

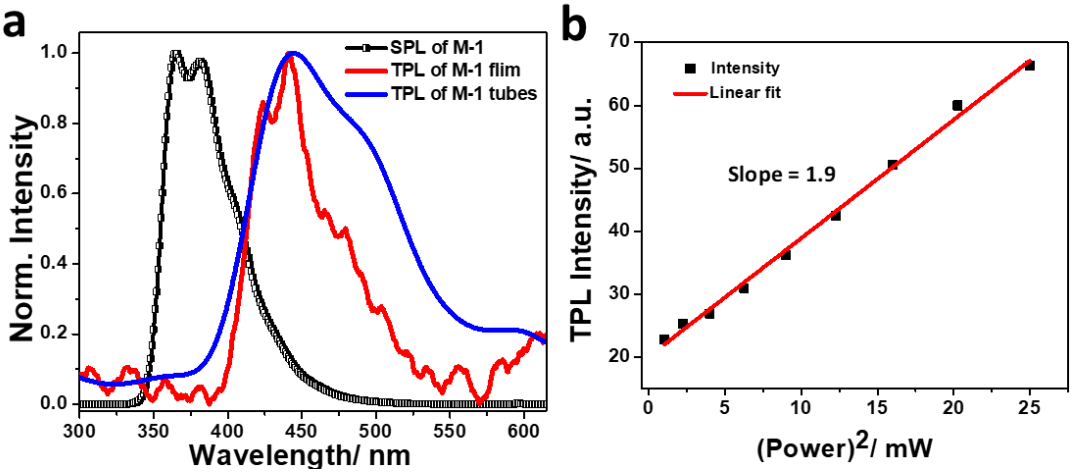

Fig.14: a) Single-photon and two-photon (800 nm) excited emission spectra of thin film of **M-1** (red line), submicro-tubes (blue line). b) The TPL intensity verse square of input pump power plot of **M-1** in thin film state. The red line shows the linear fit.

2.4. Conclusions:

In summary, the single-particle micro-FL spectroscopy experiments demonstrated the occurrence of active type polarized WGM resonances (TE or TM) from a blue emitting homo-structure submicro-tubular resonator. In comparison to the powder state, the tube showed nearly 5x times increase of the FL intensity due to the photonic cavity effect or increased light-matter interactions. Furthermore, these active type of homo-structure submicro-tubes were transformed into (active/ passive) chemically binary hetero-structures by laser burning. The burnt tip (lump) part was composed of carbonaceous visible light active matter. Remarkably, upon excitation of a visible light passive part of the hetero-structure with a 488 nm laser displayed WGM resonances in the Vis-NIR region of the electromagnetic spectrum together with Raman signals. This is the first example of a passive type organic WGM resonator and it is hoped that our original resonator design strategy can be applied to fabricate chemically heterogeneous micro-scale photonic structures with distinctive light-emitting properties for various applications.

3

Polymorphism and Micro-Crystal Shape Dependent Luminescence, Optical Waveguiding and Resonator Properties of Coumarin – 153

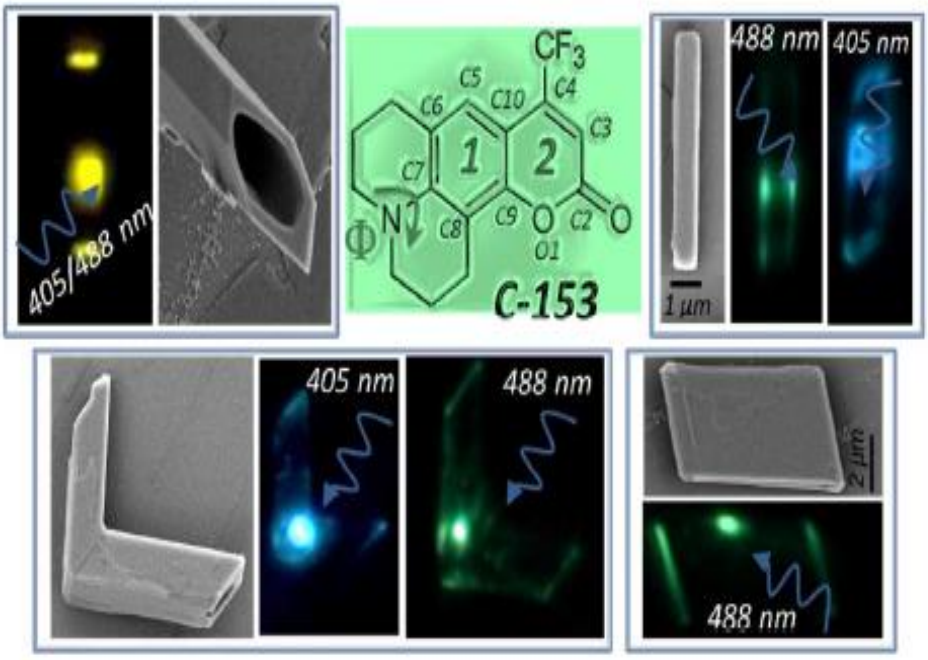

*This chapter is adapted from:

U. Venkataramudu, M. Annadhasan, M. Hemanth and R. Chandrasekar,
J. Mater. Chem. C, **2017**, *5*, 7262.

3.1. Abstract:

*Dye-based crystalline organic materials displaying molecular packing and conformation-dependent luminescence are attractive for opto-electronic and photonic applications. Hence, in this work, the opto-structural analysis of two polymorphs (**M-2** and **M-3**) of a well-known coumarin-153 (C-153) dye is undertaken. Crystal structural analysis based on the syn or anti position of C-β1 and C-β2 carbons adjacent to nitrogen in the julolidyl moieties shows that **M-2** and **M-3** polymorphs possess three and two molecular conformers, respectively. Optical excitation of single crystals of **M-2** and **M-3** radiates green and yellow FL, respectively. The presence of different conformers, strong intermolecular π–π stacking, hydrogen bonding interactions, and charge transfer states are attributed to the energetically different emission bands of these polymorphs. Depending upon the ratio of acetonitrile:water C-153 forms polymorphic micro-crystalline rods, tubes and Japanese twin tubes on glass substrates. Analysis of the single-particle Raman spectra and FL lifetime values of the rods, tubes and Japanese twin tubes clearly confirms dissimilar molecular packing within the micro-solids. Single-particle FL microscopy studies reveal remarkable polymorphism-dependent FL emissions, optical waveguiding, and optical cavity effects of the rods, tubes and Japanese twin tubes. The yellow emitting hexagonal and rectangular tubes possibly support WGMs and F-P modes, respectively, while the blue-green emitting rods and Japanese twin tubes display F-P type cavity modes. Overall this work establishes a simple and economical self-assembly route for the fabrication of C-153 photonic micro-structures demonstrating polymorphism dependent emission colours suitable for band-width tunable organic-based micro-lasers, opto-electronic and polaritonic devices.*

3.2. Introduction:

Optical band-gap tunable materials[214–224] are valuable in numerous areas such as miniaturized lasers,[214–219,225] optical resonators,[226–231] opto-electronics[232] and polaritonic devices.[233] Particle size-dependent tunable optical band-gaps have mostly been observed in materials such as carbon dots,[234] quantum dots[235] and metallic particles.[236] Recently, pure organic luminescent materials have been

emerging as excellent sources to achieve tunable light emissions.[214–224] For example, Radhakrishnan et al. reported a reversible phase (crystalline ↔ amorphous) changing organic material, namely diaminodicyanoquino-dimethane exhibiting thermally tunable emission colours.[221] Polymorphism is another convenient approach for achieving tunable emission colours.[216,217,222–224] Here by, controlling the molecular packing and/or its conformation in the solid state, the emission energy can be tuned, although it is hard to comprehend precisely the dominant factor governing the emission properties.[223,237]

Zhao and co-workers exploited the monomer and excimer emission of a well-known laser dye, 4-(Dicyanomethylene)-2-methyl-6-(4-dimethylaminostyryl)-H-pyran (DCM) to achieve wavelength tunable excimer micro-lasers.[238] In this context, Chandrasekar et al. reported a self-assembly method to achieve DCM dye micro-resonators with two different geometries by regulating the dye concentration. The resultant hemispherical- and rod-shaped particles acted as WGM and F-P photonic resonators, respectively, in the Vis-NIR emission range.[226] Furthermore, optical cavities are known to enhance[225–227] the emission intensity because of the Purcell effect.[203, 204] It should be stated that the shape and size of the micro-particles are central in determining the resonator/cavity characteristics of any photonic structures.[226-231]

Another strategy for the tuning the emission colour of FL molecule is to creating energetically different solid state aggregates (polymorphs) in a controlled way by using binary solvent mixtures. For instance, C-153 is an interesting laser dye which possesses a stiff molecular structure with a single low-lying excited state and known to display solvato-chromic behaviour.[240] A comparatively large dipole moment (μ) of 6.55 D for ground state (S_0) specifies that C-153 can be strongly solvated in the S_0 state. The μ of the excited state (S_1) increases to 14.2 - 16 D due to electron donor nature of amino group and electron acceptor nature of carbonyl group,[241] hence the solvation of the S_1 state of C-153 should be technically comparable, but greater than the solvation of the ground state leading to larger Stokes shift. Most of the studies have been performed in the solution-state and further numerous theories of varying complexity have been proposed to elucidate the observed changes in the emission energy of a C-153 in terms of the dielectric

properties of the solvent and the ground- and excited-state dipole moments of the probe.

Although solution state studies on C-153 dye are abundant, its solid state optical properties have not been investigated. Furthermore, to our knowledge, no

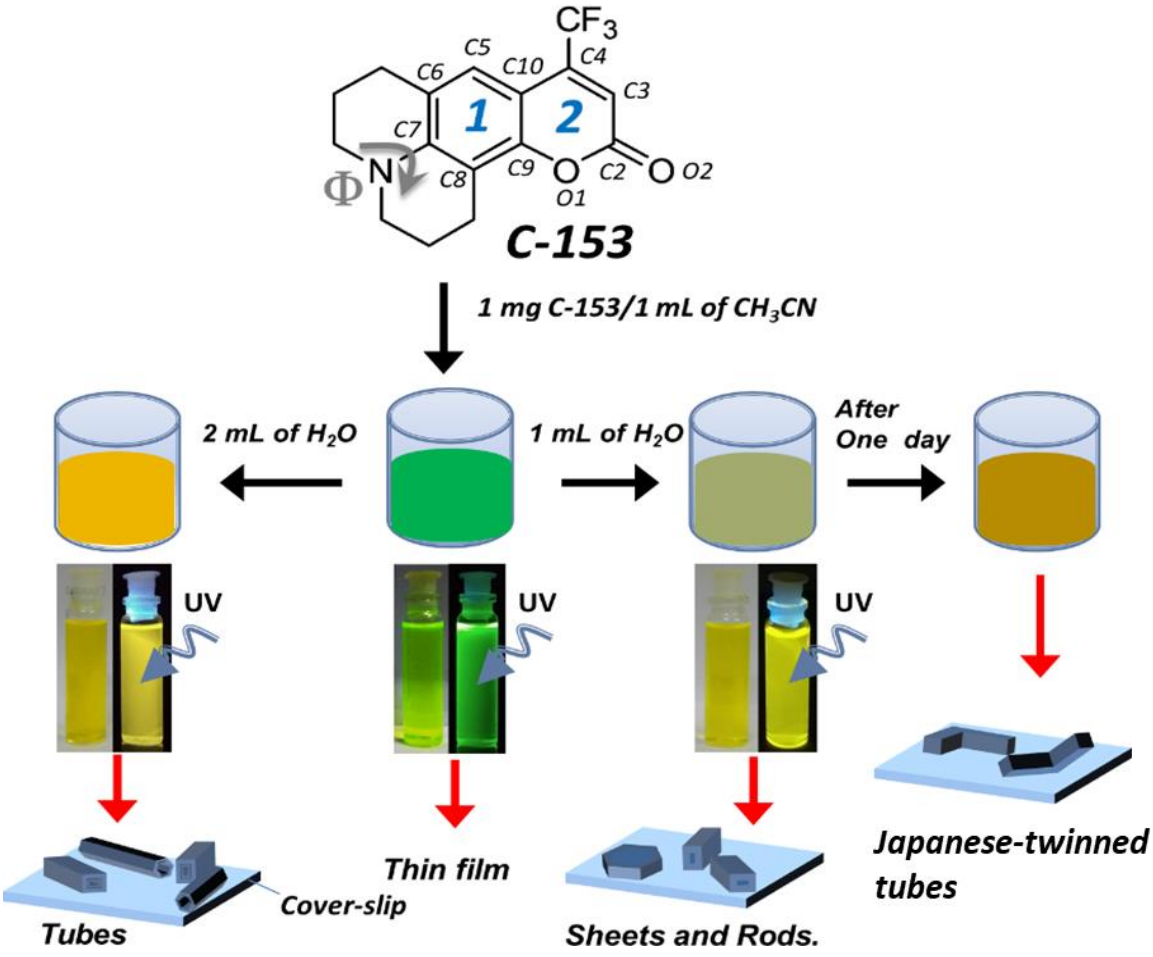

Figure 1: Self-assembly of C-153 dye in acetonitrile: water forming micro-tubes, micro-sheets, micro-rods and Japanese-twined tubes.

reports are available on the exploration of new polymorphs of C-153 and its self-assembled structures displaying aggregation-dependent FL emissions in the solid-state. Therefore in this work creation of well-defined self-assembled aggregates with diverse shapes using binary solvent mixtures i.e., by mixing relatively high dielectric (polar-protic) water (ε=80) to the (polar-aprotic) acetonitrile (ε=37.5) solution of C-153 was intended. It is expected that the solvation dynamics of acetonitrile-water (ACN-water) are dependent on the solvent structure in the mixture, which depends

upon their ratios;[242] hence it was hoped to fabricate diverse micro-structures with different molecular packing through self-assembly.

This chapter describes a distinctive polymorph-dependent emission property of a laser-dye C-153 (Figure 1). It also presents solvent mixture (ACN-water) ratio-dependent self-assembly of C-153 and subsequent formation of micro-rods, -tubes and -Japanese-twin tubes emitting diverse FL colours. Based on the polymorphs molecular packing and molecular conformations of the polymorphs, an attempt was made to correlate optical emission and solid state structure. The single-particle FL microscopy studies displaying geometry-dependent optical cavity effect of polymorphic micro-structures is also discussed.

3.3. Results and Discussion:

3.3.1. Effect of Solvents on the Optical Properties:

An ACN solution of C-153 ($c \sim 3\times10^{-6}$ M) displayed a bright green emission under 365 nm UV-light (Figure 1). The electronic spectrum of the corresponding solution of C-153 exhibited two broad absorbance bands at 262 nm (with a shoulder at 300 nm) and 419 nm ($S_1 \leftarrow S_0$ electronic transition) with a near doubling of the low-energy band intensity (Figure 2). As these C-153 molecules are known to show solvatochromism, prior to the self-assembly studies, an attempt was made to check the effect of the ACN: water ratio. The addition of different proportions of water (from 250 mL to 2.5 mL) (Millipore Milli Q, resistivity = 18 Ω cm) to an ACN solution of C-153 exhibited a shift of the absorption bands gradually to the low-energy side, i.e., from ~418 nm to ~430 nm with a decrease in the signal intensity. The corresponding FL spectra revealed a similar shifting trend in the emission maximum (λ_{em}: from~530 to 544 nm) with FL quenching. In general, the origin of Stokes shifted frequency,ν_{ss}, can be explained in terms of the ground-(μ_g) and excited- (μ_e) state dipole moments of C-153 dye and solvent(s) orientation polarizability Δf properties using the Lippert–Mataga equation.

$$\nu_{ss} = \frac{2(\mu_g - \mu_e)^2}{hca^3}\Delta f + const \quad \cdots\cdots\rightarrow 3.1$$

where, h is the Planck's constant, c is the speed of light, and a is the radius of the spherical cavity approximating the solute. Here, Δf is a function of the solvent dielectric constant (ε) and refractive index (n), which is given by the well-known Onsager function.

$$\Delta f = \frac{(\varepsilon-1)}{(2\varepsilon+1)} - \frac{(n^2-1)}{(2n^2+1)} \qquad \cdots\cdots\cdots\rightarrow 3.2$$

A recent investigation of the solvatochromism of C-153 in a binary mixture ACN: water (polar aprotic and polar protic, respectively) using a dielectric continuum model showed a nonlinear relationship of $f(\varepsilon)$ with the absorption and emission energies.[242] This indicates the contribution of H-bond formation, dielectric enhancement, or preferential solvation to the steady-state spectrum. The solvation

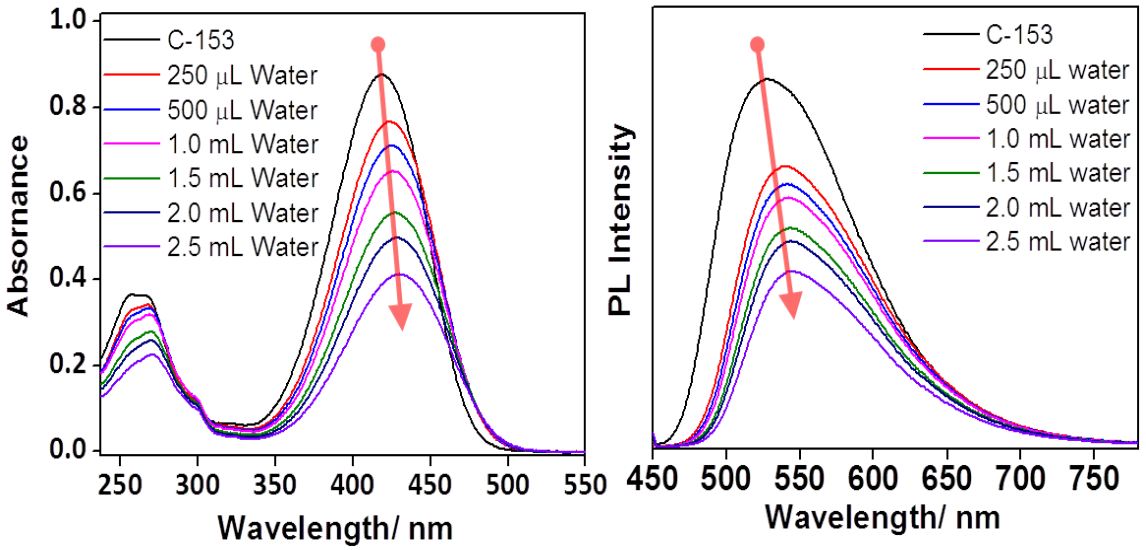

Figure 2: Steady-state absorbance and emission spectra of C-153 dye in ACN and the aggregation induced band energy shift in ACN /water mixture.

dynamics of ACN–water are known as "fast" solvents and the average solvation time is in the range of *circa* 1 ps. [243] Ultrafast experiments performed on hydrophobic C-153 dye in ACN–water mixture (at a low concentration of ACN) demonstrated that the first solvation shell was mainly composed of water molecules that hydrogen bonded with the acceptor C-153.

3.3.2. Molecular Packing of Polymorphs M-2 and M-3:

The two polymorphic forms (**M-2** and **M-3**)[244,245] of C-153 dye exihibits green and yellow FL, respectively, upon electronic excitation. Nonetheless, until now, no investigation on polymorph-dependent optical property is reported. Hence before self-assembly studies, to understand the influence of molecular packing and

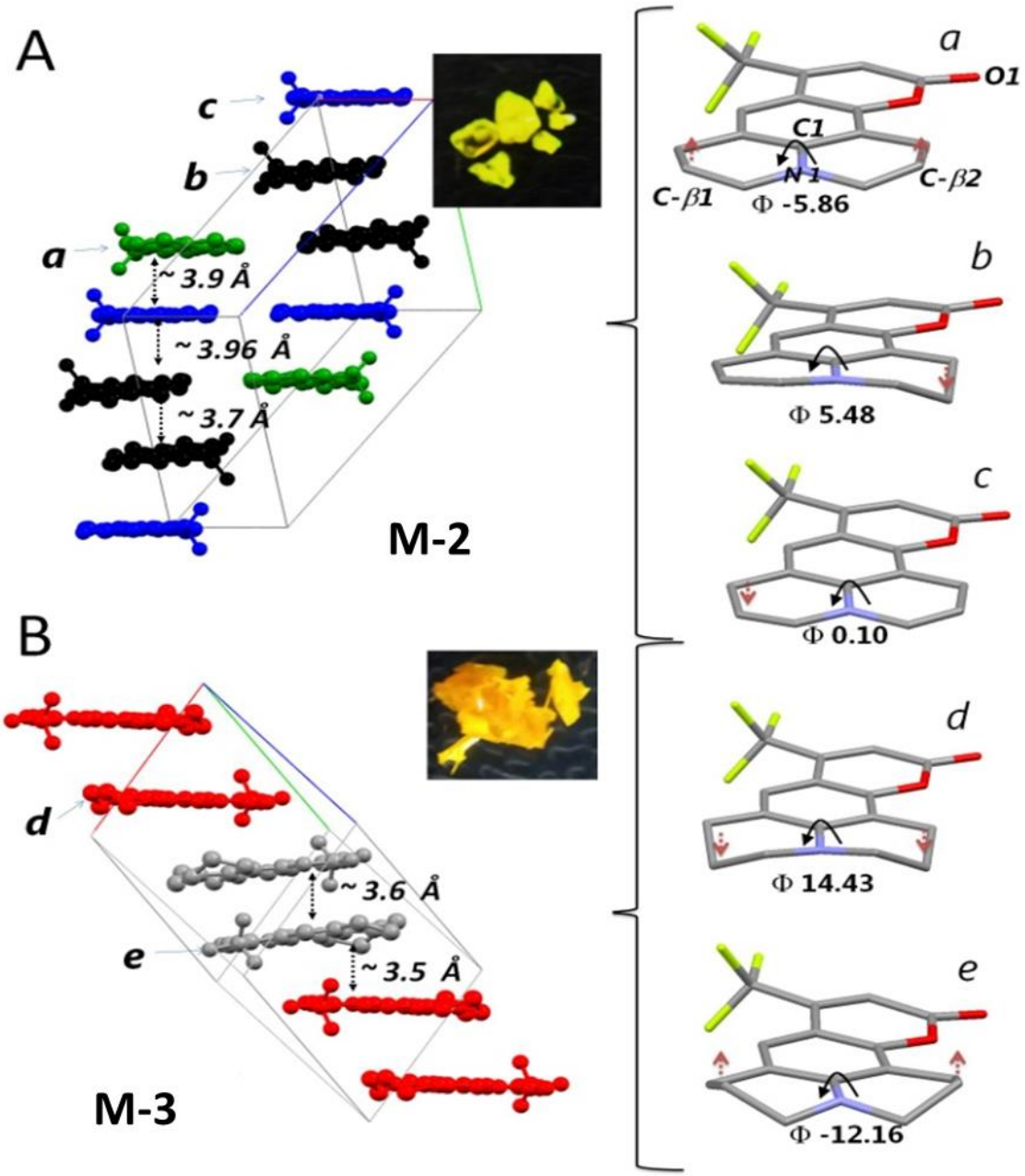

Figure 3: A and B) Single crystals x-ray structure of the two polymorphs (**M-2** and **M-3**) obtained from C-153 with different conformers. The insets show picture of crystals. The green, black, blue, red and grey molecular colour codes indicate the conformers *a*-*e*.

conformers on the emission energies of two polymorphs **M-2** and **M-3**, their crystals were grown in ACN and water-ACN (2:3), respectively and the single x-ray crystal structures are given in Figure 3. The two polymorphs exist in the *triclinic* unit cell but differ in their asymmetric unit; three molecules in **M-2** (Z'=3) and two molecules in

Table 1: Selected bond lengths and torsion angles found in the crystal structures of **M-2** and **M-3**.

C-153	**M-2**			**M-3**	
Conformers	*a*	*b*	*c*	*d*	*e*
Φ along C7-N1 (°) :	-5.86 3.81	5.48 -10.52	0.10 -1.53	14.43 -9.35	-12.16 12.60
Ω (°) :	9.67	15.48	1.63	23.78	24.67
Bond Lengths (Å) :					
C6-C7	1.416	1.419	1.414	1.423	1.428
C7-C8	1.414	1.405	1.405	1.413	1.408
C8-C9	1.381	1.376	1.381	1.387	1.383
C9-C10	1.396	1.395	1.401	1.395	1.401
C5-C10	1.402	1.398	1.398	1.407	1.406
C5-C6	1.362	1.360	1.357	1.372	1.374
C9-O1	1.381	1.384	1.387	1.384	1.379
C2-O1	1.364	1.375	1.373	1.378	1.369
C2-C3	1.422	1.430	1.437	1.449	1.449
C3-C4	1.351	1.341	1.343	1.349	1.350
C4-C10	1.431	1.432	1.438	1.439	1.435
C2-O2	1.206	1.205	1.201	1.205	1.208
C7-N1	1.369	1.373	1.376	1.375	1.374

M-3 (Z'=2). One of the notable differences in both forms is the conformation of julolidyl moieties. In **M-2**, based on the position (*syn* and *anti*) of the C-β1 and C-β2 carbons adjacent to nitrogen from the molecular plane, three (*a-c*) and two conformers (*d-e*) were found, respectively (Figure 3).

In these *a/c* conformer set, *b/c/d* conformer sets, C-β1/ C-β2 carbons were up and down from the molecular plane, respectively. Furthermore, in all five conformers

(*a*-*e*), the dihedral angle (Φ in degrees) of the rings connecting nitrogen (N1) and C(7) also varied significantly (Figure 3 and Table 1).

Conformer *a and b* interact in a head-to-head fashion to form a C-H···O(2) type hydrogen bond (~2.4 Å) of oxygen with one of the hydrogen of C-β2 carbon. Interestingly, two molecules of conformer *b* form a centro-symmetric C-H···O(2) type hydrogen bond (~2.4 Å) dimer in a head-to-head fashion, which is stabilized by the C-H···F type interaction (~2.58 Å). Furthermore, conformers *a*, *b* and *c* produce a 3×3 stacking arrangement. Here, conformers *a, c* and *b* forms head-to-head H type interactions with intermolecular separation of about 3.9 Å. The head-to-tail π-π separation between two homo-conformers of *b* is ~3.7 Å. In **M-3**, the extreme up and downward bending of C-β2 carbon of the conformer *e* is as a result of C-H···O(2) type hydrogen bond (~2.62 Å) interaction with conformer *d*. Additionally, the C-F group and C- α1 hydrogen atom of molecule *d* and molecule *e*, respectively, interact via C-F···H type bond (~2.63 Å) forming a 1D chain-like structures. Additionally, each *d* and *e* conformers make a staircase-type π-π stacking interactions (~3.5 Å) with 2×2 (...*d*-*d*-*e*-*e*-*d*-*d*...) arrangement indicating *J*-type molecular aggregation.

3.3.3. Thermal Properties of C-153 Polymorphs:

The differential scanning calorimetry (DSC) results further confirmed the influence of intermolecular interactions on the melting and crystallization points for both forms. **M-2** showed a sharp endothermic peak at 167.5 °C during the heating cycle, due to the melting of the crystalline phase and a crystallizing exothermic peak at 130.83 °C during the cooling cycle. **M-3** exhibited an endothermic peak at 165.5 °C corresponding to the

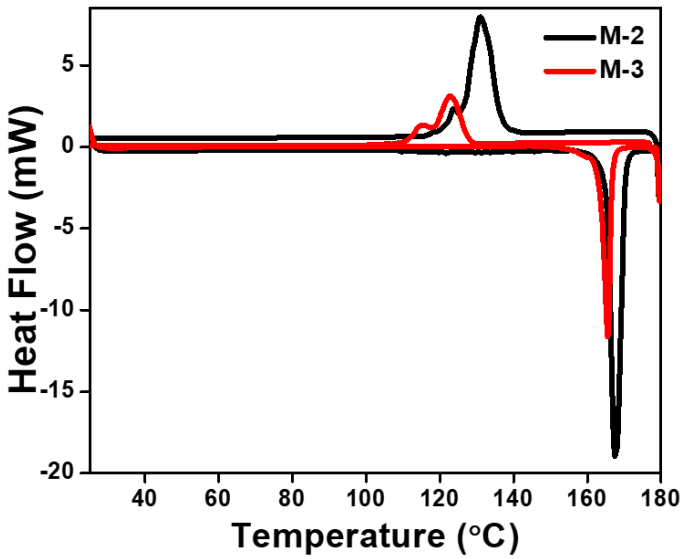

Figure 4: DSC thermogram of C-153 polymorphs **M-2** and **M-3**.

melting temperature of phase transformation from solid to liquid, and a single broad crystallizing exothermic peak at 123.0 °C (Figure 4).

3.3.4. Solid-State Optical Properties of C-153 Polymorphs:

To study the effect of intra-and inter-molecular interactions on the optical properties of **M-2** and **M-3**, UV-vis absorbance and emission features were investigated for the corresponding single crystals (Figure 5). The optical absorbance

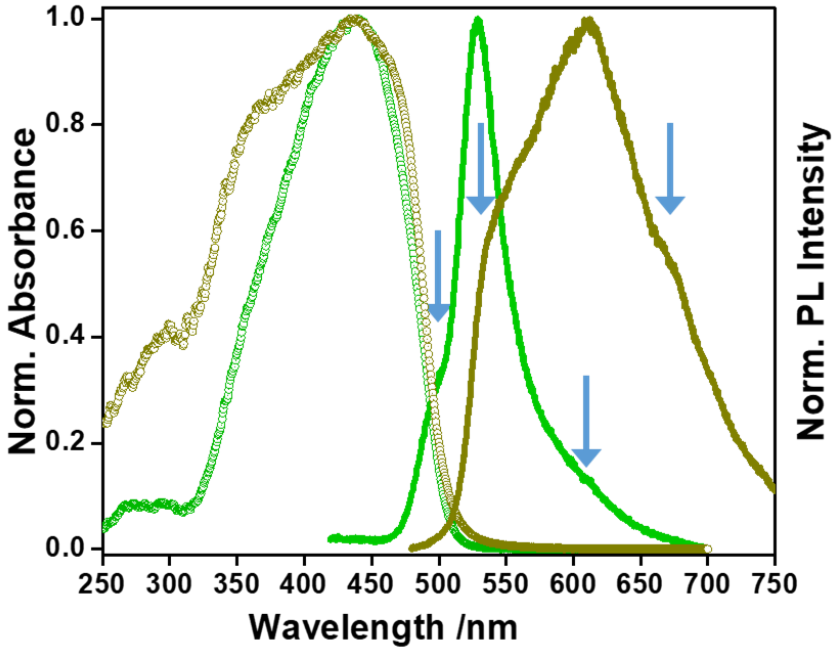

Figure 5: Normalized solid state absorbance (dotted line) and single crystal state emission (solid line) spectra of C-153 polymorphic **M-2** and **M-3** are given in green and dark yellow, respectively. The arrows show shoulder bands.

spectra of both forms displayed a strong band centered at about 438 nm, together with very weak and strong high-energy shoulders at 360 and 300 nm, respectively. The FWHM of the absorbance band of **M-2** was much wider compared with **M-3**. Interestingly the solid-state Stokes shifts and the emission features of both polymorphic forms were drastically different. **M-2** exhibited a sharp and narrow FL band at 530 nm together with feeble shoulders at 493 nm and ~613 nm, whereas **M-3** showed a strong 613 nm band with two strong shoulders at ~530 nm and ~670 nm for the same excitation wavelength (λ_{ex} = 405 nm laser). It is interesting to observe that the intensity of the emission peaks of the polymorphic single crystals was dependent on the laser excitation position, signifying the anisotropic nature of the

molecular crystals (Figure 5 and Figure 6). Noticeably, in comparison with **M-2**, the red-shifted emission band with pronounced shoulders shown by **M-3**was probably due to J-type molecular arrangements with much shorter intermolecular stacking separation (Figure 3). Apparently, the 530 nm band observed in both polymorphic forms was found even in the dilute solution state, suggesting a probable similar electronically isolated molecular state of one or more conformers in both **M-2** and **M-3** (Figure 2). It is evident that the difference in the observed emission energies was due to a drastic change in the structural conformation and molecular packing between the polymorphs.[223]

The bond distances of ring 1 and 2 in C-153 (see Figure 1) indicate the dominant resonant structures and molecular CT characteristics. The attachment of a strong electron donor amino group at the C-7 position favors intramolecular charge

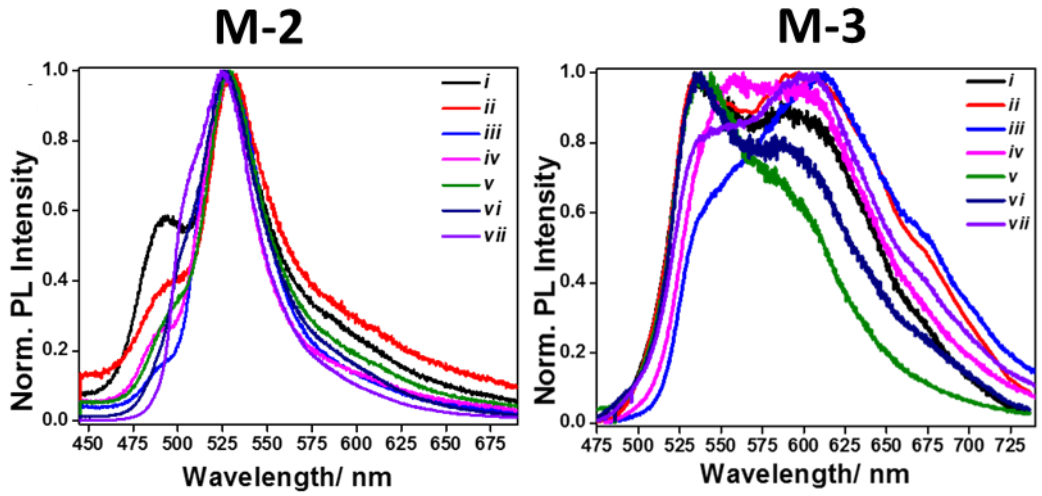

Figure 6: Laser excitation position-dependent emissions from **M-2** and **M-3** single crystals.

transfer (ICT) from ring 1 to 2 via π-conjugated pathways by forming a para-quinoidal structure (see Figure 1 for the chemical structure). This is apparent as the C5–C6 and C8–C9 bonds of ring 1 exhibited the shortest bond distances. Furthermore, the C7–N1 bond distance lies between those of pure single (1.44 Å) and double (1.27 Å) carbon-nitrogen bonds (Table 1), indicating its partial double bond character. In ring 2, the C4–C10 and C2–C3 bonds were relatively shorter than the typical C–C single bond distance (1.470 Å), which is suggestive of the contending effect of *ortho*-quinoidal and *para*-quinoidal resonance structures.

It is also expected that the presence of an electron withdrawing CF_3 group at the 4th position might enhance the ICT character of C-153.[246] Importantly, the torsion angles (Φ) of julolidyl moieties in **M-3** were different from **M-2** and they significantly deviated from an ideal sp^2 hybridization as one can see the absolute differences (Ω) between two Φ values along the C7–N1 bonds. The molecular conformations and Φ values directly affected the degree of π-conjugation and hence the optical band-gap. The solid-state structures showed that the molecular packing and intermolecular interactions in both polymorphic **M-2** and **M-3** were different. Although the Φ values of the **M-2** conformer favoured better π-conjugation than **M-3**, the observed red-shifted broadband with a low energy emission in the case of **M-3** could be attributed to dominant intermolecular (H-bond and π–π stack) J-aggregation interactions and the involvement of a possible twisted charge transfer process.

3.3.5. Self-Assembly of C-153 into Polymorphic Micro-Structures:

For self-assembly studies, 1 mg of C-153 was dissolved in 1 mL of ACN (stock solution) and 2 mL of water was added to it to induce molecular aggregation (see Figure 1). Interestingly, the colour of the solution changed from green to bright yellow

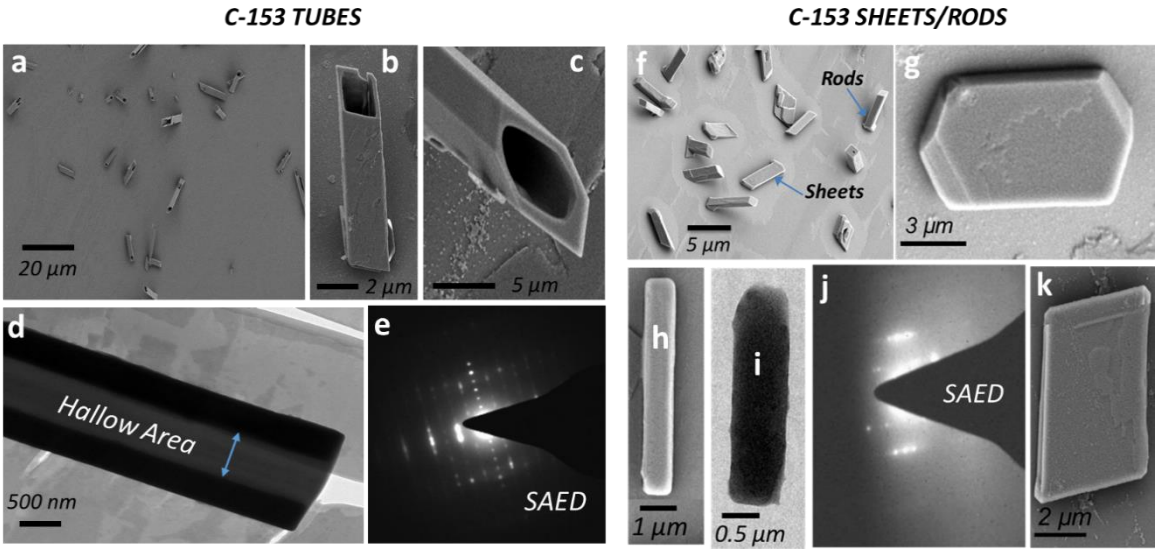

Figure 7: a-c) FESEM images of crystalline C-153 tubes with rectangular and hexagonal cross-sections. d) TEM image of a single tube displaying its hallow area. e) SAED pattern of a tube shown in figure 4d. f-i) FESEM Images of crystalline rods and sheets (hexagonal and parallelogram). j) TEM image of a single rod. k) SAED image of a rod shown in j.

and the corresponding solution exhibited a bright yellow emission upon UV-light exposure (see Figure 1). Two drops of this solution were drop-casted on a cover-slip and allowed to evaporate slowly at room temperature to grow micro-structures. FESEM images of the sample showed elongated tubular structures (Figure 7a). Interestingly, some of the tubes that were grown vertically exhibited their hexagonal and parallelogram cross-sections (Figure 7b and c). TEM images displayed a lighter contrast from the body of the tube in comparison to the dark coloured walls, confirming their extended (along the tube axis) hallow tubular geometry. Further the single crystalline nature was clearly evident from the SAED data of the tube with parallelogram geometry, which exhibited multiple high intense diffraction spots (Figure 7d).

Similarly, to another batch of C-153 stock solution, the addition of 1 mL of water displayed a visual colour change of the solution(light green to light yellow) and exhibited a yellow emission under UV light (Figure 1). This observation clearly indicated aggregation induced emission behaviour of C-153 molecules in the binary solvent system. Self-assembly of C-153 from this solution, as discussed in the case of the tubes, and examination of the sample using FESEM showed the formation of

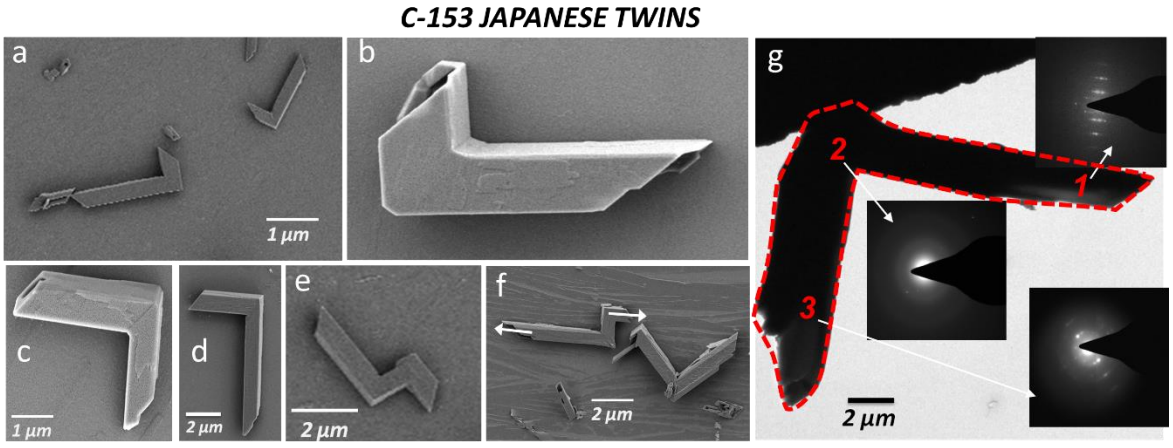

Figure 8: a-f) FESEM Images of C-153 Japanese-twined tubes. g) TEM image of a single Japanese-twined crystalline tube and the insets show the SAED pattern at locations *1*, *2* and *3* (shown in red colour).

standing micro-rods with cubic cross-sections and hexagonal and parallelogram sheets growing horizontally on the coverslip (Figure 7f-i). A close look at the FESEM images of micro-structures displayed several facets indicating their single crystalline

nature. Furthermore, TEM and SAED investigation of a selected rod showed multiple diffraction spots, which confirmed their crystalline nature (Figure 7j and k).

The above result clearly indicates that the importance of ACN:water ratio, and its implication on the shape of the self-assembled crystals. Additionally, it signifies the imperative role played by the solvating water molecules around the C-153 molecules via H-bonding interactions. The growth of the tubes with hexagonal and parallelogram cross-sections can be explained by two different mechanism; (i)

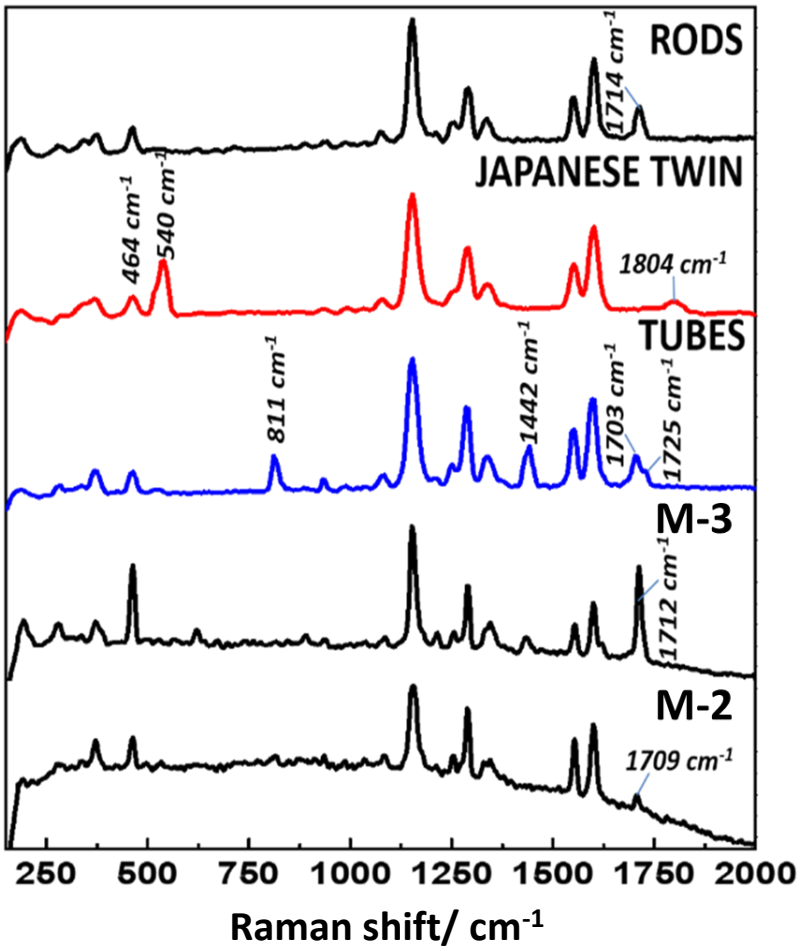

Figure 9: Single particle Raman spectra of C-153 tubes, Japanese twined tubes, rods, **M-2** and **M-3**. λ_{ex}= He-Ne 633 nm laser

solvent etching of the high energy facets of the rods with hexagonal and parallelogram cross-sections forming hallow tubes retaining the outer geometry, or (ii) swift growth of the four (parallelogram) and six (hexagonal) low energy facets from the nuclei forming inherently hallow tubular geometries with respective cross-sections. In case of rods and sheets, it is apparent that during the solvent evaporation of the ACN:water

(1 mL) mixture, it did not obstruct the complete packing of the C-153 molecules thereby forming single crystalline structures without hollowness. Here the intrinsic shape of the crystal is determined by the equilibrium thermodynamics and kinetic conditions. During the growth of a crystal under slow solvent evaporation conditions, the low-energy facets grow much faster than the high energy ones.

Surprisingly, keeping the solution used for the preparation of sheets and rods for a day and subsequent self-assembly produced L–shaped micro-structures as evident from the confocal optical microscopy examination (Figure 14a). FESEM and TEM investigations clearly pointed out the presence of two or inter-grown crystals in a symmetrical fashion at 90° angle to each other producing so-called Japanese-twined crystals (Figure 8). In twined crystals, the lattice points in one crystal are shared with lattice points in another crystal (forming a twin-boundary) adding obvious symmetry to the crystal pairs. Although this type of contact twin is common in inorganic crystals,[247] it is very rarely observed in organic crystals.

Table 2: FL life-time of micro-rods, micro-tubes, and Japanese-twinned tubes.

Micro-structure	Micro-rods	Japanese-twinned tubes	Hexagonal or rectangular micro-tubes
FL life-time (ns)	1.18	1.3-1.37	0.7-0.77

To understand the molecular packing arrangement within tubes, rods, and Japanese-twined tubes confocal Raman micro-spectroscopy studies were performed on each of these micro-structures (Figure 9). A comparative analysis of the spectra clearly indicated noticeable differences in the C-153 packing within the micro-solids. As one can see, a peak at 1714 cm^{-1} for rods is split into two peaks (1703/ 1725 cm^{-1}) in the case of the tubes and shifted to 1804 cm^{-1} for Japanese-twined tubes. The occurrence of carbonyl bond stretching at different energies indicated the variable strength of the H-bonding interactions of carbonyl groups (C-H···O=C<) in different molecular conformations. Furthermore, the tubes exhibited a distinctive peak at 811 cm^{-1}. To compare the solid state packing of micro-structures with polymorphic single crystals, Raman spectra of **M-2** and **M-3** were recorded. Analysis showed a close resemblance of the Raman spectra of the tubes and **M-3**, whereas the rods exhibited

similarity to **M-2**. The Raman spectrum of the Japanese-twinned tubes revealed unique peaks at 540 cm^{-1} and 1804 cm^{-1}, which were not observed for polymorphs **M-2** and **M-3** (Figure 9). These spectral data clearly demonstrated the presence of diverse solid-state packing in the micro-structures, which is essential for the achievement of band-width tunable emissions. This outcome was further established by single-particle fluorescence life-time imaging (FLIM) experiments, which showed life-time (τ) values of 1.18, 0.77, and 1.37 ns for the rods, tube and Japanese twin tubes, respectively (Table 2). However, it is essential to mention that the τ -values of a micro-resonator vary as a function of its quality factor as well. [228]

3.3.6. Single-Particle Photonic Studies:

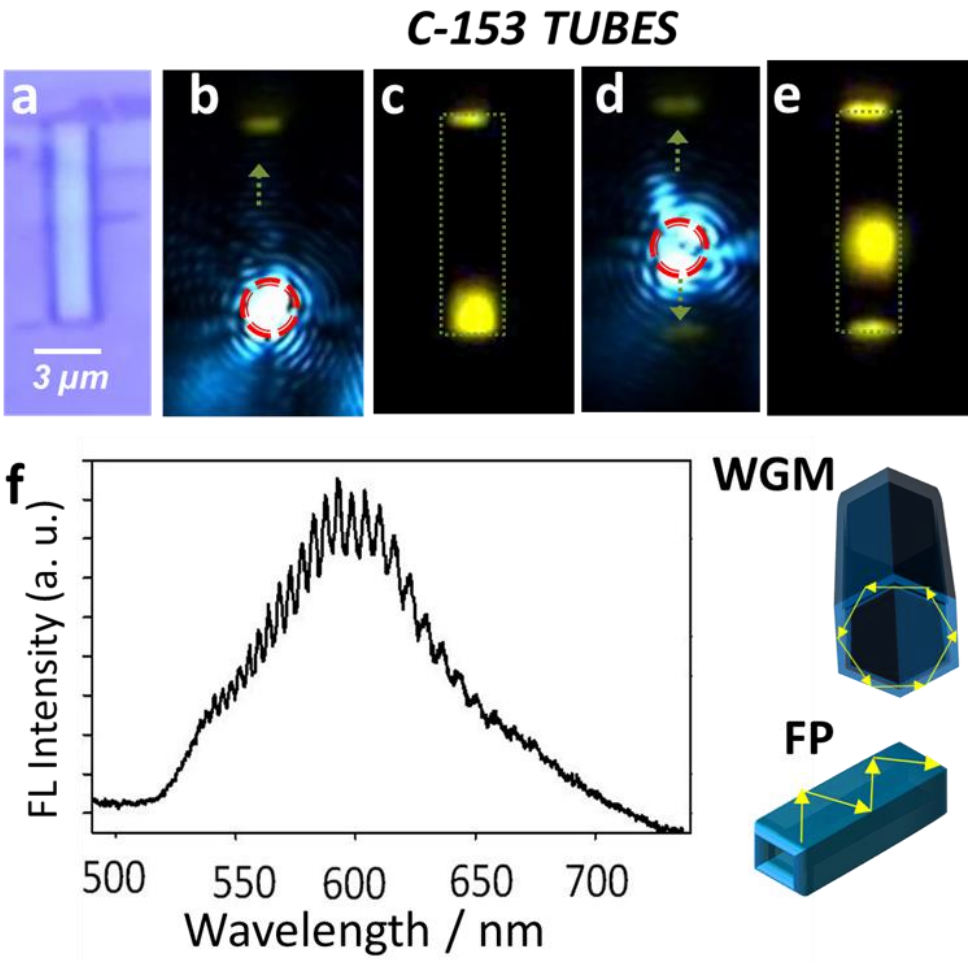

Figure 10: a) Optical image of a C-153 tube. b and d) Localized excitation of the tube (red dotted circle) with 488 nm Ar^+ laser and the corresponding FL image is shown in c and e, respectively. f) Single-particle FL spectrum of a tube displaying optical modes. The right side graphics indicate the WGM and F-P cavity action in hexagonal and rectangular tubes.

For single-particle micro-spectroscopic studies a confocal microscope (reflection mode) set-up was used with an Ar^+ (488 nm) and diode lasers (405 nm) as excitation sources. The cover-slips containing the particles (tubes, rods, sheets, and Japanese twins) were used directly for the experiment. For example, electronic excitation of C-153 tubes at one of the ends showed a brilliant yellow emission (with 488 nm long pass edge filter) and the longitudinal propagation of the FL to the

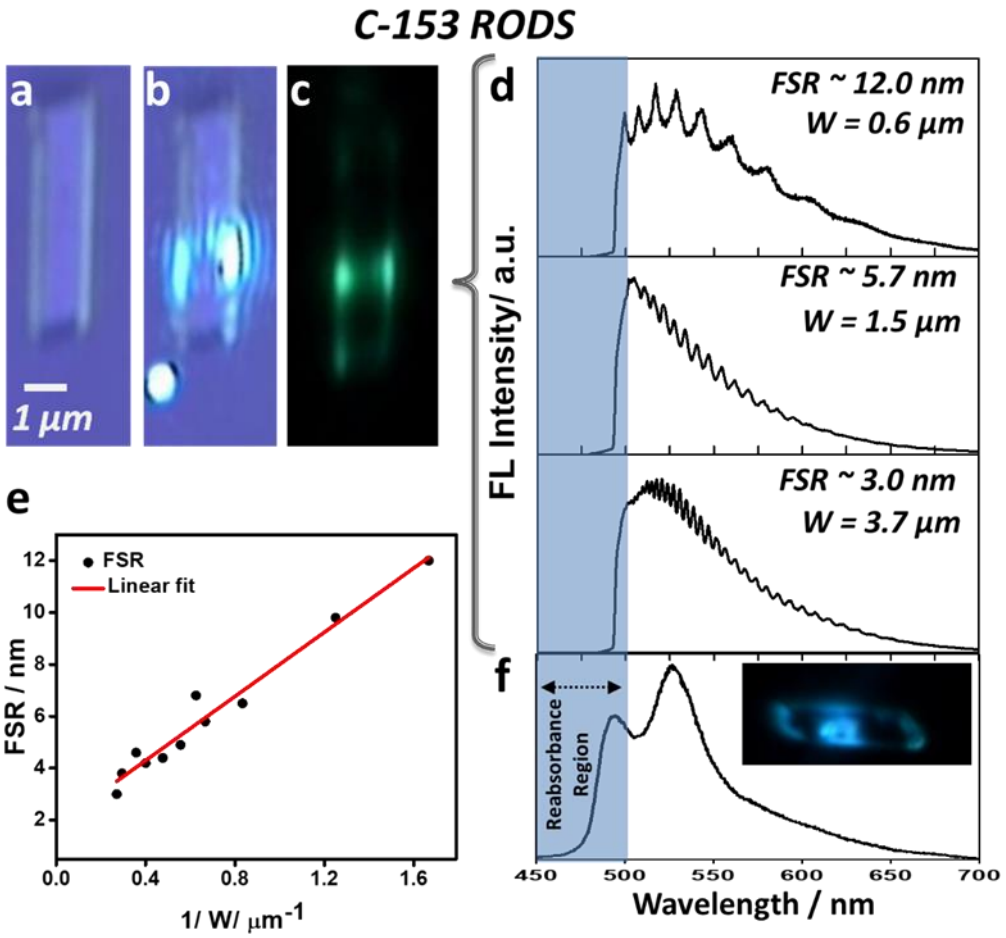

Figure 11: a) Confocal micrograph of a C-153 micro-rod. b) Localized excitation of a rod with a 488 nm Ar^+ laser. (c) The corresponding green FL image. d and e) Spectra showing rod width (W)-dependent FSR values and the corresponding plot, respectively. f) FL spectrum of a rod excited at the center with a 405 nm diode laser. The inset shows an image displaying blue FL at the center and blue-green FL at the rod tips.

opposite end of the tube (Figure 10c). Similarly, electronic excitation of the centre of the tube displayed FL wave propagation to the end facets of the tube, confirming its active type wave guiding tendency of the micro-tube (Figure 10e). The appearance of greenish-yellow colour outputs in Figure 10b and d, even without any laser source

filter, points to the mixing of the source light with the yellow FL. Furthermore, the FL spectrum collected from a single-tube exhibited a broad emission band in the range of about 500-700 nm together with periodic sharp lines (Figure 10f). Here, due to the vertical orientation of the tubes with rectangular and hexagonal cross-sections, the resonator type (F-P or WGM, respectively) of the particle is rather difficult to predict under our confocal microscope set-up. However, a horizontally grown rectangular micro-tube displayed a bright yellow PL at its longitudinal end facets as a result of light reflection from the parallel end facets analogous to F-P type resonators. In the case of the hexagonal micro-tubes, the optical feedback could have been a result of WGMs/ or F-P modes similar to ZnO hexagonal tubes.[205]

For the micro-rods, similar experiments were performed with a 488 nm laser excitation source. Focused electronic excitation at the center of a micro-rod showed bright spots along the width direction (Figure 11a–c). In contrast to the tubes, no waveguiding action along the growth axis (longitudinal) was found. The

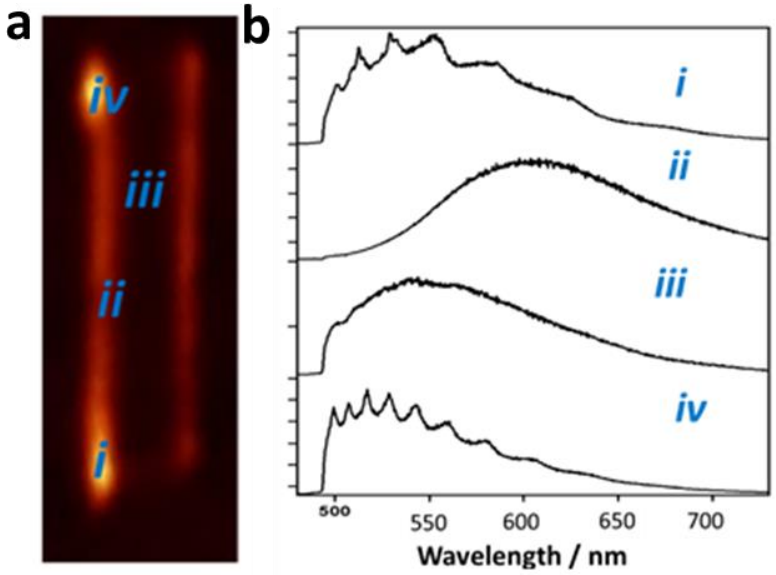

Figure 12: a) FL map of a single rod excited with a 488 nm Ar^+ laser. b) The corresponding FL spectra supporting F-P modes.

corresponding single micro-rod FL spectrum displayed a broad green emission band in the range of 500–700 nm together with optical cavity modes indicating possible F-P type action. To probe the direction of the F-P modes, experiments were performed on different rods of varying widths (W) (Figure 11d). A plot of the free spectral range (FSR) versus 1/W clearly exhibited decreasing FSR values upon increasing W, as

shown in Figure 11e. The best-fit line is nearly linear as per the equation 1.3. The linear fit confirmed that micro-rods indeed act as F-P type cavity and the standing waves are formed along the width direction. Supporting this observation, the FL map of a single micro-rod and its FL spectra at different positions showed F-P modes only from the edges with an elevated FL intensity (Figure 12).

Excitation at the center of a rod with 405 nm laser showed a bright blue FL at the excitation area and guided greenish-blue FL at the rod ends (Figure 11f). This observation can be easily understood from the absorbance spectrum of C-153 polymorphs (see Figure 4), which shows C-153 solid state absorbance tail extends up to about 510 nm. Initially, the rod generates FL light (with maxima at 494 and 597

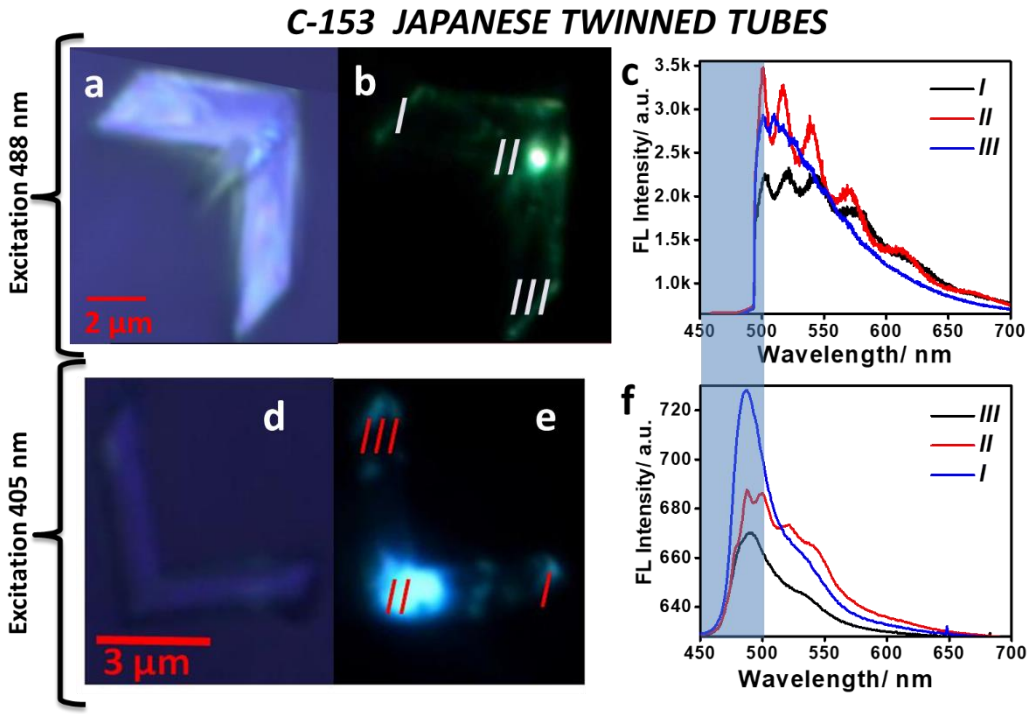

Figure 13: a, d) Confocal micrographs of a C-153 Japanese twin. b, c) Localized excitation of a single Japanese twin with a 488 nm Ar^+ laser at the twin boundary (*II*) and twin tips (*I* and *III*) and the corresponding FL spectra supporting F-P type optical modes, respectively. e, f) Excitation of a twin at different locations (*I*-*III*) with a 405 nm diode laser and the corresponding FL spectra, respectively.

nm) at the center of the rod and during wave guiding majority of the blue FL light is reabsorbed, guiding most of the unabsorbed green and residual blue-green light to the rod ends (Figure 11f inset). In case of sheets excitation at one of the edges clearly showed the propagation of green FL (500-700 nm) to other edge confirming the 2D

confinement effect. FL mapping showed F-P type resonance modes along the edges whereas as expected no modes were found in the FL collected from the center of the sheet (Figure 13).

Excitation of Japanese twined crystals with a 488 nm laser (objective 150×) at the twin boundary or one of the arms (Figure 13a and b) produced a green FL propagating to both ends. The corresponding FL spectrum supported the F-P modes as expected from the rectangular cross-section of the twinned crystals (Figure 13c). Further, the profile of the FL band indicated the possible FL maximum below ~490 nm akin to micro-rods. To understand, excitation was performed with a 405 nm diode laser (Figure 13d and e). A blue FL at the place of excitation was observed and due to reabsorption effect, only blue-green light propagated to the output end. The FL spectra recorded at different positions (labeled I –III) displayed two emission maxima at ~486 nm and ~526 nm (Figure 13f). The intensity of these bands varied depending upon the collection positions pointing out the anisotropic nature of the structure.

3.3.7. NLO Studies:

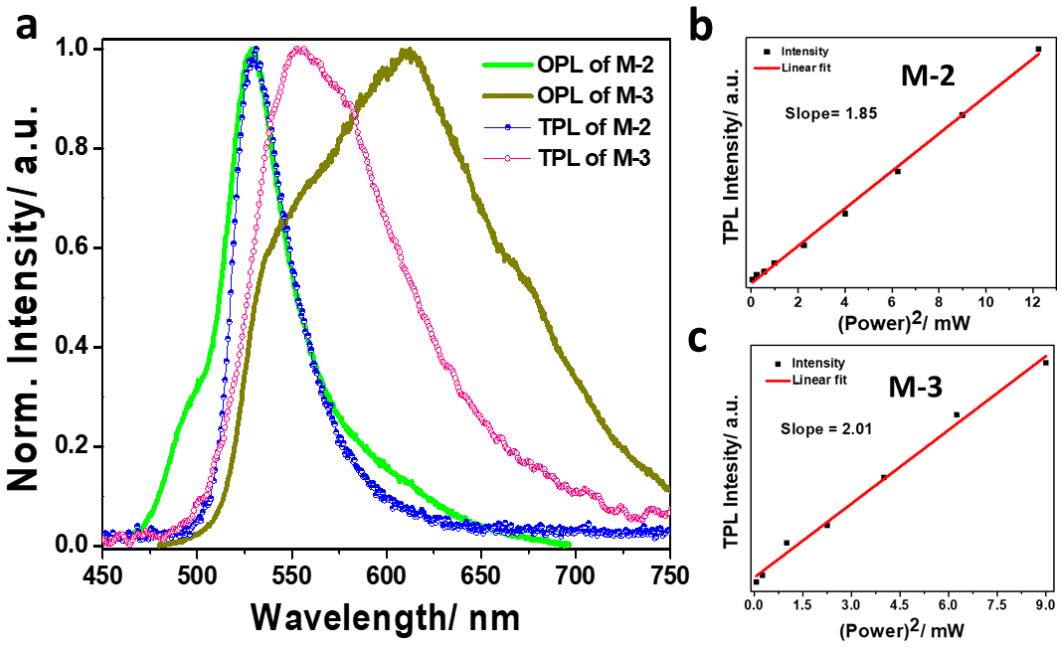

Figure 14: a) One- (400 nm) and two-photon (800 nm) excited emission spectra of polymorphs of C-153 in solid state. b, c) The TPL intensity verse square of input pump power plot of **M-2** and **M-3** respectively.

In order to study the NLO properties such as TPA or SHG from the polymorphs of **M-2** and **M-3**, a high power titanium sapphire fs laser operating at 800 nm was used to provide below band-gap excitation. With ultrashort pulses (100 fs) with a repetition rate of 1 KHz, the experiment was performed by keeping the sample at the focal volume having the spot size of 101.8 μm.

Both **M-2** and **M-3** crystals show very strong broadband up-converted emissions at 530 nm and 550 nm, respectively. As mentioned earlier, no linear absorption occurs in the spectral range from 550–800 nm for **M-2** and **M-3**. So it was concluded that absorption of simultaneous two photons (TPA) is responsible for the TPL. Figure 14a shows the TPL spectra of **M-2** and **M-3** in the crystalline state. The TPL maxima of **M-2** observed a single sharp peak at 530 nm without any shoulder peaks, whereas in the case of **M-3** a single broad peak at 554 nm is observed. The FWHM of the TPL band of **M-3** was much wider compared with **M-2**. In comparison with single-photon fluorescence, **M-2** shows the same TPL spectral patterns but **M-3**

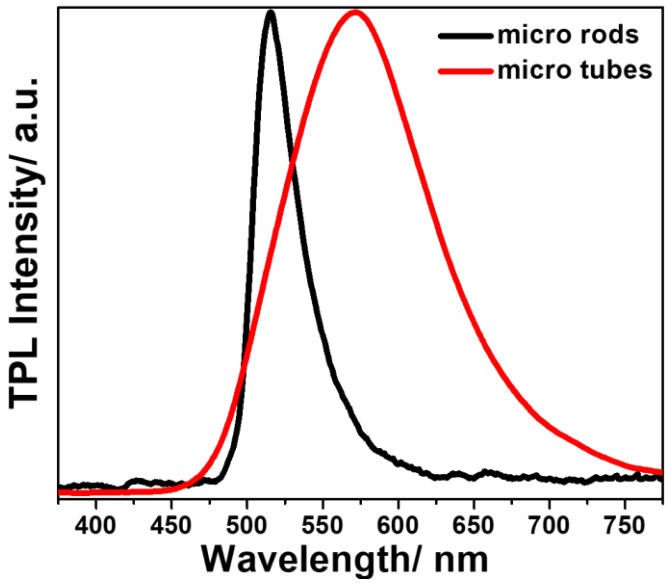

Figure 15: Two-photon (800 nm) excited emission spectra of micro-rods and micro-tubes of C-153 molecules.

was nearly the same with a blue shift, indicating their different excited-states emission process. To study pump power-dependent TPL enhancement, experiments were carried out with different pump intensity. The intensity at the focus was increased from 0.5 mW to 3.0 mW by adjusting the wave plate and the corresponding TPL spectra are shown in Figure 14a. A plot of TPL band intensity with the square of

pump power of **M-2**, showed a slope of 1.85 (Figure 14b) whereas the slope is 2.13 in the case of **M-3** (Figure 14c) within the experimental accuracy. These results revealed the second-order nature of the TPL signal. A similar experiment was performed on a sample containing self-assembled micro-structures. The micro-rods exhibited a green emission and the obtained TPL is very much similar to that of TPL and OPL from **M-2** crystal (Figure 15 black line). In the case of micro-tubes, a greenish yellow TPL was observed with a spectral pattern similar to the **M-3** crystal (Figure 15 red line) indicating similar molecular packing in both cases.

3.4. Conclusions:

In summary, the opto-structural correlation of the yellow and green emissive polymorphs (**M-2** and **M-3**) of C-153 indicated the dominant role played by the intermolecular (H-bond and π-π stack) interactions, *J*-aggregation and involvement of possible twisted charge transfer process in case of **M-3**. Further, binary solvent mixture (ACN:water) ratio-dependent self-assembly of C-153 produced rods, tubes and Japanese-twin tubes emitting aggregation dependent FL as a result of dissimilar solvation dynamics around dye molecule. Raman spectroscopy studies evidently revealed the difference in the molecular packing arrangements of all the self-assembled structures, whereas similarity in the molecular packing was found for rods and tubes with polymorphs **M-2** and **M-3**, respectively. This was further confirmed by the single particle FL microscopy examination, which revealed green and yellow FL of rods and tubes, respectively akin to **M-2** and **M-3** emissions. Moreover, these self-assembled micro-structures composed of C-153 molecules functioned as optical cavities depending upon their geometries. The NLO properties of both of crystals and self-assembled micro-structures of C-153 molecules were studied. The TPL of micro-rods same to TPL of **M-2** crystals and TPL of micro-tubes similar to **M-3** crystal TPL as a result of close molecular packing between them.

4

High Optical Energy Storage and Two-Photon Luminescence from Solution Processed Perovskite-Polystyrene Composite Micro-Resonators

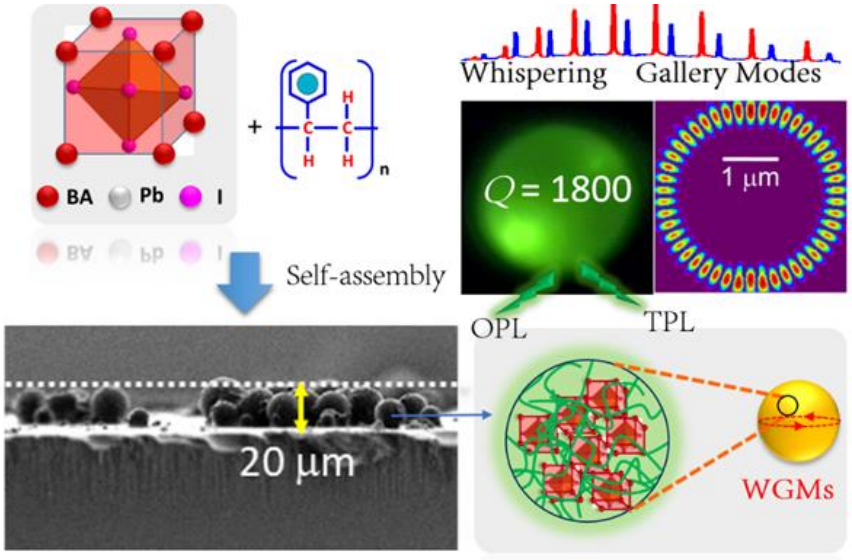

4.1. Abstract:

*Green emitting two dimensional, layered benzylammonium lead iodide (**M-4**) perovskite micro-rods are made via anti-solvent diffusion method. To stabilize the **M-4** structure and enhance its emission intensity, **M-4** was dispersed in polystyrene (PS) matrix. Optimization of the ratio of **M-4**-PS leads to defect-free micro-spheres during the self-assembly. These composite micro-spherical cavities display WGMs with high optical storage energy as evidenced by their Q-factor which is as high as ~1180. Two-dimensional finite difference time-domain calculation shows the concentration of electric field near the micro-spheres boundary with much smaller mode volume of 1.83 μm³. Remarkably, **M-4**-PS composite micro-resonators and their neat crystals exhibit brilliant TPL upon excitation with fs infrared fundamental radiation. This simplistic micro-resonator fabrication technique provides a route towards low-cost NLO micro-lasers useful for various applications.*

4.2. Introduction:

In recent years, solution-based preparation and processing technologies of organic-inorganic hybrid perovskites have attracted significant attention due to their low-cost and captivating applications in optoelectronic, photovoltaic devices and micro-lasers.[247-249] The most explored perovskites till date include methylammonium lead halides ($MAPbX_3$), tin halides ($MASnX_3$), and $CsSnX_3$ (where, X = Cl^-, Br^- and I^-). Specifically, lead halide compounds to possess suitable optical band gaps, and it has been used as a resourceful emissive species in light emitting diodes and low thresholds micro-lasers.[250,251] However, the poor stability of these materials against moisture limits their applications in various fields. The basic crystal structure of these perovskites (ABX_3) tends to hydrolyze in water that destroys the lattice structure. To overcome this drawback, aromatic amine or larger amine groups are introduced to create 2D perovskite structures. It is expected that these amine groups arranged in a layered structure increase the van der Waals interaction between the organic moieties providing high structural stability.[252,253]

Moreover, the optical band gap of these hybrid materials can be tuned over a wide range of energy by varying the organic ammonium cations or halogens or by controlling the dimensionality of inorganic cations. These chemical adjustments tend to affect the charge carrier mobility, carrier diffusion length in addition to band gap energies.[254] Various 1D to 3D perovskites were prepared depending on the structure of organic ammonium cations. [255,256] Specifically, 2D structures provide quantum

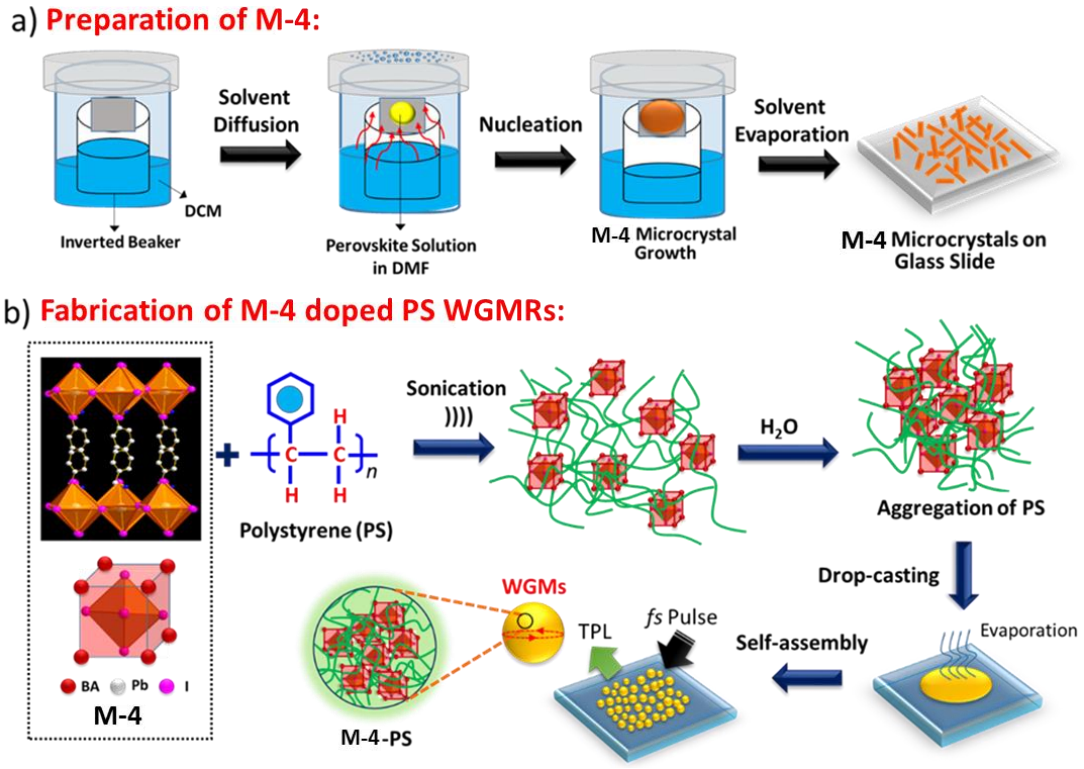

Scheme 1: a) Schematic illustration of **M-4** perovskite micro-crystal growth on a glass slide. b) Fabrication of **M-4** -polystyrene composite micro-spherical WGMRs via self-assembly method.

confinement effect and hence they are expected to display wider band gaps and narrow FL at room temperature compared to that of 3D structures.[257] Particularly, till date, a vast number of reports are available, which report the one-photon pumped optical luminescence of neat $MAPbX_3$ based compounds.[258] On the other hand, materials with NLO response such as TPL, SHG, and OR are of increasing interest. For example, Sargent et al., demonstrated TPA in $MAPbBr_3$ perovskite single crystals.[259,260] Change in the organic cation leads to the dramatic changes in the formation of perovskites in different dimensions with varied optoelectronic properties. Though the synthesis of benzylammonium lead halide ($BALX_3$)

perovskites is mainly focused in the literature, to our knowledge, its stabilization, NLO properties and extension of its use in nano-photonic materials is severely limited.[261-263] This motivated us to focus on the above often ignored issues of $BALX_3$ perovskites.

This chapter presents, the first synthesis of benzylammonium lead iodide (**M-4**) perovskite micro-crystals by a facile one-step solution self-assembly method (Scheme 1a). A comparative photonic property of pure **M-4** micro-crystal and **M-4** stabilized within PS micro-spheres is also presented. Interestingly, **M-4**-PS composite micro-spheres exhibit enhanced FL due to WGM resonance with a high *Q*-factor of 1180. The finite difference time-domain (FDTD) calculation reveals the concentration of optical field close to the boundary of the spherical structure due to WGM resonance. These results show that the layered **M-4** perovskite can act as multi-photon (infra-red) pumped optical gain media and provide a new platform for perovskite-based NLO photonic devices.

4.3. Results and Discussion:

4.3.1. Preparation of Benzyl Ammonium Iodide (3):

Initially, 5 mL of benzylamine was added to 15 mL of methanol (AR) kept at 0 °C. Then 5 mL of HI (*57 wt. % in water)* was dropped into the mixture and stirred for 1h. Then, the mixture was transferred to RT and stirred for another 2 h. The solvent retained in the mixture was evaporated by a rotary evaporator at 60 °C, leaving with only white crude product. White flake crystal of $C_6H_5CH_2NH_3I$ was finally obtained by recrystallizing the as-obtained crude product in diethyl ether and methanol.

4.3.2. Preparation of Benzyl Ammonium Lead Iodide (M-4):

At first, a thin film of $Pb(OAc)_2$ was prepared on a glass slide by spin-coating of a 20 µL solution of $Pb(OAc)_2$ in DMF (100 mg/mL). The film was dried on a hot plate for 30 min at 60 °C. **M-4** bulk crystals were synthesized by placing the Pb precursor into a solution of **3** in isopropanol (IPA) of concentration 500 mg/mL at RT. The Pb precursor coated side of the slide was kept in such a way that it faces the solution in a beaker and left undisturbed for about 24 h. Further, a similar procedure was repeated by placing the Pb precursor-coated side facing up in the solution of **3** (50

mg/mL) in IPA. The glass plates were washed using IPA to remove any residual solution on the substrate. The bulk crystals of **M-4** were analyzed with different spectroscopic techniques.

4.3.3. Synthesis and Growth of M-4 Micro-Structure:

Initially, the precursor solutions of **3** (*c* = 0.2 M) and $Pb(OAc)_2{\cdot}3H_2O$ (0.2 M) in N,N-dimethylformamide (DMF) were prepared. Prior to the synthesis, equal volumes of these precursor solutions were mixed thoroughly to give a stock solution of $C_6H_5CH_2NH_3PbI_3$ perovskite (**M-4**). In order to obtain micro-crystals, 20 µL of stock solution **M-4** was drop-casted on a 1 × 1 cm^2 coverslip. This slide was placed on a glass

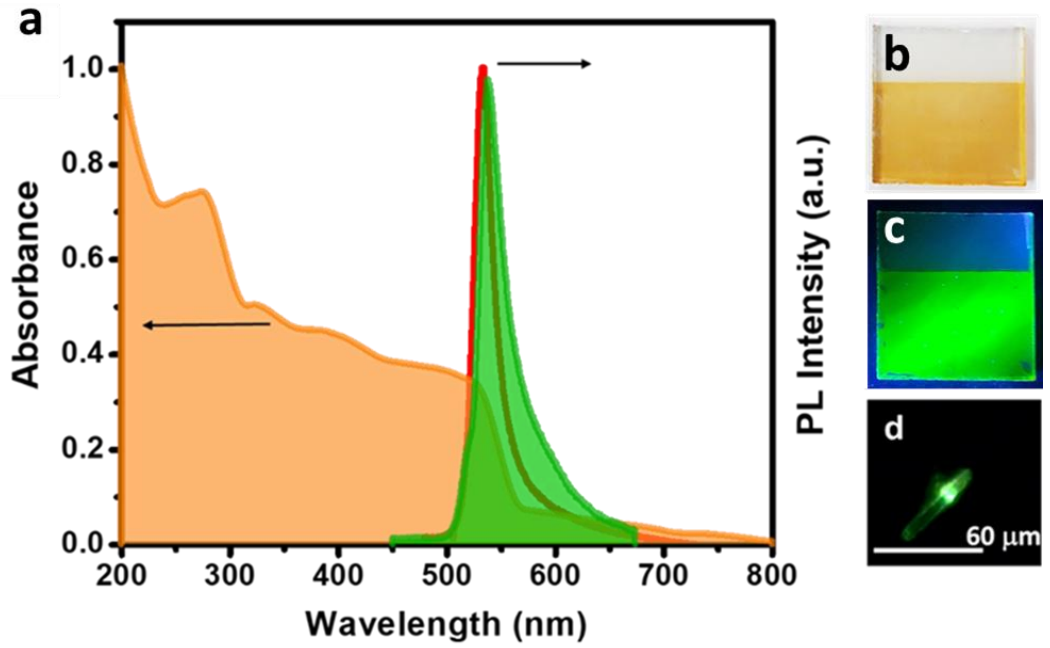

Figure 1: a) UV-visible absorbance and FL spectra of **M-4**. The green filled band (500-800 nm) exhibit FL of **M-4** thin film. The solid red line (500-700 nm) shows FL spectrum of **M-4** micro-crystal. Excited with 488 nm Ar^+ laser. b) Digital photographs of **M-4** thin film at the ambient light and c) under UV-365 nm light. d) FL image of a single micro-crystal when excited with 488 nm Ar^+ laser.

stage inside the beaker (see Scheme 1a) containing 25 mL of dichloromethane (DCM) leveled below the glass stage, and it was sealed with a porous parafilm to control the evaporation rate of both precursor solution and DCM. Here, DCM is known to act as a poor solvent for $C_6H_5CH_2NH_3PbI_3$ micro-structures and is miscible with DMF. As this DCM is highly volatile, its vapor diffuses into the solution of **M-4**, induces the

nucleation.[264,265] The formed nuclei grow into a long needle-like micro-crystals of **M-4** (Scheme 1a).

4.3.4. Spectroscopy and Microscopy Studies of M-4:

The solid-state UV-visible spectrum of pure **M-4** shows a broad absorption band from 250 nm to 800 nm with an abrupt decrease at about 560 nm. Therefore the sample was excited by a xenon lamp with the wavelength range from 450 nm to 500 nm to achieve an emission with a maximum intensity. The emission peak maximum was observed at 538 nm with a FWHM of ~30 nm (Figure 1a). The optical band gap calculated from the absorbance spectrum of **M-4** perovskite was about 2.18 eV.[265]

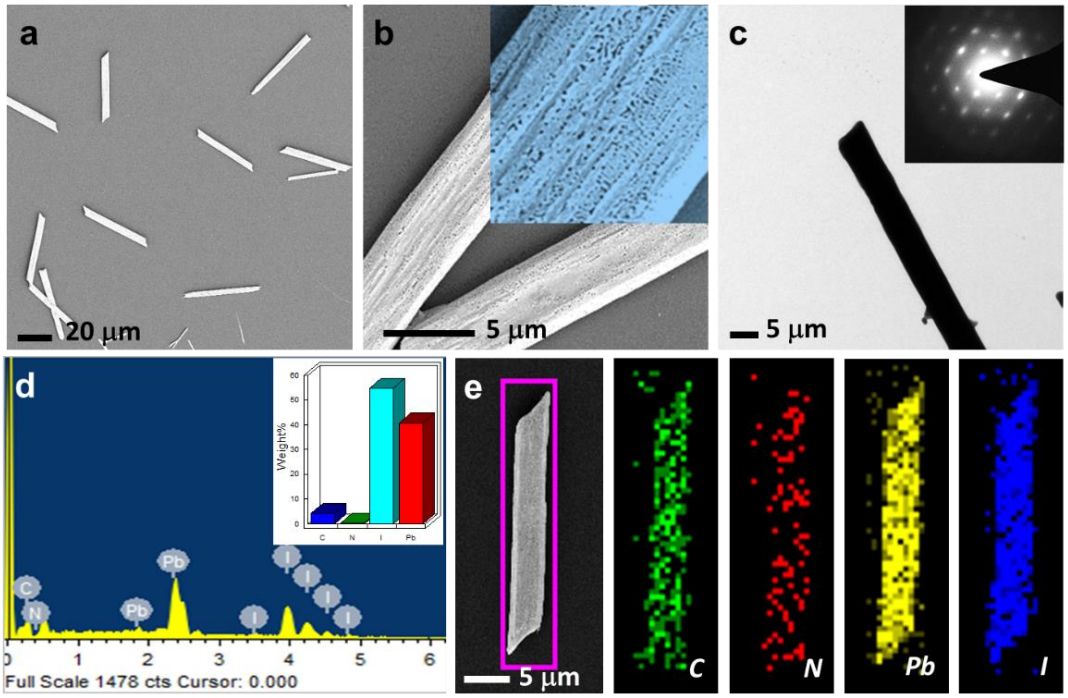

Figure 2: a, b) FESEM images and c) TEM image of **M-4** perovskite micro-rods. The inset of (b) and (c) show color-coded magnified view of porous structure of a micro-rod and its SAED pattern, respectively. d) EDS spectrum of a micro-rod and the inset shows percentage of elements present within micro-rod. e) Elemental mapping of single micro-rod.

Figure 1b,c shows a digital photograph of **M-4** thin film at the ambient light and under UV light (365 nm) excitation, respectively. At ambient temperature, the **M-4** thin layer appeared in orange color, however when the same sample was illuminated with UV light (365 nm) it exhibited a bright green emission.

The FESEM analysis showed that the micro-structures are nearly monodispersed rectangular rods (Figure 2a) with length and width in the range of 50 µm and 5 µm, respectively. A close-up view exposed the presence of nano-sized (diameter~20-50 nm) pores in the micro-rods (Figure 2b). The micro-rods were further subjected to TEM studies (Figure 2c) and the width of the micro-rod was found to be 5 ± 2 µm. The SAED pattern clearly established the single crystalline nature of **M-4** micro-rods (Figure 2c inset). The EDS spectrum clearly confirmed the presence of Pb, I, C and N elements within the micro-rods (Figure 2d). Further, the presence of these elements within the micro-structures was verified by conducting elemental mapping on a single micro-rod (Figure 2e).

To probe the waveguiding propensity of the 1D micro-rods, single-particle experiments were carried out using a 488 nm (Ar^+) CW laser as an excitation source. When a bulk of the single micro-rod was excited with the laser spot size of 6 µm provided by a 20x objective, it showed a sharp emission peak maximum at ~538 nm with a reduced FWHM of ~21 nm compared to its thin film (see the red line in Figure 1a).

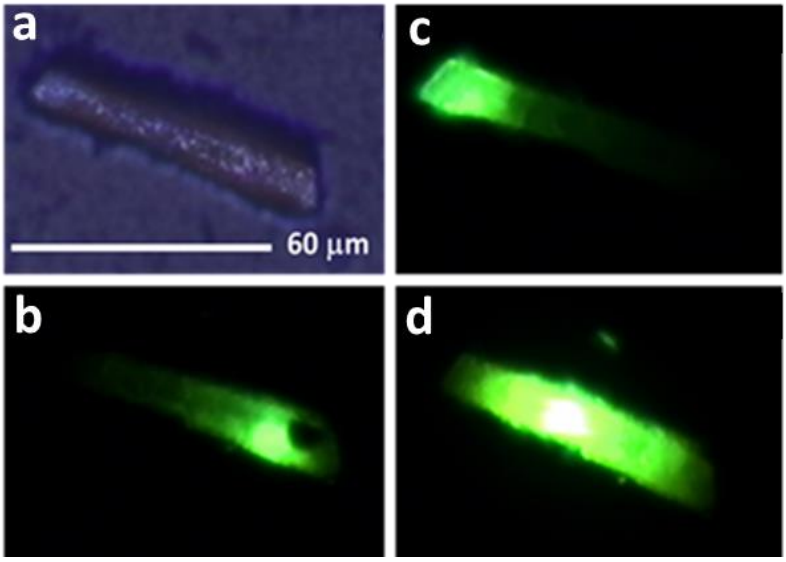

Figure 3: a) Bright field and b-d) FL images of **M-4** micro-rods excited with 488 nm laser at different positions.

Focused laser excitation (spot size: 6 µm) of one of the micro-rod ends displayed a bright localized green emission (Figure 3b, c), while excitation at the center of the micro-rod exhibited a localized bright green emission (Figure 3d). The absence of waveguiding property along the micro-rod indicated that the extended nature of nano-pores to order of microns, which leads to poor light confinement or, in other words, high optical loss of the propagating light.

4.3.5. Fabrication of M-4-PS Composite Micro-Spheres:

25 mg of PS was dissolved in 4.0 mL of THF (HPLC grade) and sonicated for one minute to dissolve the PS beads. Then 20 µL of 0.05 M **M-4** in DMF was added to the PS solution, it was mixed thoroughly and kept for 5 min. To this mixture, 1.0 mL of deionized water was added and left undisturbed for about 10 minutes to ensure the growth of high quality microspheres in the solution itself. Afterward 100 µL of this mixture was drop-casted on clean glass coverslip and the solvent was allowed to evaporate to get PS-**M-4** micro-spheres (Scheme 1b). In the case of **M-4** coated PS micro-spheres, 5µL to 20 µL of the **M-4** solution was added after the formation of micro-spheres in THF:H_2O (4:1).

4.3.6. Spectroscopy and Microscopy Studies of M-4-PS Micro-Sphere:

Since these micro-rods are very sensitive to moisture, to make use of the perovskite as an active material for photonic device applications, PS was used as a matrix to stabilize **M-4** as the former forms micro-spheres suitable for the resonator and lasing applications.[265] Earlier study in this context showed that coating of **M-4** on the surface of the silicon micro-spheres exhibiting lasing action.[266] However, an expensive atomic layer deposition method was utilized for coating the perovskite on the surface of silicon spheres and the stability of the perovskite coated on silicon micro-sphere was not fully addressed. Hence, two experiments were planned to understand the stability of **M-4**-PS composite: (i) **M-4** coated on the surface of the PS micro-sphere (see Figure 4) and (ii) **M-4** mixed with PS solution to ensure the **M-4** within the PS micro-sphere matrix. In the first approach, PS micro-spheres were coated with **M-4**, where the **M-4** was exposed to moisture. As perovskites are highly sensitive to moisture, they tend to decompose in a shorter time, hence they show less stability. In the second experiment, the **M-4**+PS were mixed (20 µL in DMF: 4 mL THF) together then water (1 mL) was added and allowed to form composite micro-spheres. The solution was left undisturbed for 20 min and it was drop casted on a glass slide and the solvents were evaporated at RT. Examination of the sample under a confocal microscope exhibited circular structures hinting the formation of micro-spheres. These **M-4** within the PS matrix show high stability compared to the coated one, as

the perovskite is embedded with the polymer matrix, the latter prevents the degradation of **M-4**.

To further confirm the shape, size and surface smoothness of these PS-**M-4** micro-spheres, FESEM analysis was carried out (Figure 4). The FESEM micro-graphs clearly explicated the presence of polydispersed PS-**M-4** micro-spheres with a smooth surface, which is essential for a micro-sphere to act as a micro-resonator (Figure 4a

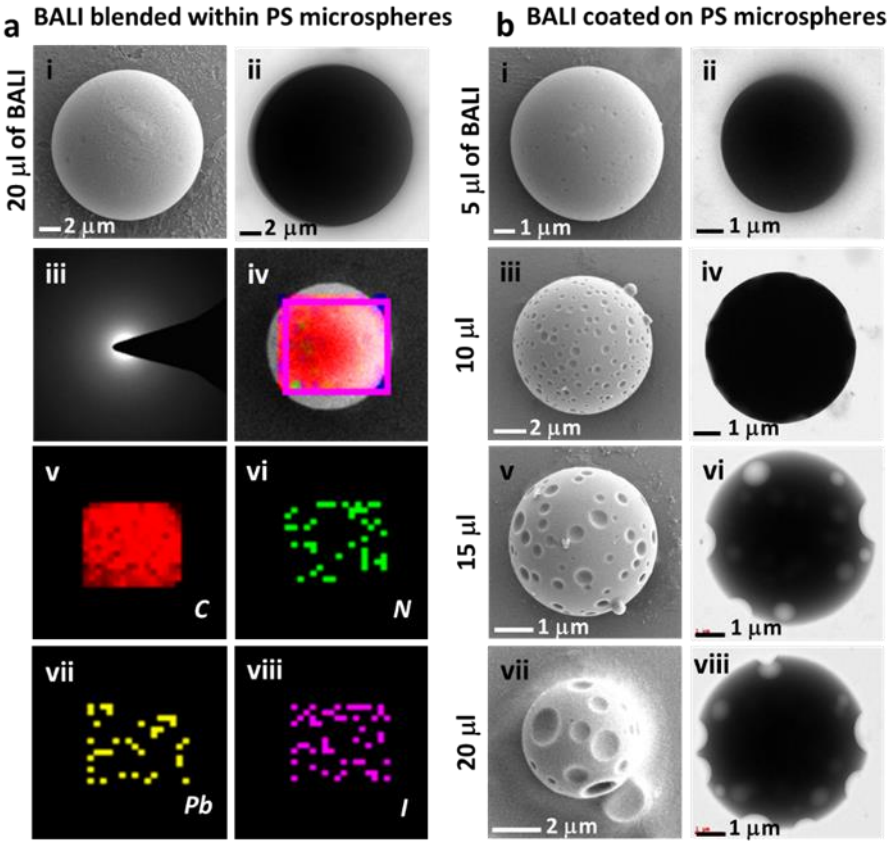

Figure 4: a (i, ii)) FESEM and TEM images of PS micro-spheres blended with **M-4**. a (iii)) SAED pattern of PS micro-spheres blended with **M-4**. a (iv-viii)) EDS elemental map of single micro-sphere. b) FESEM and TEM images of PS micro-spheres coated with different concentration of **M-4**.

(i)). The TEM images of a micro-sphere also confirmed the defect-free smooth surface as shown in Figure 4a (ii). Similarly, the FESEM micro-graphs of **M-4** (5 µL) coated on PS micro-spheres also showed a smooth surface (Figure 4b (i)). However, when the concentration of the **M-4** in isopropanol (IPA) and DMF was increased from 10 µL to 20 µL nano-concave (~100 nm to 1 µm) shaped defects were formed on the surface of these micro-spheres producing golf ball-like features (Figure 4b (iii-viii)). These

defects could be due to micro-solvent (IPA) droplets which were attached to the surface of growing PS micro-spheres.[266] High concentration of the **M-4** increases the solvent volume, which leads to the formation of golf ball-like structures. Similarly, **M-4** coated PS micro-spheres showed defect-free surfaces. The chemical composition of these micro-spheres was further confirmed by FESEM and EDS studies. The EDS elemental mapping of a single PS- **M-4** micro-sphere clearly showed the presence of C, N, Pb and I elements confirming that the **M-4** was incorporated into PS micro-sphere (Figure 4a (iv-viii)). The TEM micrographs also revealed that the defects are only on the surface (Figure 4b (iii-viii)). Further, the confocal microscopy, FESEM, and TEM evidently indicated the polydispersed nature of the micro-spheres with the size distribution of about 2-8 µm. The SAED pattern showed no diffraction spots from the microspheres (Figure 4a (iii)) indicating their amorphous nature.

4.3.7. Single-Particle Micro-Spectroscopy and Numerical Calculation of Micro-Spheres: [FDTD simulations was performed in collaboration with Prof. T. Murzina, MSU, Moscow]

The photonic properties of these micro-spheres were verified by single-particle confocal fluorescence microscopy studies. When an edge of a **M-4**-PS micro-sphere was excited with a CW laser (Ar^+ 488 nm; power: 10 mW; objective: 150x)

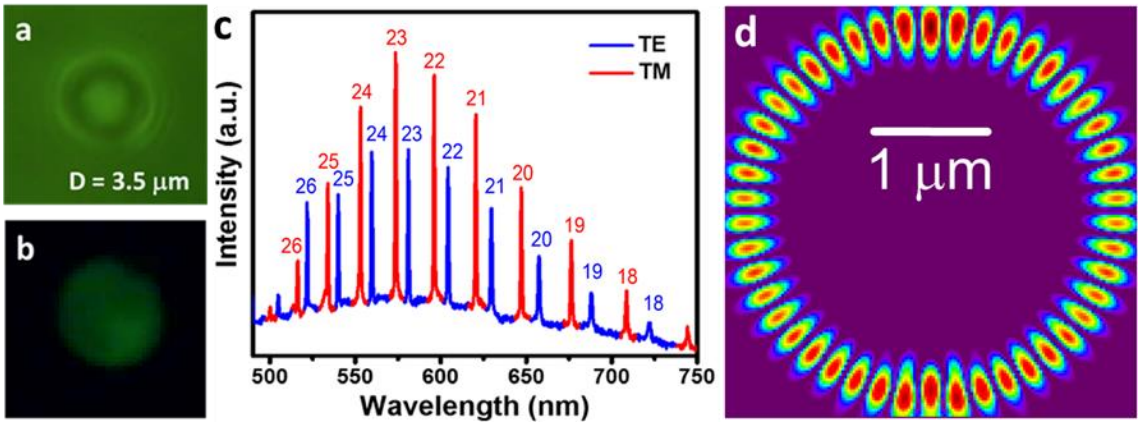

Figure 5: a) and b) Single-particle bright field and FL images of a composite M-**4**-PS micro-resonator excited with a 488 nm CW laser. c) Its corresponding single-particle FL spectrum. The TE/TM mode numbers were calculated using FDTD simulation. d) FDTD numerical simulation of a micro-spherical resonator displaying the electric field distribution for TE_{23} and the corresponding mode volume 1.83 μm^3.

beam, a bright ring-shaped FL was observed at the periphery of the micro-sphere (Figure 5b). Further, a series of distinct pairs of sharp peaks were observed in the FL spectrum (from 500 nm to 750 nm) collected from the edge of the micro-sphere. This clearly indicated the existence of WGM resonances as a result of multiple TIRs of the emitted light at the interface between the micro-sphere and air (Figure 5c).[229,267] The

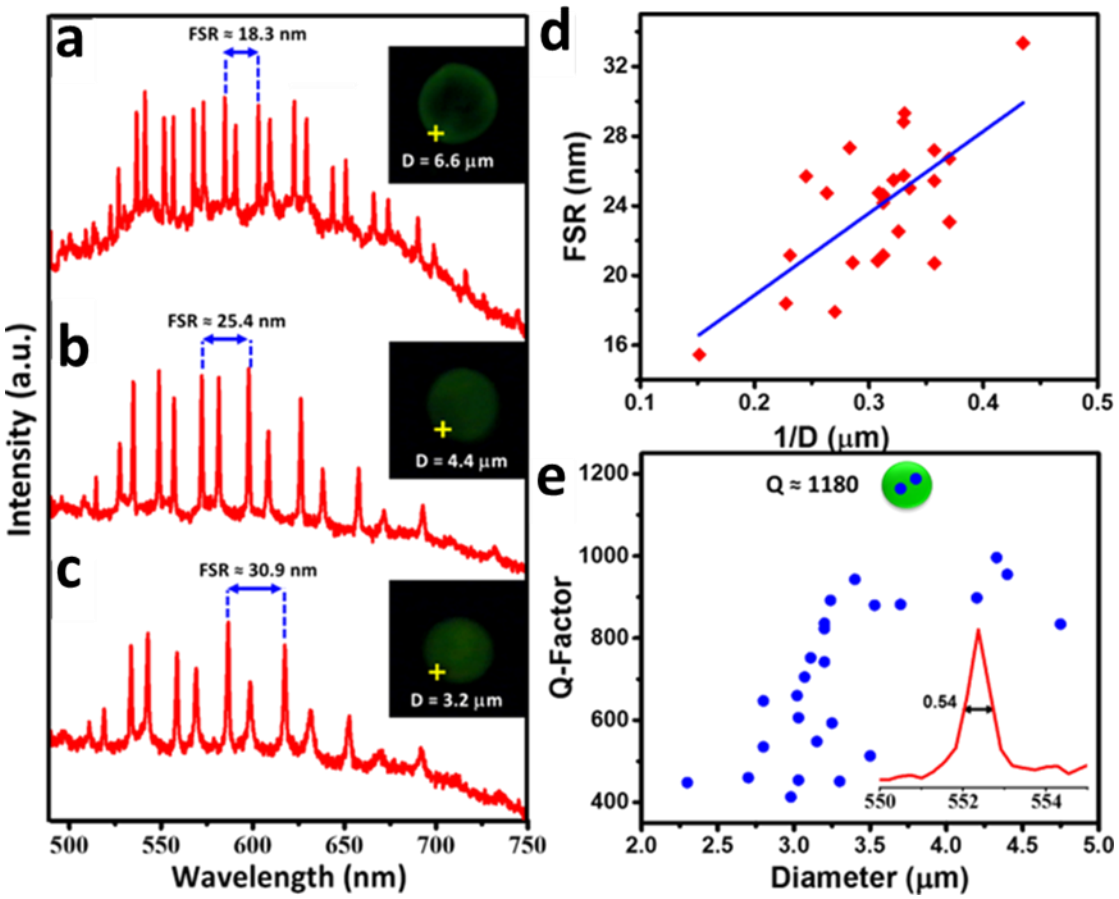

Figure 6: Single-particle FL spectra of **M-4**-PS micro-sphere with different size (a-c). The insets shows its corresponding FL images of micro-spheres. A plot of (e) Q factor versus particle diameter and (d) FSR values versus 1/D with linear base fitted line.

appearance of both TE/TM modes with nearly same intensity indicated the unpolarized nature of the WGM emission.[201,268] Another interesting feature of the WGM spectrum is the near absence of FL background, which points toward high *Q*-resonators. A two-dimensional finite difference time-domain (FDTD) method was employed to simulate the WGM spectrum (for radical mode number, r =1; polar and azimuthal mode number, m=l) and the electric field distribution within the resonator. From the calculation, the pair of peaks such as TM and TE was identified as azimuthal

mode numbers from TM_{18}-TM_{27} and TE_{18}-TE_{27}, respectively (Figure 5c). The simulated electric field distribution (for TE_{23}) within the micro-resonator showed the localization of an intense electric field around its periphery (Figure 5d). The estimated TE_{23} mode volume of the micro-spheres is 1.83 μm^3.

Similar single-particle FL studies on micro-spheres with concave surface deformation showed a broad FL spectrum centered at 540 nm without any WGMs. Moreover, the WGM parameters of individual micro-spheres with different sizes were also investigated to gain more insight about the effect of cavity size on field confinement, FSR, and *Q*-factor. Figure 6 presents the FL spectra and FL image (insets) of three distinct micro-spheres with different diameters (D) under excitation with 488 nm CW laser. Unambiguously, the FSR value was found to decrease with increase in the micro-sphere D as per the relation. Micro-sphere with D of 6.6 µm showed lower FSR value i.e., 18.3 nm (Figure 6a), however, when the value of D ~ 4.4 and 3.2 µm, the FSR values increased to 25.4 and 31 nm, respectively (Figure 6a-c). The FSR values obtained for various sizes of micro-spheres were plotted in Figure 6d. The *Q*-factor of the resonators is improved with the increase of the cavity D since the surface scattering losses of the circular resonator drop exponentially with their size. The maximum *Q*-factor achieved for the PS-**M-4** micro-sphere was about 1180 (λ= 552 nm; FWHM = 0.54 nm) (Figure 6e), which corroborated well with the absence of FL back ground in the WGM spectrum.

4.3.8. Fluorescence Life-Time Imaging:

FL life-time of the PS-**M-4** micro-spheres was investigated by confocal fluorescence life-time imaging microscopy (FLIM) measurement. The lifetime decay profile was obtained by time-correlated single photon counting (TCSPC) technique using a picosecond pulse laser (405 nm) for excitation. Life-time decay profile of PS-**M-4** micro-spheres showed average FL decay of 3.67 ns (Figure 7). When individual micro-spheres were subjected for FLIM studies, interestingly each micro-sphere showed different decay (τ) values. For example, the particle with D ~4.5 µm showed 3.34 ns life-time decay. However, when the particle size decreased to 3.2 mm, the decay time was declined to 3.1 ns (Figure 7b). This clearly indicates that the FL photon

life-time (τ_P) decay depends on the size of the photonic particles as per the following equation.

$$\tau_P = \frac{Q}{\omega} \qquad \text{..... 4.1}$$

Where ω is the angular frequency of the photons. Here the resonator size is related to its Q-factor, where the large size particles show high Q-values because of the

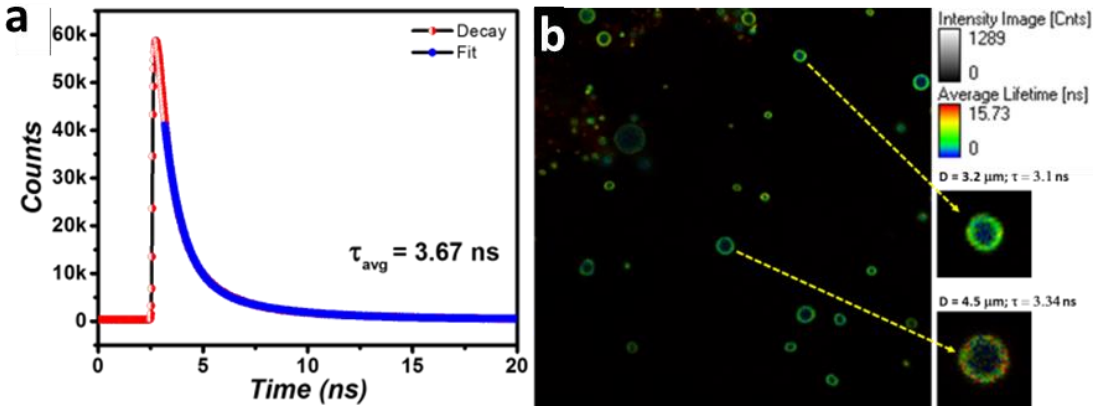

Figure 7: a) Average FL life-time decay profile of **M-4**-PS micro-spheres and (b) its corresponding FLIM image. The inset of (b) micro-sphere FLIM images show particle size dependent life-time values.

increased photon trap time within the cavity. As a result, the bigger particles traps the FL photons efficiently, this led to the increased FL life-time compared to the smaller particles, which displays lower life-time values.[269]

4.3.9. NLO Studies:

To explore the NLO property of **M-4**, experiments were carried out using high intense fs pulse laser field and compared with OPL. An ultrafast Ti:Sapphire laser system with the fundamental wavelength of 800 nm, a pulse width of 60 fs was used for the excitation of **M-4**. **M-4** crystals excited with this laser radiation showed a green TPL centered at 553 nm in contrast to one photon-pumped bright green emission observed at 537 nm (Figure 8).

This result clearly indicated that the **M-4** crystals are a multiphoton active material. A slight red shift in the TPL spectrum of **M-4** with respect to the OPL spectrum could be due to the reabsorption effect. Driven by the emanating TPL from **M-4**, experiments were carried out with a different pump to study the dependence of

TPL intensity of the material. At low (8 μJ/cm^2) pump fluence, a very weak TPL intensity was observed (Figure 8). However, an increase in the excitation intensity leads to an increase in the TPL intensity. The dependence of the TPL intensity on the fundamental radiation power corresponds to the quadratic power law (Figure 8

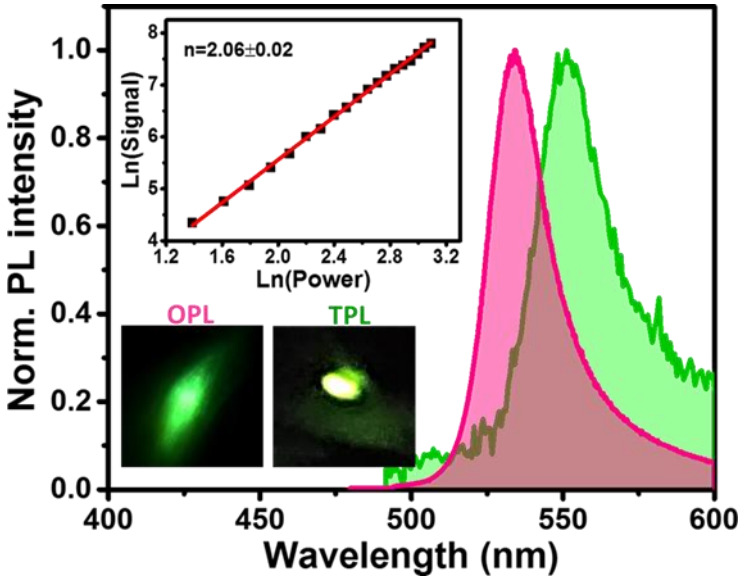

Figure 8: OPL and TPL spectra of **M-4** crystal. The inset double logarithmic power plot shows power vs TPL intensity plot, the linear power fit is shown in red colour. The inset digital photographs show one and two photon excited luminesce of **M-4** micro-crystal.

inset). In order to indirectly probe the TPA range, the sample was excited at different fundamental wavelength (760 nm to 860 nm) and 3D excitation-emission dependence was measured, which is shown in Figure 9a. The 3D NLO response from **M-4** crystals were obtained in the range of 540 nm to 590 nm (Figure 9b). The intensity distribution shows maximum around 565 nm, with an amplitude weakly

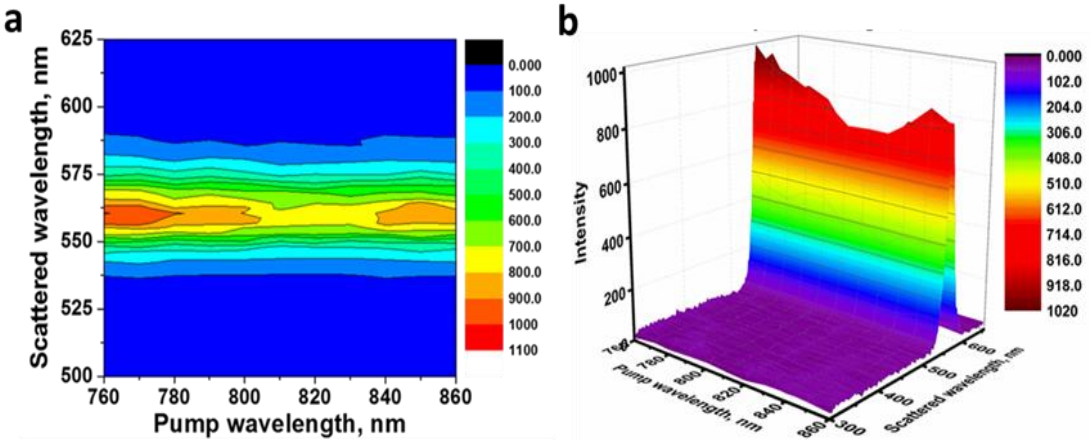

Figure 9: a) Emission-excitation spectrum of the TPL intensity for **M-4** crystal. b) The 3-d profile of TPL intensity and input power with respect wavelength.

depending on the fundamental wavelength in the range from 760 nm to 860 nm (Figure 9a). Similarly, a bunch of PS- **M-4** micro-sphere film of thickness about 20 µm (Figure 10a) also emitted two-photon pumped luminescence. The TPL spectra

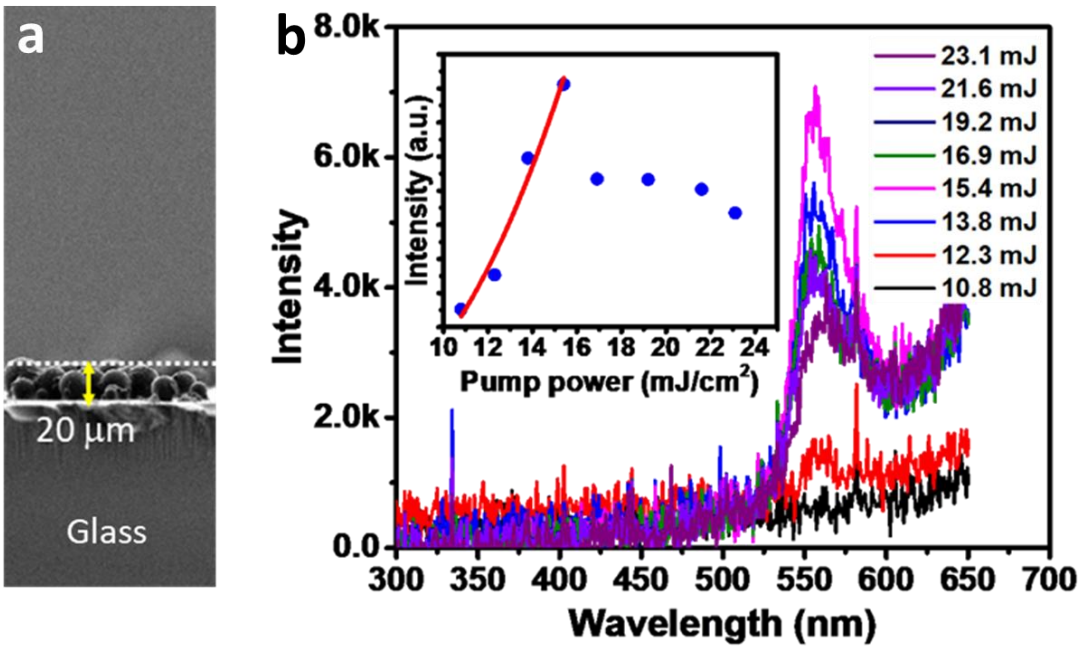

Figure 10: a) FESEM cross-sectional image PS-**M-4** of micro-sphere deposited on glass. b) TPL PS-**M-4** micro-sphere with different fundamental pump power. The inset shows a plot of intensity verses pump fluence.

collected with different pump energy are shown in Figure 10b. The intensity of the TPL spectrum increased as a square of the pump pulse energy of up to ~15.4 mJ/cm^2. Upon additional increase of the pump power, a sudden decrease of the TPL intensity was observed (Figure 10b inset), which could be due to the radiation damage of the sample.[270] Thus the laser damage threshold of the PS- **M-4** microspheres is 15 mJ/cm^2.

4.4. Conclusions:

In summary, this chapter demonstrated the preparation of 2D layered **M-4** micro-crystals on glass slides by anti-solvent diffusion method using DCM as anti-solvent. For the first time, the green emitting **M-4** perovskite was incorporated within PS to give an air-stable high-*Q* WGM resonator with the *Q*-factor as high as ~1.2 x 10^3. FDTD calculation demonstrated the localization of optical field near the micro-sphere

boundary with mode volume as small as 1.83 μm^3 for TE_{23} mode. Additionally, for the first time, the intrinsic TPL property of 2D **M-4** crystal was demonstrated and interestingly the crystal provided access to TPL in a broad range of fundamental excitation wavelengths from 860 nm – 760 nm. Importantly, a film of high *Q*-factor PS-**M-4** micro-sphere also displayed intense two-photon pumped emission to a smaller pump fluence in comparison to homogeneous thin film. The PS-**M-4** micro-sphere film was stable up to the pump fluence of ~15.4 mJ/cm^2. The NLO property of this 2D perovskite paves way for the development of new functional opto-electronic devices for direct practical applications.

5

Room Temperature Ferroelectricity, Terahertz Wave and Second Harmonic Generations from a Single-Component Polar Organic Crystal

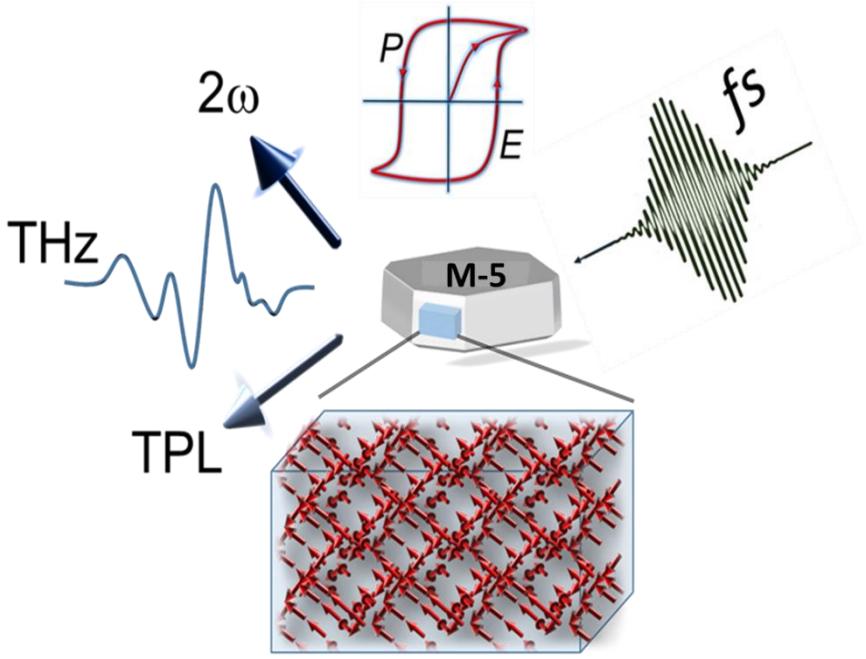

*This chapter is adapted from:

U. Venkataramudu, C. Sahoo, S. Leelashree, M.Venkatesh, D. Ganesh, S. R. G.l Naraharisetty, A. K.Chaudhary, S. Srinath, R. Chandrasekar. *J. Mater. Chem. C.*, **2018**, DOI: 10.1039/C8TC02638F

5.1. Abstract:

*Polar organic crystalline materials are known to act as ferroelectrics via electric switching of their inherent electric polarization. Principally RT organic ferroelectric materials producing both second harmonic and THz radiations are touted for use in sensors, photonics, electro-optics, and memory device applications.[140-145] On the other hand, identifying a single-component ferroelectric organic crystal, which can create the above NLO radiations is a difficult task and not reported so far. Here, this chapter reports a new moderate dipole (1.42 Debye) molecule, 4-(4-(methylthio)phenyl)-2,6-di(1H-pyrazol-1-yl)pyridine, (**M-5**) which crystallizes in an excellent polar molecular arrangement. Polar crystal, **M-5** exhibits a distinct ferroelectric hysteresis loop at room temperature, without any discontinuity in a temperature dependent dielectric (ε') measurements. Due to high second-order NLO susceptibility, superior phase matching conditions and low THz absorption, **M-5** single crystal produced both second harmonic and THz waves with an ample conversion efficiency. This result clearly establishes the practical usefulness of **M-5** for NLO and electro-optical applications at ambient temperature.*

5.2. Introduction:

Technologically, room temperature organic ferroelectric materials producing both THz and SHG are valuable owing to their transparency, light-weight, lower-cost, solution processability, and environmentally benign nature. Therefore a great deal of effort has been put into the exploration of single-component ferroelectric organic materials for both NLO and electro-optical applications.[142-147,273]

In contrast to inorganic compounds, the scarce examples of a single-component organic ferroelectrics are not surprising, as aggregating dipolar organic molecules in a 3-D condensed phase, in such a way that, all dipoles are dipole-parallel aligned is a grand challenge. Two essential ingredients in a recipe to a polar organic crystal are [271] (i) molecules possessing modest dipole moment to oppose with the dipole-antiparallel alignment, (ii) conducive intermolecular interactions to stabilize the dipole-parallel alignment. The energetics of supramolecular interactions, such as π-π

stacking and hydrogen bonding plays a pivotal role in the latter case in order to position the dipole molecules in a polar arrangement. Above all, serendipitous insight is a key element in most of the cases, including the medium-sized molecule based polar crystal presented in this work. The reason being is that, though the first ingredient of the recipe is rather probable to control synthetically, the latter is not even imaginable in medium- and large-sized molecules with multiple-rings. For smaller molecular systems, an attempt has been made earlier by Desiraju et al. to

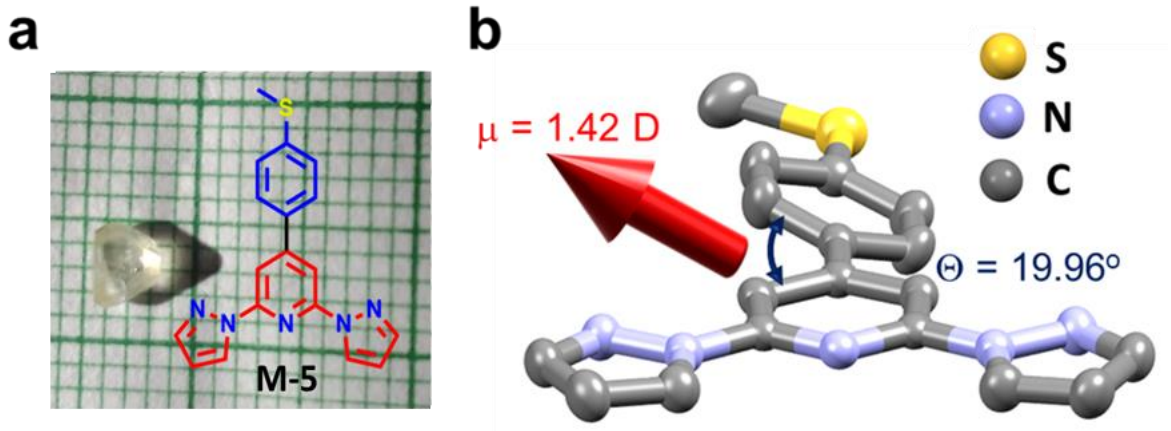

Figure 1: a) Structural formula of **M-5** is presented with the background photograph of its single crystal. b) Single crystal x-ray structure of **M-5** (30% thermal ellipsoid plot). Hydrogens atoms are omitted for clarity. The blue arrow shows the calculated (RB3LYP with basic sets 6-31G(D)) dipole moment (μ) of the molecule with the phenyl-pyridine dihedral angle, Θ = 19.96°.

guide the molecular dipoles into a polar arrangement using crystal engineering approach.[274] In this context, Choudhury et al examined the Cambridge crystallographic database and revealed the importance of selecting a symmetric molecule, i.e. molecular point group symmetry higher than C_1, to achieve ferroelectric crystals.[275] As far as the molecular functionality is concerned, after the well-known thiourea, no organosulfur group (weakly polar C-S bond) is exploited to achieve organic ferroelectrics.

Hence in this chapter, synthesis of a rather symmetric organic molecule with a methyl phenyl sulfide unit connected to electron deficient 2,6-di(1*H*-pyrazol-1-yl)pyridine (BPP) system, namely, 4-(4-(methylthio)phenyl)-2,6-di(1*H*-pyrazol-1-yl)pyridine, abbreviated as **M-5** (Figure 1a) was envisioned. In **M-5**, the BPP unit is a weak acceptor (A) and methyl(phenyl)sulfane is a modest donor (D) unit. **M-5** was

synthesized as a white powder by reacting 4-iodo-2,6-di(1*H*-pyrazol-1-yl)pyridine[276] (**1**) and 4-(methylthio)phenylboronic acid (**2**) via Suzuki cross-coupling conditions in ≈ 60% yields. The chemical structure of **M-5** was confirmed unambiguously by ^{1}H and ^{13}C NMR spectroscopy, high-resolution mass spectrometry, elemental analyses, and single crystal x-ray diffraction technique.

5.3. Results and Discussion:

5.3.1. Synthesis of M-4:

Compound 4-iodo-2,6-di(1*H*-pyrazol-1-yl)pyridine (BPP) **1** was prepared as per our reported procedure.[276]

Compound **1** (0.2 g, 0.593 mmol 1 equiv.), 4-(methylthio)phenylboronic acid (0.13 g, 0.77 mmol, 1.2 equiv.) and $Pd(PPh_3)_4$ (34 mg, 0.0003 mmol, 0.15 equiv.) were suspended in degassed 1,4-dioxane (20 mL). To this Na_2CO_3 (2.0 M, 4 mL) was added and heated at 90 °C for 3 d under the nitrogen atmosphere. The course of the reaction was monitored by thin layer chromatography (Eluent: dichloromethane/hexane). After the disappearance of starting materials the reaction mixture was cooled down to room temperature and then 1,4-dioxane was removed using a rotary solvent evaporator.

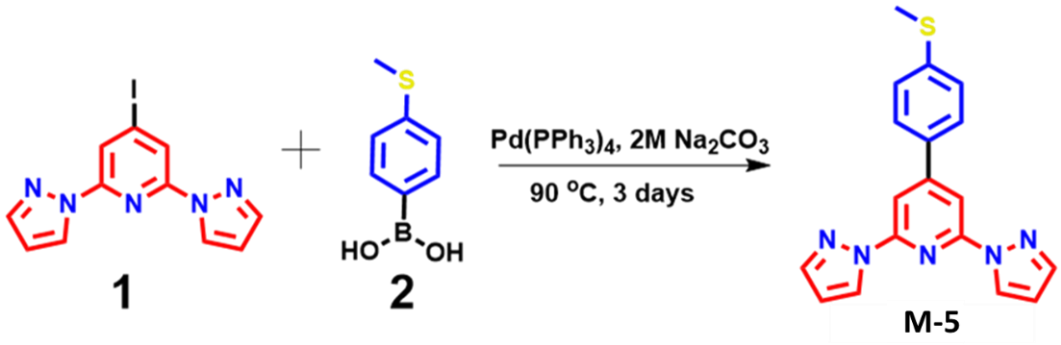

Scheme 1: Reaction scheme for the synthesis of **M-5**.

The resulting residue was treated with water and extracted with dichloromethane (DCM) solvent. The extracted organic fraction was dried over $MgSO_4$ and the solvent was removed in vacuo. The resulting white colour residue was subjected to silica gel flash column chromatography (1:1 DCM/hexane) to get compound **M-5** as a white powder (130 mg, 66% yield). ^{1}H-NMR: ^{1}H-NMR (400 MHz,

$CDCl_3$ - d_1, δ in ppm): 8.61 (s, 2H), 8.10 (s, 2H), 7.80 (s, 2H), 7.75 (d, 2H), 7.35 (d, 2H), 6.51 (s, 2H), 2.24 (s, 3H); ^{13}C NMR (100 MHz, $CDCl_3$ - d_1, δ in ppm): 153.4, 150.6, 142.5, 141.3, 133.7, 127.5, 126.3, 115.5, 109.97, 106.7, 15.3; IR (KBr): ν = 3112, 3084, 2953, 2920, 2871, 1610, 1550, 1512, 1446, 1391, 1210, 1068, 1046, 936, 893, 838, 783 cm^{-1}; ESI-MS *m/z* : [M+H] calcd for $C_{18}H_{15}N_5S$, 333.416, found 333.113. Anal.

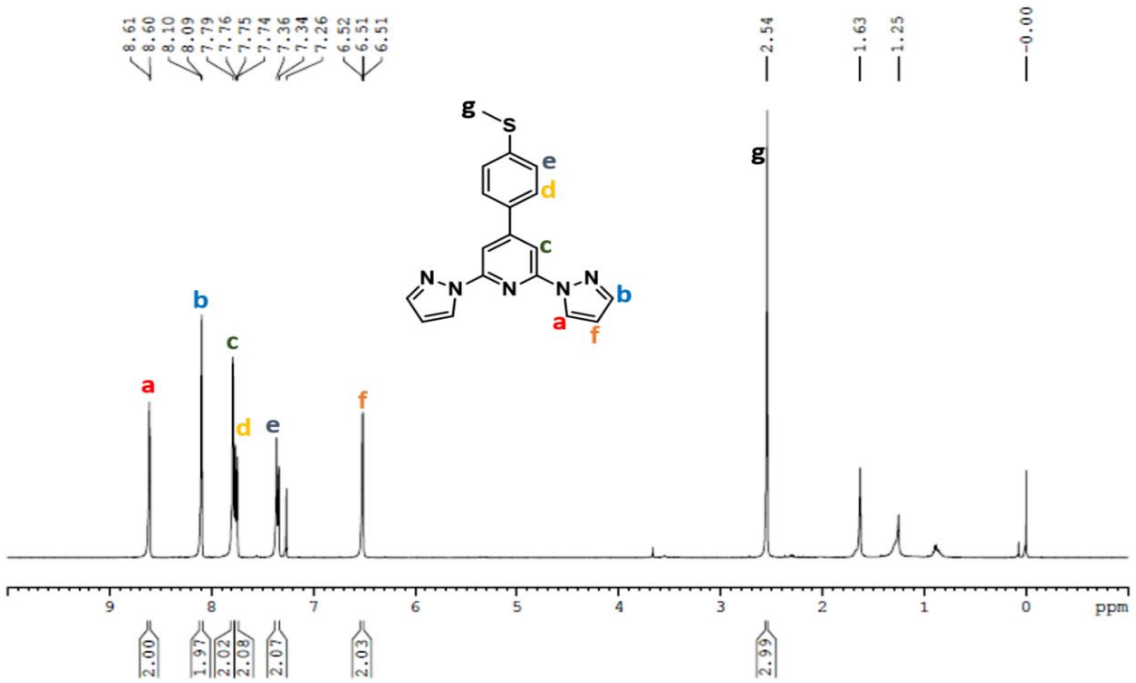

Figure 2: ^1H-NMR spectrum of **M-5**.

calcd for $C_{18}H_{15}N_5S$: C, 64.88; H, 4.53; N 21.01. found: C, 64.78; H, 4.46; N, 21.01.

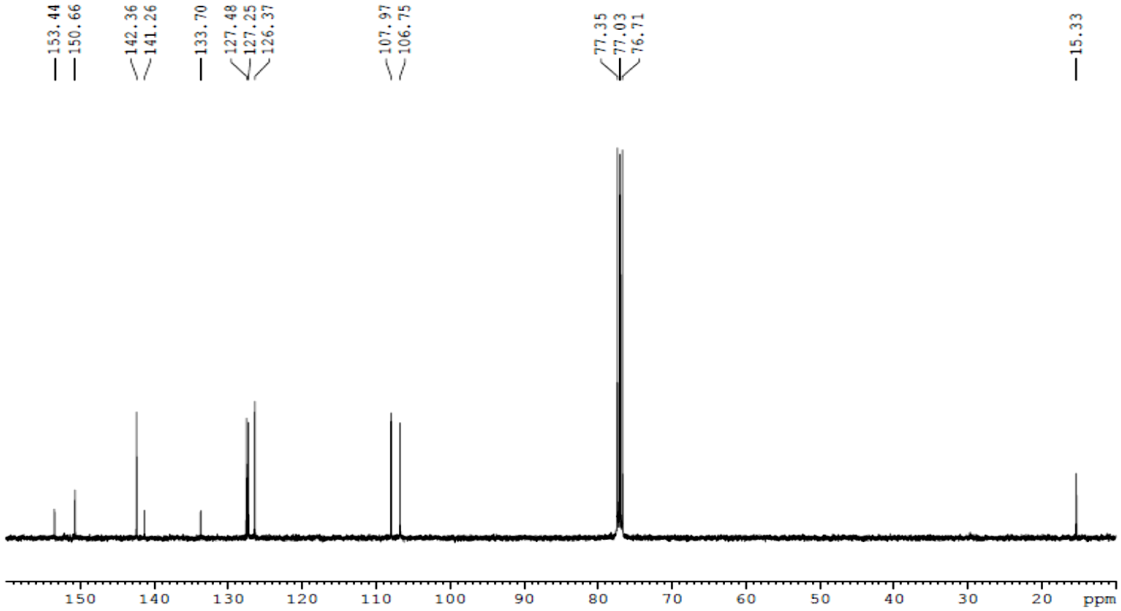

Figure 3: ^{13}C-NMR spectrum of **M-5**.

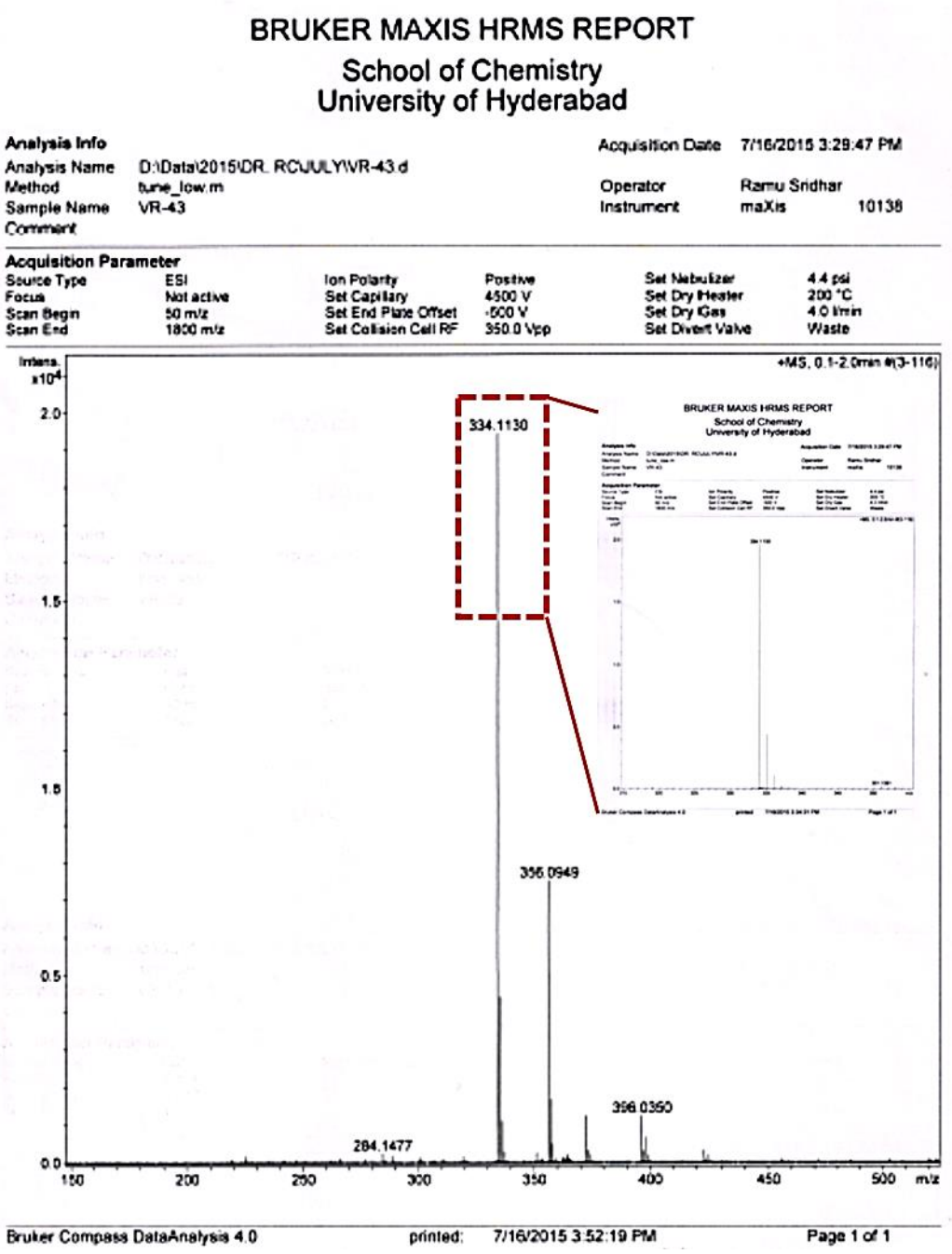

Figure 4: HR-MS of **M-5** compound.

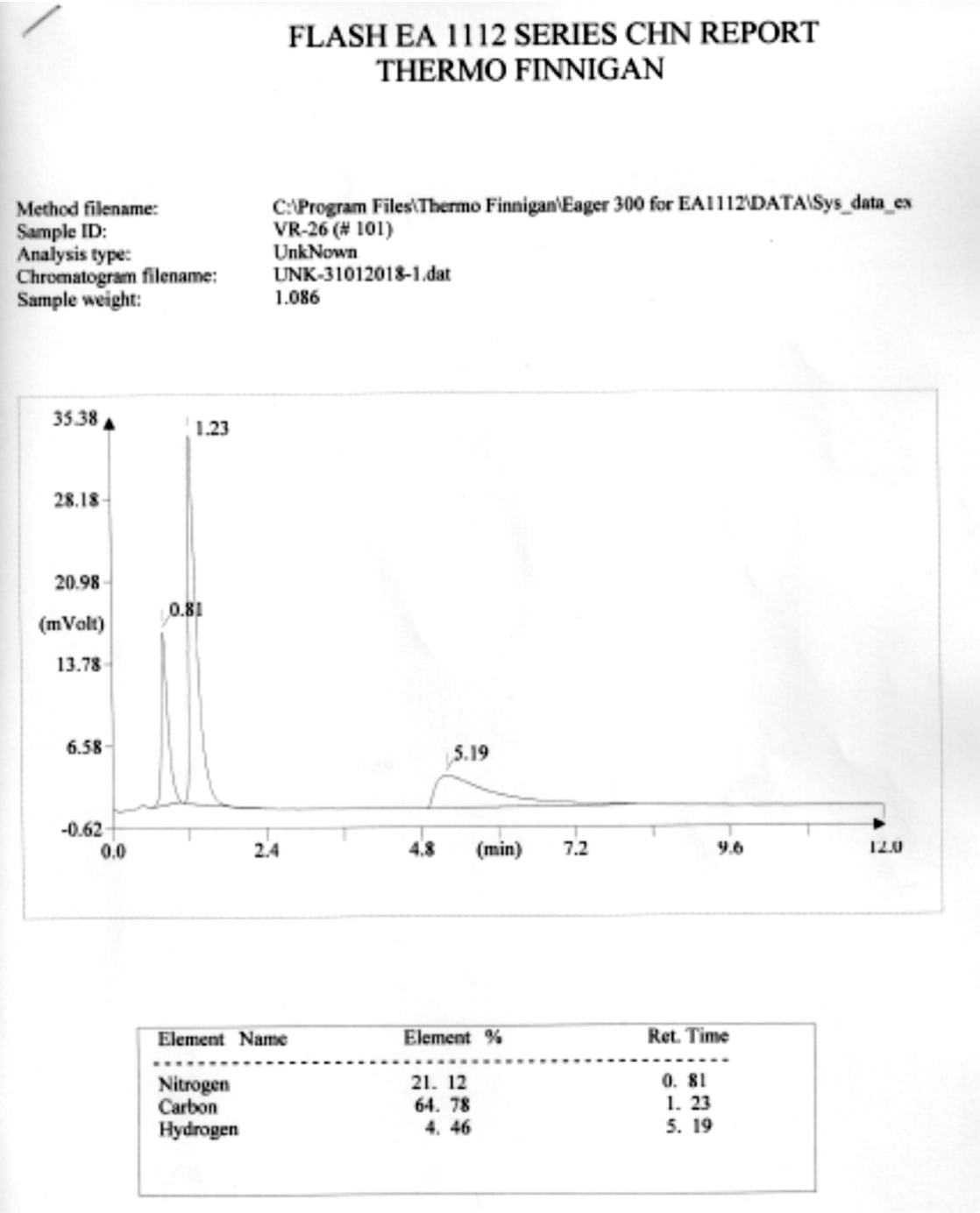

Figure 5: CHN elemental analysis of **M-5** compound.

5.3.2. Solid-State Molecular Packing and Interactions:

Colourless coffin-shaped single crystals (Figure 1a) of compound **M-5** were obtained from slow evaporation of a 3: 2 ratio mixed solution (8 mL of MeOH and 12 mL of $CHCl_3$). **M-5** compound (120 mg) was dissolved in 12 mL of chloroform and then

8 mL of methanol was added dropwise. The solution was kept under slow solvent evaporation condition for crystal growth. After 3 days colorless coffin-shaped crystals along with needle-shaped fibers were obtained.

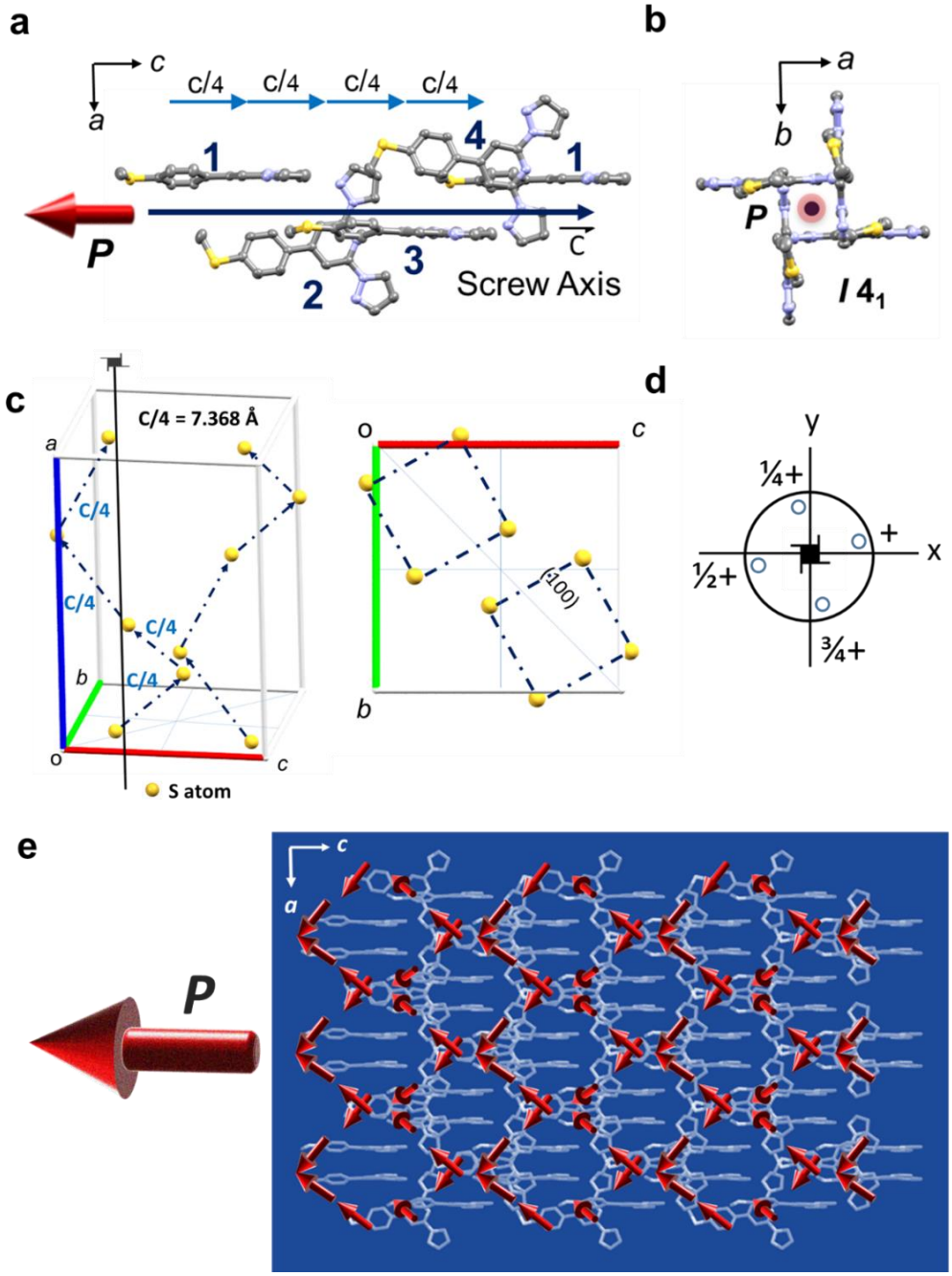

Figure 6: Polar crystal structure of M-5 with four-fold screw axis. a, b) View of four **M-5** molecules (labelled 1, 2, 3 and 4) with 90° rotation and 1/4 lattice translation in the crystallographic *c*-direction forming a four-fold screw axis. Screw axis views in the crystallographic *b* and *c* directions, respectively. c, d) Position of the S atoms along the screw axis e, f) Molecular arrangement of the ferroelectric **M-5** crystal viewed along the crystallographic *b* and *c* directions. The red arrows show the orientation of the molecular dipoles.

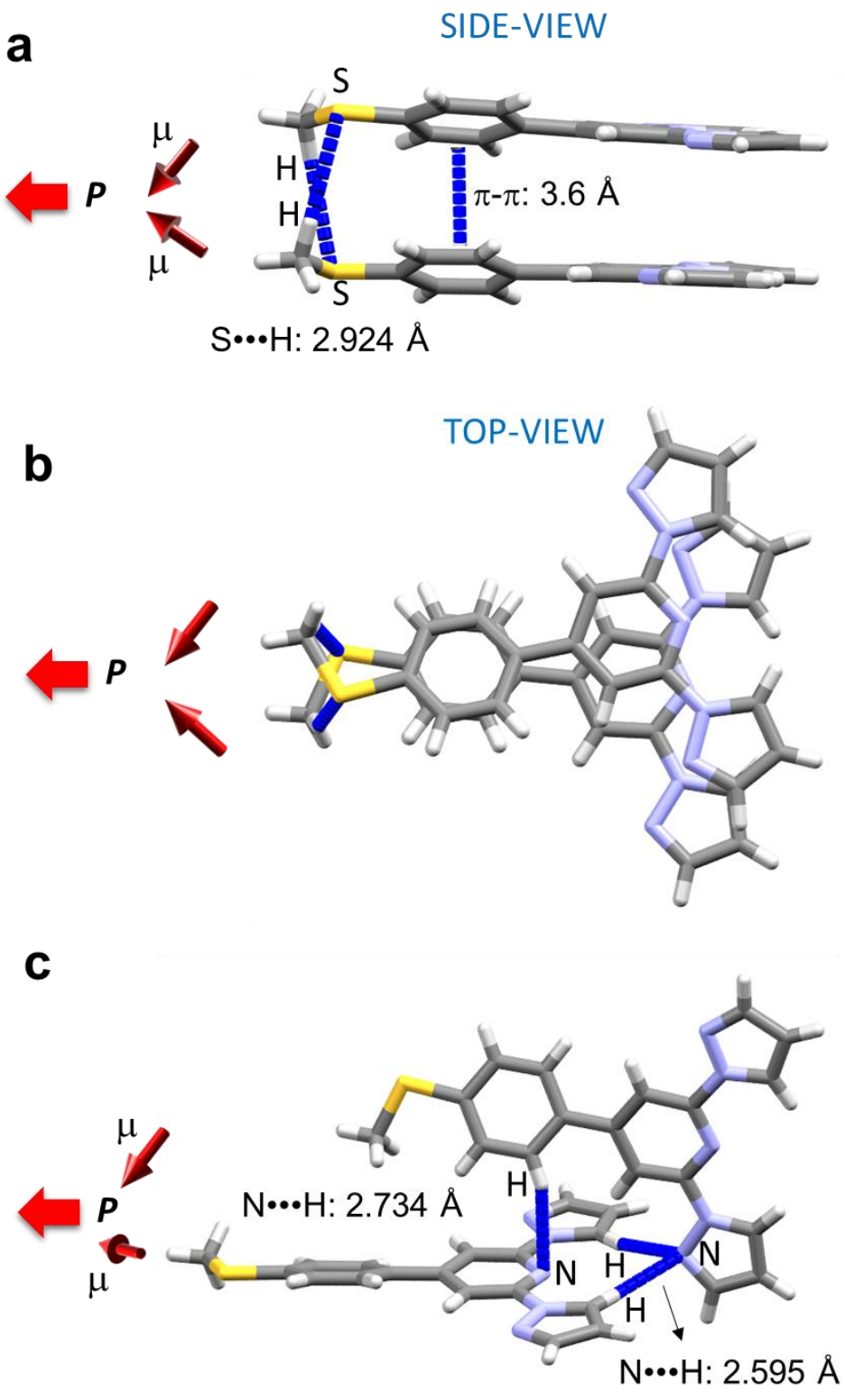

Figure 7: Intermolecular interactions in the solid state. a, b) Top and bottom views of **M-5** dimers stabilized by intermolecular C-H•••S hydrogen bonding and π-π stacking interactions. c) Two displaced molecular units along the screw axis interacting via C-H•••N interactions. The red arrows show the orientation of the molecular dipoles.

The crystal structure was examined at RT using single crystal X-ray diffraction technique. The BPP units are nearly planar to the phenyl ring with a dihedral or torsion angle (Φ) of *ca.* 19.96˚. Based on the crystal structure, the calculated (RB3LYP with basic sets 6-31G(D)) ground state dipole moment (μ) of **M-5** was 1.42 D, which is a relatively a modest value (Figure 1b). The solid-state molecular structure of **M-5** revealed a distinctive tetragonal $\boldsymbol{I4_1}$ space group with a polar point group *4*, which represents a body-centered lattice with four-fold screw axis (combination of rotation axes and lattice translation) (Figure 6a,b). In the crystal lattice, the four-fold screw axis is pointed towards the crystallographic *c*-axis with a molecule repeated distance of 29.472 Å (distance between two S atoms of first and fifth molecules). One molecule is deduced from the other by a rotation of 90° around the four-fold axis (along with the *ab*-plane) followed by a ¼ lattice translation along the crystallographic *c*-direction (Figure 6c, d). An interesting feature of the molecular packing is that all the **M-5** molecules point in one direction along the *c*-axis. As a result of this anisotropic molecular arrangement with the dipoles nearly pointing in one direction they resulting crystal qualifies as a rare polar type (Figure 6e).

To understand the reason for the polar arrangement of molecules, the weak supramolecular contacts between the molecules were investigated. At first, two intermolecular H-bonds between sulphur and methyl hydrogen atoms ($S\cdots H_{Me}$ = 2.924 Å) and π-π stacking (*d* = 3.36 Å) interactions between two phenyl rings form a non-centrosymmetric molecular dimer, resulting in a parallel arrangement of the molecular dipoles (Figure 6e and 7a,b). Secondly, the pyrazole nitrogens (N3 and N5) of each molecule participate in two intermolecular H-bond interactions with pyrazole ring protons ($N\cdots H_{Pz}$= 2.59 Å) of neighboring molecule, in a repetitive manner, with a 90° molecular rotation and ¼ translation along the *c*-direction (Figure 7c), forming a fourfold 4_1 screw axis. One of the signs that the crystal is possibly ferroelectric is the hidden non-centrosymmetric packing in the polar crystal structure. Generally, deviations from centrosymmetricity would guarantee easier polarization reversal, leading to a spontaneous polarization of the single crystal.

5.3.3. Differential Scanning Calorimetry and Variable Temperature Raman Spectroscopy Studies of M-5:

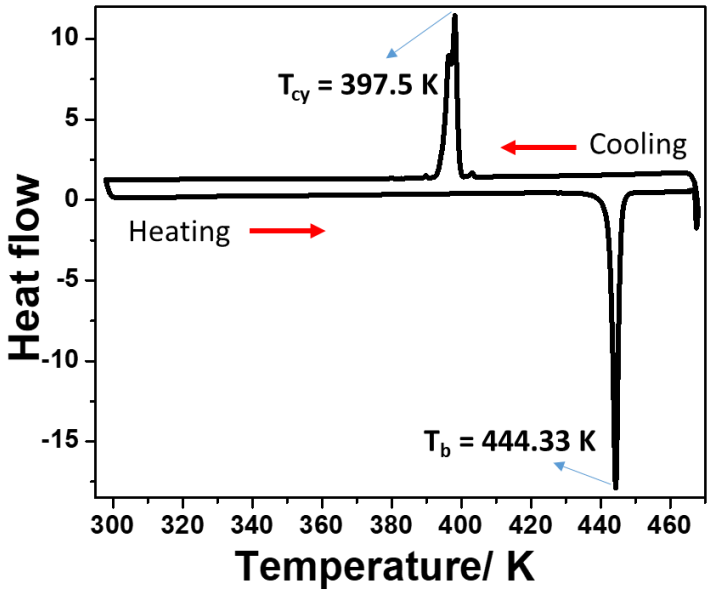

Figure 8: DSC thermogram of **M-5** crystal.

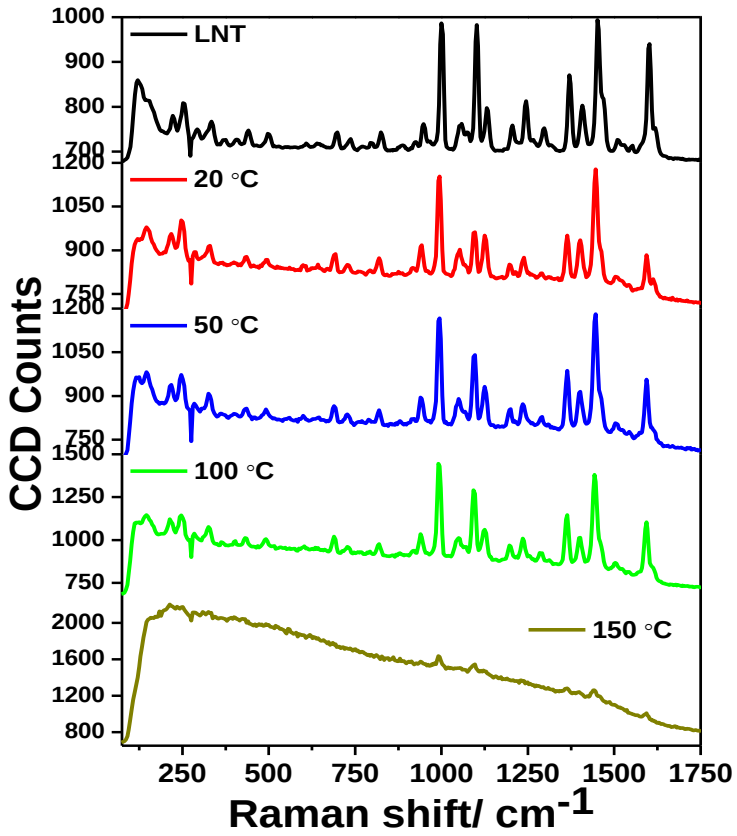

Figure 9: Variable-temperature Raman spectra of **M-5** crystal.

DSC unravels structural or phase changes of organic and inorganic crystalline compounds. Compound **M-5** showed no phase change and a single melting endotherm in DSC at a high T_{onset} of 171.33 °C (444.33 K) corresponding to the melting temperature of phase transformation solid to liquid. The exothermic peak at 124.5 °C (397.5 K) corresponds to the crystallization temperature of the phase transformation from liquid to solid. Moreover, no detectable phase transitions were found until the sample gradually starts to melt at T >447 K (Figure 8). To further probe any possible phase change variable temperature Raman spectroscopy was performed from liquid nitrogen temperature till 150 °C. The obtained Raman spectra show no significant change of the position of peaks (Figure 9). Overall these results suggest that the ferroelectric phase exists at RT and above RT.

5.3.4. Solid-State Dielectric and Electrical Properties of M-5 Crystal:

[performed in collaboration with Prof. S. Srinath, SoP, UoH]

The Curie-point is an indicator for the transition from paraelectricity to ferroelectricity; to confirm this, the temperature dependence of dielectric constant (ε') of **M-5** crystal was studied and presented in Figure 10. Interestingly, the $\varepsilon(T)$ plot shows a slight decrease of ε' without any abrupt characteristic discontinuity between 300 and 445 K at various frequencies (The m.p. of **M-5** crystal is 174 °C).[272]

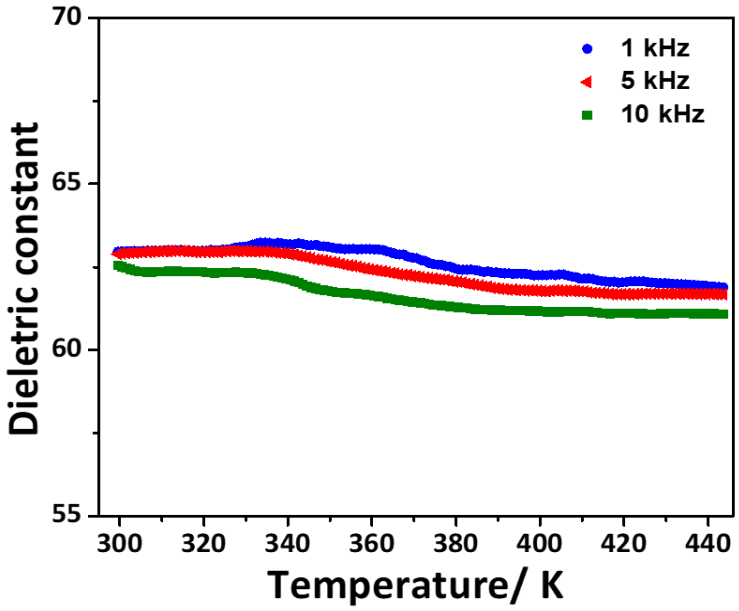

Figure 10: Temperature-dependent dielectric constant at various frequencies.

The above studies confirmed that there is no phase transition and only ferroelectric phase exists at RT. To probe the RT ferroelectric phase of **M-5** crystal, its ferroelectric properties were investigated by measuring hysteresis curves of electric polarization versus electric field $(P-E)$ at 300 K (Figure 11). As expected, from variable temperature dielectric studies, an evolution of a well-defined hysteresis loop was observed with an increase in remnant polarization, P_r and coercive field, E_c upon increasing the applied voltage at a frequency of 100 Hz. At 140 kVcm^{-1} the loop

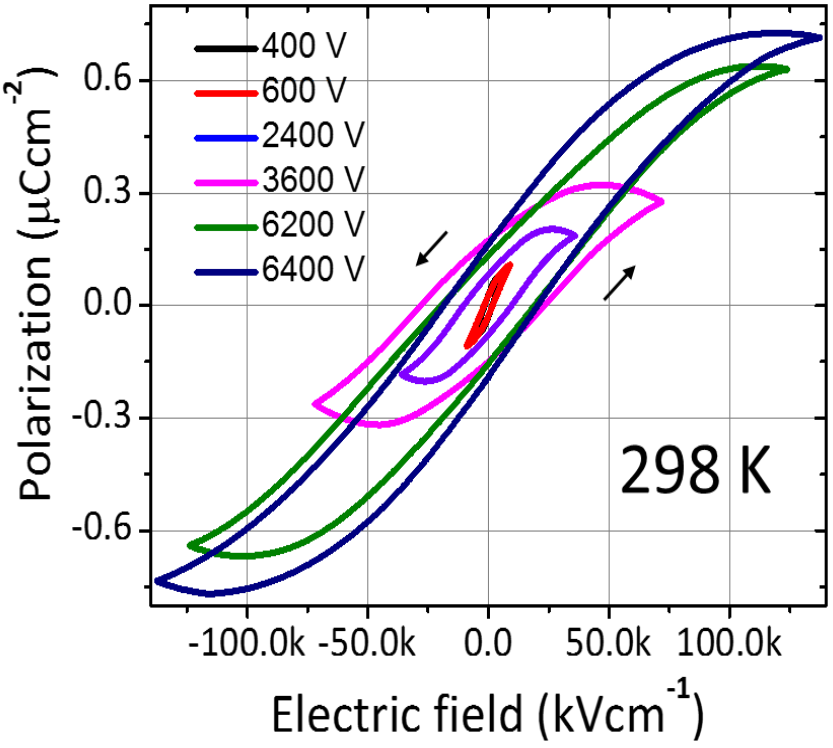

Figure 11: Ferroelectric behaviour. Electric polarization (*P*) versus electric field (*E*) hysteresis loops of **M-5** measured at 298 K at various applied voltage with AC electric field frequency of 100 Hz.

reaches its saturation with the saturation polarization, P_s = 0.715 μCcm^{-2}, P_r = 0.166 μCcm^{-2}, and the E_c of 18 kV cm^{-1}. Our attempts to detect P_s at higher electric fields were futile as a result of dielectric breakdown and crystal fracture. For all the field strengths, from low to high fields the *P-E* loops closes completely indicates a sizable contribution from the reversible polarization. Further, the origin of ferroelectric reverse polarization in **M-5** crystal is not established yet. Nevertheless, it is possible that (i) protonation of the hydrogen-bonded pyrazolyl and pyridine nitrogens (see

Figure 7c) and (ii) charge transfer mechanism have discretely or cooperatively contributed in the polarization reversal.

5.3.5. Solid-State Linear Properties of M-5:

Compound **M-5** is a typical intramolecular charge-transfer (ICT) compound. The solution and solid-state UV-Vis absorbance and fluorescence studies were performed, to understand the molecular level electronic transitions and aggregation behaviour of compound **M-5** (Figure 12a). In chloroform solution (c ~ 2× 10^{-5} M), the electronic spectrum of compound **M-5** exhibited two absorbance bands, a less intense

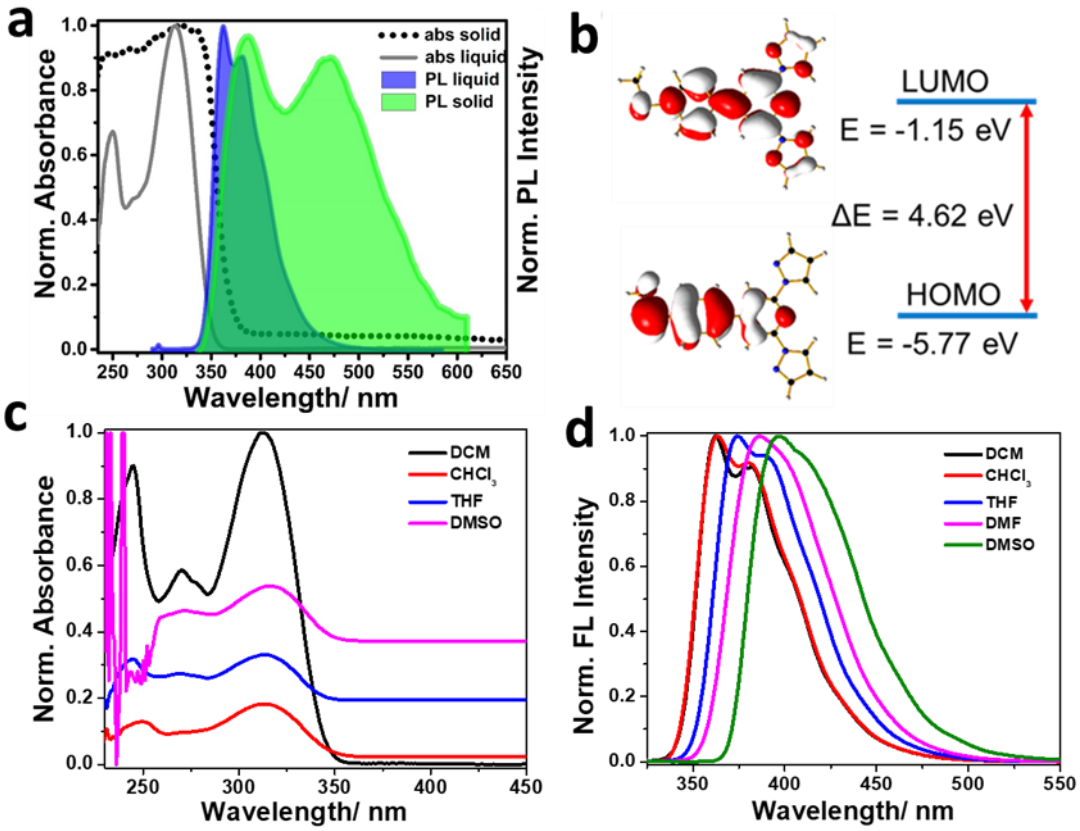

Figure 12: a) UV-Vis absorbance and FL spectra of **M-5**. b) HUMO and LUMO energy levels calculated by DFT (RB3LYP with basic sets 6-31G(D)). c) UV-Vis absorbance of **M-5** in various solvents. (d) Solvato-chromic FL shift of **M-5**.

band at 250 nm and intense band at 314 nm. In the solid state, the second band slightly shifted to a higher wavelength to 324 nm due to aggregation. The longer wavelength absorbance bands in the solid and solution state are due to ICT, which is apparent from the change of electron cloud distribution between the HOMO and the LUMO of

the compound **M-5** (Figure 12b). The estimated band gap and ground state dipole moment of **M-5** FL from density functional theory are 4.26 eV and 1.42 Debye, respectively. The spectra of compound **M-5** exhibited an emission band centered at 362 and 379 nm (Figure 12a), with prominent solvatochromic redshifts due to ICT favoured by polar solvents (Figure 12d). The solid state spectrum of **M-5** exhibited well separated broad bands at 385 nm and 469 nm (Fig. 4a), the later band could be as a consequence of charge transfer in the solid state.

5.3.6. Solid-State NLO Properties of M-5: [performed in collaboration with Dr. S. R. G. Narahari Setty, School of Physics, UoH]

In addition to ferroelectricity, due to broken inversion symmetry, $\chi^{(2)} \neq 0$ for polar crystals hence they are known for the production of SHG. Therefore, to

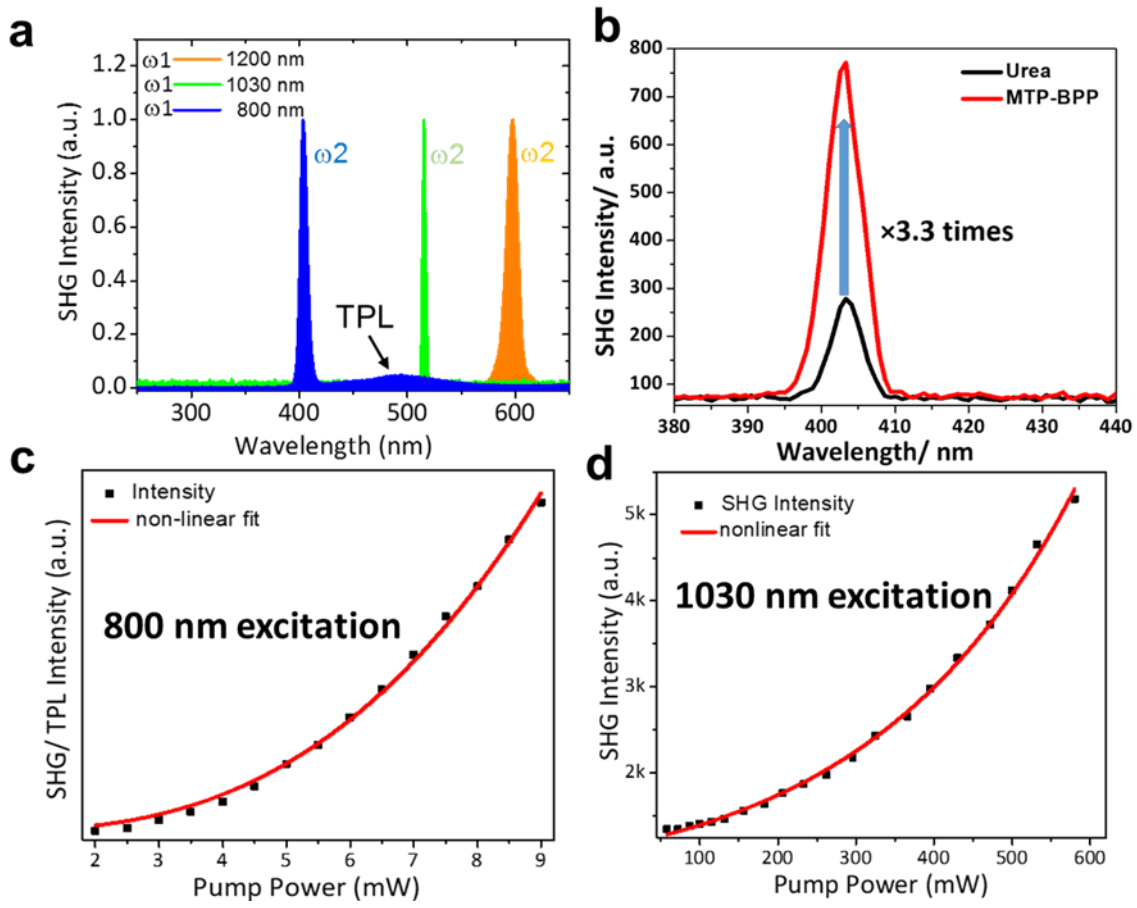

Figure 13: Second Order NLO Properties. a) SHG response of **M-5** for three representative fundamental harmonics. b) Calculation of second order non-linear coefficient (β) of **M-5** with reference to urea. The magnitude of SHG signal is 3.3 times greater than urea. c, d) Increases of the SHG NLO signal quadratically with 800 nm, 1030 nm pump powers, respectively. The red line shows the non-linear fit.

investigate the NLO properties, when the **M-5** single crystal (of thickness 1.4 mm) was excited with Ti: Sapphire pulse laser (pulse width 100 fs, repetition rate 1 kHz, linear polarization) at 800 nm, 1030 nm, and 1200 nm fundamental wavelengths, with a focal volume having a spot size of 101.8 μm, the crystal produced efficient SHG signals at 400 nm, 515 nm, and 600 nm, respectively (Figure 13a). The input pump power-

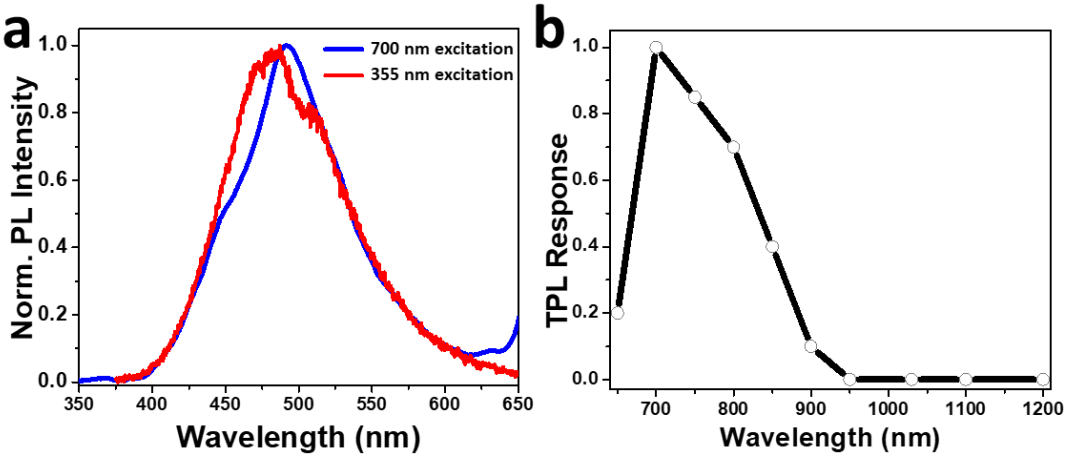

Figure 14: a) OPL and TPL spectra of a single crystal of **M-5**. b) TPL intensity as a function of fundamental excitation wavelengths.

dependent studies clearly demonstrated a quadratic increase of the SHG intensity with power endorsing the second-order non-linear origin of the signal without any (Figure 13c, d).

The magnitude of the SHG signal is also found to be about 3.3 times greater than that of the urea standard. From the signal intensities, the nonlinear absorption coefficient (β) of **M-5** was estimated [$\beta_{urea} = 3.39 \times 10^{-9}$ e.s.u., then $\beta_{\boldsymbol{M-5}} = (\beta_{urea}) \times 3.3 = 11.187 \times 10^{-9}$ e.s.u] (Figure 13b). It should be mentioned that, in addition to a weak SHG, the crystal also produced an intense TPL when it was pumped with a 700 nm fundamental light (Figure 14a). Excitation of the crystal with various input wavelengths indirectly revealed the TPA range from about 850 to 600 nm with a maximum at 700 nm (Figure 14b). As a result, the intensity of SHG steadily decreased with decreasing pump wavelengths, within the TPA domain. Further, the crystals possess good thermal and photochemical stabilities in the crystalline state.

Finally, the third-order NLO susceptibility of **M-5** in chloroform solvent was measured by using a single beam Z-scan technique (see Chapter-7 Z-scan

measurement experimental set-up). This technique allows simultaneous measurement of nonlinear refraction (NLR) and nonlinear absorption (NLA). The experiment was performed using with Ti: sapphire 800 nm fs pulse laser (a pulse width of 100 fs, a repetition rate of 1 kHz by keeping the sample at a focal volume having a spot size of 101.8 μm). The nonlinear absorption coefficient β of **M-5,**

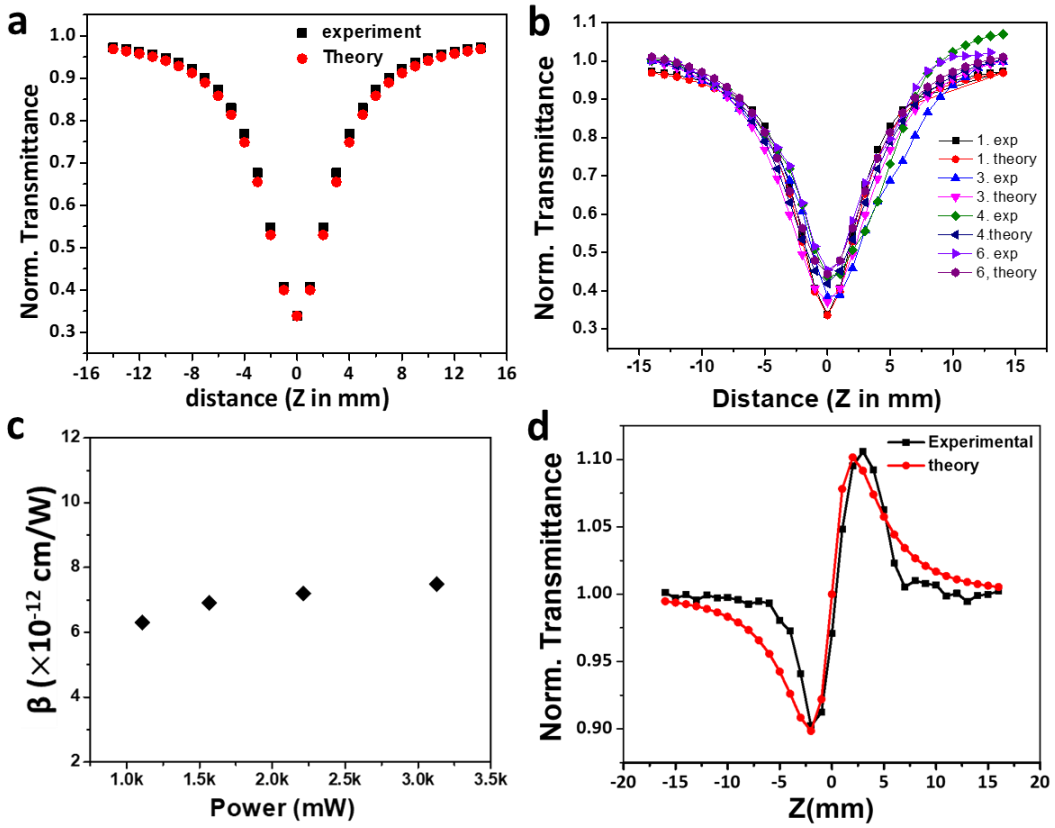

Figure 15: Third-order NLO properties of M-5. a) Open aperture Z-scan curve at 1.2 mW. b) Z-scan measurement at different input powers 1.2 mW, 1.7 mW, 2.3 mW and 3.4 mW. c) A plot of nonlinear absorption coefficient (β) of **M-5** at various input intensity. d) Normalized pure nonlinear refraction. Red solid line depicts theoretical fit.

obtained from the open aperture Z-scan curve is given in Figure 15a and the β value measured at different input laser powers is shown in Figure 15b, c. The obtained results show that β is nearly independent of the input intensity I_o due to the involvement of pure TPA process. The measured value of β is 6.3×10^{-12} cm/W and the molecular TPA cross-sections $\sigma(\lambda)$ = 585 GM. The pure nonlinear refraction curve is shown in Figure 15d. It was obtained by dividing the closed aperture data by open aperture data. The resultant characteristic peak-valley indicates the negative

nonlinear refraction or self-defocusing effect. The values of nonlinear refractive index n_2 obtained is n_2= 0.214x10^{-16} cm^2/W, it is of the order of 10^{-11} esu.

5.3.7. Terahertz Spectroscopy Studies of M-5: [performed in collaboration with Prof. A. K. Chaudhary, ACRHEM, UoH]

Finally, the second-order nonlinearity of **M-5** crystal was used to test its THz wave generation ability using optical rectification process (see Chapter-7 for Terahertz measurement experimental set-up 2). When an incident fs laser (wavelength 800 nm, pulse duration 140 fs, repetition rate 80 MHz) power of 700 mW was pumped on to the **M-5** crystal, remarkably, the crystal generated THz radiation. The temporal profile and corresponding frequency spectra of the THz radiation are shown in Figure 16 a, b, respectively. The frequency spectra of generated THz radiation covered up to 2.2 THz range with a good signal to noise ratio (200:1).

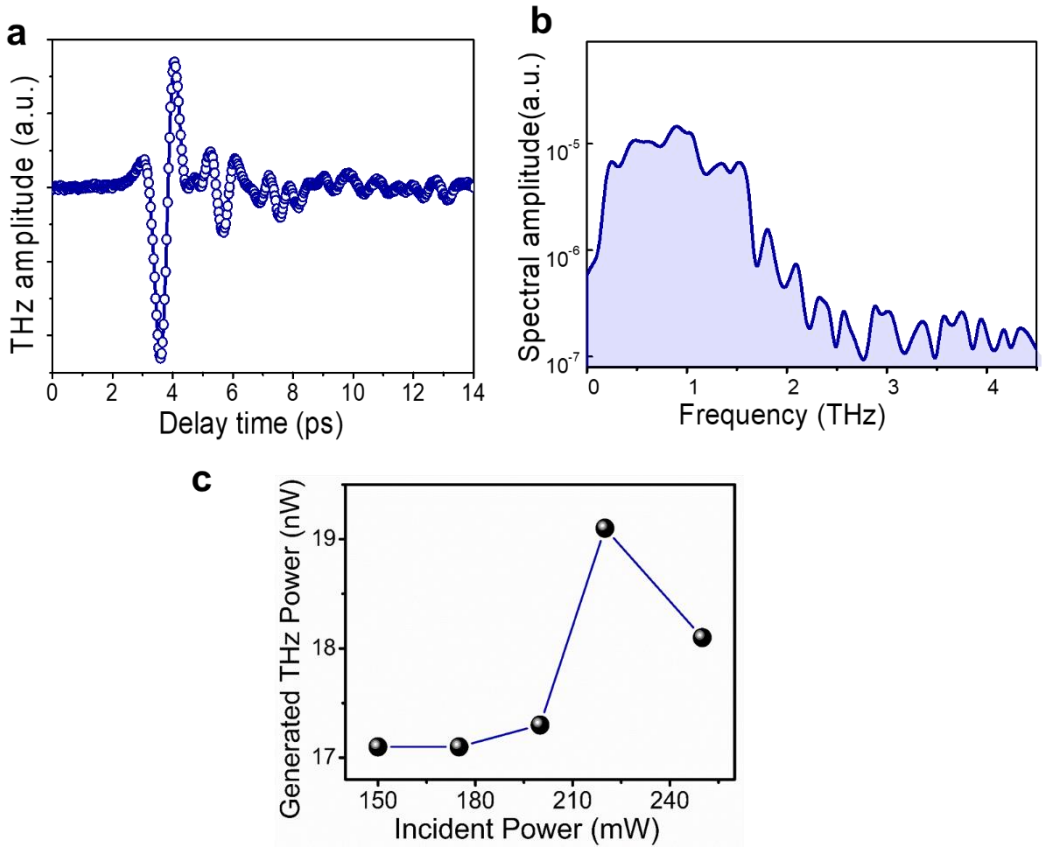

Figure 16: Optical rectification process. a,b) THz generation temporal profile and the corresponding frequency spectrum of **M-5** crystal, respectively. c) Pump energy dependent THz generation power of crystal.

To attain a maximum THz generation efficiency, the crystal was rotated vertically to identify the best phase matching position. Due to better phase-matching and a higher figure of merit, the crystal demonstrated a conversion efficiency (η = Output THz power/Input laser power) of the generated THz radiation of the order of 0.87×10^{-5}% (Figure 16c).

Further, the THz absorption and transmission data of the crystal (thickness = 18 mm) were recorded by using THz spectrometer between 0.1-2.0 THz range[277] (see Chapter-7 Terahertz measurement experimental set-up 1). The temporal (time) and frequency domain THz transmission of **M-5** crystal and Zn-Te with reference to THz

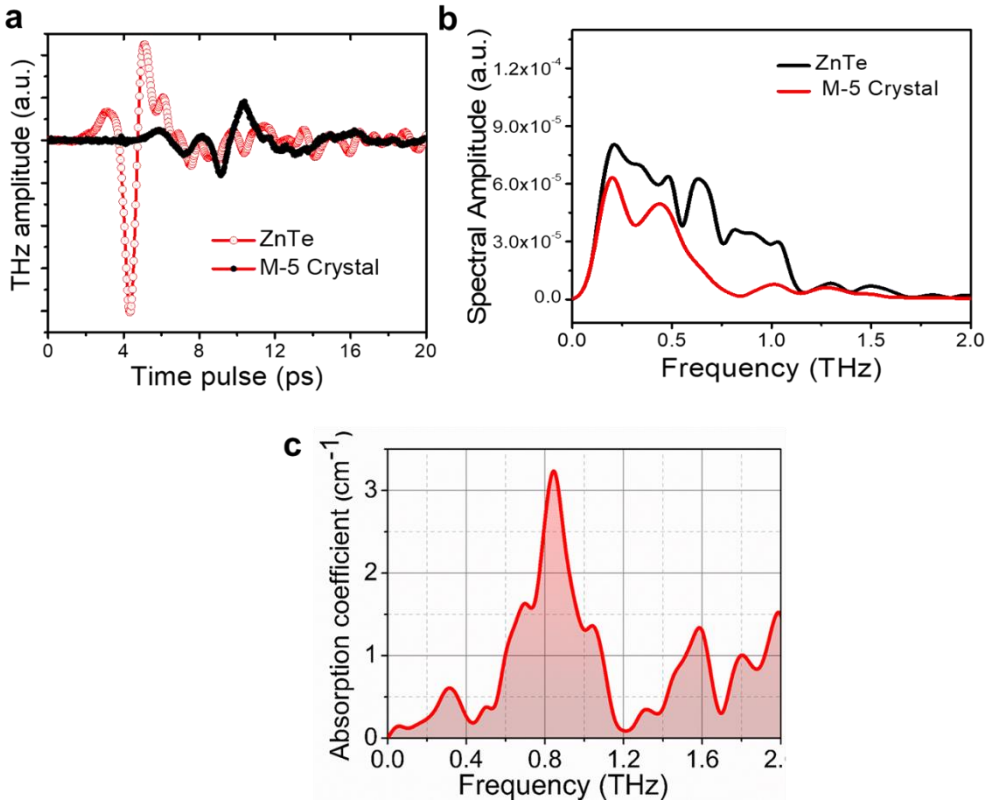

Figure 17: THz transmission studies of M-5. a) THz temporal profiles of **M-5** and ZnTe and b) their corresponding spectral amplitude of profiles, respectively. c) THz absorption profile of **M-5** crystal.

signal generated by low-temperature-grown GaAs (LT-GaAs) photoconductive antenna in the air are shown in Figure 17 a, b. From the transmission data, it is explicit that crystal is transparent over the range 0.1-2.2 THz. The absorption spectrum revealed low THz absorption with absorption coefficient, α <1.5 cm^{-1} in a large wavelength range but between 0.7 to 1 THz range (Figure 17c).

5.4. Conclusions:

In summary, a rare example of a single-component polar organic crystal based on a new **M-5** molecule was synthesized and this molecule possessing a weak dipole moment. The stabilization of dipole-parallel alignment in a three-dimensional crystal lattice indicates that the energy of the supramolecular H bonding and π-π stacking interactions overwhelmed the natural tendency of the molecular dipoles aligning in an antiparallel manner. Another exciting structural feature of the crystal is the formation of a four-fold screw axis by the molecular dipoles. The polar order of the **M-5** molecules in the crystal lattice is revealed in their above room temperature ferroelectric behavior. The emergence of SHG signal from **M-5** and its angle dependency further reinforced the anisotropic nature of the ferroelectric single-component crystal. The generation of THz with good conversion efficiency is an additional strength displayed by this rare-polar crystal. Further, the crystals possess good thermal and photochemical stabilities in the crystalline state. The presented single component organic crystal holds promise for a myriad of emerging photonic applications involving electro-optical effect.

6

Conclusions

This thesis entitled "*Photonic Properties of Organic Micro-Resonators and Ferroelectric Polar Crystal: Two-Photon Luminescence, Second Harmonic Generation, and Terahertz Wave Production*" presented nano-photonic properties of resonators self-assembled from small organic nonlinear optical (NLO) molecules and ferroelectric-NLO studies of polar organic crystal.

Chapter-1 introduced (nano) photonic properties of organic molecules and their superiority over inorganic and metallic structures in terms of EP binding energy. It also presented various nano-and micro-fabrication methods, types of optical waveguides and resonators. Their basic principles and useful parameters were discussed together with some literature examples. Later, introduction to polar organic crystals and ferroelectricity were given. Further, this Chapter presented same basic introduction to NLO properties such as two-photon luminescence (TPL), second harmonic generation (SHG), and terahertz (THz) wave production via optical rectification process.

The shape, size, and composition of the self-assembled solid structures are the three most important elements of the resonator properties. Therefore bottom-up approach was adopted throughout the thesis to achieve self-assembled organic micro-structures. **Chapter-2** presented, the self-assembly of active type WGM submicro-tubular resonators from 4,4'-bis(2,6-di(1H-pyrazol-1-yl)pyridin-4-yl)-1,1'-biphenyl (**M-1**) via a bottom-up self-assembly technique. Single-particle to single-particle transformation of an active type resonator into a passive type hetero-structure resonator using laser burning technique was discussed for the first time. A detailed investigation of the hetero-structure resonator using various microscopy techniques, comparative performance study of these active and passive type resonators using single-particle micro-FL (fluorescence) and polarization-resolved spectroscopy studies using continuous wave (CW) UV and visible lasers were also presented. Additionally,

the NLO properties like two-photon absorption (TPA) and TPL of **M-1** in the thin film and self-assembled submicro-tubes were also discussed.

Coumarin-153 (C-153) is a famous laser dye, extensively used in biology, bio-labeling, bio-imaging, spectroscopy, microscopy and recently in photonics studies. To tune the emission colour of FL molecule creation of energetically different solid-state aggregates (so-called polymorphs) is an interesting strategy. C-153 forms two kinds of polymorphic crystal structure (**M-2** and **M-3**) but its polymorphism dependent emission behavior has not been explored to date. Hence, in chapter-3, the polymorphic crystal structures (**M-2** and **M-3**) of C-153 and their opto-molecular properties were demonstrated. Further C-153 possesses strong dipole moment in the ground state and hence exploiting the binary solvent (Acetonitrile: water) mixture and solvation dynamics, several polymorphic microstructures such as rods, tubes, and Japanese twin tubes were achieved by using a simple self-assembly method. The single particle Raman spectra of these microstructures were quite different due to their dissimilar solid-state packing. Therefore, these polymorphic structures exhibit diverse emission colours ranging from blue, green and yellow. Single particle microscopic fluorescence studies disclosed that these microstructures depending upon their shape act as optical cavity and emit whispering gallery or FP modes. The study of NLO properties of **M-2** and **M-3** crystals and self-assembled micro-structures of C-153 revealed that the resulted TPL spectra of micro-rods and microtubes of C-153 were matching with TPL spectra of **M-2** crystals and **M-3** crystal.

Lead Perovskites are emerging as an important material for various applications such as solar cells and lighting devices. But its applicability in lighting and other applications suffers due to its instability at ambient conditions. Hence **Chapter-4** presents the preparation of 2D layered Perovskite micro-crystals (**M-4)** by anti-solvent diffusion method and it's composite with polystyrene. Optimization of the Formation of defect-free composite micro-sphere via self-assembly method also discussed. Single-particle microscopy investigation these composite micro-spheres gave high-quality resonators with the *Q*-factor up to ~1.2 x 10^3. Additionally, the intrinsic TPL property of these composite micro-resonators was also demonstrated. TPL mapping with respect to different fundamental wavelength clearly specified the

TPA region and power-dependent emission as well. The NLO property of this 2D perovskite paves way for the development of new functional opto-electronic devices for direct practical applications.

Polar-assembly of molecules via crystallization is an exceedingly difficult task and rarely achieved. Crystals with the above molecular order are referred to as *single-component polar organic crystals*. Supposedly, these polar organic crystals are known to produce ferroelectricity and second-order nonlinear optical properties such as SHG and THz production. On the other hand, accomplishing all these three properties experimentally is quite hard owing to several conditions (phase matching, optical transparency, crystal size, laser stability, etc.) which have to be fulfilled. Therefore, **Chapter-5** presents, an unusual example of a single-component polar organic crystal based on a new **M-5** molecule possessing a weak dipole moment. The stabilization of dipole-parallel alignment in a three-dimensional crystal lattice indicated that the energy of the supramolecular H bonding and π-π stacking interactions overcome the natural propensity of the molecular dipoles line up in an antiparallel manner. Another fascinating structural feature of the crystal is the formation of a four-fold screw axis by the molecular dipoles. The polar order of the **M-5** molecules in the crystal lattice is revealed in their above room temperature ferroelectric behavior. The emergence of SHG signal from **M-5** and its angle dependency further established the anisotropic nature of the ferroelectric single-component crystal. The production of THz with good conversion efficiency is an extra strength displayed by this rare-polar crystal. Further, the crystals possess good thermal and photochemical stabilities in the crystalline state. The presented single-component organic crystal holds promise for a myriad of emerging photonic applications involving electro-optical effect.

7

Instrumentation

Nuclear Magnetic Resonance Spectroscopy

^{1}H and ^{13}C NMR spectra were recorded on Bruker 400 & 500 MHz NMR spectrometers. Spectra were recorded using the solvent peaks as the internal standard.

Mass Spectrometry

Shimadzu LC-MS 2010A equipment was used to record the mass spectra of the isolated compounds following atmospheric pressure chemical ionization (APCI) technique. The mass spectra of high molecular weight compounds were recorded on an Electrospray ionization time-of-flight (ESI-TOF) instrument, HRMS, (Bruker Daltonik GMbH, Microtof Control, Compass 1.3 Microtof S.R3, version 3.0 SR2 Build 66).

Elemental Analysis

Elemental analysis was carried out on a Thermo Finnigan Flash EA-1112 series CHNS analyzer.

Infrared Spectroscopy

FT-IR spectra were recorded on a JASCO FT/IR-5300 or Nicolet 5700 FT-IR. Solid samples were recorded as KBr pellets and liquid samples as thin films between NaCl plates.

Differential Scanning Calorimetry

DSC was performed on a Mettler Toledo DSC 822e module. Samples were placed in crimped but vented aluminum sample pans. The typical sample size is 3-5 mg; temperature range was 25–180 °C @ 10 °C/min. Samples were purged by a stream of nitrogen flowing at 60 mL/min.

Optical Absorption Spectroscopy

Absorption spectra were recorded on a Shimadzu UV-3600 UV-Vis-NIR Spectrophotometer or Cary 100 Bio UV-Visible spectrophotometer.

Solid State Optical Absorption Studies

The solid-state absorbance spectrum was recorded on a Shimadzu UV-3600 using diffuse reflectance UV-visible (DR-UV-vis) mode. The reflectance spectrum was converted to an absorbance spectrum using Kubelka-Munk function.

Fluorescence Spectroscopy

Steady-state fluorescence emission and excitation spectra were recorded on a Jobin Yvon Horiba model Fluoromax-3 spectrofluorimeter.

Transmission Electron Microscopy

TEM images were obtained on a TECNAI G2 FEI F12 TEM at an accelerating voltage of 120 kV. Samples were prepared by placing a drop of the samples on a polymer (polyvinyl formvar) – coated copper grid (200 mesh) and air drying.

Field Emission Scanning Electron Microscopy

FESEM images were recorded on a Philips XL30 ESEM and a HITACHI S-4300SE/N FESEM respectively using beam voltages of 20 kV. The samples were fixed on aluminum platforms using carbon tapes; a conducting connection was made between samples and aluminum platform by silver paint. Samples were coated with a thin layer (3 – 5 nm) of sputtered gold prior to imaging.

Atomic Force Microscopy

Atomic Force Microscopy imaging was carried out on NT-MDT Model Solver Pro M microscope using a class 2R laser of 650 nm wavelength having a maximum output of 1 mW. All calculations and image processing was carried out by a software NOVA 1.0.26.1443 provided by the manufacturer. The images were recorded in a semi-contact mode using a non-contact mode tip purchased from NT-MDT, Moscow. The dimensions of the tip are as follows: Cantilever length = 95 (±5) μm, Cantilever width 30 (±5) μm,

and Cantilever thickness = 1.5-2.5 μm, Resonate frequency = 140-390 kHz, Force constant = 3.1-37.6 N/m, Chip size = 3.4×1.6×0.3 mm, Reflective side = Au, Tip height = 14-16 μm, Tip curvature radius = 10 nm, and Aspect ratio 3:1-5:1.

Confocal Raman Micro Spectroscopy Studies and nano-manipulation studies

Single particle micro-spectroscopy experiment was carried out on a backscattering mode set-up of the Wi-Tec alpha 300 AR laser confocal optical microscope (T-LCOM) facilities equipped with a Peltier-cooled CCD detector. Using 300 grooves/mm grating BLZ = 750 nm, the accumulation time was typically 10 s and integration time was typically 1.0 s. Ten accumulations were performed for acquiring a single spectrum. An argon ion 488 nm and 633 nm (He-Ne) laser were used as an excitation source for Raman scattering. For FL experiments 355 nm, 405 nm, and 488 nm (Ar+) lasers were used. A 150x (0.95 NA) objective was used to excite a single micro-structure. Laser power was estimated using THOR Labs power meter.

Nano-manipulation was performed using a confocal microscope equipped with an atomic force microscope.

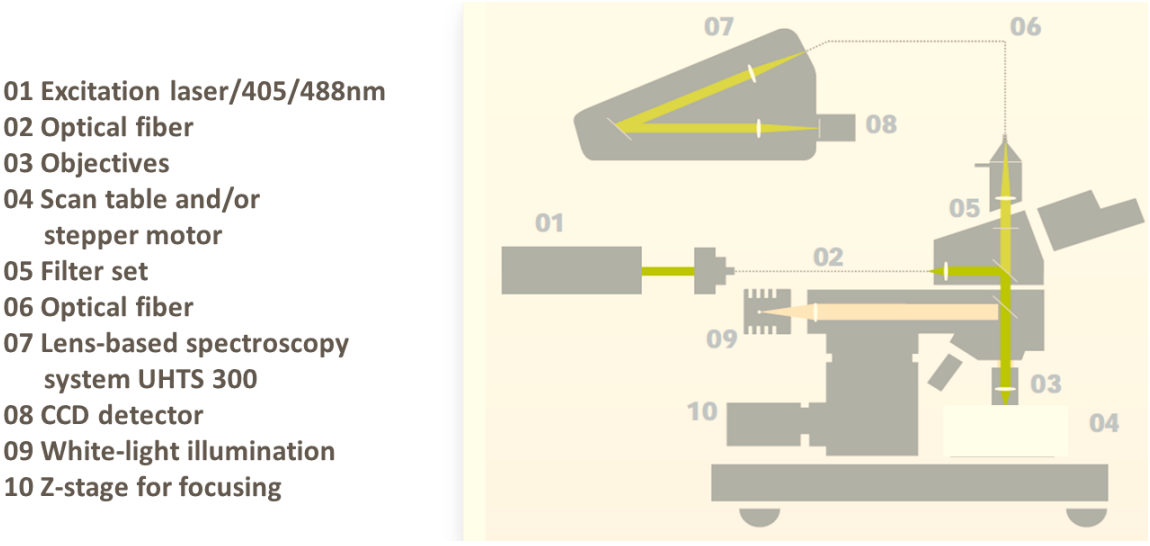

Figure 7.1: Confocal microscopy set-up

Single Crystal X-ray Diffraction: Data Collection, Solution and Refinement

The X-ray intensity data of crystals were collected on a Bruker Nonius SMART APEX CCD area detector system equipped with a graphite monochromator and a MoKα fine-focus sealed tube (λ = 0.71073 Å) (40 kV, 35 mA). The detector was placed at a distance of 6.003 cm from the crystal. The frames were integrated by Bruker SAINT and the

structure was solved and refined using the direct method analysis in Bruker SHELXTL Software Package.

Ferroelectric and Dielectric Measurements

Temperature-dependent dielectric constant and ferroelectric hysteresis measurements were performed on a single crystal of **M-5**. Then the crystal was painted by silver paste on the opposite sides to have a metal-insulator-metal configuration. The crystal was treated thermally at 60˚C for 30 minutes to increase the adhesion between the sample and the electrodes. All measurements were performed at room temperature.

The dielectric measurement was carried out using LCR meter (Agilent E4980A) for the frequency range between 20 Hz to 2 MHz. And the ferroelectric measurement was done using Precision Premier II (Radiant Technologies).

Experimental Setup for SHG and TPL

For SHG/ TPL measurement a home build experimental set up was developed by using a commercial Ti: Sapphire laser having central wavelength 800 nm, pulse width 100 fs, Repetition rate 1 KHz. The laser output is directed by a half-wave plate and polarizer combination to control the laser power, a lens having a focal length of 50 cm is used to focus the laser beam on the sample. The reflected beam is filtered by a notch filter to

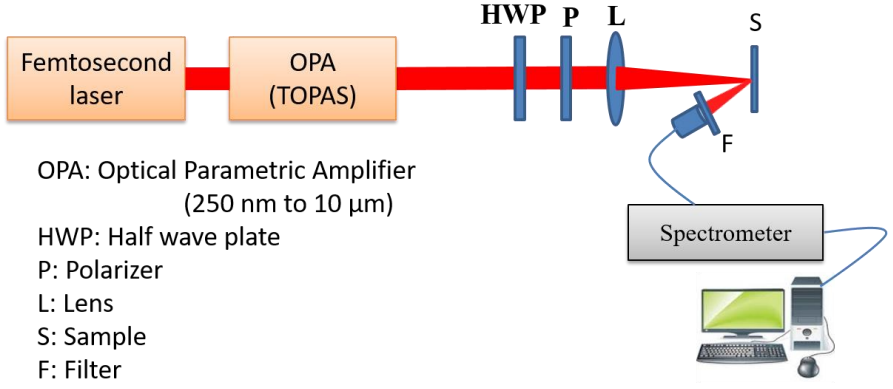

Figure 7.2: NLO experimental setup

cut down the fundamental excitation wavelength, the filtered beam is collected by a fiber-coupled spectrometer, and the spectrometer output is displayed by a computer. The experiment is performed by keeping the sample at focal volume having a spot size of 102 µm and is exposed to linearly polarized light with different input powers.

Powder SHG measurement for calculation of the second-order nonlinear optical coefficient

The powder SHG measured by the Kurtz–Perry method. The samples were placed in a quartz cell and measured SHG signals at 800 nm Ti: Sapphire pulse laser (pulse width 100 fs, repetition rate 1 kHz, linear polarization). We measured the intensity of the frequency-doubled output emitted from the sample using a photomultiplier tube. The second harmonic efficiency of the sample was compared to that of a standard powder sample of Urea.

Variable Temperature Raman Spectroscopy Studies

Raman spectra of the samples were recorded on a WI-Tec confocal Raman spectrometer equipped with a Peltier-cooled CCD detector. Using a 600 grooves/mm grating BLZ = 500 nm, the accumulation time was typically 10 s and integration time was typically 2.0000 s. Ten accumulations were performed for acquiring a single spectrum. An Ar^{+} ion 785 nm laser was used as an excitation source for the Raman scattering.

Nonlinear Optical Absorption Coefficient (β) Measurements (Z-scan)

The β values are determined by carrying out open aperture Z-scan measurements. Briefly, in a typical Z-scan experimental technique, a single laser beam with a Gaussian profile was focused by using a lens. The sample in a 1 mm thick cell was then translated along the direction of the focused beam. At the focal point, the sample experiences maximum intensity, which gradually decreases in both directions from the focus. The thickness of the sample was chosen such that it was smaller than the Rayleigh range of the focused beam, which was nearly 1 mm, well-calibrated neutral density filters were used to control the laser intensity. The data were then recorded by scanning the cell across the focus, and the value of β was obtained by fitting the nonlinear transmission expression (given below) for an open aperture z-scan curve. $T = 1 - \frac{\beta L_{eff} I_0}{2^{3/2}\left[1+\left(\frac{z}{z_0}\right)^2\right]}$ where z is the sample position, $z_0 = {}^{\pi\omega_0^2}/_{\lambda}$ is the Rayleigh range, ω_0 is the beam waist at the focal point (z= 0), λ is the laser excitation wavelength, Io is the intensity on the sample

at focus, effective optical path length in the sample of length L is given as $L_{eff} = 1 - e^{-\alpha_0 L}/\alpha_0$, and α_0 is the linear absorption coefficient. In capter-5 the figure 16 shows the open aperture z-scan curve recorded for **M-5** (black dotted lines); the red dotted lines represent the theoretical fit obtained by using the above equation.

THzmeasurement set-up 1

The experimental layout for measurement of THz intensity is shown below.

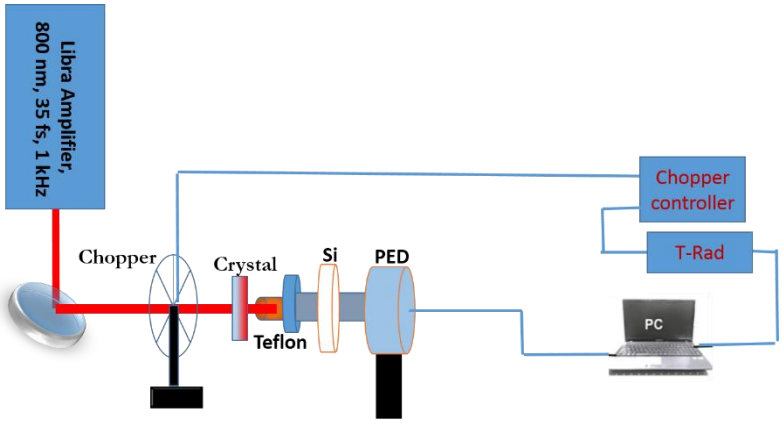

Figure 7.3: THz experimental set-up 1. Si; silicon plate, PED; pyroelectric detector.

Coherent LIBRA amplifier pulse having pulse width 35 fs at 0.8 mm wavelength was used as a pump to generate THz radiation from the crystal. Teflon sheet and silicon plate were used to filter out the unconverted pump from THz. The optical chopper (23.5 Hz) is used as a reference for the pyroelectric detector (PED). The intensity of THz was measured by focusing on a pyro-electric detector connected to a T-Rad system and the output of the T-Rad was fed to the personal computer for measuring the power of the generated THz signal.

THz measurement set-up 2

The THz generation was achieved using a coherent chameleon ultra-II laser which provides an output wavelength of 800nm, pulse duration 140 fs at a repetition rate 80 MHz. A variable attenuator was used to attenuate the incident laser pulses and the laser beam with selective average power was allowed to an incident on the UOH1 nonlinear crystal to generate the THz signal. The employed pump and probe beam powers were ~ 700 mW, and ~175 mW for emission and detection of THz radiation, respectively. Teflon filter was used to eliminate the unconverted pump beam from the crystal. The

generated THz was detected by dipole photoconductive antennas (gap ~5 µm, length ~20 µm) using photoconductive sampling technique. The antenna output was

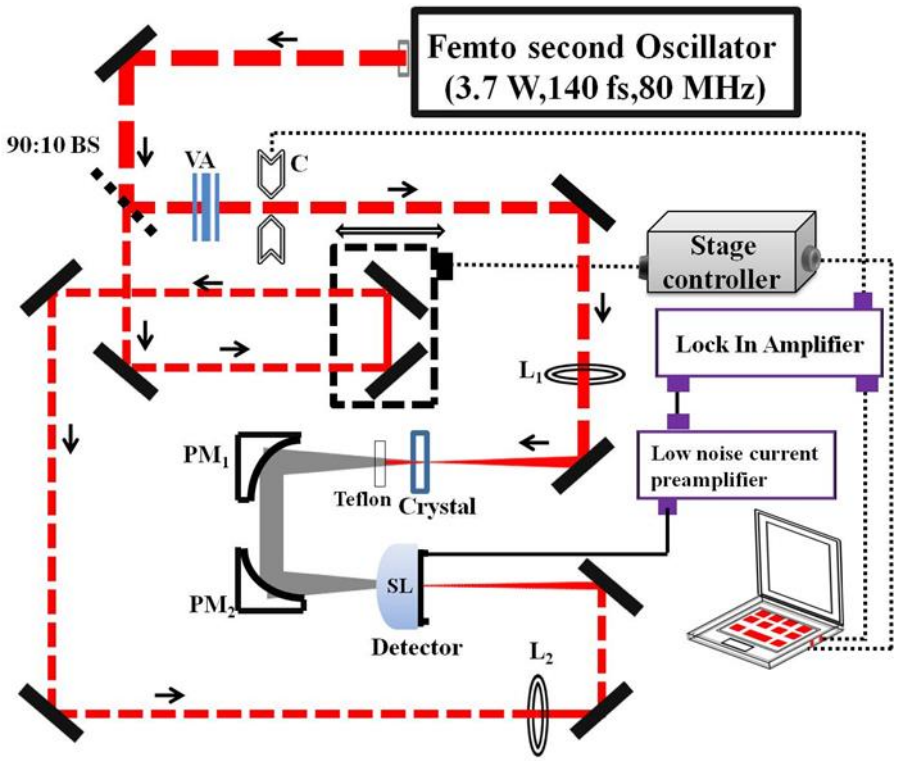

Figure 7.4: THz experimental set-up 2. VA- Variable attenuator, BS-Beam splitter, PM_1 & PM_2: Parabolic mirror, L_2 & L_1: Lenses, Crystal: **M-5**, Detector: Photoconductive antenna, C: chopper.

connected to low noise current preamplifier which is fed to the Lock-in Amplifier (Stanford Research Systems, Model no.SR830). The S/N ratio is enhanced using a mechanical chopper operating at 1.569 kHz frequency. The temporal profile of THz radiation is measured by varying the delay of the probe beam with respect to THz pulse reaching to the antenna.

Fluorescence Life-Time Decay Studies (FLIM)

PL decays and PL lifetime images were recorded on a time-resolved Micro-Time 200 confocal fluorescence lifetime imaging microscopy (FLIM) setup (PicoQuant) equipped with an inverted microscope (Olympus IX 71). Measurements were performed under ambient conditions, at room temperature, on microparticles deposited cover-slip. Samples were excited by a 405 nm ps diode pulse laser with a stable repetition rate of 20 MHz (FWHM: 176 ps). The data acquisition was performed with a SymPhoTime software controlled PicoHarp 300 time-correlated single-photon counting (TCSPC)

module in a time-tagged time-resolved mode. The overall resolution of the setup was 4 ps. The FLIM images of microspheres were recorded using a 60× Nikon objective with a scanned speed of 0.60 ms/pixel. The image pixels for micro-particles are 72×72 and 512×512, respectively.

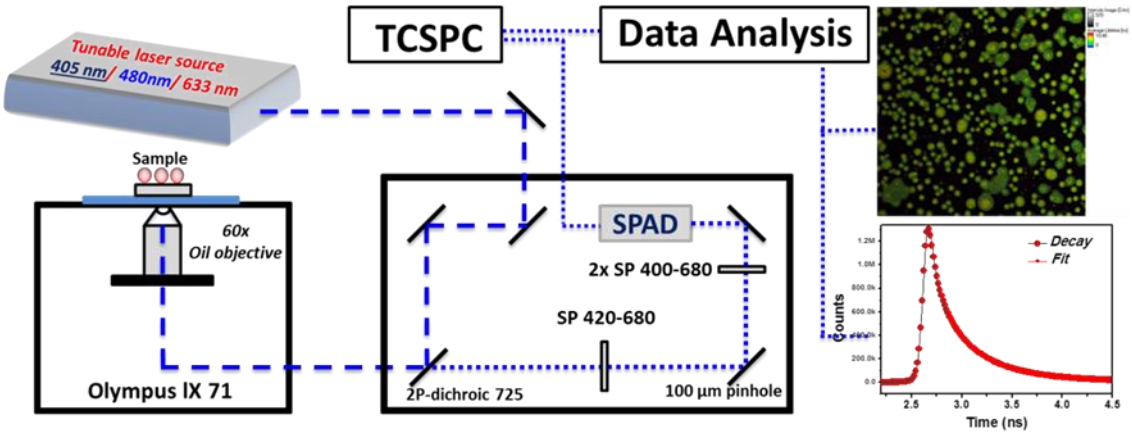

Figure 7.5: FL life-time decay experimental set-up.

DFT (density functional theory)

DFT (density functional theory) calculations were performed using B3LYP hybrid functional and 6-31G(d) basis set for all the atoms as incorporated in *Gaussian 09* software. Optimization of molecular structures with consequent frequency test provided structures with close similarity to the X-ray crystallographic geometry.

Appendix

Appendix A

Materials

Acetic anhydride	Finar Chemicals Pvt. Ltd.
Acetonitrile	Aldrich, 98%
Benzyl amine	TCI Chemicals Pvt. Ltd. 99%
Citrazinicacid	Aldrich, 98%
Chloroform	Aldrich, 98%
Chloroform-D	Aldrich, 98%
C-153 Dye	Aldrich, 98%
CuI	Avra Synthesis Pvt. Ltd. 98%
$(COCl)_2$	Avra Synthesis Pvt. Ltd. 98%
Ethanol	Avra Synthesis Pvt. Ltd. 98%
Hydrogenbromide	Sigma Aldrich, 99.5%
HIO_3	Sigma Aldrich, 99.5%
I_2	Finar Reagents, 99.5%
KI	Merck Chemicals Pvt. Ltd. 99%
Lead bromide	Avra Synthesis Pvt. Ltd. 98%
Lead acetate	Avra Synthesis Pvt. Ltd. 98%
Monoglyme	Aldrich, 98%
(4-(methylthio)phenyl)boronic acid	Aldrich, 98%
NaH	Avra Synthesis Pvt. Ltd. 98%
PPh_3	Avra Synthesis Pvt. Ltd. 98%
$Pd(PPh_3)_2Cl_2$	Aldrich, 99%
$Pd(PPh_3)_4$	Aldrich, 99%
Pyrazole	Aldrich, 98%
Piperdine	Finar Chemicals Pvt. Ltd.
$POCl_3$	Avra Synthesis Pvt. Ltd. 98%
Potassium Hydroxide	Avra Synthesis Pvt. Ltd. 98%
Trifluoroacetic acid	Avra Synthesis Pvt. Ltd. 98%
Triphenylamine	Aldrich, 98%

Appendix B

Table A1: Crystal data and structure refinement parameters of **M-1**

Chemical Formula	$C_{34}H_{24}N_{10}$
FW	572.22
Color	Color-less
Crystal system	Trigonal
Space group	R-3
a	37.186(5)
b	37.186(5)
c	5.3407(7)
α	90.0
β	90.0
γ	120.0
V (Å)	6395.7(15)
Z	3
ρ (g/cm^3)	1.274
T	298 K
λ(Å)	0.71073
F (000)	2886.0
Theta	27.530
Index Ranges (h, k, l)	48,48,6
R1 (Reflections)	0.0862(1483)
Goodness of Fit on F^2. S	1.031

Table A2: Crystal data and structure refinement parameters of **M-5** (CCDC: 1824689)

Chemical Formula	C_{18} H_{15} N_5 S
FW	333.41
Color	Color-less
Crystal system	Tetragonal
Space group	I 4_1
a	12.8855(4)
b	12.8855(4)
c	19.6018(10)
α	90.0
β	90.0
γ	90.0
V (Å)	3254.6(3)
Z	8
ρ (g/cm^3)	1.361
T	298 K
λ (Å)	1.54184
F (000)	1392.0
Theta	0.530
Index Ranges (h, k, l)	15,15,24
R1 (Reflections)	0.0348(1989)
Goodness of Fit on F^2. S	1.042

RESEARCH PUBLICATIONS FROM THE THESIS

1. **U. Venkataramudu**, M. Annadhasan, and R. Chandrasekar, (submitted)
2. **U. Venkataramudu**, C. Sahoo, S. Leelashree, M. Venkatesh, D. Ganesh, S. R. G. Naraharisetty, A. K. Chaudhary, S. Srinath, and R. Chandrasekar, Second-Harmonic- and Terahertz Radiation- Generation from a Single-Component Polar Organic Ferroelectric Crystal. *J. Mater. Chem. C,* **2018**. DOI: 10.1039/C8TC02638F.
3. **U. Venkataramudu**, M. Annadhasan, H. Maddali, and R. Chandrasekar, *Polymorphism and microcrystal shape dependent luminescence, optical waveguiding and resonator properties of coumarin – 153. J. Mater. Chem. C,* **2017**, *5*, 7262-7269.
4. **U. Venkataramudu**, D. Venkatakrishnarao, N. Chandrasekhar, M. A. Mohiddon, and R. Chandrasekar**,** *Single-particle to single-particle transformation of an active type organic microtubular homo-structure photonic resonator into a passive type hetero-structure resonator. Phys. Chem. Chem. Phys.,* **2016**, *18*, 15528-15533.

OTHER RESEARCH PUBLICATIONS

5. **U. Venkataramudu**, S. Basak, M. A. Mohiddon, and R. Chandrasekar, *Hierarchical lithographic patterning of two abrupt spin cross-over Fe(II) complexes into micro-cross-stripes. J. Chem. Sci,* **2018**, *130:77,* 1-6**.**
6. M. V. Rasna, K. P. Zuhail, **U. V. Ramudu**, R. Chandrasekar**,** and S. Dhara, *Dynamics of electro-orientation of birefringent microsheets in isotropic and nematic liquid crystals. Phys. Rev. E.***,* **2016,** *94,* 032701.
7. **U. Venkataramudu**, N. Chandrasekhar, S. Basak, M. D. Prasad, and R. Chandrasekar, *Fabrication of High Resolution 4,8²-Type Archimedean Nano-Lattice Composed of Solution Processable Spin Cross-Over Fe(II) Metallo-Supramolecular Polymer. Macromol. Rapid Commun.*, **2015**, *36*, 647-653.
8. M. V. Rasna, K. P. Zuhail, **U. V. Ramudu**, R. Chandrasekar**,** D. Jayashri, and S. Dhara, *Orientation, interaction and laser-assisted self-assembly of organic single-crystal micro-sheets in nematic liquid crystal. Soft Mater***,* **2015,** *11, 7674-7679.*

9. M. V. Rasna**, U. V. Ramudu**, R. Chandrasekar, and S. Dhara, *Propelling and spinning of micro-sheets in nematic liquid crystal. Phys. Rev. E.,* **2017,** *95,* 012710.

Presentations in Conferences and Symposiums

1. Presented a poster in **13th Eurasia conference on chemical sciences, Indian Institute of Science, Bangalore, India.** December 14-18, **2014**. (International)
2. Presented a poster in **1th Indo-Taiwan Symposium on Recent Trends in Chemical Sciences**, University of Hyderabad, India. November 17-18, **2014.** (International)
3. Presented a poster in **RSC India Road Show**, University of Hyderabad, India, November 07, **2014.** (International)
4. Presented an oral in **3rd International Conference on Polymer Processing and Characterization (ICPPC-2014)**, Mahatma Gandhi University, Kerala, India. October 11-13, 2014. (International) (Invited talk)
5. Presented a poster in **Chemfest-2016**, 13th Annual In-House Symposium in School of Chemistry**,** University of Hyderabad, Hyderabad, India. Feb 24-25, 2016.
6. Presented an oral in **Chemfest-2017**, 14th Annual In-House Symposium in School of Chemistry**,** University of Hyderabad, Hyderabad, India. March 2-3, 2017.
7. Presented an oral in **ESA8 Dyes and Pigments**, NIIST-Tiruvanathapuram, Kerala, India. Septmber 20-22, 2017. (International)
8. Attented a two days work shop on ***Brining the Nanoworld Together-2017*** *by Oxford Instruments,* University of Hyderabad, Hyderabad, India. Decmeber 5-6, 2017.

References

References:

1. R. Kirchain, and L. Kimerling, *Nat. Photonics*. **2007**, *1*, 303.
2. (a) R. Feynman, **1959**, *There is plenty of room at the bottom* (Caltech: American Physical Society) http://www.its. Caltech.edu/~ Feyman/plenty.html; (b) R. P. Feynman, *Eng. Sci*. **1960**, *23*, 22.
3. K. E. Drexler, *Engines of Creation: The Coming Era of Nanotechnolog. (*Publisher-Doubleday*,* **1986**).
4. M. A. Baldo, D. F. O'Brien, Y. You, A. Shoustikov, S. Sibley, M. E. Thompson, and S. R. Forrest, *Nature* **1998**, *395*, 151.
5. J. Clark, and G. Lanzani, *Nat. Photonics*. **2010**, *4*, 438.
6. C. Zhang, Y. Yan, Y.S. Zhao, and J. Yao, *Acc. Chem. Res.* **2014**, *47*, 3448.
7. R. G. Hunsperger, *Integrated Optics: Theory and Technology* (Springer, Berlin, 5th edition, **2002)**.
8. M. Bruchez, M. Moronne, P. Gin, S. Weiss, and A. P. Alivisatos, *Science.* **1998**, *281*, 2013.
9. Y.S. Zhao, H. Fu, A. Peng, Y. Ma, Q. Liao, and J. Yao, *Acc. Chem. Res.* **2010**, *43*, 409.
10. S. R. Forrest, and M. K. Thompson, *Chem. Rev*. **2007**, *107*,923.
11. Y. Yan, and Y. S. Zhao, *Chem. Soc. Rev.* **2014**, *43*, 4325.
12. R. X. Yan, D. Gargas and P. D. Yang, *Nat. Photonics*. **2009**, *3*, 569.
13. I. D. W. Samuel, and G. A. Turnbull, *Chem. Rev.* **2007**, *107*, 1272.
14. E. Reichmanis, and O. Nalamasu, *Science*. **2002**, *297*, 349.
15. E. Kim, Y. Xia, and G. M. Whitesides, *Nature.* **1995**, *376,* 581.
16. Y. Xia, E. Kim, and G. M. Whitesides, *Chem. Mater.* **1996**, *8*, 1558.
17. S. Christopoulos, G. B. H. von Hogersthal, A. J. D. Grundy, P. G. Lagoudakis, A. V. Kavokin, and J. J. Baumberg, *Phys. Rev*. **2007**, *98*, 126405.
18. J. Kasprzak, M. Richard, S. Kundermann, A. Baas, P. Jeambrun, J. M. J. Keeling, F. M. Marchetti, M. H. Szymanska, R. André, J. L. Staehli, V. Savona, P. B. Littlewood, B. Deveaud, and L. S. Dang, *Nature.* **2006**, *443,* 409.
19. R. Balili, V. Hartwell, D. Snoke, L. Pfeier, and K. West, *Science.* **2007**, *316*, 1007.

References

20. Y. Zhang, Y.Liu, C. Li, X. Chen, and Q. Wang, *J. Phys. Chem. C*. **2014**, *118,* 4918.
21. J. Keeling, and N. G. Berlo, *Contemp. Phys*. **2011**, *52*, 131.
22. V. Timofeev, and D. Sanvitto, *Springer*. **2012**, Vol. 172.
23. J. Keeling, and N. G. Berlo, *Contemp. Phys*, **2011**, *52*, 131.
24. M. Pope, and C. E. Swenberg, *Electronics Processes in Organic Crystals and Polymers* (2nd Edition, New York: Oxford, **1999***).*
25. C. Weissm, C. Wagner, R. Temirov, and F. S. Tautz, *J. Am. Chem. Soc*. **2010**, *132*, 11864.
26. Wannier, and Gregory, *Phys. Rev*. **1937**, *52*, 191.
27. J. J. Hopfield, *Phys. Rev.* **1958**, *112*, 1555.
28. J. Frenkel, *Phys. Rev*. **1931**, *37,* 17.
29. S. Grimme. *Angew. Chem. Int. Ed*. **2008**, *47*, 3430.
30. E. Busseron, Y. Ruff, E. Moulin, and N. Giuseppone, *Nanoscale*. **2013**, **5**, 7098.
31. H. Kar and S. Ghosh, *Chem. Commun.* **2014**, *50*, 1064.
32. G. M. Whitesides and B. Grzybowski, *Science.* **2002**, *295*, 2418.
33. Q. X. Tang, L. Jiang, Y. H. Tong, H. X. Li, Y. L. Liu, Z. H. Wang, W. P. Hu, Y. Q. Liu and D. B. Zhu, *Adv. Mater.* **2008**, *20*, 2947.
34. A. Schmidt-Mende, K. Fechtenkotter, E. Mullen, R. Moons, H. Friend and J. D. MacKenzie, *Science.* **2001**, *293*, 1119.
35. M. R. Ghadiri, J. R. Granja, R. A. Milligan, D. E. McRee, and N. Khazanovich, *Nature.* **1993**, *366*, 324.
36. Y.S. Zhao, J. Wu and J. Huang, *J. Am. Chem. Soc*. **2009**, *131*, 3158.
37. A. Ajayaghosh, V. K. Praveen, and C. Vijayakumar, *Chem. Soc. Rev.* **2008**, *37*, 109.
38. P. Jonkheijm, P. V. D. Schoot, A. P. H. J. Schenning, and E. W. Meijier, *Science.* **2006**, *313*, 80.
39. Y. S. Zhao, H. Fu, A. Peng, Y. Ma, D. Xiao, and J. Yao, *Adv. Mater.* **2008**, *20*, 285.
40. A. Patra, C. G. Chandaluri, and T. P. Radhakrishnan, *Nanoscale.* **2012**, *4*, 343.
41. Ch. G. Chandaluri, and T. P. Radhakrishnan, *Angew. Chem. Int. Ed.* **2012**, *51*, 11849.
42. T. Yamaguchi, N. Ishii, K. Tashiro, and T. Aida, *J. Am. Chem. Soc.* **2003**, *125*, 13934.
43. G. M. Whitesides, J. P. Mathias, and C. T. Seto, *Science.* **1991**, *254*, 1312.

References

44. A. L. Briseno, S. C. B. Mannsfeld, M. M. Ling, S. H. Liu, R. J. Tseng, C. Reese, M. E. Roberts, Y. Yang, F. Wudl, and Z. N. Bao, *Nature*, **2006**, *444*, 913.
45. S. M. Sze, *Semiconductor Devices, Physics and Technology*, (Publisher-John Weily & Sons, authorized reprint by Wiley, India, 2nd Edition, **1985**).
46. M. D. Austin, H. X. Ge, W. Wu, M. T. Li, Z. N. Yu, D. Wasserman, S. A. Lyon, and S. Y. Chou, *Appl. Phys. Lett.* **2004**, *84*, 5299.
47. V. Rein, K. Ulijn, M. Andrew, and J. Smith. *Chem. Soc. Rev*. **2008**, 37, 664.
48. F. Di Benedetto, A. Camposeo, S. Pagliara, E. Mele, L. Persano, R. Stabile, R. Cingolani, and D. Pisignano, *Nat. Nanotechn*. **2008**, *3*, 614.
49. E. Menard, M. A. Meitl, Y. Sun, J. U. Park, D. J. Shir, Y. S. Nam, S. Jeon, and J. A. Rogers, *Chem. Rev*. **2007**, *107*, 1117.
50. C. F. J. Grinvald, and M. Antonietti, *Adv. Mater.* **2003**, *15*, 673.
51. T. W. Odom, J. C. Love, D. B. Wolfe, K. E. Paul, and G. M. Whitesides, *Langmuir*, **2002**, *18*. 5315.
52. X. M. Zhao, Y. Xia, and G. M. Whitesides, *Adv. Mater*. **1996**, *8*, 837.
53. X. M. Zhao, S. P. Smith, S. J. Waldman, G. M. Whitesides, and M. Prentiss, *Appl. Phys. Lett*. **1997**, *71*, 1017.
54. E. Kim, Y. Xia, and G. M. Whitesides, *Nature.* **1995**, *376,* 581.
55. Y. Xia, E. Kim, and G. M. Whitesides, *Chem. Mater.* **1996**, *8*, 1558.
56. S. Zhang, *Nat. Biotechnol.* **2003,** *21,* 1171.
57. S. Lal, S. Link, and N. J. Halas, *Nat. Photonics*. **2007**, *1*, 641.
58. M. Schiek, F. Balzer, K. Al. Shamery, J. R. Brewer, A. Lutzen, and H.-G. Rubahn, *small*, **2008**, *4*, 176.
59. C. K. Kao, *Ericsson Rev*. **1979**, *56*, 92–94.
60. K. Takazawa, *Chem. Phys. Lett*. **2008**, *452*, 168.
61. Y. S. Zhao, H.B. Fu, A .D. Peng, Y. Ma, D. B. Xiao, and J. N. Yao, *Adv. Mater*. **2008**, *20*, 2859.
62. R. Chandrasekar, *Phys. Chem. Chem. Phys*. **2014**, *16*, 7173.
63. N. Chandrasekhar, and R. Chandrasekar, *Angew. Chem. Int. Ed.* **2012**, *51*, 3556; N. Chandrasekhar, and R. Chandrasekar, *Angew. Chem.* **2012**, *124*, 3616.

References

64. K. Takazawa, J.-I Inoue, and K. Mitshichi, *ACS Appl. Mater. Interfaces.* **2013**, *5*, 6182.
65. K. Takazawa, J.-I. Inoue, K. Mitsuishi, and T. Takamasu, *Adv. Mater*. **2011**, *23*, 3659.
66. Q. H. Cui, Y. S. Zhao, and J. N. Yao, *J. Mater. Chem.* **2012**, *22*, 4136.
67. Y. S. Zhao, J. Xu, A. Peng, H. Fu, Y. Ma, L. Jiang, and J. Yao, *Angew. Chem. Int. Ed.* **2008**, *47*, 7301.
68. N. Chandrasekhar, R. Reddy, M. D. Prasad, M. S. Rajadurai, and R. Chandrasekar, *Cryst. Eng. Comm.* **2014**, *2*, 1404.
69. N. Chandrasekhar, M. A. Mohiddon, and R. Chandrasekar, *Adv. Opt. Mater*. **2013**, *1*, 305.
70. S. Basak, and R. Chandrasekar, *Adv. Funct. Mater*. **2011**, *21*, 667.
71. P. B. Li, S. Y. Gao, and F. L. Li, *Phys. Rev. A.* **2011**, *83*, 054306.
72. J. Fürst, D. Strekalov, D. Elser, A. Aiello, U. Andersen, C. Marquardt, and G. Leuchs, *Phys. Rev. Lett.* **2011**, *106*, 113901.
73. V. D. Ta, R. Chen, L. Ma, Y. J. Ying, and H. D. Sun, *Laser Photonics Rev.* **2013**, *7*, 133.
74. B. Piccione, C. H. Cho, L. K. van Vugt, and R. Agarwal, *Nat. Nanotechnol.* **2012**, *7*, 640.
75. K. An, J. J. Childs, R. R. Dasari, and M. S. Feld, *Phys. Rev. Lett.* **1994**, *73*, 3375.
76. A. Kiraz, P. Michler, C. Becher, B. Gayral, A. Imamoglu, L. Zhang, E. Hu, W. Schoenfeld, and P. Petroff, *Appl. Phys. Lett.* **2001**, *78*, 3932.
77. R. Chen, V. D. Ta, and H. D. Sun, *ACS Photonics.* **2014**, *1*, 11.
78. K. J. Vahala, *Nature*. **2003,** *424*, 839.
79. B. Guilhabert, C. Foucher, A. M. Haughey, E. Mutlugun, Y. Gao, J. Herrnsdorf, H. D. Sun, H. V. Demir, M. Dawson, N. Laurand, *Opt. Express.* **2014**, *22*, 7308.
80. Y. P. Rakovich, J. F. Donegan, *Laser Photonics Rev.* **2010**, *4*, 179.
81. V. D. Ta, R. Chen, D. Nguyen, and H. D. Sun, *Appl. Phys. Lett.* **2013**, *102*, 031107.
82. F. Gu, L. Zhang, X. Yin, and L. Tong, *Nano Lett.* **2008**, *8*, 2757.
83. I. D. Samuel, E. B. Namdas, and G. A. Turnbull, *Nat. Photonics.* **2009,** *3*, 546.
84. D. Armani, B. Min, A. Martin, and K. J. Vahala, *Appl. Phys. Lett.* **2004**, *85,* 5439.
85. R. Chen, V. D. Ta, and H. D. Sun, *Sci. Rep.* **2012**, *2*, 244.
86. R. Symes, R. M. Sayer, and J. P. Reid, *Phys. Chem. Chem. Phys.* **2004**, *6*, 474.
87. L. Yang, and K. Vahala, *Opt. Lett.* **2003,** *28,* 592.

References

88. N. Tessler, G. J. Denton, and R. H. Friend, *Nature* **1996**, *382*, 695.

89. T. Byrnes, N. Y. Kim and Y. Yamamoto, *Nat. Phys.* **2014**, *31*, 3143.

90. A. Kiraz, A. Kurt, M. Dündar, and A. Demirel, *Appl. Phys. Lett.* **2006**, *89*, 081118.

91. C. Fabry, and A. Perot, *Ann. Chim. Phys*. **1889**, *16*, 7.

92. Q. H. Cui, Y. S. Zhao, and J. Yao, *Adv. Mater*. **2014**, *26*, 6852.

93. C. Zhang, C. L. Zou, Y. Yan, R. Hao, F. W. Sun, Z.-F. Han, Y. S. Zhao, and J. Yao, *J. Am. Chem. Soc.* **2011**, 133, 7276.

94. Y. S. Zhao, P. Zhan, J. Kim, C. Sun, and J. Huang, *ACS Nano*. **2010**, *4*, 1630.

95. W. Zhang, Y. Yan, J. Gu, J. Yao, and Y. S. Zhao, *Angew. Chem., Int. Ed*. **2015**, *54*, 7125.

96. S. Z. Bisri, K. Sawabe, M. Imakawa, K. Maruyama, T. Yamao, S. Hotta, Y. Iwasa and T.Takenobu, *Sci. Rep.* **2012** *2*, 985.

97. L. Rayleigh, *Philos. Mag.* **1910**, *20*, 1001.

98. L. Rayleigh, *Philos. Mag.* **1914**, *27*, 100.

99. C. V. Raman, and G. A. Sutherland, *Nature* **1921**, *108*, 42.

100. V. B. Braginsky, M. L. Gorodetsky, V. S. Ilchenko, *Phys. Lett.* **1989**, *137*, 394.

101. D. V. Krishnarao, E. A. Mamonov, T. V. Murzina, and R. Chandrasekar, *Adv. Optical Mater.* **2018**, 1800343.

102. D. J. Gargas, M. C. Moore, A. Ni, S.-W. Chang, Z. Zhang, S.-L. Chuang, and P. Yang, *ACS. Nano.* **2010**, *4*, 3270.

103. V. D. Ta, R. Chen, and H. D. Sun, *Adv. Mater.* **2012**, *24*, 60.

104. S. Yang, Y. Wang, and H. Sun, *Adv. Opt. Mater*. **2015**, *3*, 1136.

105. J. Haase, S. Shinohara, P. Mundra, G. Risse, V. Lyssenko, H. Fröb, M. Hentschel, A. Eychmüller, and K. Leo, *Appl. Phys. Lett.* **2010**, *97*, 211101.

106. U. Venkataramudu, M. Annadhasan, H. Maddali, and R. Chandrasekar, *J. Mater. Chem. C.* **2017**, *5*, 7262.

107. M. Gao, C. Wei, X. Lin, Y. Liu, F. Hu, and Y. S. Zhao, *Chem. Commun.* **2017**, *53*, 3102.

108. H. Dong, C. Zhang, X. Lin, Z. Zhou, J. Yao, and Y. S. Zhao, *Nano Lett.* **2017**, *17*, 91.

109. R. Vattikunta, D. Venkatakrishnarao, C. Sahoo, S. R. G. Naraharisetty, D. N. Rao, K. Müllen, and R. Chandrasekar, *ACS Appl. Mater. Interfaces*. **2018**, *10*, 16723.

References

110. B. Tang, H. Dong, L. Sun, W. Zheng, Q. Wang, F. Sun, X. Jiang, A. Pan, and L. Zhang, *ACS Nano*. **2017**, *11*, 10681.
111. X. Wang, Q. Liao, Q. Kong, Y. Zhang, Z. Xu, X. Lu, and H. Fu, *Angew. Chem.* **2014**, *126*, 5973.
112. Y. Wang, V. D. Ta, Y. Gao, T. C. He, R. Chen, E. Mutlugun, H. V. Demir, and H. D. Sun, *Adv. Mater.* **2014**, *26*, 2954.
113. G. Righini, Y. Dumeige, P. F. Eron, M. Ferrari, G. N. Conti, D. Ristic, and S. Soria, *Riv. Nuovo Cimento.* **2011**, *34*, 435.
114. S. Yang, Y. Wang, and H. Sun, *Adv. Optical Mater.* **2015**, *3*, 1136–1162.
115. C. Zhang, C.-L. Zou, Y. Yan, C. Wei, J.-M. Cui, F.-W. Sun, J. Yao, and Y. S. Zhao, *Adv. Opt. Mater.* **2013**, *1*, 357.
116. P. Sandeep, and P. B. Bisht, *Chem, phys, Lett*. **2003**, *371*, 327.
117. M. S. Nawrocka, T. Liu, X. Wang, and R. R. Panepucci, *Appl. Phys. Lett.* **2006**, *89*, 071110.
118. D. Y. Curtin, and I. C. Paul, *Chem. Rev.* **1981**, *81*, 525.
119. T. Miyano, T. Sakai, I. Hisaki, H. Ichida, Y. Kanematsu, and N. Tohnai, *Chem. Commun.* **2016**, *52*, 13710.
120. Y. Han, Y. Liu, X. Xing, C. Tian, P. Lina, and S. Du, *Chem. Commun.* **2015**, *51*, 14481.
121. A. D.Mighell, V. L. Himes, and J. R. Rodgers, *Acta Crystallogr., Sect. A: Found. Crystallogr*. **1983**, *39*, 737.
122. A. I. Kitaigorodskii, *in Organic Chemical Crystallography, Consultant Bureau, New York, NY*, **1961**.
123. G. R. Desiraju, *Acc. Chem. Res.* **2002**, *35*, 565.
124. M. Ohkita, T. Suzuki, K. Nakatani, and T. Tsuji, *Chem. Commun.* **2001**, 1454.
125. B. K. Saha, A. Nangia, and J. Nicoud, *Cryst. Growth Des*. **2006**, *6*, 1278.
126. N. Chen, M. Li, P. Yang, X. M. Shao, and S. Zhu, *Cryst. Growth Des.* **2013**, *13*, 2650.
127. R. Centore and A. Tuzi, *Acta Crystallogr., Sect. C: Cryst. Struct. Commun.* **2001**, *57*, 698.
128. O. P. Kwon, S. J. Kwon, M. Jazbinsek, F. D. J. Brunner, J. I. Seo, C. Hunziker, A. Schneider, H. Yun, Y. S. Lee, and P. Günter, *Adv. Funct. Mater.* **2008**, *18*, 3242.

References

129. M. E. Lines, and A. M. Glass, *Principles, and applications of ferroelectrics and related materials* (Oxford Univ. Press, New York, **1977**).
130. J. Valasek, *Phys. Rev.* **1921**, *17*, 475.
131. M. Dawber, K. M. Rabe, and J. F. Scott, *Rev. Mod. Phys.* **2005**, *77*, 1083.
132. T. Furukawa, M. Date, and E. Fukada, *J. Appl. Phys.* **1980**, *51*, 1135.
133. K. Noda, K. Ishida, A. Kubono, T. Horiuchi, H. Yamada, and K. Matsushige, *J. Appl. Phys.* **2003**, *93*, 2866.
134. A. Comotti, S. Bracco, T. Ben, S. Qiu, and P. Sozzani, *Angew. Chem. Int. Ed.* **2014**, *53*, 1043.
135. A. L. Solomon, *Phys. Rev.* **1956**, *104*, 1191.
136. T. Mitsui, *Phys. Rev.* **1958**, *111*, 1259.
137. G. J. Goldsmith, and J. G. White, *J. Chem. Phys.* **1959**, *31*, 1175.
138. A. S. Tayi, A. Kaeser, M. Matsumoto, T. Aida, and S. I. Stupp, *Nat. Chem.* **2015**, *7*, 281.
139. Z. Zikmund, *Ferroelectrics.* **1994**, *58*, 223.
140. J. Feder, *Ferroelectrics*. **1976**, *12*, 71–84.
141. L. X. Chen, K. L. Wang, J. F. Stoddart, and I. S. Stupp, *Nature*. **2012**, *488*, 485.
142. S. Horiuchi, and Y. Tokura, *Nat. Mater.* **2008**, *7*, 357.
143. R. A. Reddy, and C. Tschierske, *J. Mater. Chem.* **2006**, *16*, 907.
144. P. P. Shi, Y. Y. Tang, P. F. Li, W. Q. Liao, Z. X. Wang, Q. Ye, and R. G. Xion, *Chem. Soc. Rev*. **2016**, *45*, 3811.
145. J. Valasek, *Phys. Rev*. **1920**, *15*, 537.
146. A. S. Tayi, A. Kaeser, M. Matsumoto, T. Aida, and S. I. Stupp, *Nat. Chem*. **2015**, *7*, 281.
147. S. Horiuchi, Y. Okimoto, R. Kumai, and Y. Tokura, *Science.* **2003**, *299*, 229.
149. K. Singer, J. Sohn, and S. Lalama, *Appl. Phys. Lett*. **1986**, *49*, 248.
150. G. Ashwell, R. Hargreaves, C. Baldwin, G. Bahra, and C. Brown, *Nature.* **1992**, *357*, 393.
151. M. Liu, H. Y. Hwang, H. Tao, A. C. Strikwerda, K. Fan, G. R. Keiser, A. J. Sternbach, K. G. West, S. Kittiwatanakul, J. Lu, S. A. Wolf, F. G. Omenetto, X. Zhang, K. A. Nelson, and R. D. Averitt, *Nature.* **2012**, *487*, 345.

References

152. T. Kubacka, J. A. Johnson, M. C. Hoffmann, C. Vicario, S. de Jong, P. Beaud, S. Grübel, S. W. Huang, L. Huber, L. Patthey, Y. D. Chuang, J. J. Turner, G. L. Dakovski, W. S. Lee, M. P. Minitti, W. Schlotter, R. G. Moore, C. P. Hauri, S. M. Koohpayeh, V. Scagnoli, G. Ingold, S. L. Johnson, and U. Staub, *Science.* **2014**, *343*, 1333.
153. C. Vicario, C. Ruchert, F. A. Lamas, P. M. Derlet, B. Tudu, J. Luning, and C. P. Hauri, *Nat. Photonics.* **2013**, *7*, 720.
154. T. Qi, Y. H. Shin, K. L. Yeh, K. A. Nelson, A. M. Rappe, *Phys. Rev. Lett.* **2009**, *102*, 247603.
155. A. Dienst, M. C. Hoffmann, D. Fausti, J. C. Petersen, S. Pyon, T. Takayama, H. Takagi, and A. Cavalleri, *Nat. Photonics.* **2011**, *5*, 485.
156. T. H. Maiman, *Nature.* **1960**, *187*, 493.
157. G. C. Baldwin, *Introduction to Nonlinear Optics,* (Plenum Press. New York, **1969**).
158. M. D. Levenson, and S. S. Kano, *Introduction to Nonlinear Laser Spectroscopy,* (Academic Press, New York **1988**).
159. D. S. Bethune, R. W Smith, and Y R. Shen, *Phys. Rev. Lett.* **1976.** *37,* 431.
160. D. S. Bethune, *Opt. Lett.* **1981,** *6,* 287.
161. D. S. Bethune, *Phys. Rev. A.* **1981,** *23,* 3139.
162. R. M. Macfarlane, and R. M. Shelby, *Opt. Commun.* **1981,** *39,* 169.
163. N. Wenjiang, *Adv. Mater.* **1993**, *5*, 520.
164. C. Bosshard, *Adv. Mater.* **1996**, *8*, 385.
165. R. W. Boyd, *Nonlinear Optics, 2nd ed.*; Academic Press: London, **2003**.
166. J. Zyss, D. S. Chemla, and Eds, *Nonlinear Optical Properties of Organic Molecules and Crystals*. (Academic Press: London, **1987**).
167. D. F. Eaton, *Science*. **1991**, *253*, 281.
168. N. B. Delone, *Fundamentals of Nonlinear Optics of Atomic Gases*. (Wiley, New York, **1988**).
169. S. Rosenne, E. Grinvald, E. Shirman, L. Neeman, S. Dutta, O. B.-Elli, R. B.-Zvi, E. Oksenberg, P. Milko, V. Kalchenko, H. Weissman, D. Oron, and B. Rybtchinski, *Nano Lett.* **2015**, *15*, 7232.
170. D. R. Kanis, M. A. Ratner and T. J. Marks, *Chem. Rev.* **1994**, *94*, 195.
171. B. Ferguson, and X. C. Zhang, *Nat. Mater*. **2002**, *1*, 26.

References

172. H. Hashimoto, H. Takahashi, T. Yamada, K. Kuroyanagi, and T. Kobayashi, *J. Phys. Condens. Matter.* **2001**, *13*, L529.
173. J. J. Carey, R. T. Bailey, D. Pugh, J. N. Sherwood, F. R. Cruickshank, and K. Wynne, *Appl. Phys. Lett.* **2002**, **81**, 4335.
174. A. M. Sinyukov, M. R. Leahy, L. M. Hayden, M. Haller, J. Luo, A. K. Y. Jen, and L. R. Dalton, *Appl. Phys. Lett*. **2004**, *85*, 5827.
175. A. Nahata, D. H. Auston, C. Wu, and J. T. Yardley, *Appl. Phys. Lett*. **1995**, *67*, 1358.
176. K. Kuroyanagi, K. Yanagi, A. Sugita, H. Hashimoto, H. Takahashi, S. Aoshima, and Y. Tsuchiya, *J. Appl. Phys*. **2006**, *100*, 043117.
177. A. Schneider, I. Biaggio, and P. Gunter, *Appl. Phys. Lett*. **2004**, *84*, 2229.
178. A. Schneider, M. Stillhart, and P. Gunter, *Opt. Express.* **2006**, *14*, 5376.
179. R. C. Miller, *Phys. Rev.* **1964**, *134*, A1313.
180. S. E. Skipetrov, *Nature.* **2004**, *432*, 285.
181. G. D Boyd, A. Ashkin, J. M. Dziedzic, and D. A. Kleinman, *Phys. Rev.***1965**, *137*, A1305.
182. C. F. Dewey, and L. O. Hocker, *Appl. Phys. Lett.* **1975**, *26*, 442.
183. M. Göppert-Mayer, *Ann. Phys.* **1931**, *401*, 273–294.
184. W. Kaiser, and C. G. B. Garrett, *Phys. Rev. Lett.* **1961**, 7, 229.
185. M. Pawlicki, H. A. Collins, R. G. Denning, and H. L. Anderson, *Angew. Chem., Int. Ed.* **2009**, 1*8*, 3244.
186. W. R. Zipfel, R. M. Williams, and W. W. Webb, *Nat. Biotechnol*. **2003**, *21*, 1369.
187. G. S. He, L. S. Tan, Q. Zheng, and P. N. Prasad, *Chem. Rev.* **2008,** 108, 1245.
188. P. N. Prasad, *Nanophotonics*; John Wiley: New York, 2004.
189. R. R. Birge, J. A. Bennett, B. M. Pierce, and T. M. Thomas, *J. Am. Chem. Soc*. **1978**, *100*, 1533.
190. B. A. Reinhardt, L. L. Brott, S. J. Clarson, A. G. Dillard, J. C. Bhatt, R. Kannan, L. Yuan, G.S. He, and P. N. Prasad, *Chem. Mater*. **1998**, *10*, 1863.
191. J. L. Bredas, C. Adant, P. Tackx, A. Persoons, and B. M. Pierce, *Chem. Rev.* **1994**, *94*, 243.
192. F. S. Kim, G. Ren, and S. A. Jenekhe, *Chem. Mater.* **2011**, *23*, 682.

References

193. V. K. Praveen, C. Ranjith, E. Bandini, A. Ajayaghosh, and N. Armaroli, *Chem. Soc. Rev*. **2014**, *43*, 4222.
194. S. S. Babu, V. K. Praveen, and A. Ajayaghosh, *Chem. Soc. Rev*. *2014*, *114*, 1973.
195. C. Zhang, Y. S. Zhao and J. Yao, *Phys. Chem. Chem. Phys*. **2011**, *13*, 9060.
196. K. Takazawa, J.-I. Inoue, K. Mitsuishi, and T. Kuroda, *Adv. Funct. Mater.* **2013**, *23*, 839.
197. N. Chandrasekhar, S. Basak, M. A. Mohiddon, and R. Chandrasekar, *ACS Appl. Mater. Interfaces.* **2014**, *6*, 1488.
198. X. Wang, Q. Liao, X. Lu, H. Li, Z. Xu, and H. Fu, *Sci. Rep.* **2014**, *4*, 7011.
199. J. Yu, Y. Cui, H. Xu, Y. Yang, Z. Wang, B. Chen, and G. Qian, *Nat. Commun*. **2013**, *4*, 2719.
200. D. Venkatakrishnarao, M. A. Mohiddon, N. Chandrasekhar, and R. Chandrasekar, *Adv. Opt. Mater*. **2015**, *3*, 1035.
201. Y. S. L. V. Narayana, D. V. Krishnarao, M. A. Mohiddon, A. Biswas, N. Viswanathan, and R. Chandrasekar, *ACS Appl. Mater. Interfaces.* **2016**, *8*, 952.
202. S. Yang, Y. Wang, and H. Sun, *Adv. Opt. Mater*. **2015**, *3*, 1136.
203. E. M. Purcell, *Phys. Rev*. **1946**, *69*, 37.
204. D. V. Krishnarao, and R. Chandrasekar, *Adv. Opt. Mater*. **2015**, *4*, 112.
205. H. Dong, Z. Chen, L. Sun, W. Xie, H. Hoe Tan, J. Lu, C. Jagadishb, and X. Shen, *J. Mater. Chem*. **2010**, *20*, 5510.
206. M. Mariano, F. J. Rodríguez, P. Romero-Gomez, G. Kozyreff, and J. Martorell, *Sci. Rep.* **2014**, *4*, 4959.
207. P. Hui, and R. Chandrasekar, *Adv. Mater*. **2013**, *25*, 2963.
208. N. Chandrasekhar, and R. Chandrasekar, *Chem. Commun*. **2010**, *46*, 2915.
209. J. Wiersig, *Phys. Rev. A: At., Mol., Opt. Phys.* **2003**, *67*, 023807.
210. S. Basak, and R. Chandrasekar, *J. Mater. Chem. C.* **2014**, *2*, 1404.
211. J. Wang, T. Zhan, G. Huang, P. K. Chu, and Y. Mei, *Laser Photonics Rev*. 2**014**, *8*, 521.
212. Q. Kong, Q. Liao, Z. Xu, X. Wang, J. Yao, and H. Fu. *J. Am. Chem. Soc.* **2014**, *136*, 2382.

References

213. R. P. N. Tripathi, A. Dasgupta, R. Chikkaraddy, P. P. Patra, A. B. Vasista, and G. V. Pavan Kumar, *J. Opt*. **2016**, *18*, 065002.
214. W. Zhang, J. Yao, and Y. S. Zhao, *Acc. Chem. Res.* **2016**, *49*, 1691.
215. H. Dong, Y. Wei, W. Zhang, C. Wei, C. Zhang, J. Yao, and Y. S. Zhao, *J. Am. Chem. Soc.* **2016**, *138*, 1118.
216. X. Gu, J. Yao, G. Zhang, Y. Yan, C. Zhang, Q. Peng, Q. Liao, Y. Wu, Z. Xu, Y. Zhao, H. Fu, and D. Zhang, *Adv. Funct. Mater.* **2012**, *22*, 4862.
217. H. Dong, C. Zhang, J. Yao, and Y. S. Zhao, *Chem. – Asian J.* **2016**, *11*, 2656.
218. C. Wei, M. Gao, F. Hu, J. Yao, and Y. S. Zhao, *Adv. Opt. Mater.* **2016**, *4*, 1009.
219. S. W. Eaton, A. Fu, A. B. Wong, C.-Z. Ning, and P. Yang, *Nat. Rev. Mater.* **2016**, *1*, 16028.
220. H. Siegrist, C. Kloc, R. A. Laudise, H. E. Katz, and R. C. Haddon, *Adv. Mater.* **1998**, *10*, 379.
221. P. Srujana, and T. P. Radhakrishnan, *Angew. Chem., Int. Ed.* **2015**, *54*, 7270.
222. Z. He, L. Zhang, J. Mei, T. Zhang, J. W. Y. Lam, Z. Shuai, Y. Q. Dong, and B. Z. Tang, *Chem. Mater.* **2015**, *27*, 6601.
223. K. Wang, H. Zhang, S. Chen, G. Yang, J. Zhang, W. Tian, Z. Su, and Y. Wang, *Adv. Mater.* **2014**, *26*, 6168.
224. S. Varghese, and S. Das, *J. Phys. Chem. Lett.* **2011**, *2*, 863.
225. D. Venkatakrishnarao, Y. S. L. V. Narayana, M. A. Mohiddon, E. A.Mamonov, N.Mitetelo, I. A. Kolmychek, A. I. Maydykovskiy, V. B. Novikov, T. V. Murzina, and R. Chandrasekar, *Adv. Mater.* **2017**, *29*, 1605260.
226. D. Venkatakrishnarao, and R. Chandrasekar, *Adv. Opt. Mater.* **2016**, *4*, 112.
227. U. Venkataramudu, D. Venkatakrishnarao, N. Chandrasekhar, M. A. Mohiddon, and R. Chandrasekar, *Phys. Chem. Chem. Phys.* **2016**, *18*, 15528.
228. D. Venkatakrishnarao, M. A. Mohiddon, and R. Chandrasekar, *Adv. Opt. Mater.* **2016**, *5*, 1600613.
229. K. Tabata, D. Braam, S. Kushida, L. Tong, J. Kuwabara, T. Kanbara, A. Beckel, A. Lorke, and Y. Yamamoto, *Sci. Rep.* **2014**, *4*, 5902.
230. C. Wei, S. Y. Liu, C.-L. Zou, Y. Liu, J. Yao, and Y. S. Zhao, *J. Am. Chem. Soc.* **2015**, *137*, 62.

References

231. K. Takazawa, J. Inoue, K. Mitsuishi, K. Mitsuishi and T. TaKamasu, *Phys. Rev. Lett.* **2010**, *105*, 067401.
232. Z. Xie, B. Yang, F. Li, G. Cheng, L. Liu, G. Yang, H. Xu, L. Ye, M. Hanif, S. Liu, D. Ma, and Y. Ma, *J. Am. Chem. Soc.* **2005**, *12*, 14152.
233. D. Sanvitto, and S. Kéna-Cohen, *Nature.* **2016**, *15*, 1061.
234. L. Cao, M. J. Meziani, S. Sahu, and Y.-P. Sun, *Acc. Chem. Res.* **2013**, *46*, 171.
235. I. Moreels, K. Lambert, D. Smeets, D. DeMuynck, T. Nollet, J. C. Martins, F. Vanhaecke, A. Vantomme, C. Delerue, G. Allan, and Z. Hens, *ACS Nano.* **2009**, *3*, 3023.
236. S. Link, and M. A. El-Sayed, *J. Phys. Chem. B.* **1999**, *103*, 4212.
237. Y. Wang, G. Zhang, W. Zhang, X. Wang, Y. Wu, T. Liang, X. Hao, H. Fu, Y. S. Zhao, and D. Zhang, *Small.* **2016**, *12*, 6554.
238. C. Wei, M. Gao, F. Hu, J. Yao, and Y. S. Zhao, *Adv. Opt. Mater.* **2016**, *4*, 1009.
239. R. Vattikunta, D. V. Krishnarao, M. A. Mohiddon, and R. Chandrasekar, *ChemPhysChem.* **2016**, *17*, 3425.
240. M. Salomon, M. Uchiyama, M. Xu, and S. Petrucci, *J. Phys. Chem.* **1989**, *93*, 4374.
241. M. L. Horng, J. A. Gardecki, A. Papazyan, and M. Maroncelli, *J. Phys. Chem.* **1995**, *99*, 17311.
242. S. Koley and S. Ghosh, *Chem.Phys.Chem.* **2015**, *16*, 3518.
243. G. V. Gridunova, D. S. Yufit, Y. T. Struchkov, O. R. Khrolova, A. Z. Reznichenko, and M. A. Tavrizova, *Kristallografiya.* **1992**, *37*, 366.
244. B. C. Yip, F. M. Moo, K. S. Lok, H. K. Fun, and K. Sivakumar, *Acta Crystallogr., Sect. C: Cryst. Struct. Commun.* **1996**, *52*, 477.
245. X. Liu, J. M. Cole, P. G. Waddell, T.-C. Lin, and S. M. Kechnie, *J. Phys. Chem. C*. **2013**, *117*, 14130.
246. T. Z. Ren, Z. He, H. Fan, H. Lia, and Z. Y. Yuan, *Cryst Eng Comm.* **2014**, *16*, 11013.
247. J. Burschka, N. Pellet, S. J. Moon, R. H. Baker, P. Gao, M. K. Nazeeruddin, and M. Gratzel, *Nature.* **2013**, *499*, 316.
248. P. Gao, M. Gratzel, and M. K. Nazeeruddin, *Energy Environ. Sci.* **2014**, *7*, 2448.
249. H. Zhang, Q. Liao, X. Wang, J. Yao, and H. Fu, *Adv. Optical Mater.* **2016**, *4*, 1718.
250. Q. Liao, K. Hu, H. Zhang, X. Wang, J. Yao, and H. Fu, *Adv. Mater*. **2015**, *27*, 3405.

References

251. S. A. Veldhuis, P. P. Boix, N. Yantara, M. Li, T. C. Sum, N. Mathews, and S. G. Mhaisalkar, *Adv. Mater*. **2016**, *28*, 6804.
252. N. Kawano, M. Koshimizu, Y. Sun, N. Y. Yahaba, Fujimoto, T. Yanagida, and K. Asai, *J. Phys. Chem. C.* **2014**, *118*, 9101.
253. W.-Q. Liao, Y. Zhang, C.-L. Hu, J.-G. Mao, H.-Y. Ye, and P.-F. Li, *Nat. Commun*. **2015**, *6*, 7338.
254. Y. Chen, H. T. Yi, X. Wu, R. Haroldson, Y. N. Gartstein, Y. I. Rodionov, K. S. Tikhonov, A. Zakhidov, X.-Y. Zhu, and V. Podzorov, *Nat. Commun*. **2016**, *7*, 12253.
255. D. Ma, Y. Fu, L. Dang, J. Zhai, I. A. Guzei, and S. Jin, *Nano Research.* **2017**, *10*, 2117.
256. L. Mao, H. Tsai, W. Nie, L. Ma, J. Im, C. C. Stoumpos, C. D. Malliakas, F. Hao, M. R. Wasielewski, A. D. Mohite, and M. G. Kanatzidis, *Chem. Mater*. **2016**, *28*, 7781.
257. L. Dou, A. B. Wong, Y. Yu, M. Lai, N. Kornienko, S. W. Eaton, A. Fu, C. G. Bischak, J. Ma, T. Ding, N. S. Ginsberg, L.- W. Wang, A. P. Alivisatos, and P. Yang, *Science.* **2015**, *349*, 1518.
258. C. C. Stoumpos, L. Frazer, D. J. Clark, Y. S. Kim, S. H. Rhim, A. J. Freeman, J. B. Ketterson, J. I. Jang, and M. G. Kanatzidis, *J. Am. Chem. Soc.* **2015**, *137*, 6804.
259. G. Walters, B. R. Sutherland, S. Hoogland, D. Shi, R. Comin, D. P. Sellan, O. M. Bakr, and E. H. Sargent, *ACS Nano*. **2015**, *9*, 9340.
260. E. W. VanStryland, H. Vanherzeele, M. A. Woodall, M. J. Soileau, A. L. Smirl, S. Guha, and T. F. Boggess, *Opt. Eng*. **1985**, *24*, 613.
261. D. Liang, Y.Peng, Y. Fu, M. J. Shearer, J. Zhang, J. Zhai, Y. Zhang, R. J. Hamers, T. L Andrew, and S. Jin, *ACS Nano.* **2016**, *10*, 6897.
262. F. Wang, W. Geng, Y. Zhou, H.-H. Fang, C.-J. Tong, M. A. Loi, L.-M. Liu, and N. Zhao, *Adv. Mater*. **2016**, *28*, 9986.
263. Z. Yuan, Y. Shu, Y. Tian, Y. Xin, and B. Ma, *Chem. Commun*. **2015**, *51*, 16385.
264. D. Shi, V. Adinolfi, R. Comin, M. Yuan, E. Alarousu, A. Buin, Y. Chen, S. Hoogland, A. Rothenberger, K. Katsiev, Y. Losovyj, X. Zhang, P. A. Dowben, O. F. Mohammed, E. H. Sargent, and O. M. Bakr, *Science*. **2015**, *347*, 519.
265. H. Zhou, Z. Nie, J. Yin, Y. Sun, H. Zhuo, D. Wang, D. Li, J. Dou, X. Zhang, and T. Ma, *RSC Adv*. **2015**, *5*, 85344.

References

266. B. R. Sutherland, S. Hoogland, M. M. Adachi, C. T. O. Wong, and E. H. Sargent, *ACS Nano.* **2014**, *8*, 10947.
267. P. T. Snee, Y. Chan, D. G. Nocera, and M. G. Bawendi, *Adv. Mater*. **2005**, *17*, 1131.
268. D. Venkatakrishnarao, C. Sahoo, V. Radhika, M. Annadhasan, S. R. G. Naraharisetty, and R. Chandrasekar, *Adv. Opt. Mater*. **2017**, *5*, 1700695.
269. P. Sandeep, and P. B. Bisht, *Chem. Phys. Lett*. **2003**, *371*, 327.
270. W. Liu, J. Xing, J. Zhao, X. Wen, K. Wang, P. Lu, and Q. Xiong, *Adv. Opt. Mater*. **2017**, *5*, 1601045.
271. R. Glaser, N. Knotts, and H. Wu, *Chemtracts-Organic Chemistry.* **2003**, *16*, 643.
272. T. Qi, Y. H. Shin, K. L. Yeh, K. A. Nelson, and A. M. Rappe, *Phys. Rev. Lett.* **2009**, *102*, 247603.
273. T. F. Nova, A. Cartella, A. Cantaluppi, M. Först, D. Bossini, R. V. Mikhaylovskiy, A. V. Kimel, R. Merlin, and A. Cavalleri, *Nat. Phys*. **2017**, *13*, 132.
274. M. Muthuraman, Y. L. Fur, M. B. Beucher, R. Masse, J. F. Nicoud, and G. R. Desiraju, *J. Mater. Chem.* **1999**, *9*, 2233.
275. R. R. Choudhury, and R. Chitra, *Cryst. Res. Technol.* **2006**, *41*, 1045.
276. C. Rajadurai, F. Schramm, S. Brink, O. Fuhr, M. Ghafari, R. Kruk, and M. Ruben, *Inorg. Chem*. **2006**, *45*, 10019.
277. K. S. Rao, A. K. Chaudhary, M. Venkatesh, K. Thirupugalmani, and S. Brahadeeswaran, *Curr. Appl. Phys.* **2016**, *16*, 777.
278. D. V. krishnarao, Y. S. L. V. Narayana, M. A. Mohaiddon, E. A. Mamonov, I. A. Kolmychek, A. I. Maydykovskiy, N. V. Mitetelo, V. B. Novikov, T. V. Murzina, and R. Chandrasekar, *Adv. Mater*. **2017**, *29*, 1605260.
279. H. A. Hafez, S. Kovalev, J. C. Deinert, Z. Mics, B. Green, N. Awari, M. Chen, S. Germanskiy, U.Lehnert, J. Teichert, Z. Wang, K. J. Tielrooij, Z. Liu, Z. Chen, A. Narita, K. Müllen, M. Bonn, M. Gensch, and D. Turchinovich, *Nature*, **2018**, DOI: 10.1038/S41586-018-0508-1.

Ph. No: +91-9985774275
E-mail: ramu.ugam@gmail.com

Curriculum Vitae

Personal Details:

Name: Uppari Venkataramudu

Father's name: U. Sreeramulu garu

Date of Birth & Place: 30. April 1990, Kurnool, India

Nationality: Indian

Marital Status: Not Married

Education Details:

November '12 - July '18	**Ph. D. in Materials Chemistry** under the supervision of Prof. R. Chandrasekar, School of Chemistry, University of Hyderabad, India. **Thesis Title**: "Photonic Properties of Organic Micro-resonators and Ferroelectric Polar Crystal: Two-Photon Luminescence, Second Harmonic Generation, and Terahertz Wave Production"
June '10- May '12	**M. Sc in General Chemistry** with 72.3% at Department of Chemistry, S. V. University, Tirupati , Andhra Pradesh, India.
July '07- May '10	**B. Sc in Chemistry**, **Micro-Biology and Botany** with 68.7% at Silver Jubilee Govt. College, Kurnool, Andhra Pradesh, India.
June '05- May '07	**Intermediate in Chemistry, Physics and Biology** with 75% at Vavilala Junior College, Kurnool, Andhra Pradesh, India.
June '10 - May '05	**S. S. C. in Science** with 73.3% at Z. P. High School, Kurnool, Andhra Pradesh, India.

Awards and Recognitions:

- **Nov 2014** Winner of **"RSC Best Poster Award"** presented at **RSC India Road Show**, University of Hyderabad, India.
- **2014-2017** Awarded as a **Senior Research Fellow** by CSIR-India.
- **February-2012** Qualified **GATE** in All India Level by New Delhi, India.
- **December-2011** Qualified All India Level **CSIR-JRF** by New Delhi, India.
- Secured 2nd position in Higher Secondary Education (S.S.C.).

Photonic Properties of Organic Micro-Resonators and Ferroelectric Polar Crystal: Two-Photon Luminescence, Second Harmonic Generation, and Terahertz Wave Production

by Uppari Venkataramudu

Submission date: 07-Sep-2018 10:25AM (UTC+0530)
Submission ID: 998118949
File name: thesis_PDF.pdf (13.7M)
Word count: 27098
Character count: 146142

Photonic Properties of Organic Micro-Resonators and Ferroelectric Polar Crystal: Two-Photon Luminescence, Second Harmonic Generation, and Terahertz Wave Production

ORIGINALITY REPORT

36%	7%	31%	7%
SIMILARITY INDEX	INTERNET SOURCES	PUBLICATIONS	STUDENT PAPERS

PRIMARY SOURCES

1	Uppari Venkataramudu, Dasari Venkatakrishnarao, Naisa Chandrasekhar, Mahamad Ahamad Mohiddon, Rajadurai Chandrasekar. "Single-particle to single-particle transformation of an active type organic μ-tubular homo-structure photonic resonator into a passive type hetero-structure resonator", Physical Chemistry Chemical Physics, 2016 Publication	8%
2	Uppari Venkataramudu, Chakradhar Sahoo, Solaiappan Leelashree, Mottamchetty Venkatesh et al. "Terahertz radiation and second-harmonic generation from a single-component polar organic ferroelectric crystal", Journal of Materials Chemistry C, 2018 Publication	7%
3	Submitted to University of Hyderabad, Hyderabad	4%

Student Paper

4	Wenjiang Nie. "Optical Nonlinearity:Phenomena, applications, and materials", Advanced Materials, 07/1993 Publication	2%
5	Daichi Okada, Stefano Azzini, Hiroki Nishioka, Anna Ichimura et al. "π-Electronic Co-crystal Microcavities with Selective Vibronic-Mode Light Amplification: Toward Förster Resonance Energy Transfer Lasing", Nano Letters, 2018 Publication	1%
6	tesisenxarxa.net Internet Source	1%
7	Zhang, Wei, Yongli Yan, Jianmin Gu, Jiannian Yao, and Yong Sheng Zhao. "Low-Threshold Wavelength-Switchable Organic Nanowire Lasers Based on Excited-State Intramolecular Proton Transfer", Angewandte Chemie International Edition, 2015. Publication	1%
8	Dasari Venkatakrishnarao, Evgeniy A. Mamonov, Tatiana V. Murzina, Rajadurai Chandrasekar. "Advanced Organic and Polymer Whispering-Gallery-Mode Microresonators for Enhanced Nonlinear Optical Light", Advanced Optical Materials, 2018 Publication	1%

9	Chandrasekar, Rajadurai. "Organic photonics: prospective nano/micro scale passive organic optical waveguides obtained from π-conjugated ligand molecules", Physical Chemistry Chemical Physics, 2014. Publication	1%
10	Dasari Venkatakrishnarao, Chakradhar Sahoo, Radhika Vattikunta, Mari Annadhasan et al. "2D Arrangement of Polymer Microsphere Photonic Cavities Doped with Novel N-Rich Carbon Quantum Dots Display Enhanced One- and Two-Photon Luminescence Driven by Optical Resonances", Advanced Optical Materials, 2017 Publication	1%
11	scholar.lib.vt.edu Internet Source	<1%
12	openscholarship.wustl.edu Internet Source	<1%
13	Shancheng Yang, Yue Wang, Handong Sun. "Advances and Prospects for Whispering Gallery Mode Microcavities", Advanced Optical Materials, 2015 Publication	<1%
14	Christoph Hunziker. "Configurationally locked, phenolic polyene organic crystal 2-{3-(4-hydroxystyryl)-5,5-dimethylcyclohex-2-	<1%

enylidene}malononitrile: linear and nonlinear optical properties", Journal of the Optical Society of America B, 10/01/2008
Publication

---

15 Yoshinori Tokura. "Organic ferroelectrics", Nature Materials, 05/2008 <1%
Publication

---

16 Tayi, Alok S., Adrien Kaeser, Michio Matsumoto, Takuzo Aida, and Samuel I. Stupp. "Supramolecular ferroelectrics", Nature Chemistry, 2015. <1%
Publication

---

17 P. Poornesh, Seetharam Shettigar, G. Umesh, K.B. Manjunatha, K. Prakash Kamath, B.K. Sarojini, B. Narayana. "Nonlinear optical studies on 1,3-disubstituent chalcones doped polymer films", Optical Materials, 2009 <1%
Publication

---

18 Tatiana Molotsky, Dan Huppert. "Solvation Statics and Dynamics of Coumarin 153 in Dioxane−Water Solvent Mixtures", The Journal of Physical Chemistry A, 2003 <1%
Publication

---

19 Radhika Vattikunta, Dasari Venkatakrishnarao, Chakradhar Sahoo, Sri Ram Gopal Naraharisetty et al. "Photonic Microresonators from Charge Transfer in Polymer Particles: <1%

Toward Enhanced and Tunable Two-Photon Emission", ACS Applied Materials & Interfaces, 2018
Publication

---

20 Naisa Chandrasekhar, Rajadurai Chandrasekar. ""Click-Fluors": Synthesis of a Family of π-Conjugated Fluorescent Back-to-Back Coupled 2,6-Bis(triazol-1-yl)pyridines and Their Self-Assembly Studies", The Journal of Organic Chemistry, 2010 <1%
Publication

---

21 www.lasun-jlu.cn <1%
Internet Source

---

22 San-Hui Chi. "Thick Optical-Quality Films of Substituted Polyacetylenes with Large, Ultrafast Third-Order Nonlinearities and Application to Image Correlation", Advanced Materials, 09/03/2008 <1%
Publication

---

23 web.mit.edu <1%
Internet Source

---

24 Dasari Venkatakrishnarao, Yemineni S. L. V. Narayana, Mahamad A. Mohaiddon, Evgeniy A. Mamonov et al. "Two-Photon Luminescence and Second-Harmonic Generation in Organic Nonlinear Surface Comprised of Self-Assembled Frustum Shaped Organic <1%

Microlasers", Advanced Materials, 2017
Publication

25	photonicswiki.org Internet Source	<1%
26	Yong Sheng Zhao, Hongbing Fu, Aidong Peng, Ying Ma, Qing Liao, Jiannian Yao. "Construction and Optoelectronic Properties of Organic One-Dimensional Nanostructures", Accounts of Chemical Research, 2010 Publication	<1%
27	www.research-collection.ethz.ch Internet Source	<1%
28	Zhang, Chuang, Yongli Yan, Yong Sheng Zhao, and Jiannian Yao. "Synthesis and applications of organic nanorods, nanowires and nanotubes", Annual Reports Section "C" (Physical Chemistry), 2013. Publication	<1%
29	Submitted to UC, Boulder Student Paper	<1%
30	Xiaogang Liu, Jacqueline M. Cole, Paul G. Waddell, Tze-Chia Lin, Scott McKechnie. "Molecular Origins of Optoelectronic Properties in Coumarins 343, 314T, 445, and 522B", The Journal of Physical Chemistry C, 2013 Publication	<1%

31	Wei Zhang, Jiannian Yao, Yong Sheng Zhao. "Organic Micro/Nanoscale Lasers", Accounts of Chemical Research, 2016 Publication	<1%
32	Yang, Shancheng, Yue Wang, and Handong Sun. "Advances and Prospects for Whispering Gallery Mode Microcavities", Advanced Optical Materials, 2015. Publication	<1%
33	Yongchao Dong, Keyi Wang, Xueying Jin. "Package of a dual-tapered-fiber coupled microsphere resonator with high Q factor", Optics Communications, 2015 Publication	<1%
34	cora.ucc.ie Internet Source	<1%
35	Chuang Zhang, Yongli Yan, Yong Sheng Zhao, Jiannian Yao. "From Molecular Design and Materials Construction to Organic Nanophotonic Devices", Accounts of Chemical Research, 2014 Publication	<1%
36	Submitted to Oesterbro International School Student Paper	<1%
37	Submitted to RMIT University Student Paper	<1%

38	documents.mx Internet Source	<1%
39	spie.org Internet Source	<1%
40	K. Kumar. "One- and two-photon-pumped luminescence studies on DAST and UDAST organic dye molecules", Applied Physics B, 05/15/2009 Publication	<1%
41	Chandrasekhar, Naisa, Md Ahamad Mohiddon, and Rajadurai Chandrasekar. "Organic Submicro Tubular Optical Waveguides: Self-Assembly, Diverse Geometries, Efficiency, and Remote Sensing Properties", Advanced Optical Materials, 2013. Publication	<1%
42	Venkataramudu, Uppari, Naisa Chandrasekhar, Supratim Basak, Muvva D. Prasad, and Rajadurai Chandrasekar. "Fabrication of High-Resolution 4,82 -Type Archimedean Nanolattices Composed of Solution Processable Spin Cross-Over Fe(II) Metallosupramolecular Polymers", Macromolecular Rapid Communications, 2015. Publication	<1%
43	Submitted to University of Central Florida Student Paper	<1%

44	Soft and Biological Matter, 2015. Publication	<1%
45	Centore, Roberto, Mojca Jazbinsek, Angela Tuzi, Antonio Roviello, Amedeo Capobianco, and Andrea Peluso. "A series of compounds forming polar crystals and showing single-crystal-to-single-crystal transitions between polar phases", CrystEngComm, 2012. Publication	<1%
46	Springer Theses, 2016. Publication	<1%
47	porto.polito.it Internet Source	<1%
48	Zhao, Yong Sheng, and Jiannian Yao. "Organic One-Dimensional Nanostructures: Construction and Optoelectronic Properties", One-Dimensional Nanostructures Principles and Applications, 2013. Publication	<1%
49	www.chemweb.com Internet Source	<1%
50	M. Bass. "Optical Rectification", Physical Review, 04/1965 Publication	<1%
51	Jinxu Qi, Qian Yao, Kun Qian, Liang Tian, Zhen	<1%

Cheng, Dongmei Yang, Yihong Wang. "Synthesis, antiproliferative activity and mechanism of gallium(III)-thiosemicarbazone complexes as potential anti-breast cancer agents", European Journal of Medicinal Chemistry, 2018

Publication

---

52 Supratim Basak, Pramiti Hui, Sathyanarayana Boodida, Rajadurai Chandrasekar. "Micropatterning of Metallopolymers: Syntheses of Back-to-Back Coupled Octylated 2,6-Bis(pyrazolyl)pyridine Ligands and Their Solution-Processable Coordination Polymers", The Journal of Organic Chemistry, 2012 <1%

Publication

---

53 Yemineni S. L. V. Narayana, Dasari Venkatakrishnarao, Arani Biswas, Mahamad Ahamad Mohiddon et al. " Visible–Near-Infrared Range Whispering Gallery Resonance from Photonic μ-Sphere Cavities Self-Assembled from a Blend of Polystyrene and Poly[4,7-bis(3-octylthiophene-2-yl)benzothiadiazole- -2,6-bis(pyrazolyl)pyridine] Coordinated to Tb(acac) ", ACS Applied Materials & Interfaces, 2015 <1%

Publication

---

54 T. Gustavsson, L. Cassara, V. Gulbinas, G. Gurzadyan, J.-C. Mialocq, S. Pommeret, M. <1%

Sorgius, P. van der Meulen. "Femtosecond Spectroscopic Study of Relaxation Processes of Three Amino-Substituted Coumarin Dyes in Methanol and Dimethyl Sulfoxide", The Journal of Physical Chemistry A, 1998

Publication

---

55 Guang S. He, Loon-Seng Tan, Qingdong Zheng, Paras N. Prasad. "Multiphoton Absorbing Materials: Molecular Designs, Characterizations, and Applications", Chemical Reviews, 2008 <1%

Publication

---

56 dyuthi.cusat.ac.in <1%

Internet Source

---

57 boa.unimib.it <1%

Internet Source

---

58 Radhika Vattikunta, Dasari Venkatakrishnarao, Chakradhar Sahoo, Sri Ram Gopal Naraharisetty et al. "Photonic Microresonators from Charge-Transfer in Polymer Particles - toward Enhanced and Tunable Two-Photon Emission", ACS Applied Materials & Interfaces, 2018 <1%

Publication

---

59 Sava A. Denev. "Probing Ferroelectrics Using Optical Second Harmonic Generation", Journal of the American Ceramic Society, 09/2011 <1%

	Publication	
60	Submitted to Ajou University Graduate School Student Paper	<1%
61	Submitted to National University of Singapore Student Paper	<1%
62	polen.itu.edu.tr Internet Source	<1%
63	researchbank.rmit.edu.au Internet Source	<1%
64	mro.massey.ac.nz Internet Source	<1%
65	Submitted to Indian Institute of Science, Bangalore Student Paper	<1%
66	Mariacristina Rumi. "Two-Photon Absorbing Materials and Two-Photon-Induced Chemistry", Photoresponsive Polymers I, 2008 Publication	<1%
67	Sufang Han, Wei Zhang, Bing Qiu, Haiyun Dong, Wenjie Chen, Manman Chu, Yingying Liu, Xinzheng Yang, Fengqin Hu, Yong Sheng Zhao. "Controlled Assembly of Organic Composite Microdisk/Microwire Heterostructures for Output Coupling of Dual-Color Lasers", Advanced Optical Materials,	<1%

2018
Publication

68	Zhao, Yong Sheng, Hongbing Fu, Aidong Peng, Ying Ma, Qing Liao, and Jiannian Yao. "Construction and Optoelectronic Properties of Organic One-Dimensional Nanostructures", Accounts of Chemical Research, 2010. Publication	<1%
69	Zhi-Zhou Li, Yi-Chen Tao, Xue-Dong Wang, Liang-Sheng Liao. "Organic Nanophotonics: Self-Assembled Single-Crystalline Homo-/Heterostructures for Optical Waveguides", ACS Photonics, 2018 Publication	<1%
70	Swapna, Battini, Kuthuru Suresh, and Ashwini Nangia. "Color polymorphs of aldose reductase inhibitor epalrestat: configurational, conformational and synthon differences", Chemical Communications, 2016. Publication	<1%
71	Jasmina M. Dimitrić Marković. "Delphinidin–Aluminum(III) Complexes in Aqueous and Non-Aqueous Media: Spectroscopic Characterization and Theoretical Study", Monatshefte für Chemie - Chemical Monthly, 12/2007 Publication	<1%

72	www.freepatentsonline.com Internet Source	<1%
73	Submitted to Heriot-Watt University Student Paper	<1%
74	Submitted to Université Claude Bernard Lyon 1 Student Paper	<1%
75	Gopal S. Jayabalan, Josef F. Bille. "Confocal and Multiphoton Imaging of Cornea", Elsevier BV, 2018 Publication	<1%
76	L. He. "Whispering gallery microcavity lasers", Laser & Photonics Review, 02/27/2012 Publication	<1%
77	Submitted to Ewha Womans University Student Paper	<1%
78	Submitted to University of KwaZulu-Natal Student Paper	<1%
79	Supratim Basak. "Multiluminescent Hybrid Organic/Inorganic Nanotubular Structures: One-Pot Fabrication of Tricolor (Blue-Red-Purple) Luminescent Parallepipedic Organic Superstructure Grafted with Europium Complexes", Advanced Functional Materials, 02/22/2011 Publication	<1%

80	Submitted to Sahyadri College of Engineering and Management Student Paper	<1%
81	S Olariu. "Nuclear Multiphoton Transitions Induced by Modulated Hyperfine Electric-Field Gradients", EPL (Europhysics Letters), 11/01/1986 Publication	<1%
82	Heremans, Paul, Gerwin H. Gelinck, Robert Müller, Kang-Jun Baeg, Dong-Yu Kim, and Yong-Young Noh. "Polymer and Organic Nonvolatile Memory Devices†", Chemistry of Materials, 2011. Publication	<1%
83	Submitted to Univerza v Ljubljani Student Paper	<1%
84	Cong Wei, Si-Yun Liu, Chang-Ling Zou, Yingying Liu, Jiannian Yao, Yong Sheng Zhao. "Controlled Self-Assembly of Organic Composite Microdisks for Efficient Output Coupling of Whispering-Gallery-Mode Lasers", Journal of the American Chemical Society, 2015 Publication	<1%
85	Sarojadevi, Muthusamy. "Influence of Graphene Oxide on Thermal, Electrical, and	<1%

Morphological Properties of New Achiral Polyimide.(Report)", Polymer Engineering and Science
Publication

86	Bian, Y.. "Raman spectroscopic characteristics of phthalocyanine and naphthalocyanine in sandwich-type phthalocyaninato and porphyrinato rare earth complexes", Vibrational Spectroscopy, 20030506 Publication	<1%
87	Keqian Zhang, Dejie Li. "Electromagnetic Theory for Microwaves and Optoelectronics", Springer Nature America, Inc, 1998 Publication	<1%
88	publications.polymtl.ca Internet Source	<1%
89	researchportal.hw.ac.uk Internet Source	<1%
90	Submitted to Imperial College of Science, Technology and Medicine Student Paper	<1%
91	Supratim Basak, Yemineni S. L. V. Narayana, Martin Baumgarten, Klaus Müllen, Rajadurai Chandrasekar. "White Light Emitting Films from Eu(III) Complexed Copolymers of Alternating Fluorene and Bis(pyrazolyl)pyridine Derivatives", Macromolecules, 2013	<1%

Publication

92	scholarbank.nus.edu.sg Internet Source	<1%
93	www.ccsenet.org Internet Source	<1%
94	Xuedong Wang, Hui Li, Yishi Wu, Zhenzhen Xu, Hongbing Fu. "Tunable Morphology of the Self-Assembled Organic Microcrystals for the Efficient Laser Optical Resonator by Molecular Modulation", Journal of the American Chemical Society, 2014 Publication	<1%
95	Lidong Li. "Oligomerization and Polymerization of Olefins with Iron and Cobalt Catalysts Containing 2,6-Bis(imino)pyridine and Related Ligands", Catalysis by Metal Complexes, 2011 Publication	<1%
96	Biao Lu, Yongchun Fang, Ning Sun. "Global stabilization of inertia wheel systems with a novel sliding mode-based strategy", 2016 14th International Workshop on Variable Structure Systems (VSS), 2016 Publication	<1%
97	www.patents.com Internet Source	<1%
98	www.scm.com	

Internet Source

<1%

Exclude quotes	On	Exclude matches	< 10 words
Exclude bibliography	On		